

UC Santa Barbara

UC Santa Barbara Electronic Theses and Dissertations

Title

Charge-Carrier Dynamics and Structural Characterization of Layered Hybrid Halide Perovskites

Permalink

<https://escholarship.org/uc/item/2kn3j1t3>

Author

Venkatesan, Naveen

Publication Date

2020

Copyright Information

This work is made available under the terms of a Creative Commons Attribution License, available at <https://creativecommons.org/licenses/by/4.0/>

Peer reviewed|Thesis/dissertation

University of California
Santa Barbara

Charge-Carrier Dynamics and Structural Characterization of Layered Hybrid Halide Perovskites

A dissertation submitted in partial satisfaction
of the requirements for the degree

Doctor of Philosophy
in
Materials

by

Naveen Raj Venkatesan

Committee in charge:

Professor Michael L. Chabinyc, Chair
Professor Jon A. Schuller
Professor Craig J. Hawker
Professor Stephen D. Wilson

March 2020

The Dissertation of Naveen Raj Venkatesan is approved.

Professor Jon A. Schuller

Professor Craig J. Hawker

Professor Stephen D. Wilson

Professor Michael L. Chabinye, Committee Chair

March 2020

Charge-Carrier Dynamics and Structural Characterization of Layered Hybrid Halide
Perovskites

Copyright © 2020

by

Naveen Raj Venkatesan

Acknowledgements

The work presented in this text would not have been possible without the help and support of many people. First and foremost, I am indebted to my advisor, Michael, for taking a chance on me and giving me an opportunity to take on a problem that I had very little expertise in. He really gave me the freedom to learn and suffer (at times) while I treaded the relatively uncharted waters of inorganic chemistry and solid-state physics. Without his guidance and support, I would not be the capable, independent scientist that I am today.

The other members of the Chabinye research group were also integral in creating a wonderful research environment over my time at UCSB. I would like to acknowledge John for being a great resource to bounce ideas off of when I was a new graduate student in the group. To the perovskite “team”, we were very productive and achieved a lot together, carving our own niche in a new research field. To the group members working on organic projects, I always learned something new at every group meeting/conference presentation, and it allowed me to see my own work with a new perspective.

I also must acknowledge Professor Nitash Balsara, who introduced me to the world of academic research as a young undergraduate. His support, along with the guidance of my graduate student mentors Shrayesh and Jacob, left an impression on me and drove me to pursue graduate studies. I thank them and the entire Balsara group for bringing me in and treating me as one of their own.

To friends (old and new), these past few years would not have been nearly as fun without you. I had the privilege of traveling quite a bit during my time in graduate school, from Reykjavik to Havana to Montreal, all because I had a great group of people to go with.

I am so thankful to have family that has always supported me to pursue my passions and dreams. My mother, Lali, was my main academic motivator growing up but passed

away when I was in high school – these moments are always a little bittersweet without her, but I am sure she would have been proud. My father, Raj, has done so much for me and my little sister, raising us through some of the more formative years of our lives by himself. For this, I will forever be grateful. My sister, Neesha, is an all-around great person – out of the two of us, she’s the one who got the street smarts. Finally, my grandparents in India have always been very supportive of my goals and proud of my accomplishments.

I would like to thank everyone that I have crossed paths with, both from my time at UC Berkeley and here at UC Santa Barbara. In one way or another, all these interactions have led me to the person I am today.

Curriculum Vitæ

Naveen Raj Venkatesan

Education

- 2020 Ph.D. in Materials (Expected), University of California, Santa Barbara.
- 2015 M.S. in Materials Science and Engineering, University of California, Berkeley.
- 2014 B.S. in Chemical Engineering and Materials Science, University of California, Berkeley.

Publications

12. R. A. DeCrescent, **N. R. Venkatesan**, C. J. Dahlman, R. M. Kennard, X. Zhang, W. Li, X. Du, M. L. Chabinyc, R. Zia, and J. A. Schuller, Bright magnetic dipole radiation from two-dimensional lead-halide perovskites, *Sci. Adv.*, **2020**, 6 (6), eaay4900.
11. R. A. DeCrescent, **N. R. Venkatesan**, C. J. Dahlman, R. M. Kennard, M. L. Chabinyc, and J. A. Schuller, Optical constants and effective-medium origins of large optical anisotropies in layered hybrid organic/inorganic perovskites, *ACS Nano*, **2019**, 13 (9), 10745 – 10753.
10. **N. R. Venkatesan**, A. Mahdi, B. Barraza, G. Wu, M. L. Chabinyc, and R. Seshadri, Enhanced yield-mobility products in hybrid halide Ruddlesden–Popper compounds with aromatic ammonium spacers, *Dalton Trans.*, **2019**, 48 (37), 14019 – 14026.
9. C. J. Dahlman, R. A. DeCrescent, **N. R. Venkatesan**, R. M. Kennard, G. Wu, M. A. Everest, J. A. Schuller, and M. L. Chabinyc, Controlling solvate intermediate growth for phase-pure organic lead iodide Ruddlesden–Popper $(C_4H_9NH_3)_2(CH_3NH_3)_{n-1}Pb_nI_{3n+1}$ perovskite thin films, *Chem. Mater.*, **2019**, 31 (15), 5832 – 5844.
8. **N. R. Venkatesan**, R. M. Kennard, R. A. DeCrescent, H. Nakayama, C. J. Dahlman, E. E. Perry, J. A. Schuller, and M. L. Chabinyc, Phase intergrowth and structural defects in organic metal halide Ruddlesden–Popper thin films, *Chem. Mater.*, **2018**, 30 (23), 8615 – 8623.
7. J. G. Labram, E. E. Perry, **N. R. Venkatesan**, and M. L. Chabinyc, Steady-state microwave conductivity reveals mobility-lifetime product in methylammonium lead iodide, *Appl. Phys. Lett.*, **2018**, 113 (15), 153902.

6. E. E. Perry, J. G. Labram, **N. R. Venkatesan**, H. Nakayama, and M. L. Chabinyc, N-type surface doping of MAPbI₃ via charge transfer from small molecules, *Adv. Electron. Mater.*, **2018**, *4*, 1800087.
5. B. McDearmon, E. Lim, I.-H. Lee, L. M. Kozycz, K. O'Hara, P. I. Robledo, **N. R. Venkatesan**, M. L. Chabinyc, and C. J. Hawker, Effects of Side-Chain Topology on Aggregation of Conjugated Polymers, *Macromolecules*, **2018**, *51* (7), 2580 – 2590.
4. **N. R. Venkatesan**, J. G. Labram, and M. L. Chabinyc, Charge-carrier dynamics and crystalline texture of layered Ruddlesden–Popper hybrid lead iodide perovskite thin-films, *ACS Energy Lett.*, **2018**, *3*, 380 – 386.
3. J. G. Labram[†], **N. R. Venkatesan**[†], C. J. Takacs, H. A. Evans, E. E. Perry, F. Wudl, and M. L. Chabinyc, Charge transport in a two-dimensional hybrid metal halide thiocyanate compound, *J. Mater. Chem. C*, **2017**, *5*, 5930 – 5938. ([†]These authors contributed equally)
2. J. L. Thelen, S. Inceoglu, **N. R. Venkatesan**, N. G. Mackay, and N. P. Balsara, The relationship between ion dissociation, melt morphology, and electrochemical performance of lithium and magnesium single-ion conducting block copolymers, *Macromolecules*, **2016**, *49* (23), 9139 – 9147.
1. M. Chintapalli, T. N. P. Le, **N. R. Venkatesan**, N. G. Mackay, A. A. Rojas, J. L. Thelen, X. C. Chen, D. H. Devaux, and N. P. Balsara, Structure and ionic conductivity of polystyrene-*block*-poly(ethylene oxide) in the high salt concentration limit, *Macromolecules*, **2016**, *49* (5), 1770 – 1780.

Abstract

Charge-Carrier Dynamics and Structural Characterization of Layered Hybrid Halide Perovskites

by

Naveen Raj Venkatesan

Hybrid organic-inorganic perovskite (HOIP) compounds have garnered widespread research attention due to their outstanding optoelectronic properties while being solution-processable semiconductors. When used as the active material in a photovoltaic device, three-dimensionally connected HOIPs based on methylammonium lead iodide ($\text{CH}_3\text{NH}_3\text{PbI}_3$) and associated alloys have demonstrated power conversion efficiencies that have increased at an unprecedented rate, from an initial value of 3.8%, to present day efficiencies exceeding 25% in just a decade. This has made perovskites competitive with existing thin film solar cell technologies like CdTe and CIGS. Additionally, dispersions of nanoparticles of similar perovskite materials have shown controllable optical emission properties with narrow emission linewidths and large ($\sim 95\%$) photoluminescence quantum yields, making them attractive materials for light emitting applications. However, three-dimensionally connected perovskites typically suffer from poor ambient stability, impeding their feasibility in devices for long term use.

Numerous recent research efforts have shown that lower dimensional perovskites, notably two-dimensional layered structures, possess increased ambient material stability. Layered perovskite compounds correspond to structures in which the 3D perovskite structure has been sliced along a specific crystallographic direction, leading to a loss of connectivity in one dimension. Therefore, champion photovoltaic devices made with layered perovskites have only achieved efficiencies around 15% due to the loss of charge transport in one direc-

tion, presenting a fundamental tradeoff between stability and performance. Understanding the optoelectronic and structural properties of layered perovskites is therefore essential for both optimizing device efficiencies and proposing design rules for future materials discovery.

Layered perovskite compounds can be generated through two strategies – partial anion or partial cation substitution during synthesis. This report will discuss the synthesis and characterization of three different systems – one generated through the partial anionic substitution of iodide (I^-) anions with the pseudohalide thiocyanate (SCN^-), and two by partial cationic substitution of methylammonium ($CH_3NH_3^+$) with butylammonium ($C_4H_9NH_3^+$) and 2-(4-biphenyl)ethylammonium ($C_6H_5C_6H_4CH_2CH_2NH_3^+$), respectively. Structural characterization with X-ray and electron diffraction reveals the difficulties in producing phase pure samples from solution processing, and the origin and impact of these impurities on electronic properties will be discussed. Transport properties were measured with contactless time-resolved microwave conductivity measurements and compared with values seen in 3D perovskites. We find that the layered perovskite systems possess similar in-plane mobilities to their three-dimensional counterparts, but with increased higher-order carrier recombination, resulting in shorter lifetimes.

Contents

Curriculum Vitae	vi
Abstract	viii
1 Introduction	1
1.1 The Perovskite Crystal Structure	1
1.2 Hybrid Organic-Inorganic Perovskites	3
1.3 Optoelectronic Properties of Hybrid Perovskites	5
1.4 Deficiencies of Three-Dimensional Perovskites	9
1.5 Layered Perovskite Structures	11
1.6 Properties of Layered Perovskites	13
1.7 Outlook	15
1.8 References	17
2 Simulation and Processing of Two-Dimensional X-Ray Diffraction Data	27
2.1 Introduction	27
2.2 Diffraction scans in reciprocal space	29
2.3 GIWAXS pattern simulation program	32
2.4 Converting binary files from synchrotron to images	44
2.5 Processing two-dimensional X-ray diffraction images	49
2.6 References	61
3 Charge Transport in a Two-Dimensional Hybrid Metal Halide Thiocyanate Compound	62
3.1 Abstract	62
3.2 Introduction	63
3.3 Results and Discussion	65
3.4 Conclusion	74
3.5 Appendix	75
3.6 Acknowledgments	89
3.7 Permissions and Attributions	90

3.8	References	91
4	Charge-Carrier Dynamics and Crystalline Texture of Layered Ruddlesden-Popper Hybrid Lead Iodide Perovskite Thin Films	100
4.1	Abstract	100
4.2	Introduction	101
4.3	Results and Discussion	102
4.4	Conclusion	113
4.5	Appendix	114
4.6	Acknowledgments	129
4.7	Permissions and Attributions	129
4.8	References	130
5	Phase Intergrowth and Structural Defects in Organic Metal Halide Ruddlesden-Popper Thin Films	136
5.1	Abstract	136
5.2	Introduction	137
5.3	Results and Discussion	139
5.4	Conclusion	153
5.5	Appendix	154
5.6	Acknowledgments	176
5.7	Permissions and Attributions	176
5.8	References	177
6	Enhanced Yield-Mobility Products in Hybrid Halide Ruddlesden-Popper Compounds with Aromatic Ammonium Spacers	183
6.1	Abstract	183
6.2	Introduction	184
6.3	Results and Discussion	186
6.4	Conclusion	195
6.5	Appendix	196
6.6	Acknowledgments	204
6.7	Permissions and Attributions	204
6.8	References	205

Chapter 1

Introduction

1.1 The Perovskite Crystal Structure

With the constant pursuit of alternative energy sources to reduce our reliance on fossil fuel based energy, a class of materials that has shown great promise in the past decade are hybrid organic-inorganic halide perovskites (HOIPs). While inorganic semiconductors typically require high-temperature, energy-intensive processing methods to achieve electronic grade purity, HOIP materials are solution-processable, allowing low temperature deposition from solution as a means to produce efficient semiconductors.¹⁻¹⁰ These HOIP materials, in turn, have displayed a wide range of useful optoelectronic properties including excellent light absorption¹¹⁻¹³ and long carrier lifetimes,¹⁴⁻²² making them attractive for light harvesting and emitting applications.

The term “perovskite” refers to a specific crystal structure, given to the mineral calcium titanate (CaTiO_3), which was originally mined in the Ural Mountains of Russia and named after minerologist Lev Perovski.²³ In the times since its initial naming, perovskite has become a term to describe all compounds that crystallize with the same structure as CaTiO_3 . The perovskite crystal structure, shown in Figure 1.1, has a formula unit of ABX_3 . The X

anions surround the central B cation with octahedral coordination, while the A cations sit at the cell corners.

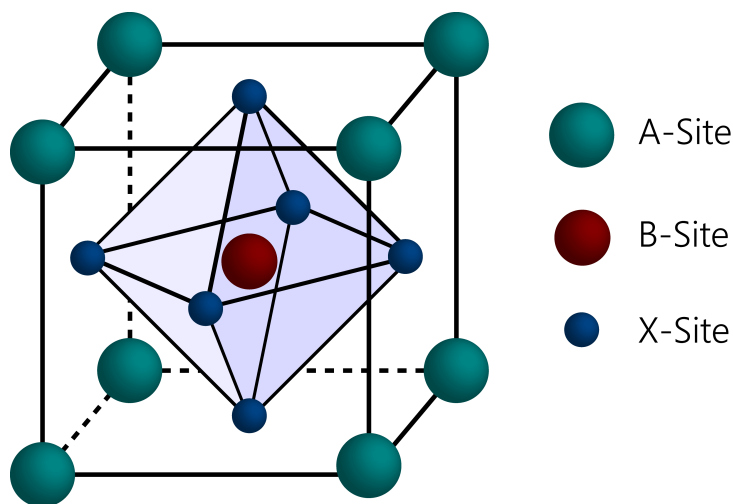


Figure 1.1: The cubic perovskite crystal structure, with formula unit ABX_3 . Compounds are commonly visualized as shown, with X anions surrounding the central B cation with octahedral coordination. The A cations then sit at the corners of the cell.

Compounds with the perovskite crystal structure have been widely studied in the past for their unique properties, such as ferroelectricity^{24,25} and high magnetoresistance,^{26,27} with the majority of materials, like $SrTiO_3$, being oxides. In contrast, HOIPs are halides, and therefore have a halide ion (I^- , Cl^- , Br^-) in the X site of the crystal structure as opposed to O^{2-} . This results in the requirement that the valencies of the A and B sites be 1+ and 2+ (half that of the equivalent oxide), respectively. The term “hybrid” in HOIP is due to the fact that the A site is typically an organic molecular cation, while the B site is a metal such as lead (Pb), tin (Sn), or bismuth (Bi).²⁸⁻³² HOIPs, therefore, typically consist of an inorganic network with molecular cations in the interstitial spaces, though there are entirely inorganic halide perovskites.³³⁻³⁵ The canonical hybrid perovskite, methylammonium lead iodide ($CH_3NH_3PbI_3$) is shown in Figure 1.2, and illustrates these organic and inorganic sublattices.

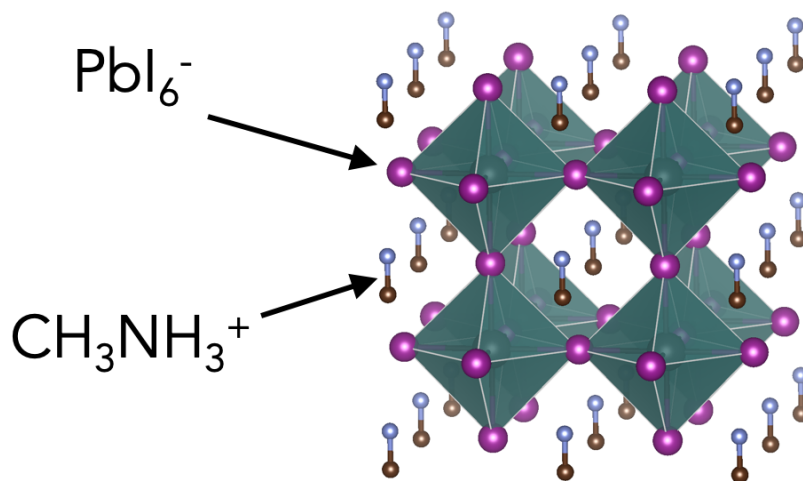


Figure 1.2: Crystal structure of methylammonium lead iodide (CH₃NH₃PbI₃), illustrating the inorganic framework consisting of PbI₆⁻ octahedra, with organic CH₃NH₃⁺ cations in the interstitial spaces.

1.2 Hybrid Organic-Inorganic Perovskites

The first report on a perovskite photovoltaic (PV) cell was published just over 10 years ago from Professor Tsutomu Miyasaka's research group in Yokohama, in which methylammonium lead iodide (1.2) was used as the sensitizer.¹ The power conversion efficiency of the reported cell was a mere 3.8%, however this result marked the beginning of a perovskite research revolution. Figure 1.3 illustrates the number of publications from 2009 to present day with the keyword "perovskite solar cell" (results from Web of Science). Total publications exceeded 3000 in the year 2019, an average of nearly 10 per day. This widespread research excitement has produced an unprecedented rise in the efficiencies of perovskite-based photovoltaic absorbers, with modern-day research cells possessing efficiencies consistently over 20%, with the highest-ever being 25.2%.³⁶ This progress is shown in Figure 1.4, which shows the NREL-certified power conversion efficiencies of perovskite photovoltaics relative to other thin film PV technologies (CIGS, CdTe, organic, and a-Si:H).

The efficiency of perovskite-based PVs has either equaled or surpassed these other thin film technologies, already making them commercially competitive. Additionally, the current state-of-the-art hybrid perovskite materials are essentially alloys, simultaneously utilizing multiple A, B, and X ions to produce increases in performance.^{33,34,37,38}

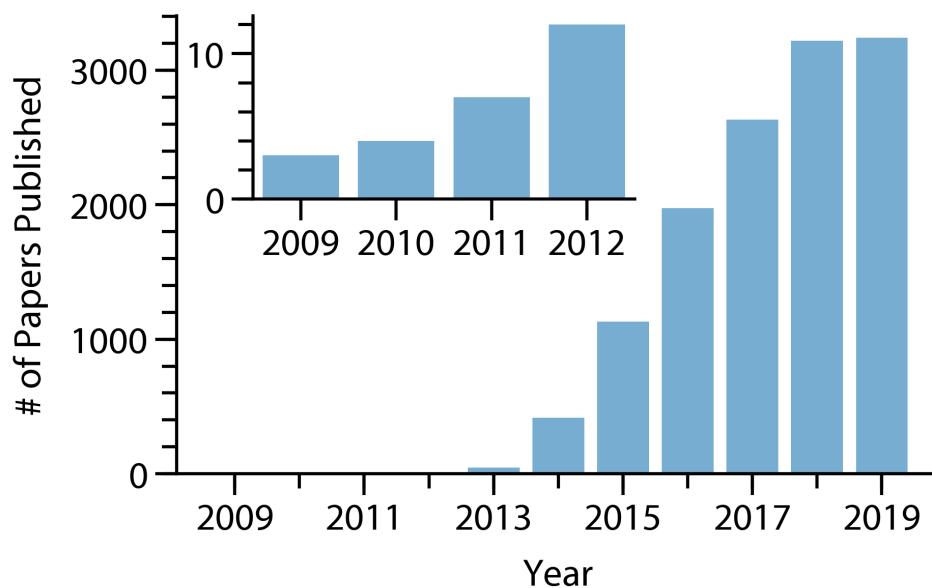


Figure 1.3: Number of publications with the keyword “perovskite solar cell” from the year 2009 to present day, illustrating the exponential rise in research interest and productivity in the field. Data collected from Web of Science, Clarivate Analytics, © 2020.

More recently, perovskite nanoparticles have been explored as a means for light emission with narrow linewidths due to their more controlled synthesis.^{39–43} By tuning the composition of the nanoparticles, control of emission over a wide range of wavelengths has been achieved, and is shown in Figure 1.5.⁴² Additionally, by reducing the size of the perovskite crystals to the nanoscale, a sharp increase in the photoluminescence quantum yield (PLQY) is also achieved, bringing values to in excess of 95%.^{41,42}

Certain low dimensional perovskite crystals have also surprisingly exhibited broadband, white-light emission,^{44,45} and example of which is presented in Figure 1.6.⁴⁶ The origin of these interesting emission properties has been attributed to a rich energetic landscape, re-

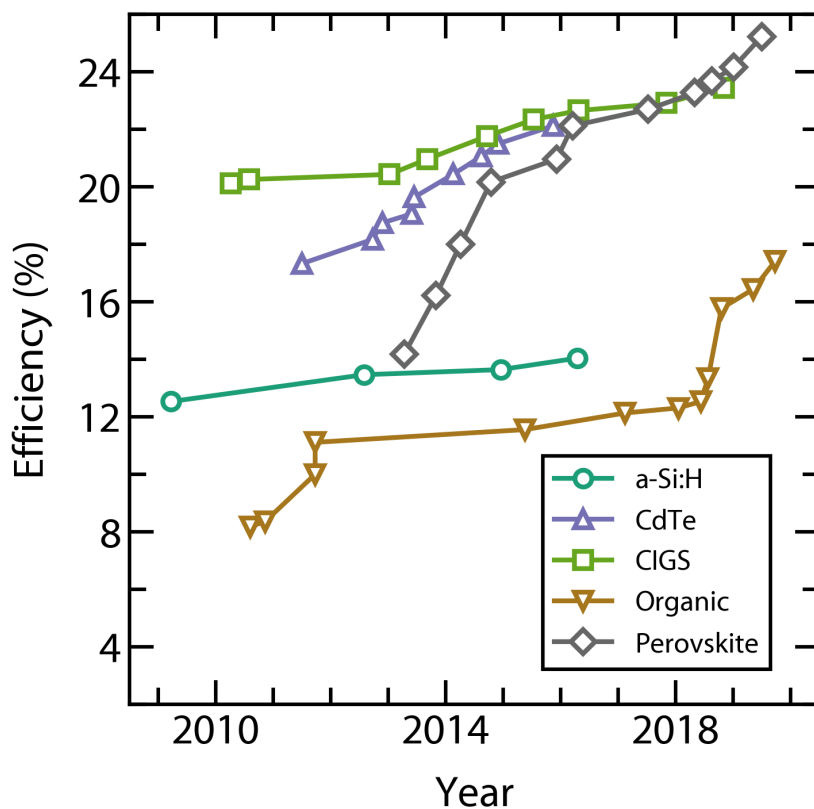


Figure 1.4: Photovoltaic power conversion efficiencies of thin film solar technologies, as certified by the National Renewable Energy Laboratory. Efficiencies of perovskite solar cells have risen at an unprecedented rate and are now higher than all the other thin film technologies. Adapted from original data from NREL at <https://www.nrel.gov/pv/>.

sulting in the self-trapping of excitons.^{44–47} Perovskite materials with this broadband emission represent an alternative to phosphor-based solid-state lighting.

1.3 Optoelectronic Properties of Hybrid Perovskites

The optoelectronic properties of hybrid perovskite materials are extraordinary by many metrics. While reported mobility values of carriers in methylammonium lead iodide are moderate compared to inorganic semiconductors like silicon and gallium arsenide, the lifetimes of carriers is large, on the order of microseconds.^{16,28,48–55} This leads to an increased

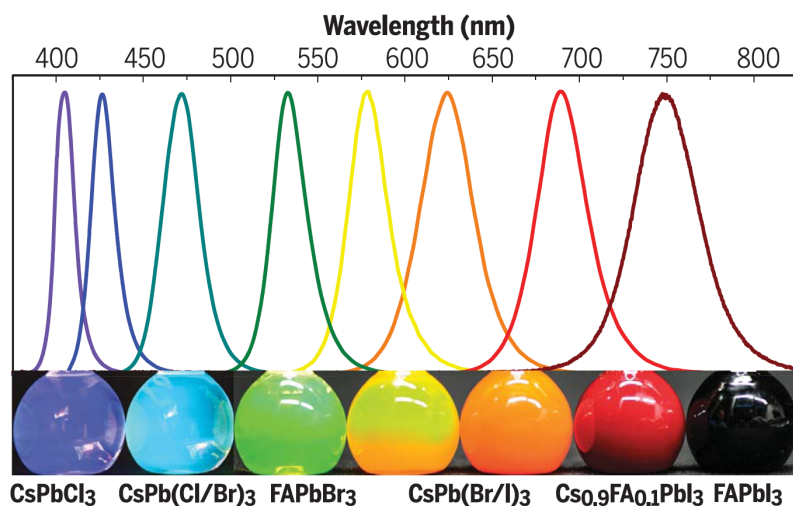


Figure 1.5: Colloidal dispersions of lead halide perovskite nanoparticles illustrating tunable emission wavelengths with narrow linewidths, making them an attractive material for light emitting applications. Reproduced with permission from the American Association for the Advancement of Science, Copyright © 2017.

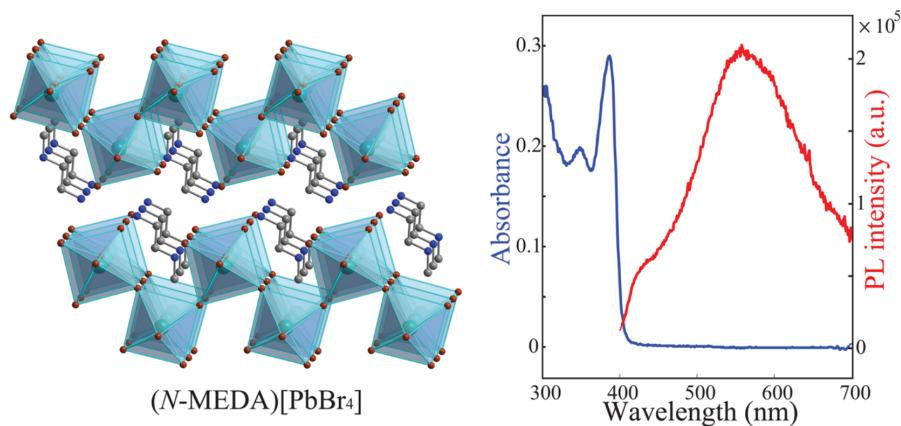


Figure 1.6: Crystal structure of the low-dimensional perovskite compound *N*-methylethane-1,2-diammonium lead bromide (*N*-MEDA) PbBr_4 along with optical absorbance and emission data, showing broadband white-light emission. Reproduced with permission from the American Chemical Society, Copyright © 2016.

mobility-lifetime product, allowing charge carriers to be extracted into the external circuit prior to recombination. Much like organic active materials, hybrid halide perovskites have efficient optical absorption due to their direct bandgaps,^{11–13} prompting their initial use as a PV active material.¹ However, unlike in organic semiconductors, where the dielectric

constants are small, hybrid perovskite have low exciton binding energies, often reported to be below kT at room temperature.^{56–58} Therefore, separation of excitons into charge carriers is trivial and planar structures utilizing perovskite active layers can be fabricated instead of bulk heterojunctions, where donors and acceptors must be phase separated on the nanoscale.^{59–61} This unique combination of optical and electronic properties presents a compromise between typical inorganic semiconductor active materials like silicon (high mobility and lifetime) and solution-processable technologies like organic photovoltaics (large optical absorbance).

The long lifetimes of carriers in perovskites have been long debated and focus on two separate mechanisms: large polarons and Rashba splitting. Figure 1.7 presents a schematic of both of these mechanisms. In the large polaron model, the lattice distortion caused by the charge carriers extends over many unit cells, effectively screening electron-hole pairs from mutual Coulombic interaction and recombination. This theory has been supported by various methods of dielectric spectroscopy and structural measurements under photoexcitation.^{20,21,52,62,63} Rashba splitting, on the other hand, occurs due to the breaking of inversion symmetry upon excitation, causing the conduction and valence bands to split into two degenerate bands with opposite spin values. Carriers excited across the gap then relax into the minima of these two bands, and direct recombination back to the valence band is forbidden.^{22,50,64–66} The result is a material that appears to absorb light like a direct-gap semiconductor but emit light like an indirect-gap semiconductor.

Another spectacular property of methylammonium lead iodide is the lack of shallow electronic trap states. This can be seen in Figure 1.8, which shows absorption coefficient measurements of various semiconductors over a wide magnitude range, measured using photothermal deflection spectroscopy.¹³ At the onset of optical absorption, there is a region that follows an exponential increase called the Urbach tail, and the slope of this region corresponds to the Urbach disorder energy.^{67–69} The relevant formula is presented in Equation

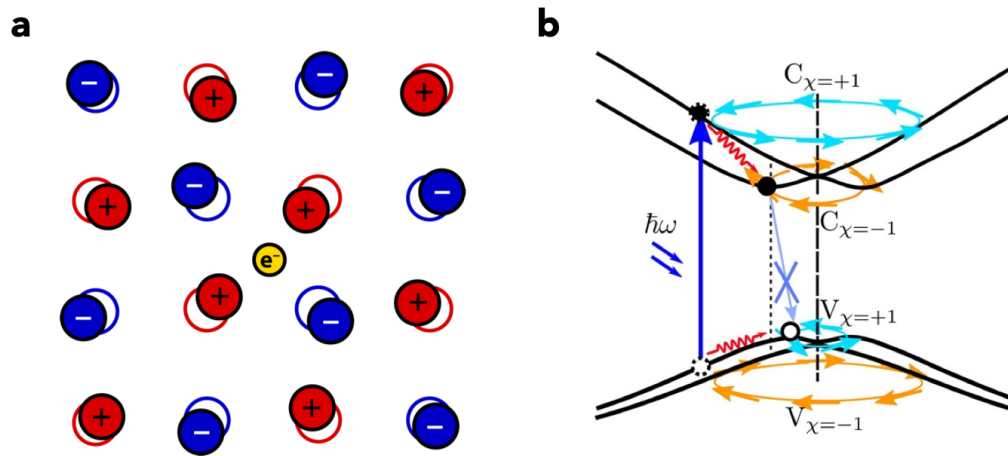


Figure 1.7: (a) Schematic of a large polaron in a crystal lattice showing the distortion of the surrounding ions from their equilibrium positions in response to the Coulombic interaction with the electron. (b) Band structure of material exhibiting the Rashba effect – the conduction and valence bands split into degenerate bands with different spin values, preventing direct recombination. Reproduced with permission from the American Chemical Society, Copyright © 2015.

1.1, where α is the absorption coefficient (α_g is the absorption coefficient at the optical gap), E_g is the energy corresponding to the optical bandgap, and E_0 is the Urbach disorder energy.⁶⁸

$$\alpha(E) = \alpha_g \exp\left(\frac{E - E_g}{E_0}\right) \quad (1.1)$$

The reason that the absorption onset has a finite slope is due to absorption of sub-bandgap photons by electronic defect states. The steeper the slope, the smaller the electronic disorder. Figure 1.8 illustrates the sharp Urbach tail of methylammonium lead iodide relative to that of other semiconductors, with a fitted value of 15 meV, relative to 7.5 meV in gallium arsenide and 11 meV in crystalline silicon.¹³

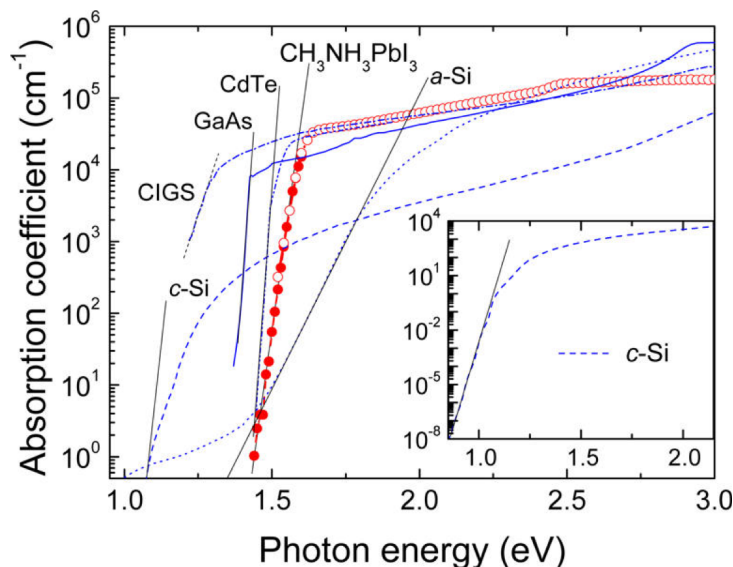


Figure 1.8: Photothermal deflection spectroscopy (PDS) measurements of various semiconductors, illustrating absorption coefficients over a wide magnitude range. The onset of optical absorption increases at an exponential rate, and the slope of this onset corresponds to the Urbach disorder energy, indicative of the amount of electronic disorder due to sub-bandgap defects. Reproduced with permission from the American Chemical Society, Copyright © 2014.

1.4 Deficiencies of Three-Dimensional Perovskites

Hybrid-halide perovskites, despite their objectively impressive electronic properties, have been shown to have poor ambient stability. Previous studies have shown unencapsulated materials stabilities only on the order of days – well below the 25 year stability requirement typically guaranteed in commercial photovoltaic modules.⁷⁰ Measurements of solar efficiencies over time illustrate this steep dropoff, and structural and optical measurements reveal a stark material color change to yellow, indicative of the precursor lead iodide (PbI_2) as confirmed by X-ray diffraction measurements.⁷¹ This suggests that the degradation occurs through the reverse reaction of the material synthesis (shown in Equation 1.2).



Proposed degradation pathways have extensively focused on the role of moisture in this reverse reaction to lead iodide.⁷² In addition, studies exploring the role of other external factors such as heat and prolonged light exposure have concluded that these also contribute to material instability.^{70,73–76} Efficient encapsulation methods to prevent water ingress are one route to preserving materials integrity,^{77,78} but designing new materials with innate stability provides a more robust solution to the perovskite degradation issue. Therefore, by using the perovskite structure as a motif for new materials design, new structures can be discovered that have an appropriate balance between stability and electronic performance.

The major issues with chemical design of new perovskite structures are the limits in the size of atoms that can be placed in the A, B, and X sites of the structure. Equation 1.3 shows the Goldschmidt Tolerance Factor, a metric that can be used to predict whether certain atoms would crystallize in the perovskite structure based on their ionic radii.⁷⁹ Based on the value of this tolerance factors, the resulting crystal structure can be a perovskite with either cubic or distorted symmetry, or an entirely other structure – these expected structures are shown in Table 1.1. Due to these size limitations, only a few organic molecules have been successfully used in the A-site of a three-dimensional perovskite, with the majority of studies focusing on methylammonium (CH_3NH_3^+) and formamidinium ($\text{HC}(\text{NH}_2)_2^+$).^{1,3,80} Part of the reason for the difficulty in incorporating molecular organic cations is the ambiguity in assigning ionic radii to dynamically-moving molecules.^{81,82} Relaxation of this constraint results in the breaking of connectivity in the perovskite structure, resulting in zero, one, and two-dimensional structures.⁵ Several examples of such structures include vacancy-ordered perovskites,⁸³ double perovskites,⁸⁴ hollow perovskites,⁸⁵ and layered perovskites⁸⁶ – the focus of this work will be on layered perovskite systems.

$$t = \frac{r_A + r_X}{\sqrt{2}(r_B + r_X)} \quad (1.3)$$

Table 1.1: Expected structures based on the value of the Goldschmidt Tolerance Factor.

t	Structure
> 1	Hexagonal/Tetragonal
0.9 – 1	Cubic
0.71 – 0.9	Orthorhombic/Rhombohedral
< 0.71	Different Structure (Non-Perovskite)

1.5 Layered Perovskite Structures

Layered perovskite structures are synthesized through partial inclusion of atoms that are too large to fit into the perovskite structure. This can be achieved through two strategies – partial anionic and partial cationic substitution. Partial anionic substitution aims to swap some of the halide ions in the structure with a larger but chemically similar ion. In this work, this was achieved with the polyatomic ion thiocyanate (SCN^-), which selectively substitutes axial iodide anions in the structure. The large size of the SCN^- ion causes the structure to be physically broken into pseudo two-dimensional slabs, a structure previously described for the compound K_2NiF_4 .^{87–95}

Partial cationic substitution aims to create this layered structure through the incorporation of larger molecular cations that physically separate the inorganic regions.^{96–100} This structure is called a Ruddlesden–Popper phase and is the natural layered analog of the perovskite structure.^{101,102} In these Ruddlesden–Popper phases, an important characteristic is the n value, which is representative of the thickness of the layers between the organic regions, and is then number of lead iodide octahedra present in the layer stacking direction. This is illustrated in Figure 1.9 – A' represents the larger organic cation, and the overall stoichiometry is $A'_2A_{n-1}B_nX_{3n+1}$, with n corresponding to the n value of the particular structure.

The potential advantage of using an anion substituted layered perovskite over a

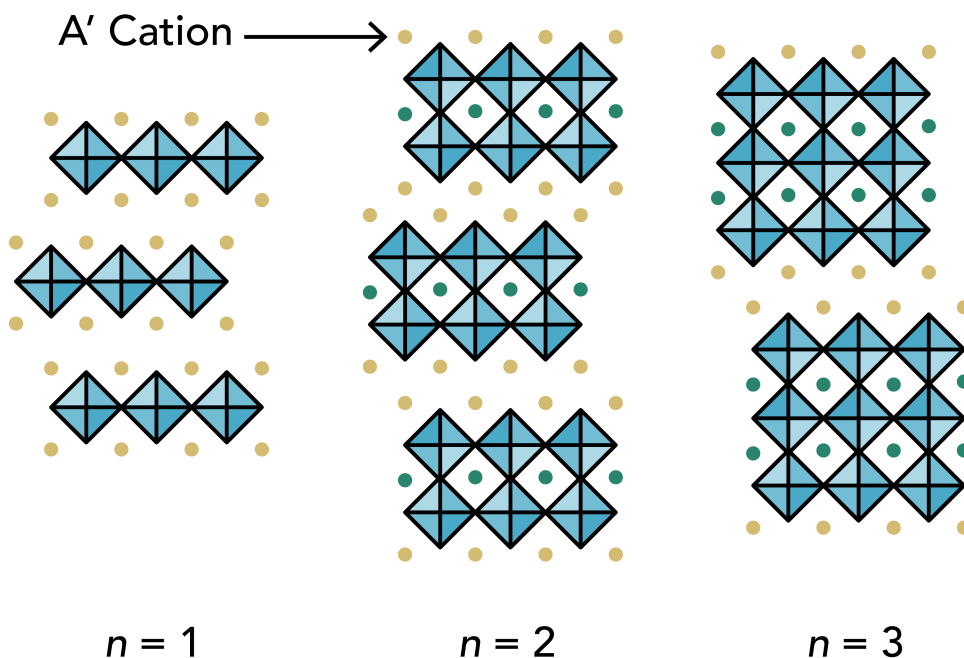


Figure 1.9: Schematic of the Ruddlesden–Popper crystal structure, illustrating the difference in n values. Each subsequent layer in the structure is slipped by half of a unit cell from the one below and above it. The A' cation is labeled – in hybrid halide Ruddlesden–Popper phases this is often a larger organic molecular cation, while in oxides can typically be the same as the A cation.

Ruddlesden–Popper phase is the smaller interlayer spacing. This is shown in Figure 1.10, with a Ruddlesden–Popper phase with n -butylammonium ($C_4H_9NH_3^+$) compared to the thiocyanate substituted $(CH_3NH_3)_2Pb(SCN_2)I_2$.

Major excitement in the development of layered perovskite materials in recent years is due to their drastically improved materials stability.^{86,103–105} A recent study showed stability for one year in photovoltaic efficiency consisting of a mixture of methylammonium lead iodide and a Ruddlesden–Popper perovskite utilizing aminovaleric acid iodide ($HOOC(CH_2)_4NH_3I$) as the larger cation.¹⁰⁶ The efficiencies are however, still modest compared to fully three-dimensional perovskites, with champion devices based on layered perovskites only achieving maximum efficiencies of around 15%.⁹⁶ Despite this, these studies represent a substantial advancement towards more stable perovskite materials.

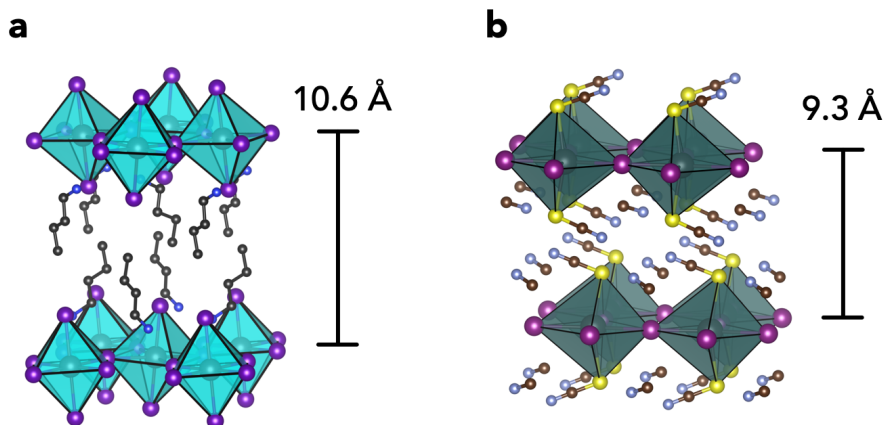


Figure 1.10: Comparison of the interlayer spacings of the cation substituted (a) $(\text{C}_4\text{H}_9\text{NH}_3)_2\text{PbI}_4$ and the anion substituted (b) $(\text{CH}_3\text{NH}_3)_2\text{Pb}(\text{SCN})_2\text{I}_2$, showing closer spacing between layers with anion substitution.

1.6 Properties of Layered Perovskites

Due to the loss of three dimensional connectivity in layered perovskite materials, their optical and electronic properties become highly anisotropic. This is due to the fact that the layered perovskites form a natural quantum well structure, as shown in Figure 1.11, with alternating semiconducting and insulating layers. This results in poor electronic coupling between subsequent semiconducting layers along this direction.^{88,107} Charge transport in this direction is therefore likely not bandlike, but can be possible through a hopping mechanism. Regardless, the fast transport directions are within the plane of the lead iodide sheets. This becomes an issue in device fabrication, where these semiconducting sheets must be oriented along the desired direction of transport for efficient performance. At higher n value Ruddlesden–Popper phases, however, it has been found that these sheets naturally orient perpendicularly to the substrate surface, which has allowed fabrication of vertical photovoltaic devices.^{96,99,108} Due to this structural anisotropy, synthetic control over the

crystalline texture is important for device integration.

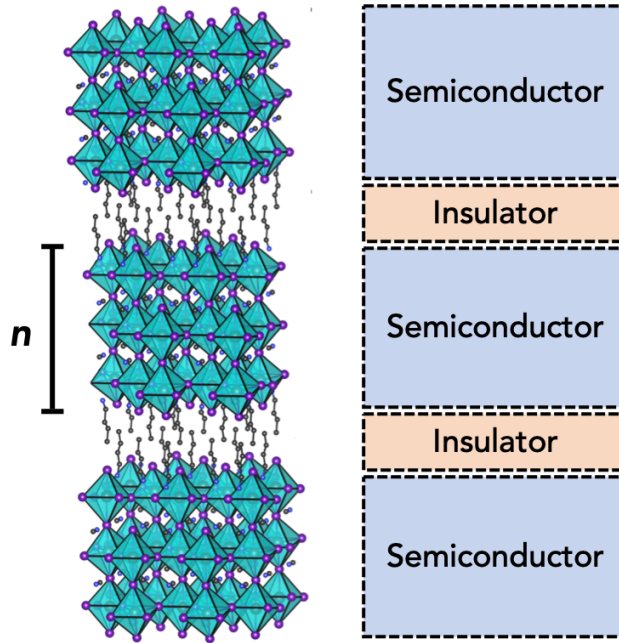


Figure 1.11: Hybrid halide Ruddlesden–Popper phase with arbitrary n value, illustrating naturally-formed quantum well structure of alternating semiconducting and insulating layers.

The structural confinement of the semiconductor layer in Ruddlesden–Popper phases also results in a material that exhibits highly excitonic optical properties.^{56,109–112} An exciton is quasiparticle comprising an electron-hole pair that is still bound by its mutual Coulombic attraction.¹¹³ This electrostatic attraction leads to a stabilization and lowering in the overall energy of the exciton, called the exciton binding energy (E_b). This corresponds to the energy needed to ionize the exciton back into a free electron and hole. For this reason, excitonic absorption appears as a peak slightly lower in energy than the true optical gap of a material.¹¹³

An exciton can be thought of using an hydrogenic model – the exciton Bohr radius cor-

responds to the distance between the electron hole pair.¹¹⁴ When a material is sufficiently large in all dimensions (*i.e.* much larger than the exciton Bohr radius), dissociation of excitons (provided there is sufficient energy to ionize the exciton) is trivial. However, as these dimensions grow smaller and closer to order of this radius, as in layered perovskite phases, dissociation of the exciton is much more difficult and the binding energies of these excitons are typically $\sim 200 - 300$ meV.^{58,90} Additionally, the effective dielectric environment in the layered perovskite phase is different – because of the organic layer, the dielectric constant is lower.^{114,115} This reduces the screening between the electron-hole pair and increases its binding energy.

This excitonic nature of layered perovskites is highly detrimental to the performance of perovskite photovoltaic devices. This is because current must be extracted into the external circuit by virtue of electrons and holes flowing through to opposite contacts. Bound excitons are quasiparticles with no net charge – this exciton therefore does not separate and get extracted as charge from the device, leading to a lower overall efficiency. For light emitting applications, however, excitonic absorption results in narrow emission linewidths which, if coupled with large photoluminescence quantum yields, can result in efficient light emitting devices.^{39,41,42}

1.7 Outlook

Layered perovskite phases clearly represent an interesting class of materials that have potential for widespread use due to their increased material stability over their three-dimensional counterparts. As previously described, the breaking of 3D connectivity in producing layered perovskite phases leads to highly anisotropic structural, optical, and electronic properties which much be well-understood for future materials design and optimization. This work elucidates the structural and optoelectronic behavior of some of

these layered perovskites as functional thin films for devices. The first section of this work discusses the anion substituted $(\text{CH}_3\text{NH}_3)_2\text{Pb}(\text{SCN})_2\text{I}_2$, revealing transport properties similar to three-dimensional methylammonium lead iodide.⁹⁵ The following chapters discuss an in-depth thin film study of a series of Ruddlesden–Popper phases utilizing *n*-butylammonium as the larger organic cation, $(\text{C}_4\text{H}_9\text{NH}_3)_2(\text{CH}_3\text{NH}_3)_{n-1}\text{Pb}_n\text{I}_{3n+1}$.^{98,99} We find that these phases have a gradual crystalline texture change with *n*, where lead iodide sheets move from being entirely parallel to the substrate surface, to almost entirely perpendicular as *n* increases. The charge carrier dynamics show shorter lifetimes than $\text{CH}_3\text{NH}_3\text{PbI}_3$ and show considerable higher-order carrier recombination whose average order also increases as *n* increases.⁹⁹ The nanoscale thin film structure of these films was then probed with synchrotron X-ray diffraction and transmission electron microscopy and found to exhibit significant phase impurity. However, these impurity phases appear to be well-isolated electronically as they do not contribute significantly to the electronic disorder, leading us to believe that energy migration of excited carriers to the lower bandgap phase impurities dominates the optical and device properties of Ruddlesden–Popper perovskite thin films.⁹⁸ Finally, an aromatic ammonium cation is used to generate Ruddlesden–Popper phases with a larger effective dielectric constant in an attempt to improve charge screening and promote the formation of free charge carriers over excitons. The yield-mobility products appear enhanced by an order of magnitude, suggesting that the use of higher dielectric organic cations in the formation of layered perovskite phases can result in improved electronic performance.¹⁰⁰

1.8 References

1. Kojima, A., Teshima, K., Shirai, Y. & Miyasaka, T. Organometal Halide Perovskites as Visible-Light Sensitizers for Photovoltaic Cells. *Journal of the American Chemical Society* **131**, 6050–6051 (2009).
2. Mitzi, D. B., Chondroudis, K. & Kagan, C. R. Organic-Inorganic Electronics. *IBM Journal of Research and Development* **45**, 29–45 (2001).
3. Berry, J., Buonassisi, T., Egger, D. A., Hodes, G., Kronik, L., Loo, Y.-L., Lubomirsky, I., Marder, S. R., Mastai, Y., Miller, J. S., Mitzi, D. B., Paz, Y., Rappe, A. M., Riess, I., Rybtchinski, B., Stafsudd, O., Stevanovic, V., Toney, M. F., Zitoun, D., Kahn, A., Ginley, D. & Cahen, D. Hybrid Organic-Inorganic Perovskites (HOIPs): Opportunities and Challenges. *Advanced Materials* **27**, 5102–5112 (2015).
4. Kagan, C. R., Mitzi, D. B. & Dimitrakopoulos, C. D. Organic-Inorganic Hybrid Materials as Semiconducting Channels in Thin-Film Field-Effect Transistors. *Science* **286**, 945–947 (1999).
5. Saparov, B. & Mitzi, D. B. Organic-Inorganic Perovskites: Structural Versatility for Functional Materials Design. *Chemical Reviews* **116**, 4558–4596 (2016).
6. Papavassiliou, G. C., Mousdis, G. A. & Koutselas, I. B. Some New Organic-Inorganic Hybrid Semiconductors Based on Metal Halide Units: Structural, Optical and Related Properties†. *Advanced Materials for Optics and Electronics* **9**, 265–271 (1999).
7. Lee, M. M., Teuscher, J., Miyasaka, T., Murakami, T. N. & Snaith, H. J. Efficient Hybrid Solar Cells Based on Meso-Superstructured Organometal Halide Perovskites. *Science* **338**, 643–647 (2012).
8. Snaith, H. J. Perovskites: The Emergence of a New Era for Low-Cost, High-Efficiency Solar Cells. *The Journal of Physical Chemistry Letters* **4**, 3623–3630 (2013).
9. Stranks, S. D., Eperon, G. E., Grancini, G., Menelaou, C., Alcocer, M. J. P., Leijtens, T., Herz, L. M., Petrozza, A. & Snaith, H. J. Electron-Hole Diffusion Lengths Exceeding 1 Micrometer in an Organometal Trihalide Perovskite Absorber. *Science* **342**, 341–344 (2013).
10. Grätzel, M. The Rise of Highly Efficient and Stable Perovskite Solar Cells. *Accounts of Chemical Research* **50**, 487–491 (2017).
11. Kazim, S., Nazeeruddin, M. K., Grätzel, M. & Ahmad, S. Perovskite as Light Harvester: A Game Changer in Photovoltaics. *Angewandte Chemie International Edition* **53**, 2812–2824 (2014).
12. Quarti, C., Mosconi, E., Ball, J. M., D’Innocenzo, V., Tao, C., Pathak, S., Snaith, H. J., Petrozza, A. & Angelis, F. D. Structural and Optical Properties of Methylammonium Lead Iodide across the Tetragonal to Cubic Phase Transition: Implications for Perovskite Solar Cells. *Energy & Environmental Science* **9**, 155–163 (2016).

13. De Wolf, S., Holovsky, J., Moon, S.-J., Löper, P., Niesen, B., Ledinsky, M., Haug, F.-J., Yum, J.-H. & Ballif, C. Organometallic Halide Perovskites: Sharp Optical Absorption Edge and Its Relation to Photovoltaic Performance. *The Journal of Physical Chemistry Letters* **5**, 1035–1039 (2014).
14. Yamada, Y., Nakamura, T., Endo, M., Wakamiya, A. & Kanemitsu, Y. Photocarrier Recombination Dynamics in Perovskite $\text{CH}_3\text{NH}_3\text{PbI}_3$ for Solar Cell Applications. *Journal of the American Chemical Society* **136**, 11610–11613 (2014).
15. Yamada, Y., Yamada, T., Phuong, L. Q., Maruyama, N., Nishimura, H., Wakamiya, A., Murata, Y. & Kanemitsu, Y. Dynamic Optical Properties of $\text{CH}_3\text{NH}_3\text{PbI}_3$ Single Crystals As Revealed by One- and Two-Photon Excited Photoluminescence Measurements. *Journal of the American Chemical Society* **137**, 10456–10459 (2015).
16. Bi, Y., Hutter, E. M., Fang, Y., Dong, Q., Huang, J. & Savenije, T. J. Charge Carrier Lifetimes Exceeding 15 μs in Methylammonium Lead Iodide Single Crystals. *The Journal of Physical Chemistry Letters* **7**, 923–928 (2016).
17. Ponseca, C. S., Savenije, T. J., Abdellah, M., Zheng, K., Yartsev, A., Pascher, T., Harlang, T., Chabera, P., Pullerits, T., Stepanov, A., Wolf, J.-P. & Sundström, V. Organometal Halide Perovskite Solar Cell Materials Rationalized: Ultrafast Charge Generation, High and Microsecond-Long Balanced Mobilities, and Slow Recombination. *Journal of the American Chemical Society* **136**, 5189–5192 (2014).
18. Xing, G., Mathews, N., Sun, S., Lim, S. S., Lam, Y. M., Grätzel, M., Mhaisalkar, S. & Sum, T. C. Long-Range Balanced Electron- and Hole-Transport Lengths in Organic-Inorganic $\text{CH}_3\text{NH}_3\text{PbI}_3$. *Science* **342**, 344–347 (2013).
19. Oga, H., Saeki, A., Ogomi, Y., Hayase, S. & Seki, S. Improved Understanding of the Electronic and Energetic Landscapes of Perovskite Solar Cells: High Local Charge Carrier Mobility, Reduced Recombination, and Extremely Shallow Traps. *Journal of the American Chemical Society* **136**, 13818–13825 (2014).
20. Ivanovska, T., Dionigi, C., Mosconi, E., De Angelis, F., Liscio, F., Morandi, V. & Ruani, G. Long-Lived Photoinduced Polarons in Organohalide Perovskites. *The Journal of Physical Chemistry Letters* **8**, 3081–3086 (2017).
21. Straus, D. B., Hurtado Parra, S., Iotov, N., Gebhardt, J., Rappe, A. M., Subotnik, J. E., Kikkawa, J. M. & Kagan, C. R. Direct Observation of Electron–Phonon Coupling and Slow Vibrational Relaxation in Organic–Inorganic Hybrid Perovskites. *Journal of the American Chemical Society* **138**, 13798–13801 (2016).
22. Stranks, S. D. & Plochocka, P. The Influence of the Rashba Effect. *Nature Materials* **17**, 381–382 (2018).
23. Hirose, K., Sinmyo, R. & Hernlund, J. Perovskite in Earth’s Deep Interior. *Science* **358**, 734–738 (2017).
24. Zhong, W., King-Smith, R. D. & Vanderbilt, D. Giant LO-TO Splittings in Perovskite Ferroelectrics. *Physical Review Letters* **72**, 3618 (1994).

25. Scott, J. F. & Dawber, M. Oxygen-Vacancy Ordering as a Fatigue Mechanism in Perovskite Ferroelectrics. *Applied Physics Letters* **76**, 3801–3803 (2000).
26. McCormack, M., Jin, S., Tiefel, T. H., Fleming, R. M., Phillips, J. M. & Ramesh, R. Very Large Magnetoresistance in Perovskite-like La-Ca-Mn-O Thin Films. *Applied Physics Letters* **64**, 3045–3047 (1994).
27. Moritomo, Y., Asamitsu, A., Kuwahara, H. & Tokura, Y. Giant Magnetoresistance of Manganese Oxides with a Layered Perovskite Structure. *Nature* **380**, 141–144 (1996).
28. Slavney, A. H., Hu, T., Lindenberg, A. M. & Karunadasa, H. I. A Bismuth-Halide Double Perovskite with Long Carrier Recombination Lifetime for Photovoltaic Applications. *Journal of the American Chemical Society* **138**, 2138–2141 (2016).
29. Park, B.-W., Philippe, B., Zhang, X., Rensmo, H., Boschloo, G. & Johansson, E. M. J. Bismuth Based Hybrid Perovskites $A_3Bi_2I_9$ (A: Methylammonium or Cesium) for Solar Cell Application. *Advanced Materials* **27**, 6806–6813 (2015).
30. Hao, F., Stoumpos, C. C., Cao, D. H., Chang, R. P. H. & Kanatzidis, M. G. Lead-Free Solid-State Organic–Inorganic Halide Perovskite Solar Cells. *Nature Photonics* **8**, 489–494 (2014).
31. Noel, N. K., Stranks, S. D., Abate, A., Wehrenfennig, C., Guarnera, S., Haghighirad, A.-A., Sadhanala, A., Eperon, G. E., Pathak, S. K., Johnston, M. B., Petrozza, A., Herz, L. M. & Snaith, H. J. Lead-Free Organic-Inorganic Tin Halide Perovskites for Photovoltaic Applications. *Energy & Environmental Science* **7**, 3061–3068 (2014).
32. Hu, Y., Hutter, E. M., Rieder, P., Grill, I., Hanisch, J., Aygüler, M. F., Hufnagel, A. G., Handloser, M., Bein, T. & Hartschuh, A. Understanding the Role of Cesium and Rubidium Additives in Perovskite Solar Cells: Trap States, Charge Transport, and Recombination. *Advanced Energy Materials* **8**, 1703057 (2018).
33. Saliba, M., Matsui, T., Seo, J.-Y., Domanski, K., Correa-Baena, J.-P., Khaja Nazeeruddin, M., Zakeeruddin, S. M., Tress, W., Abate, A., Hagfeldt, A. & Grätzel, M. Cesium-Containing Triple Cation Perovskite Solar Cells: Improved Stability, Reproducibility and High Efficiency. *Energy & Environmental Science* **9**, 1989–1997 (2016).
34. McMeekin, D. P., Sadoughi, G., Rehman, W., Eperon, G. E., Saliba, M., Hörantner, M. T., Haghighirad, A., Sakai, N., Korte, L., Rech, B., Johnston, M. B., Herz, L. M. & Snaith, H. J. A Mixed-Cation Lead Mixed-Halide Perovskite Absorber for Tandem Solar Cells. *Science* **351**, 151–155 (2016).
35. Hamaguchi, R., Yoshizawa-Fujita, M., Miyasaka, T., Kunugita, H., Ema, K., Takeoka, Y. & Rikukawa, M. Formamidine and Cesium-Based Quasi-Two-Dimensional Perovskites as Photovoltaic Absorbers. *Chemical Communications* **53**, 4366–4369 (2017).
36. NREL. *Best Research-Cell Efficiency Chart* <https://www.nrel.gov/pv/cell-efficiency.html>. 2020.

37. Yang, W. S., Park, B.-W., Jung, E. H., Jeon, N. J., Kim, Y. C., Lee, D. U., Shin, S. S., Seo, J., Kim, E. K., Noh, J. H. & Seok, S. I. Iodide Management in Formamidinium-Lead-Halide-Based Perovskite Layers for Efficient Solar Cells. *Science* **356**, 1376–1379 (2017).
38. Li, M., Wang, Z.-K., Zhuo, M.-P., Hu, Y., Hu, K.-H., Ye, Q.-Q., Jain, S. M., Yang, Y.-G., Gao, X.-Y. & Liao, L.-S. Pb–Sn–Cu Ternary Organometallic Halide Perovskite Solar Cells. *Advanced Materials* **30**, 1800258 (2018).
39. Weidman, M. C., Seitz, M., Stranks, S. D. & Tisdale, W. A. Highly Tunable Colloidal Perovskite Nanoplatelets through Variable Cation, Metal, and Halide Composition. *ACS Nano* **10**, 7830–7839 (2016).
40. Tyagi, P., Arveson, S. M. & Tisdale, W. A. Colloidal Organohalide Perovskite Nanoplatelets Exhibiting Quantum Confinement. *The Journal of Physical Chemistry Letters* **6**, 1911–1916 (2015).
41. Weidman, M. C., Goodman, A. J. & Tisdale, W. A. Colloidal Halide Perovskite Nanoplatelets: An Exciting New Class of Semiconductor Nanomaterials. *Chemistry of Materials* **29**, 5019–5030 (2017).
42. Kovalenko, M. V., Protesescu, L. & Bodnarchuk, M. I. Properties and Potential Optoelectronic Applications of Lead Halide Perovskite Nanocrystals. *Science* **358**, 745–750 (2017).
43. Protesescu, L., Yakunin, S., Bodnarchuk, M. I., Krieg, F., Caputo, R., Hendon, C. H., Yang, R. X., Walsh, A. & Kovalenko, M. V. Nanocrystals of Cesium Lead Halide Perovskites (CsPbX₃, X= Cl, Br, and I): Novel Optoelectronic Materials Showing Bright Emission with Wide Color Gamut. *Nano Letters* **15**, 3692–3696 (2015).
44. Smith, M. D. & Karunadasa, H. I. White-Light Emission from Layered Halide Perovskites. *Accounts of Chemical Research* **51**, 619–627 (2018).
45. Smith, M. D., Jaffe, A., Dohner, E. R., Lindenberg, A. M. & Karunadasa, H. I. Structural Origins of Broadband Emission from Layered Pb–Br Hybrid Perovskites. *Chemical Science* **8**, 4497–4504 (2017).
46. Hu, T., Smith, M. D., Dohner, E. R., Sher, M.-J., Wu, X., Trinh, M. T., Fisher, A., Corbett, J., Zhu, X.-Y., Karunadasa, H. I. & Lindenberg, A. M. Mechanism for Broadband White-Light Emission from Two-Dimensional (110) Hybrid Perovskites. *The Journal of Physical Chemistry Letters* **7**, 2258–2263 (2016).
47. Li, J., Wang, J., Ma, J., Shen, H., Li, L., Duan, X. & Li, D. Self-Trapped State Enabled Filterless Narrowband Photodetections in 2D Layered Perovskite Single Crystals. *Nature Communications* **10**, 806 (2019).
48. Hutter, E. M., Eperon, G. E., Stranks, S. D. & Savenije, T. J. Charge Carriers in Planar and Meso-Structured Organic–Inorganic Perovskites: Mobilities, Lifetimes, and Concentrations of Trap States. *The Journal of Physical Chemistry Letters* **6**, 3082–3090 (2015).

49. Zhu, H., Miyata, K., Fu, Y., Wang, J., Joshi, P. P., Niesner, D., Williams, K. W., Jin, S. & Zhu, X.-Y. Screening in Crystalline Liquids Protects Energetic Carriers in Hybrid Perovskites. *Science* **353**, 1409–1413 (2016).
50. Zheng, F., Tan, L. Z., Liu, S. & Rappe, A. M. Rashba Spin–Orbit Coupling Enhanced Carrier Lifetime in $\text{CH}_3\text{NH}_3\text{PbI}_3$. *Nano Letters* **15**, 7794–7800 (2015).
51. Johnston, M. B. & Herz, L. M. Hybrid Perovskites for Photovoltaics: Charge-Carrier Recombination, Diffusion, and Radiative Efficiencies. *Accounts of Chemical Research* **49**, 146–154 (2016).
52. Chen, T., Chen, W.-L., Foley, B. J., Lee, J., Ruff, J. P. C., Ko, J. Y. P., Brown, C. M., Harriger, L. W., Zhang, D., Park, C., Yoon, M., Chang, Y.-M., Choi, J. J. & Lee, S.-H. Origin of Long Lifetime of Band-Edge Charge Carriers in Organic–Inorganic Lead Iodide Perovskites. *Proceedings of the National Academy of Sciences*, 201704421 (2017).
53. Dong, Q., Fang, Y., Shao, Y., Mulligan, P., Qiu, J., Cao, L. & Huang, J. Electron-Hole Diffusion Lengths > 175 Mm in Solution-Grown $\text{CH}_3\text{NH}_3\text{PbI}_3$ Single Crystals. *Science* **347**, 967–970 (2015).
54. Wehrenfennig, C., Eperon, G. E., Johnston, M. B., Snaith, H. J. & Herz, L. M. High Charge Carrier Mobilities and Lifetimes in Organolead Trihalide Perovskites. *Advanced Materials* **26**, 1584–1589 (2014).
55. de Quilletes, D. W., Vorpahl, S. M., Stranks, S. D., Nagaoka, H., Eperon, G. E., Ziffer, M. E., Snaith, H. J. & Ginger, D. S. Impact of Microstructure on Local Carrier Lifetime in Perovskite Solar Cells. *Science* **348**, 683–686 (2015).
56. Galkowski, K., Mitioglu, A., Miyata, A., Plochocka, P., Portugall, O., E. Eperon, G., Tse-Wei Wang, J., Stergiopoulos, T., D. Stranks, S., J. Snaith, H. & J. Nicholas, R. Determination of the Exciton Binding Energy and Effective Masses for Methylammonium and Formamidinium Lead Tri-Halide Perovskite Semiconductors. *Energy & Environmental Science* **9**, 962–970 (2016).
57. Miyata, A., Mitioglu, A., Plochocka, P., Portugall, O., Wang, J. T.-W., Stranks, S. D., Snaith, H. J. & Nicholas, R. J. Direct Measurement of the Exciton Binding Energy and Effective Masses for Charge Carriers in Organic-Inorganic Tri-Halide Perovskites. *Nature Physics* **11**, 582–587 (2015).
58. Herz, L. M. Charge-Carrier Dynamics in Organic-Inorganic Metal Halide Perovskites. *Annual Review of Physical Chemistry* **67**, 65–89 (2016).
59. Grancini, G., Maiuri, M., Fazzi, D., Petrozza, A., Egelhaaf, H.-J., Brida, D., Cerullo, G. & Lanzani, G. Hot Exciton Dissociation in Polymer Solar Cells. *Nature Materials* **12**, 29–33 (2013).
60. Guerrero, A., Loser, S., Garcia-Belmonte, G., Bruns, C. J., Smith, J., Miyauchi, H., Stupp, S. I., Bisquert, J. & Marks, T. J. Solution-Processed Small Molecule:Fullerene Bulk-Heterojunction Solar Cells: Impedance Spectroscopy Deduced Bulk and Interfacial Limits to Fill-Factors. *Physical Chemistry Chemical Physics* **15**, 16456 (2013).

61. Casalini, R., Tsang, S. W., Deininger, J. J., Arroyave, F. A., Reynolds, J. R. & So, F. Investigation of the Role of the Acceptor Molecule in Bulk Heterojunction Photovoltaic Cells Using Impedance Spectroscopy. *The Journal of Physical Chemistry C* **117**, 13798–13804 (2013).
62. Miyata, K. & Zhu, X.-Y. Ferroelectric Large Polarons. *Nature Materials* **17**, 379–381 (2018).
63. Zhu, X.-Y. & Podzorov, V. Charge Carriers in Hybrid Organic–Inorganic Lead Halide Perovskites Might Be Protected as Large Polarons. *The Journal of Physical Chemistry Letters* **6**, 4758–4761 (2015).
64. Zhai, Y., Baniya, S., Zhang, C., Li, J., Haney, P., Sheng, C.-X., Ehrenfreund, E. & Vardeny, Z. V. Giant Rashba Splitting in 2D Organic-Inorganic Halide Perovskites Measured by Transient Spectroscopies. *Science Advances* **3**, e1700704 (2017).
65. Yu, Z.-G. The Rashba Effect and Indirect Electron-Hole Recombination in Hybrid Organic–Inorganic Perovskites. *Physical Chemistry Chemical Physics* **19**, 14907–14912 (2017).
66. Mosconi, E., Etienne, T. & De Angelis, F. Rashba Band Splitting in Organohalide Lead Perovskites: Bulk and Surface Effects. *The Journal of Physical Chemistry Letters* **8**, 2247–2252 (2017).
67. Ledinsky, M., Schönfeldová, T., Holovský, J., Aydin, E., Hájková, Z., Landová, L., Neyková, N., Fejfar, A. & De Wolf, S. Temperature Dependence of the Urbach Energy in Lead Iodide Perovskites. *The Journal of Physical Chemistry Letters*, 1368–1373 (2019).
68. Johnson, S. R. & Tiedje, T. Temperature Dependence of the Urbach Edge in GaAs. *Journal of Applied Physics* **78**, 5609–5613 (1995).
69. Sutter-Fella, C. M., Miller, D. W., Ngo, Q. P., Roe, E. T., Toma, F. M., Sharp, I. D., Longergan, M. C. & Javey, A. Band Tailing and Deep Defect States in $\text{CH}_3\text{NH}_3\text{Pb}(\text{I}_{1-x}\text{Br}_x)_3$ Perovskites As Revealed by Sub-Bandgap Photocurrent. *ACS Energy Letters* **2**, 709–715 (2017).
70. Zhao, X. & Park, N.-G. Stability Issues on Perovskite Solar Cells. *Photonics* **2**, 1139–1151 (2015).
71. Aristidou, N., Sanchez-Molina, I., Chotchuangchutchaval, T., Brown, M., Martinez, L., Rath, T. & Haque, S. A. The Role of Oxygen in the Degradation of Methylammonium Lead Trihalide Perovskite Photoactive Layers. *Angewandte Chemie International Edition* **54**, 8208–8212 (2015).
72. Mosconi, E., Azpiroz, J. M. & De Angelis, F. Ab Initio Molecular Dynamics Simulations of Methylammonium Lead Iodide Perovskite Degradation by Water. *Chemistry of Materials* **27**, 4885–4892 (2015).

73. Abraha Berhe, T., Su, W.-N., Chen, C.-H., Pan, C.-J., Cheng, J.-H., Chen, H.-M., Tsai, M.-C., Chen, L.-Y., Aregahegn Dubale, A. & Hwang, B.-J. Organometal Halide Perovskite Solar Cells: Degradation and Stability. *Energy & Environmental Science* **9**, 323–356 (2016).
74. Li, Y., Xu, X., Wang, C., Ecker, B., Yang, J., Huang, J. & Gao, Y. Light-Induced Degradation of $\text{CH}_3\text{NH}_3\text{PbI}_3$ Hybrid Perovskite Thin Film. *The Journal of Physical Chemistry C* **121**, 3904–3910 (2017).
75. Divitini, G., Cacovich, S., Matteocci, F., Cinà, L., Di Carlo, A. & Ducati, C. *In Situ* Observation of Heat-Induced Degradation of Perovskite Solar Cells. *Nature Energy* **1**, 15012 (2016).
76. Zhao, L., Kerner, R. A., Xiao, Z., Lin, Y. L., Lee, K. M., Schwartz, J. & Rand, B. P. Redox Chemistry Dominates the Degradation and Decomposition of Metal Halide Perovskite Optoelectronic Devices. *ACS Energy Letters* **1**, 595–602 (2016).
77. Liu, Y., Akin, S., Pan, L., Uchida, R., Arora, N., Milić, J. V., Hinderhofer, A., Schreiber, F., Uhl, A. R., Zakeeruddin, S. M., Hagfeldt, A., Dar, M. I. & Grätzel, M. Ultrahydrophobic 3D/2D Fluoroarene Bilayer-Based Water-Resistant Perovskite Solar Cells with Efficiencies Exceeding 22%. *Science Advances* **5**, eaaw2543 (2019).
78. Chen, Y., Sun, Y., Peng, J., Zhang, W., Su, X., Zheng, K., Pullerits, T. & Liang, Z. Tailoring Organic Cation of 2D Air-Stable Organometal Halide Perovskites for Highly Efficient Planar Solar Cells. *Advanced Energy Materials* **7**, 1700162 (2017).
79. Goldschmidt, V. M. Die Gesetze der Krystallochemie. *Naturwissenschaften* **14**, 477–485 (1926).
80. Park, N.-G., Miyasaka, T. & Grätzel, M. *Organic-Inorganic Halide Perovskite Photovoltaics* (Springer, 2016).
81. Gélvez-Rueda, M. C., Cao, D. H., Patwardhan, S., Renaud, N., Stoumpos, C. C., Schatz, G. C., Hupp, J. T., Farha, O. K., Savenije, T. J., Kanatzidis, M. G. & Grozema, F. C. Effect of Cation Rotation on Charge Dynamics in Hybrid Lead Halide Perovskites. *The Journal of Physical Chemistry C* **120**, 16577–16585 (2016).
82. Panzer, F., Li, C., Meier, T., Köhler, A. & Huettner, S. Impact of Structural Dynamics on the Optical Properties of Methylammonium Lead Iodide Perovskites. *Advanced Energy Materials* **7**, 1700286 (2017).
83. Maughan, A. E., Ganose, A. M., Scanlon, D. O. & Neilson, J. R. Perspectives and Design Principles of Vacancy-Ordered Double Perovskite Halide Semiconductors. *Chemistry of Materials* **31**, 1184–1195 (2019).
84. Wei, F., Deng, Z., Sun, S., Zhang, F., Evans, D. M., Kieslich, G., Tominaka, S., Carpenter, M. A., Zhang, J., Bristowe, P. D. & Cheetham, A. K. Synthesis and Properties of a Lead-Free Hybrid Double Perovskite: $(\text{CH}_3\text{NH}_3)_2\text{AgBiBr}_6$. *Chemistry of Materials* **29**, 1089–1094 (2017).

85. Spanopoulos, I., Ke, W., Stoumpos, C. C., Schueller, E. C., Kontsevoi, O. Y., Seshadri, R. & Kanatzidis, M. G. Unraveling the Chemical Nature of the 3D “Hollow” Hybrid Halide Perovskites. *Journal of the American Chemical Society* **140**, 5728–5742 (2018).
86. Smith, I. C., Hoke, E. T., Solis-Ibarra, D., McGehee, M. D. & Karunadasa, H. I. A Layered Hybrid Perovskite Solar-Cell Absorber with Enhanced Moisture Stability. *Angewandte Chemie International Edition* **126**, 11414–11417 (2014).
87. Tang, G., Yang, C., Stroppa, A., Fang, D. & Hong, J. Revealing the Role of Thiocyanate Anion in Layered Hybrid Halide Perovskite $(\text{CH}_3\text{NH}_3)_2\text{Pb}(\text{SCN})_2\text{I}_2$. *The Journal of Chemical Physics* **146**, 224702 (2017).
88. Xiao, Z., Meng, W., Saparov, B., Duan, H.-S., Wang, C., Feng, C., Liao, W., Ke, W., Zhao, D., Wang, J., Mitzi, D. B. & Yan, Y. Photovoltaic Properties of Two-Dimensional $(\text{CH}_3\text{NH}_3)_2\text{Pb}(\text{SCN})_2\text{I}_2$ Perovskite: A Combined Experimental and Density Functional Theory Study. *The Journal of Physical Chemistry Letters* **7**, 1213–1218 (2016).
89. Xiao, Z., Meng, W., Wang, J. & Yan, Y. Defect Properties of the Two-Dimensional $(\text{CH}_3\text{NH}_3)_2\text{Pb}(\text{SCN})_2\text{I}_2$ Perovskite: A Density-Functional Theory Study. *Physical Chemistry Chemical Physics* **18**, 25786–25790 (2016).
90. Umeyama, D., Lin, Y. & Karunadasa, H. I. Red-to-Black Piezochromism in a Compressible Pb–I–SCN Layered Perovskite. *Chemistry of Materials* **28**, 3241–3244 (2016).
91. Jiang, Q., Rebollar, D., Gong, J., Piacentino, E. L., Zheng, C. & Xu, T. Pseudohalide-Induced Moisture Tolerance in Perovskite $\text{CH}_3\text{NH}_3\text{Pb}(\text{SCN})_2\text{I}$ Thin Films. *Angewandte Chemie International Edition* **54**, 7617–7620 (2015).
92. Halder, A., Chulliyil, R., Subbiah, A. S., Khan, T., Chatteraj, S., Chowdhury, A. & Sarkar, S. K. Pseudohalide (SCN^-) -Doped MAPbI_3 Perovskites: A Few Surprises. *The Journal of Physical Chemistry Letters* **6**, 3483–3489 (2015).
93. Ganose, A. M., Savory, C. N. & Scanlon, D. O. $(\text{CH}_3\text{NH}_3)_2\text{Pb}(\text{SCN})_2\text{I}_2$: A More Stable Structural Motif for Hybrid Halide Photovoltaics? *The Journal of Physical Chemistry Letters* **6**, 4594–4598 (2015).
94. Daub, M. & Hillebrecht, H. Synthesis, Single-Crystal Structure and Characterization of $(\text{CH}_3\text{NH}_3)_2\text{Pb}(\text{SCN})_2\text{I}_2$. *Angewandte Chemie International Edition* **54**, 11016–11017 (2015).
95. Labram, J. G., Venkatesan, N. R., Takacs, C. J., Evans, H. A., Perry, E. E., Wudl, F. & Chabynyc, M. L. Charge Transport in a Two-Dimensional Hybrid Metal Halide Thiocyanate Compound. *Journal of Materials Chemistry C* **5**, 5930–5938 (2017).

96. Tsai, H., Nie, W., Blancon, J.-C., Stoumpos, C. C., Asadpour, R., Harutyunyan, B., Neukirch, A. J., Verduzco, R., Crochet, J. J., Tretiak, S., Pedesseau, L., Even, J., Alam, M. A., Gupta, G., Lou, J., Ajayan, P. M., Bedzyk, M. J., Kanatzidis, M. G. & Mohite, A. D. High-Efficiency Two-Dimensional Ruddlesden-Popper Perovskite Solar Cells. *Nature* **536**, 312–316 (2016).
97. Koh, T. M., Febriansyah, B. & Mathews, N. Ruddlesden-Popper Perovskite Solar Cells. *Chem* **2**, 326–327 (2017).
98. Venkatesan, N. R., Kennard, R. M., DeCrescent, R. A., Nakayama, H., Dahlman, C. J., Perry, E. E., Schuller, J. A. & Chabinyk, M. L. Phase Intergrowth and Structural Defects in Organic Metal Halide Ruddlesden–Popper Thin Films. *Chemistry of Materials* **30**, 8615–8623 (2018).
99. Venkatesan, N. R., Labram, J. G. & Chabinyk, M. L. Charge-Carrier Dynamics and Crystalline Texture of Layered Ruddlesden–Popper Hybrid Lead Iodide Perovskite Thin Films. *ACS Energy Letters* **3**, 380–386 (2018).
100. Venkatesan, N. R., Mahdi, A., Barraza, B., Wu, G., Chabinyk, M. L. & Seshadri, R. Enhanced Yield-Mobility Products in Hybrid Halide Ruddlesden–Popper Compounds with Aromatic Ammonium Spacers. *Dalton Transactions* **48**, 14019–14026 (2019).
101. Ruddlesden, S. N. & Popper, P. New Compounds of the K_2NiF_4 Type. *Acta Crystallographica* **10**, 538–539 (1957).
102. Ruddlesden, S. N. & Popper, P. The Compound $Sr_3Ti_2O_7$ and Its Structure. *Acta Crystallographica* **11**, 54–55 (1958).
103. Lee, J.-W., Dai, Z., Han, T.-H., Choi, C., Chang, S.-Y., Lee, S.-J., Marco, N. D., Zhao, H., Sun, P., Huang, Y. & Yang, Y. 2D Perovskite Stabilized Phase-Pure Formamidinium Perovskite Solar Cells. *Nature Communications* **9**, 3021 (2018).
104. Schlipf, J., Hu, Y., Pratap, S., Bießmann, L., Hohn, N., Porcar, L., Bein, T., Docampo, P. & Müller-Buschbaum, P. Shedding Light on the Moisture Stability of 3D/2D Hybrid Perovskite Heterojunction Thin Films. *ACS Applied Energy Materials* (2019).
105. Tsai, H., Nie, W., Blancon, J.-C., Stoumpos, C. C., Soe, C. M. M., Yoo, J., Crochet, J., Tretiak, S., Even, J., Sadhanala, A., Azzellino, G., Brenes, R., Ajayan, P. M., Bulović, V., Stranks, S. D., Friend, R. H., Kanatzidis, M. G. & Mohite, A. D. Stable Light-Emitting Diodes Using Phase-Pure Ruddlesden–Popper Layered Perovskites. *Advanced Materials* **30**, 1704217 (2018).
106. Grancini, G., Roldán-Carmona, C., Zimmermann, I., Mosconi, E., Lee, X., Martineau, D., Nabey, S., Oswald, F., Angelis, F. D., Graetzel, M. & Nazeeruddin, M. K. One-Year Stable Perovskite Solar Cells by 2D/3D Interface Engineering. *Nature Communications* **8**, 15684 (2017).
107. Stoumpos, C. C., Cao, D. H., Clark, D. J., Young, J., Rondinelli, J. M., Jang, J. I., Hupp, J. T. & Kanatzidis, M. G. Ruddlesden–Popper Hybrid Lead Iodide Perovskite 2D Homologous Semiconductors. *Chemistry of Materials* **28**, 2852–2867 (2016).

108. Zhang, X., Wu, G., Yang, S., Fu, W., Zhang, Z., Chen, C., Liu, W., Yan, J., Yang, W. & Chen, H. Vertically Oriented 2D Layered Perovskite Solar Cells with Enhanced Efficiency and Good Stability. *Small* **13**, 1700611 (2017).
109. Straus, D. B. & Kagan, C. R. Electrons, Excitons, and Phonons in Two-Dimensional Hybrid Perovskites: Connecting Structural, Optical, and Electronic Properties. *The Journal of Physical Chemistry Letters* **9**, 1434–1447 (2018).
110. D’innocenzo, V., Grancini, G., Alcocer, M. J. P., Kandada, A. R. S., Stranks, S. D., Lee, M. M., Lanzani, G., Snaith, H. J. & Petrozza, A. Excitons versus Free Charges in Organo-Lead Tri-Halide Perovskites. *Nature Communications* **5**, 3586 (2014).
111. Wu, X., Trinh, M. T. & Zhu, X.-Y. Excitonic Many-Body Interactions in Two-Dimensional Lead Iodide Perovskite Quantum Wells. *The Journal of Physical Chemistry C* **119**, 14714–14721 (2015).
112. Blancon, J.-C., Tsai, H., Nie, W., Stoumpos, C. C., Pedesseau, L., Katan, C., Kepenekian, M., Soe, C. M. M., Appavoo, K., Sfeir, M. Y., Tretiak, S., Ajayan, P. M., Kanatzidis, M. G., Even, J., Crochet, J. J. & Mohite, A. D. Extremely Efficient Internal Exciton Dissociation through Edge States in Layered 2D Perovskites. *Science* **355**, 1288–1292 (2017).
113. Muljarov, E. A., Tikhodeev, S. G., Gippius, N. A. & Ishihara, T. Excitons in Self-Organized Semiconductor/Insulator Superlattices: PbI-Based Perovskite Compounds. *Physical Review B* **51**, 14370–14378 (1995).
114. Hirasawa, M., Ishihara, T., Goto, T., Uchida, K. & Miura, N. Magnetoabsorption of the Lowest Exciton in Perovskite-Type Compound (CH₃NH₃)PbI₃. *Physica B: Condensed Matter* **201**, 427–430 (1994).
115. DeCrescent, R. A., Venkatesan, N. R., Dahlman, C. J., Kennard, R. M., Chabinye, M. L. & Schuller, J. A. Optical Constants and Effective-Medium Origins of Large Optical Anisotropies in Layered Hybrid Organic/Inorganic Perovskites. *ACS Nano* **13**, 10745–10753 (2019).

Chapter 2

Simulation and Processing of Two-Dimensional X-Ray Diffraction Data

2.1 Introduction

X-ray diffraction techniques on thin film samples require special consideration. If we categorize and place samples on a spectrum of crystalline texture, as shown in Figure 2.1, this requirement becomes clear.¹ In a powder diffraction experiment, the crystals exist equally in all measurable orientations – therefore, measurement of diffracton intensity along one radial direction in reciprocal space is sufficient. This is because the directionally-isotropic nature of the sample results in diffraction peaks represented as spherical shells of intensity. On the other end of the spectrum are samples of single-crystalline quality (*i.e.* single-crystals or epitaxially-grown thin films), where samples have a very well-defined in-plane and out-of-plane orientation. The result of this crystalline texturing requires collection of diffraction intensity across three-dimensional reciprocal space to fully characterize crystalline orientation.

The sample of interest in this text, and more widely in many solution-processable thin

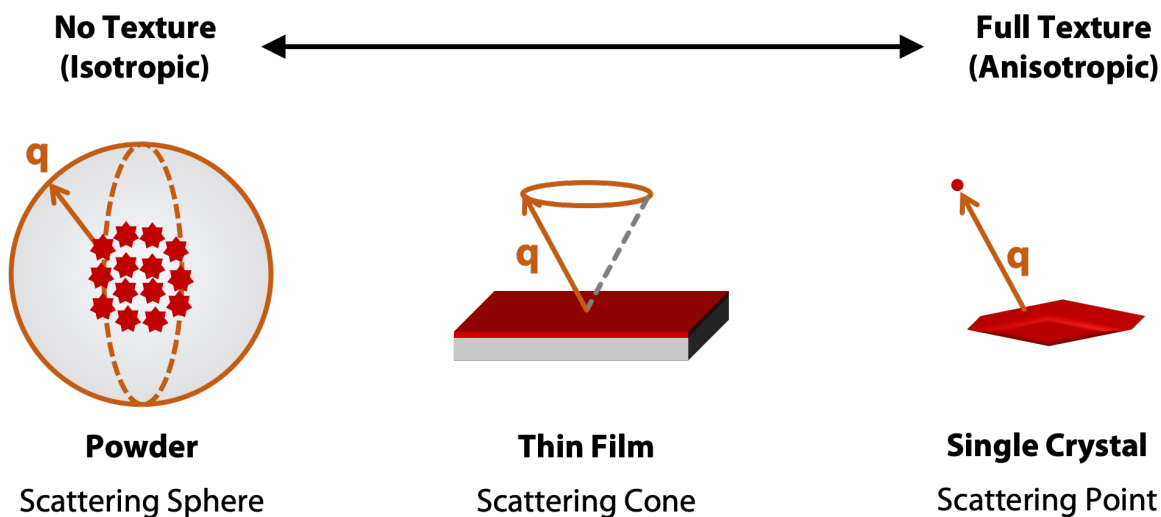


Figure 2.1: Spectrum of samples with differing amounts of crystalline texture and the resulting collected diffraction intensities. The intensity of a diffraction peak measured at \vec{q} in a powder sample traces out a spherical shell while, in a single-crystal, results in a specific diffraction spot. In a polycrystalline thin film similar to ones studied in text, the scattering vector traces out a cone in reciprocal space.

film deposition techniques, is that of a polycrystalline sample with fiber texturing. In a film deposited by spin-coating, the out-of-plane orientation of the crystals is well-defined and is seen in powder XRD as intense diffraction peaks along a particular family of lattice planes. In-plane, however, since no method of rigorously orienting crystal along the substrate surface is used, crystals are rotated randomly. This results in rotationally-isotropic in-plane diffraction patterns with a well-defined out-of-plane texture. This is known as fiber-texturing – a term derived from the diffraction patterns of drawn metal fibers.²

In addition to possessing fiber-texturing, thin films require an underlying substrate to grow. Since films are not free-standing, transmission diffraction techniques are difficult and X-ray intensity will likely be severely attenuated travelling through the substrate material. Therefore, utilizing a reflection geometry is necessary, but in order to collect in-plane orientation, a small ($\sim 0.1 - 0.5^\circ$) incidence angle is used. This technique, grazing-incidence X-ray diffraction (GIXRD) or grazing-incidence (wide-angle) X-ray scattering (GIWAXS), is

a commonly-used technique to measure texturing of thin film samples.¹⁻⁴ Measurements are commonly conducted at synchrotron facilities with a CCD detector collecting two-dimensional diffraction information. Due to the asymmetric nature of the scan however (fixed incidence angle with changing detector angle), analysis of the data is more complicated than standard powder diffraction.

2.2 Diffraction scans in reciprocal space

Before analyzing the results of a two-dimensional diffraction patterns, it is necessary to observe how manipulating motors on a diffractometer affect motions in reciprocal space. Figure 2.2 shows the two most commonly-used motors, ω (incidence angle), and 2θ (scattering angle).

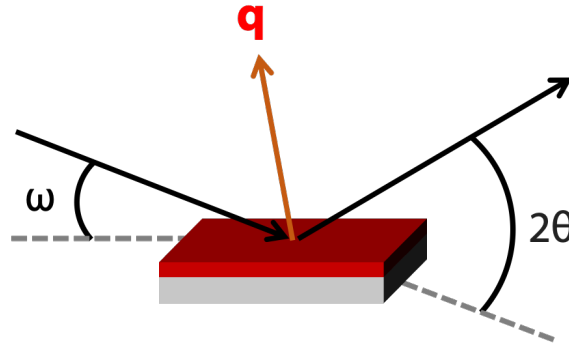


Figure 2.2: Incident angle (ω) and scattering angle (2θ), along with scattering vector (\vec{q}) in reflection geometry diffraction experiment.

In all X-ray characterizations presented in this text, we are collecting elastic scattering, and the detected X-ray has the same momentum as the incident beam, $2\pi/\lambda$, but with a different propagation direction. Our scattering vector, \vec{q} , is therefore described by equation 2.1 as the difference between the final and initial momentum vectors (\vec{k}).

$$\vec{q} = \vec{k}_f - \vec{k}_i \quad (2.1)$$

With reference to the sample surface, the outgoing angle becomes $2\theta - \omega$, and we can solve for the components of the scattering vector in-plane (q_{\parallel}) and out-of-plane (q_{\perp}), shown in Equations 2.2 and 2.3.

$$q_{\parallel} = \left(\frac{2\pi}{\lambda}\right) \cdot [\cos(2\theta - \omega) - \cos(\omega)] \quad (2.2)$$

$$q_{\perp} = \left(\frac{2\pi}{\lambda}\right) \cdot [\sin(2\theta - \omega) + \sin(\omega)] \quad (2.3)$$

When the X-ray diffraction scan is symmetric as in a $\theta/2\theta$ scan on a powder diffractometer, the constraint of $\omega = \theta$ results in the q_{\parallel} term going to zero, leaving us with the familiar equation for the scattering vector in a typical symmetric and transmission diffraction measurement (Equation 2.4). Additionally, if we take the magnitude of the scattering vector formed by the components in 2.2 and 2.3 and use the trigonometric identities $\sin^2(\theta) + \cos^2(\theta) = 1$ along with the sum and difference formulas for sines and cosines, we arrive at Equation 2.4, as shown below.

$$q = \left(\frac{4\pi}{\lambda}\right) \cdot \sin(\theta) \quad (2.4)$$

$$|q| = \sqrt{(q_{\parallel})^2 + (q_{\perp})^2}$$

$$|q| = \left(\frac{2\pi}{\lambda}\right) \sqrt{2 - 2\cos(2\theta - \omega)\cos(\omega) + 2\sin(2\theta - \omega)\sin(\omega)}$$

$$|q| = \left(\frac{2\pi}{\lambda}\right) \sqrt{2 - 2\cos(2\theta)} = \left(\frac{2\pi}{\lambda}\right) \sqrt{2 - 4\sin^2(\theta) - 2}$$

$$|q| = \left(\frac{4\pi}{\lambda} \right) \cdot \sin(\theta)$$

The result of Equation 2.4 is important because it shows that, regardless of the measurement geometry, the magnitude of the scattering vector is *only* dependent upon the scattering angle 2θ . Using all this information, different X-ray scans in reciprocal space are shown in Figure 2.3, illustrating the result of manipulating the ω and 2θ motors individually, or together.

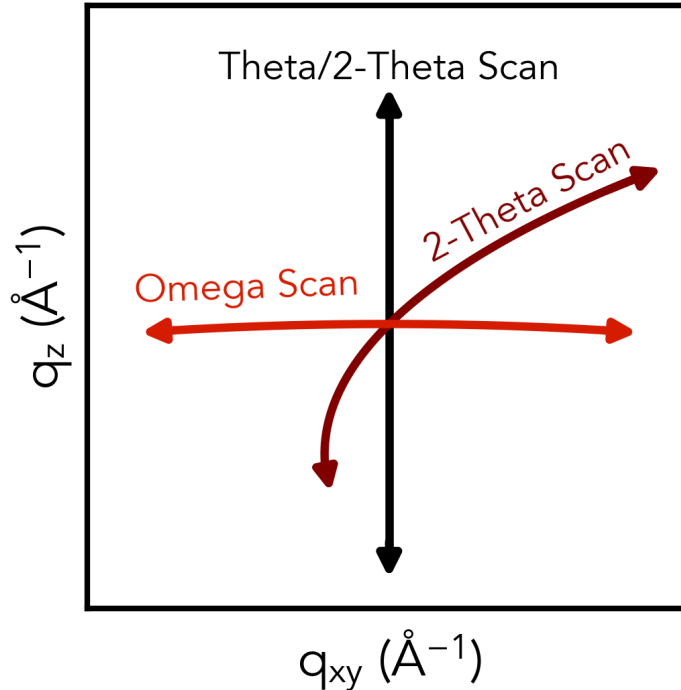


Figure 2.3: Path traversed through reciprocal space by different X-ray diffraction scans, illustrating a 2θ scan, ω scan (rocking curve), and symmetric $\theta/2\theta$ or powder diffraction scan.

The symmetric $\theta/2\theta$ scan, as expected, traces a straight line through reciprocal space entirely along the q_z direction (q_z and q_{\perp} can be used interchangeably as can q_{\parallel} and q_{xy}) because the scattering vector only has a component along this direction as shown in Equation 2.4. Since the magnitude of \vec{q} only depends on the scattering angle, moving the ω

motor results in a scan in which only the angle of \vec{q} changes. This scan is also known as a rocking curve and measures the misorientation of a particular diffraction peak from the normal. Scanning the 2θ motor results in a highly nonlinear path through reciprocal space, the shape of which becomes important in analyzing GIWAXS patterns, as this represents the case of a fixed incidence (ω) angle.

2.3 GIWAXS pattern simulation program

In this section, we present a program to simulate grazing-incidence wide-angle X-ray scattering patterns (GIWAXS) – with both script and GUI-based options. Both programs were written using Python 3 and require the following dependencies in order to run: PyQt5, sys, numpy, pathlib, tiff file, and matplotlib. The simplest way to install a Python 3 distribution to use with this program is to install the Anaconda package: [Download Anaconda Python distribution](#).⁵ After installation, the only dependencies you will probably need to additionally install are PyQt5, pathlib, and tiff file. Doing so is quite simple, and you can use this command in order to install any specific Python package you may need in the future.

```
python -m pip install package_name
```

So, as an example, if we needed to install the `tiff file` dependency to run the program:

```
python -m pip install tiff file
```

Once all the packages have been installed, we can now easily run the program by navigating to the folder with the program and executing the following:

python program_name.py

We have supplied both a command-window script based and GUI versions of the program, both of which operations will be detailed below.

2.3.1 Generating structure factors from crystal structure file

In order to correctly calculate the intensities of the diffraction reflections in our simulated image, we need to calculate the structure factors of all the reflections. To do this, we employ the aid of VESTA to do the calculation for us. If you do not have VESTA, you can download it for free from this link: [Download VESTA](#).⁶ Assuming that we already have the CIF file of the crystal structure of interest, we first open the file in VESTA as follows:

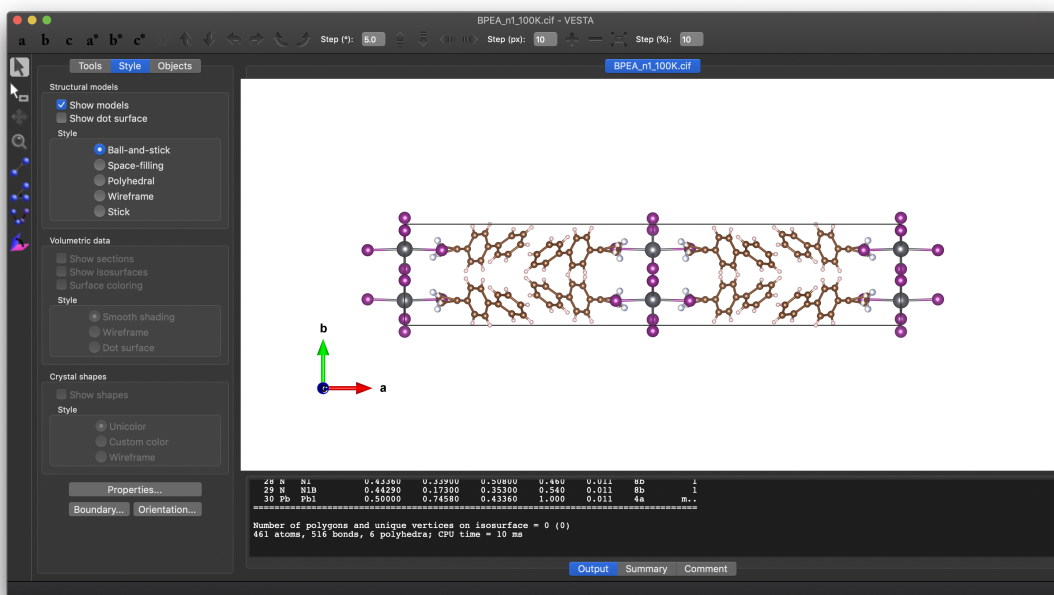


Figure 2.4: Crystal structure of $(\text{BPEA})_2\text{PbI}_4$ opened in VESTA.

The first thing we must do is to remove the symmetry from the crystal structure. The reason for this is that the diffraction information when the structure factors are calculated

include multiplicities due to the fact that certain reflections are equivalent by crystal symmetry. An example of this is shown in Figure 2.5, for a cubic structure. Since there is a four-fold rotation axis through each face of the cube, the vector pointing along the 111 crystallographic direction, indicated by the black arrow, is equivalent to the red arrows passing through all the corners of the cube because of symmetry. The reason we want to remove this symmetry is so that all of these directions are explicitly calculated when we do our simulation since our thin films are anisotropic. We can remove the symmetry by going through the file menus as following:

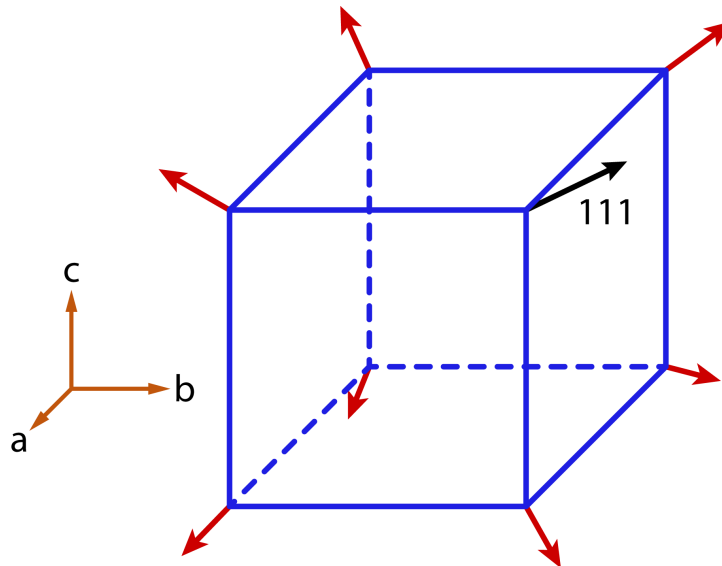


Figure 2.5: Illustration of the effect of cubic symmetry on the 111 crystallographic direction. Due to the perpendicular four-fold rotation axes through each of the cube faces, this reflection is equivalent to vectors originating from all the corners of the cube (shown in red).

1. Navigate through the file menu: Edit > Edit Data > Unit Cell
2. Click the “Remove symmetry” button at the bottom of the window (shown in Figure 2.6)
3. Click “OK” at the bottom of the window to close it and accept the changes

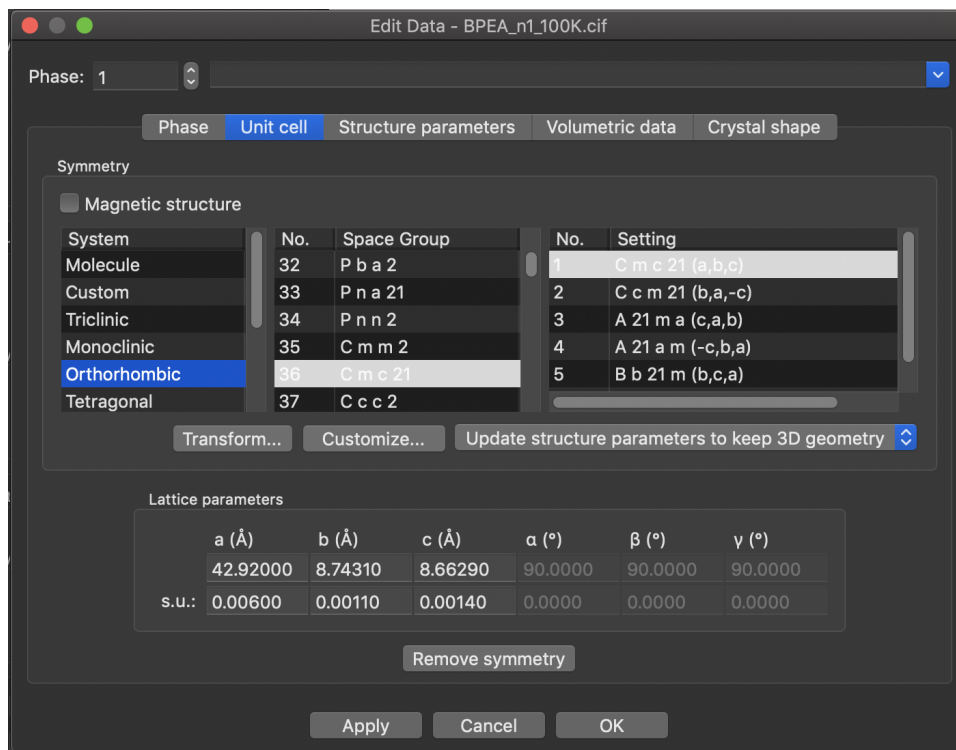


Figure 2.6: Window to edit unit cell information and remove the symmetry from the crystal – the resulting space group after removal of symmetry should be P 1, corresponding to a primitive lattice in which the only symmetry element is the identity operation, *i.e.* bringing the structure back into itself.

Once we have removed the symmetry from the unit cell, we can now calculate the structure factors for all of the reflections present in the system. To do this, we use the file menus as following:

1. Navigate through the file menu: Utilities > Structure Factors – you should see a window pop up that looks like the one in Figure 2.7
2. Enter the wavelength of the X-ray radiation used – VESTA will default to the value of Cu-K α of 1.54 Å but in this case we will use 0.976 Å, which is approximately 12.7 keV, the energy of the X-ray radiation at Beamline 11-3 at Stanford Synchrotron Radiation Lightsource (SSRL)
3. Click the “Calculate” button to determine the parameters of all the diffraction reflec-

tions in the crystal

- Since the structure factor has a real and imaginary component, the value of interest to us is the magnitude of structure factor or $|F|$. The intensity that we see in the diffraction experiment is proportional to the square of this structure factor magnitude, $I \propto |F|^2$
- To save this structure factor data for use with our program, we press the “Export” button and save as the default text file

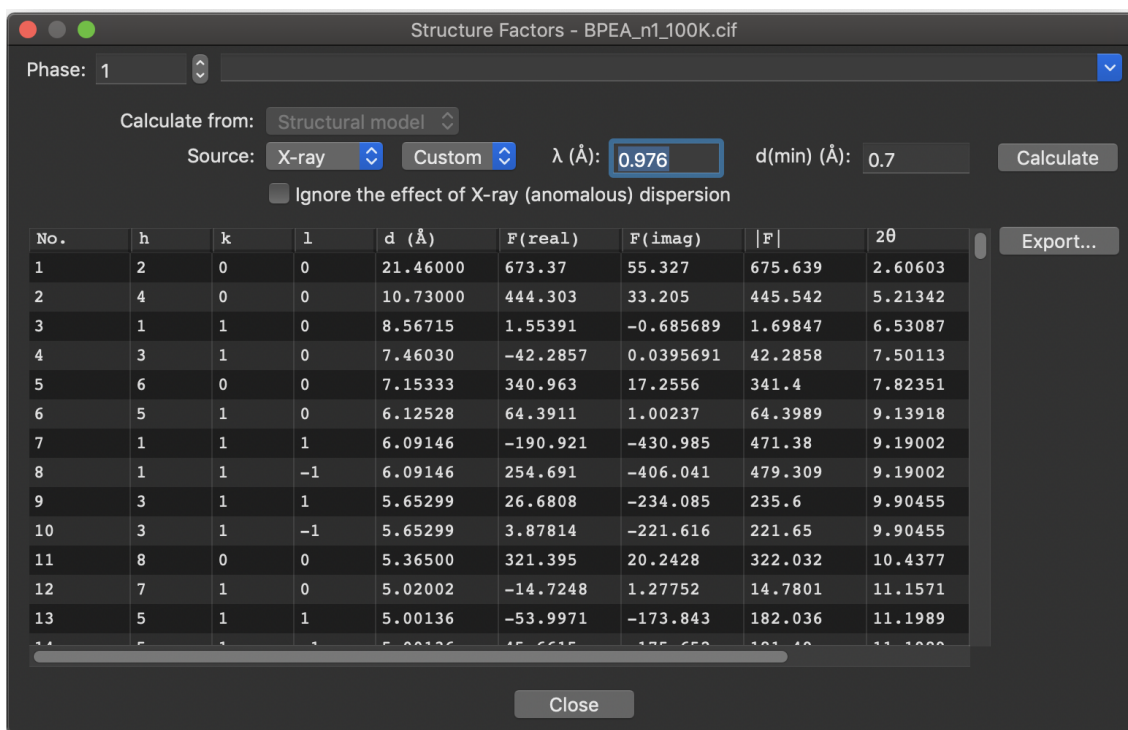


Figure 2.7: Window to calculate structure factors from the crystal structure – by entering the X-ray wavelength and pressing the “Calculate” button, the parameters for all the lattice reflections in the crystal will be computed. Although the structure factor has a real and imaginary component in phase space, the value of interest to us is the magnitude $|F|$.

When you close the CIF file in VESTA, it will ask you if you want to save changes – you *should not* save if you want to retain the symmetry information in the CIF file. Overwriting

the changes will not make any changes to the actual structure, but the space group of your crystal will now just be P 1 so you will lose space group information. We have now have all the files needed in order to simulate the GIWAXS image from our given CIF file – the following sections will describe how use both the script and GUI-based programs.

2.3.2 Script-based GIWAXS simulation operating procedure

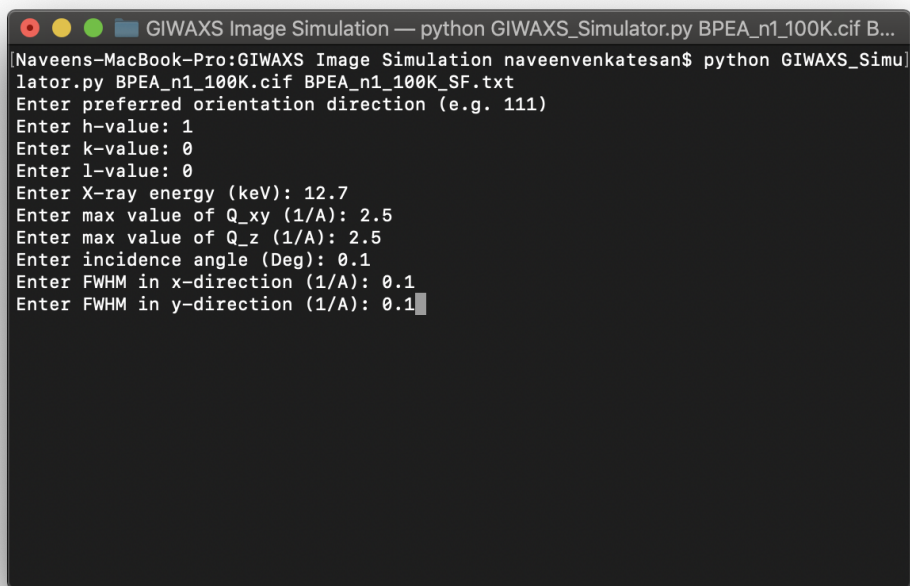
For the script-based program, all inputs to the program are done through the terminal or command prompt. It is *very helpful* but not necessary to have both the CIF file and structure factor file in the same directory as the Python script. In order to start the script, we must provide two arguments: the CIF file and structure factor file locations. For this reason, it is easier to have the files all the same directory. We use the following command to start the program:

```
python GIWAXS_Simulator.py 'CIF Filename' 'Structure Factor Filename'
```

We will continue our earlier example of $(\text{BPEA})_2\text{PbI}_4$ and simulate the GIWAXS pattern. When we see the crystal structure of $(\text{BPEA})_2\text{PbI}_4$ (Figure 2.4) in VESTA, we see that the perovskite layers stack along the a axis, or the 100 crystallographic direction. Keeping that in mind, we now invoke the simulation script with the following command (we have saved the structure factors in a file called “BPEA_n1_100K_SF.txt”):

```
python GIWAXS_Simulator.py BPEA_n1_100K.cif BPEA_n1_100K_SF.txt
```

The program will then prompt for a series of inputs in order to the simulate the image (shown in Figure 2.8). In order they are as following:



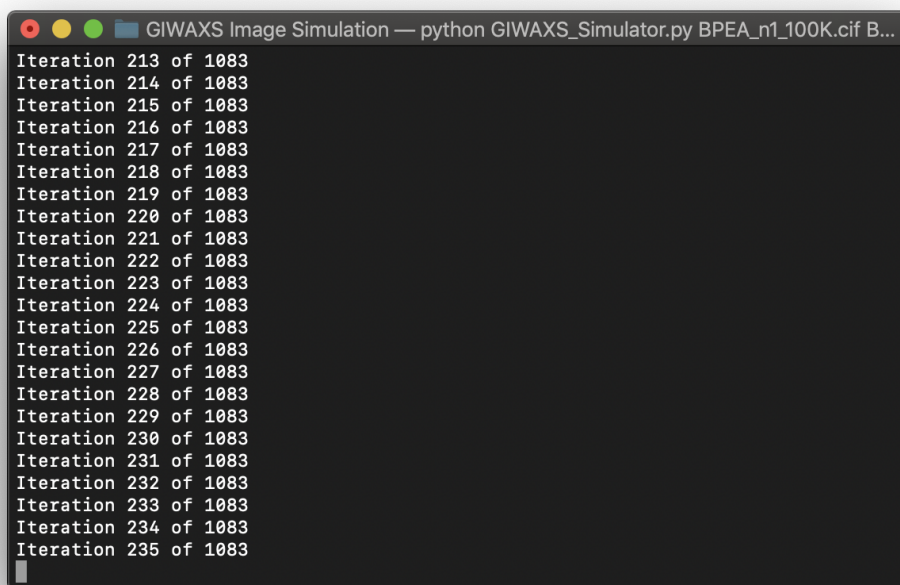
```
GIWAXS Image Simulation — python GIWAXS_Simulator.py BPEA_n1_100K.cif B...
[Naveens-MacBook-Pro:GIWAXS Image Simulation naveenvenkatesan$ python GIWAXS_Simul
ator.py BPEA_n1_100K.cif BPEA_n1_100K_SF.txt
Enter preferred orientation direction (e.g. 111)
Enter h-value: 1
Enter k-value: 0
Enter l-value: 0
Enter X-ray energy (keV): 12.7
Enter max value of Q_xy (1/A): 2.5
Enter max value of Q_z (1/A): 2.5
Enter incidence angle (Deg): 0.1
Enter FWHM in x-direction (1/A): 0.1
Enter FWHM in y-direction (1/A): 0.1
```

Figure 2.8: GIWAXS simulation script window with all the prompted values to enter, which determine peak shape and preferred orientation.

1. **Enter h-value** – Preferred orientation h-value (1 in this case - from 100)
2. **Enter k-value** – Preferred orientation k-value (0 in this case - from 100)
3. **Enter l-value** – Preferred orientation l-value (0 in this case - from 100)
4. **Enter X-ray energy (keV)** – Enter the energy of the X-ray source in keV
5. **Enter max value of Q_{xy} (1/Å)** – Maximum value of Q_{xy} in Å^{-1} for simulation
6. **Enter max value of Q_z (1/Å)** – Maximum value of Q_z in Å^{-1} for simulation
7. **Enter incidence angle (Deg)** – Incident angle for the experiment in degrees ($^{\circ}$)
8. **Enter FWHM in x-direction (1/Å)** – Full-width at half-maximum (FWHM) in the x-direction in Å^{-1} (along the Q_{xy} axis)

9. **Enter FWHM in y-direction (1/A)** – Full-width at half-maximum (FWHM) in the y-direction in \AA^{-1} (along the Q_z axis)

Once all the information has been entered, the script will start to calculate the reflection intensities with the constraints that you have provided. While the calculation is proceeding, the status will be shown in the terminal windows as “Iteration x of y”, as shown in Figure 2.9



```
GIWAXS Image Simulation — python GIWAXS_Simulator.py BPEA_n1_100K.cif B...
Iteration 213 of 1083
Iteration 214 of 1083
Iteration 215 of 1083
Iteration 216 of 1083
Iteration 217 of 1083
Iteration 218 of 1083
Iteration 219 of 1083
Iteration 220 of 1083
Iteration 221 of 1083
Iteration 222 of 1083
Iteration 223 of 1083
Iteration 224 of 1083
Iteration 225 of 1083
Iteration 226 of 1083
Iteration 227 of 1083
Iteration 228 of 1083
Iteration 229 of 1083
Iteration 230 of 1083
Iteration 231 of 1083
Iteration 232 of 1083
Iteration 233 of 1083
Iteration 234 of 1083
Iteration 235 of 1083
```

Figure 2.9: During simulated pattern calculation, the program will update the status by listing the current iteration.

At the conclusion of all iterations, the final GIWAXS image will open in a new window as shown in Figure 2.10. In addition to this, the program will save a TIFF image file with the simulated image. You will notice that the axes will be in pixels rather than reciprocal space, this issue will be discussed later in Section 2.4.

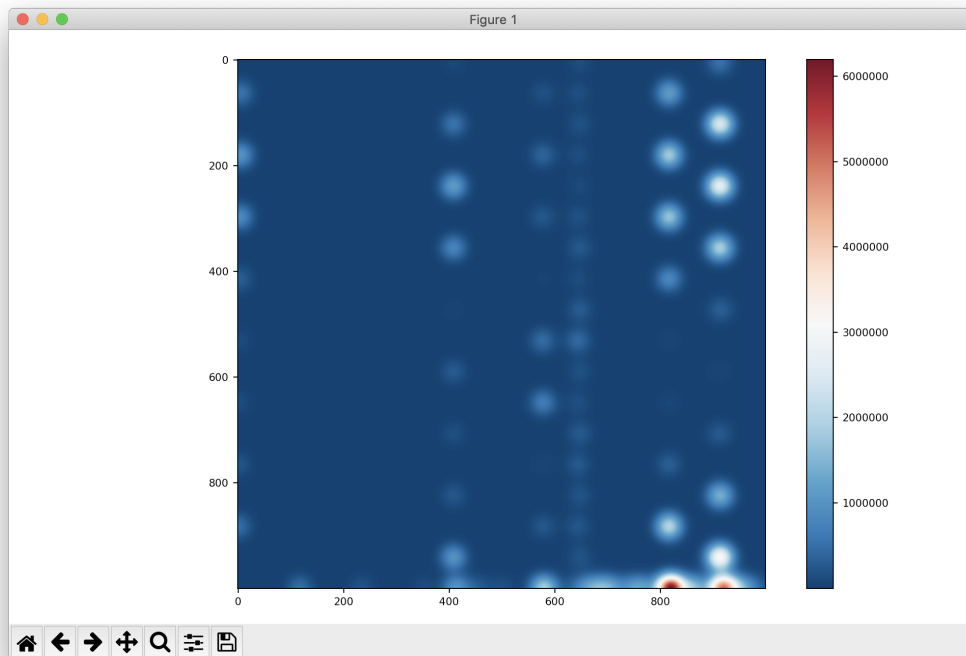


Figure 2.10: Final simulated GIWAXS image that opens at the conclusion of the calculation. This image is also automatically saved as a TIFF file in the same directory – although the axes are in pixels, the reasoning for this will be described later.

2.3.3 GUI-based GIWAXS simulation operating procedure

For the GUI-based program, we will again use the terminal to initially invoke the program, but all subsequent operations will be point-and-click through the program interface. Future development may result in a full standalone deployment of the program, but at this time, the program must still be run through Python and have the same dependencies as in the script-based program above. To open the program, we run the following command:

```
python GIWAXS_Simulator_GUI.py
```

The window that opens will look like the one in Figure 2.11 – the various required inputs

are described below:

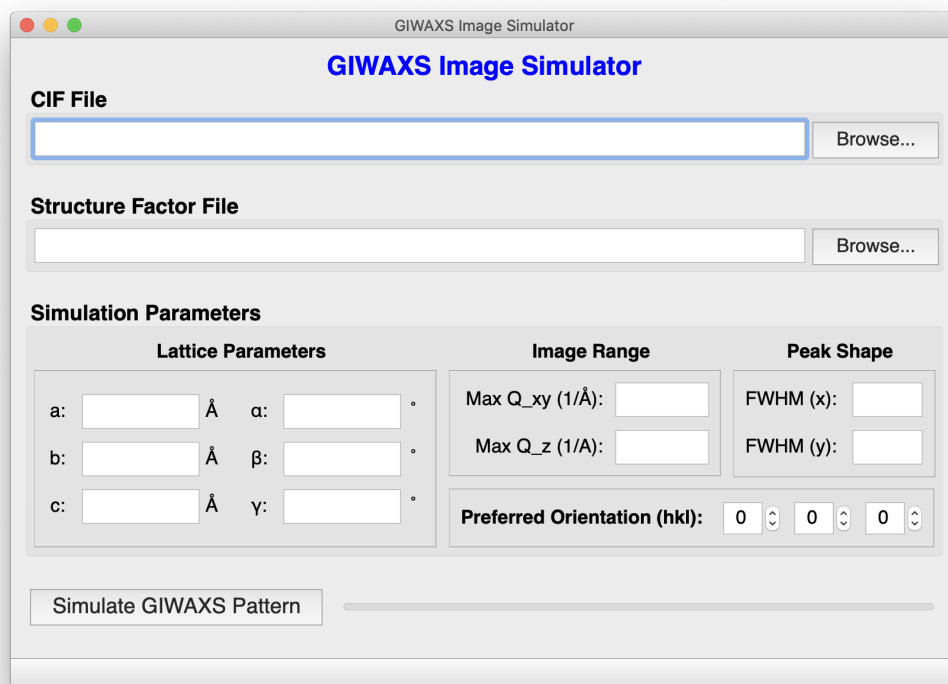


Figure 2.11: GIWAXS simulation software GUI with required inputs for image simulation.

1. **CIF File** – Clicking the “Browse...” button allows you to navigate to the location of the CIF file.
2. **SF File** – Clicking the “Browse...” button allows you to navigate to the location of the file with your saved structure factors.
3. **Lattice Parameters** – Once you locate the CIF file, the fields corresponding to the lattice parameters and angles should populate automatically – If these values are not correct, the fields are editable and you may change the numbers as desired.

4. **Max Q_{xy} and Q_z** – The maximum values of Q_{xy} and Q_z for the simulated image, the default values are 2.5 \AA^{-1} for both.
5. **FWHM (x) and FWHM (y)** – The full-width at half-maximum of the 3D Gaussian functions in the x-direction (along Q_{xy} axis) and y-direction (along Q_z axis), the default values are 0.1 \AA^{-1} for both.
6. **Preferred Orientation** – These spin boxes allow us to set the preferred orientation of the crystal in terms of h, k, and l – in this case, we again enter 100.
7. **Simulate GIWAXS Pattern** – Clicking this button will start the simulation – the progress bar will update as the calculation proceeds. If your inputs are insufficient, an error message will pop up and prompt you on where the problem may be.

At the conclusion of the calculation, a window should pop up with the calculate image. This simulated image should look identical to one shown in Figure 2.10.

2.3.4 Processing TIFF files

Rastered images with intensity values are often stored in TIFF files, also known as Tagged Image File Format. The images outputted by the GIWAXS simulation programs as seen in Figure 2.10 only have pixel values along the x and y axes, rather than the actual values in reciprocal space. This is because the method by which images are encoded only has information corresponding to pixel locations and intensity. Additionally, the TIFF files from the program probably will not be rendered properly by your computer's default image viewer. This is because by default, each pixel in a TIFF file contains an intensity value that is represented by a 16-bit integer, meaning that the range of intensity is between 0 and 65535. The consequence of this limited range is that values are binned into this range during the image save process. In order to work around this, the `tifffile` package allows

us to save a TIFF file with each pixel containing a larger precision value with an increased range. If we process images using Python with the `tifffile` package, we can accurately load this data. Additionally, we can use MATLAB to process the images with the built-in `imread` functions.

The other issue is fixing the axes to show the values in reciprocal space. To assist with this, the saved image filenames are designed to contain the max Q_{xy} and Q_z values that were used during simulation. The filename from our examples should be:

```
BPEA_n1_100K_100_qxy_2.5_qz_2.5_GIXRD.tif
```

The first part of the filename (BPEA_n1_100K) contains the same name as the CIF file loaded for the simulation. The second part of the filename (100) is the preferred orientation used for the simulation. Finally, the next part of the filename (qxy_2.5_qz_2.5) contains the maximum Q_{xy} and Q_z values used in the simulation. Using this information, we can use the following commands in Python and MATLAB to manipulate the images and have accurate reciprocal space axis values:

Python

```
from tifffile import imread, imshow
import matplotlib.pyplot as plt

img = imread('BPEA_n1_100K_100_qxy_2.5_qz_2.5_GIXRD.tif')
imshow(img, extent=(0, 2.5, 0, 2.5), cmap='RdBu_r')
plt.show()
```

MATLAB

```
img = imread('BPEA_n1_100K_100_qxy_2.5_qz_2.5_GIXRD.tif')
imshow(img, [], 'XData', [0 2.5], 'YData', [0 2.5])
```

You should now have a simulated image with the correct x and y axis values (Figure 2.12). You may now proceed to manipulate the plot properties to reflect your personal preference (fonts, linewidths, ticks, *etc.*) and save the final plot for publication/presentation, an example of which is shown in Figure 2.13.

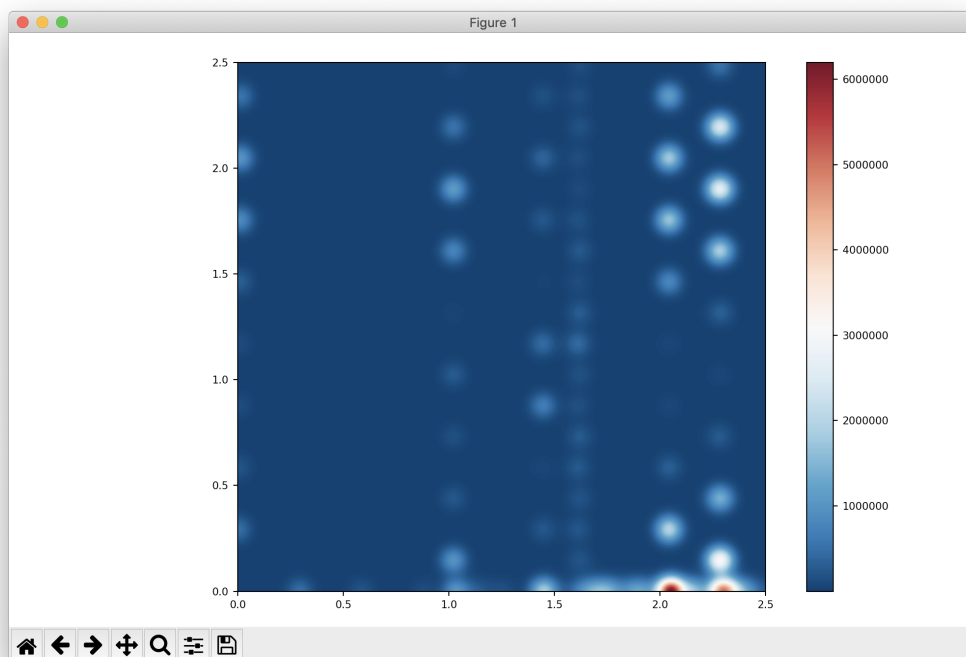


Figure 2.12: Simulated GIWAXS image after running the Python code to shift axes values from pixels to reciprocal space.

2.4 Converting binary files from sychrotron to images

Synchrotron diffraction images are often encoded in binary files – which are non-text files in which the information is listed byte-by-byte. In order to convert these into tractable images that we can process, we must reshape this stream of bytes into a two-dimensional image. This can be automated through scripts, and we have provided a simple GUI that makes this process very quick. In order to use this program, which is also written with

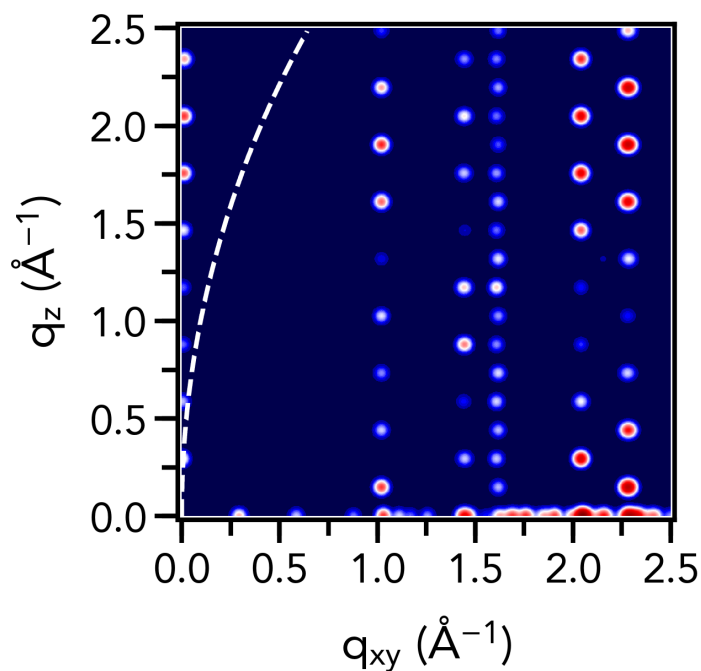


Figure 2.13: Final publication-quality simulated GIWAXS image after manipulation of axis properties.

Python 3, you must have the same dependencies as the previous section on simulating GIWAXS images with the addition of the package `struct`. Again, you can very simply install this package (if you do not already have it) with the following code:

```
python -m pip install struct
```

After having all the correct packages installed, we open the program with the following code:

```
python ConvertBinaryToTIFF.py
```

We will see a window as presented in Figure 2.14 – the different input fields are described below:

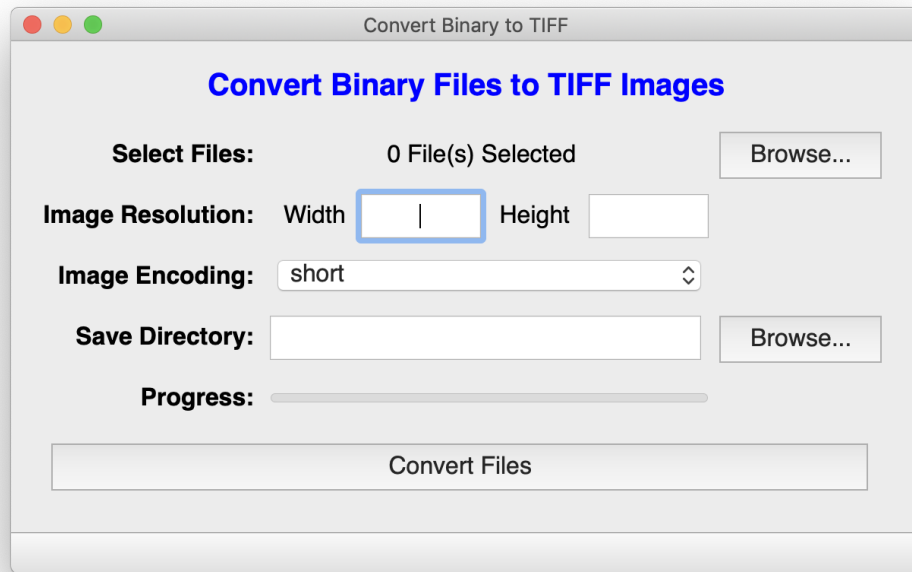


Figure 2.14: Main GUI window for program to convert binary files to TIFF images.

1. **Select Files** – Clicking the “Browse...” button allows you to select binary files that you would like to convert. Data from Beamline 7.3.3. at the Advanced Light Source (ALS) are stored as General Binary (.gb) files, but binary files may have an arbitrary file extension. You have the ability to select multiple files by either holding down the Ctrl/Command or Shift key while selecting. The label that originally said “0 File(s) Selected” should have now changed to the number of files that you selected.
2. **Image Resolution** – One of the two pieces of information you must know is the resolution of the image on the detector. This is because the binary file is just a stream of bytes, so the program needs to know how to reshape these bytes into a two-dimensional image. You can enter the width and heights of the image in pixels in the two boxes.

3. **Image Encoding** – The other piece of information you must know before converting is the precision and format of the numbers used in the file. For data from Beamline 7.3.3 at ALS, the binary files are stored as single precision floating point numbers, so we would choose `float` from the drop-down menu. The encoding is important because it tells the program how many bytes to associate with each pixel of the image, since different precision numbers utilize a different number of bytes. The ranges and number of bits of each data type is shown for reference in Table 2.1 – these are values for a 64-bit operating system. The range of both floating point types (`float` and `double`) are very large but they both have varying precisions (7 decimal places vs. 16 decimal places).
4. **Save Directory** – This directory should default to the same folder as where your loaded binary files are. If you wish to change the save directory, you can click the “Browse...” button to choose a new folder in which to save the converted TIFF images.
5. **Convert Files** – Clicking this button starts the conversion process and the progress bar directly above the button will update as files are converted. If one of your inputs is insufficient, you should receive an error message that is related to the issue. Once the conversion is finished, a window will pop up, indicating completion. Your converted files should be in the save directory, with the same filenames as the binary files, but with the extension ‘`.tif`’.

Again, due to the fact that we use the `tiff` environment to save our image with the data types in their original format, we have to use this package to open the TIFF files, or use MATLAB. Refer to Section for the required code to do this. For an example of what the original binary file (opened in a text editor) and converted image look like, refer to Figures 2.15 and 2.16.

Table 2.1: Numerical data types in a 64-bit operating system, along with the number of bits and range.

Data Type	Bits	Range
short	16	−32768 to 32767
unsigned short	16	0 to 65535
int	32	−2147483648 to 2147483647
unsigned int	32	0 to 4294967295
long	32	−2147483648 to 2147483647
unsigned long	32	0 to 4294967295
long long	64	−9223372036854775808 to 9223372036854775807
unsigned long long	64	0 to 18446744073709551615
float	32	-3.4×10^{38} to 3.4×10^{38}
double	64	-1.7×10^{308} to 1.7×10^{308}

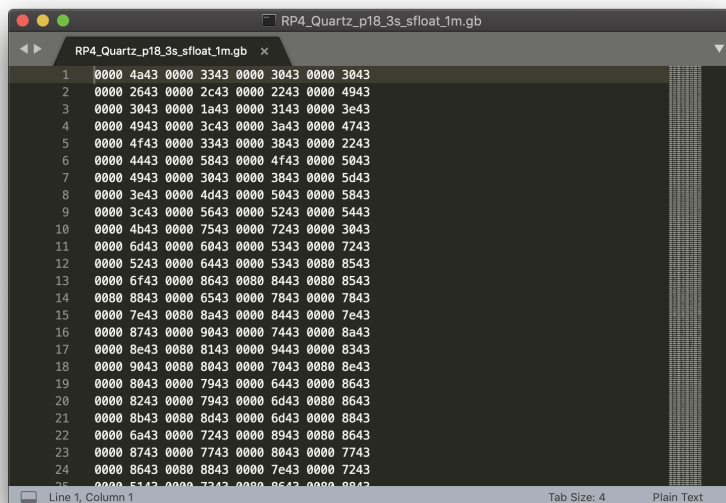


Figure 2.15: Original binary file from Beamline 7.3.3 at ALS opened in a text editor, showing the bytes representing the intensities.

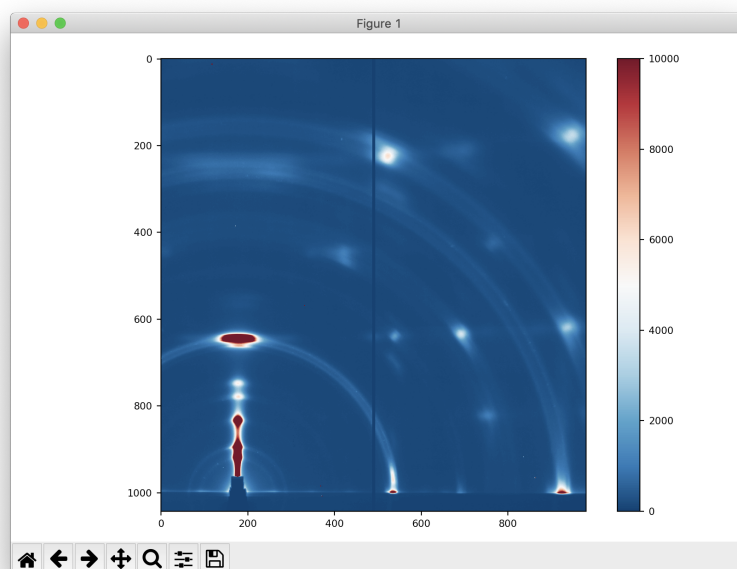


Figure 2.16: TIFF file after conversion, visualized using Python.

2.5 Processing two-dimensional X-ray diffraction images

To process the two-dimensional X-ray diffraction data we collect from synchrotron beamlines, we require *two* things: (1) a diffraction image of interest that we want to process, and (2) a diffraction image of a calibrant with known d -spacings that we can use to calibrate the sample-to-detector distance and beam center. Two commonly used calibrants for X-ray scattering measurements are lanthanum hexaboride (LaB_6 – used at SSRL Beamline 11-3) and silver behenate ($\text{AgC}_{22}\text{H}_{43}\text{O}_2$ – used at ALS Beamline 7.3.3).

We have developed a script to quickly process image files collected from the synchrotron for both of these calibrants. To invoke the program, again we must have the same Python dependencies as described in previous sections, and we use the following command:

```
python XRS_Analyzer.py
```

The program will open and show a window that will look like the one presented in Figure 2.17

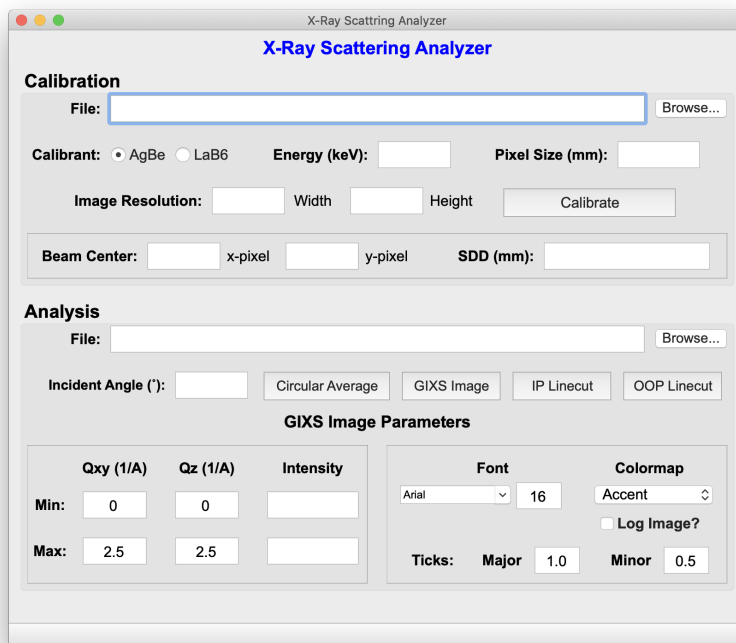


Figure 2.17: X-ray scattering analyzer program to process two-dimensional diffraction data from the synchrotron.

You must first calibrate the beam center pixel and the sample-to-detector distance. To do this, we will utilize the functions in the “Calibration” section at the top of the program window. Once this is complete, you may analyze the synchrotron data, and we have provided a fairly simple plot editor interface to generate a publication quality plot with the diffraction data correctly reshaped geometrically.

2.5.1 Calibration

The calibration panel at the top of the program is what we will use to determine the beam center pixel and the sample-to-detector distance in our experiment. If you already

know this information, you may fill in the boxes for the beam center x-pixel, y-pixel, and the SDD. To proceed with the full calibration as normal, we follow the following steps:

1. **Calibration File:** – Using the “Browse...” button, you may navigate to a diffraction image collected of the calibrant used in the experiment
2. **Calibrant** – You may choose the calibrant used, whether it was silver behenate (AgBe) or lanthanum hexaboride (LaB₆)
3. **Energy (keV):** – The energy of the X-ray source used in the experiment (default is 10 keV for ALS 7.3.3 and 12.7 keV for SSRL 11-3)
4. **Pixel Size (mm):** – The physical size of the pixels on the detector (defaults are 0.172 mm for the Pilatus 2M at ALS 7.3.3 and 0.078242 mm for the Rayonix MX225 at SSRL 11-3)
5. **Image Resolution:** – The resolution of the diffraction image in *pixels* - these fields should automatically populate when you load the TIFF image of the calibrant from step 1. If these are blank, you have selected an invalid image file, but the default are 1475 × 1679 for the Pilatus 2M at ALS 7.3.3 and 3072 × 3072 for the Rayonix MX225 at SSRL 11-3.
6. **Calibrate** – Once all the previous fields are filled, you may press this button to start the calibration process

When you initiate the calibration process, a window will pop up with the image of the calibrant and ask you click points along a specific diffraction ring. The title of the plot will tell you which of the rings (3rd for AgBe and 2nd for LaB₆) – you can click up to 30 points or hit “Enter” when you are done selecting points. At this point, the program will fit the points you have clicked to a circle and extract its radius and center. The center gives the

beam center pixel and the radius can be used to determine the sample-to-detector distance since the diffraction ring is at a known d -spacing. Once the fit is complete, this will be plotted as an overlay onto the diffraction image, as shown in Figure 2.18, and you may close this window. If the fit does not look sufficient, you may click the “Calibrate” button again and redo the point selection. You can also use the zoom tool in the Python window to zoom in closer on the ring, but make sure you right click a couple of times after zooming to ensure that no points have been selected.

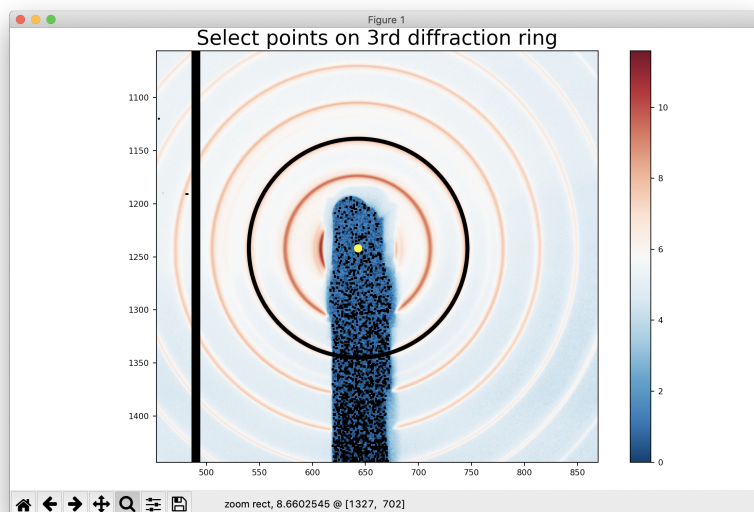


Figure 2.18: Finished calibration of beam center and sample-to-detector distance for an image of silver behenate (AgBe) from ALS Beamline 7.3.3, showing the circle fit and the yellow point indicating the beam center.

2.5.2 Analysis

The analysis section of the program has four main functions: circular averaging for isotropic samples, generating a publication-quality GIXS image with the correct geometric reshaping, and calculating in-plane and out-of-plane intensity cuts for the same GIXS sample. We will go through how to operate the four different functions in the following

sections. Firstly, you must load a diffraction image using the “Browse...” button and enter the incidence angle used if it was a grazing-incidence measurement.

Circular Averaging

If the sample you are measuring has isotropic diffraction, *i.e.* displays Debye-Scherrer rings in its diffraction image, you probably want to do a 1D averaging to collapse the data into simply intensity as a function of the scattering vector (\vec{q}). If you press the button labeled “Circular Average” once you have loaded an image file, this will be computed and displayed as in Figure 2.19. Concurrently, the averaged data will be saved as a .csv file in the same directory as the original image. For this example, we used the same image of the calibrant silver behenate shown in Figure 2.18. If you are interested to try and process these averages yourself, we have included a snippet of code below that is the heart of this averaging program. We are essentially calculating all possible radii from the center of the image in an increment of one pixel and taking the median at each of these radii. The reason that we are using the median operation is to avoid having to explicitly mask values from the beamstop – the median should capture the real value and give some resistance to random fluctuations and noise in our image. We also use a 1 pixel bin less than and greater than the radius we are currently calculating.

```
# Get image parameters
a = img.shape[0]
b = img.shape[1]

[X, Y] = np.meshgrid(np.arange(b) - cen_x, np.arange(a) - cen_y)
R = np.sqrt(np.square(X) + np.square(Y))

rad = np.arange(1, np.max(R), 1)
intensity = np.zeros(len(rad))
```

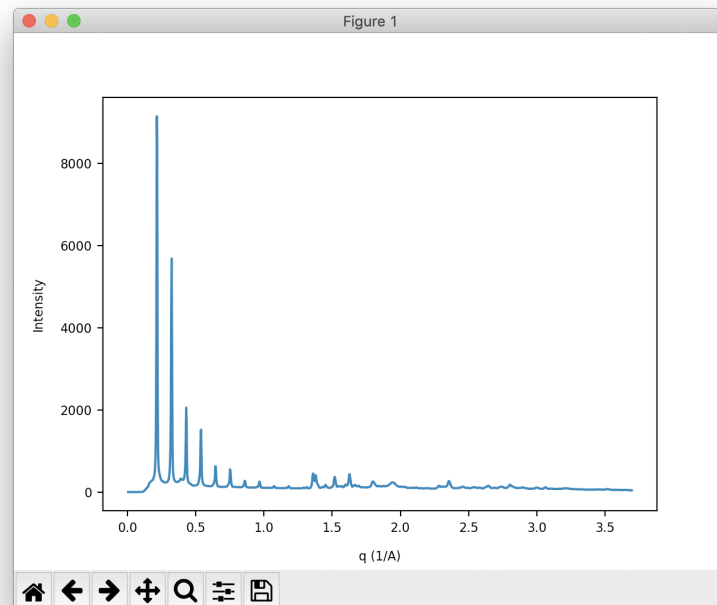


Figure 2.19: Circularly averaged diffraction data of isotropic silver behenate (AgBe) sample.

```
counter = 0

for i in rad:
    mask = (np.greater(R, i - 1) & np.less(R, i + 1))
    values = img[mask]
    intensity[counter] = np.median(values)
    counter += 1

    # Update the progress bar on the screen based on
    # the iteration of the loop
    QtWidgets.QApplication.processEvents()

# Calculate scattering vector values at each radius
q = (4*np.pi/xlam)*np.sin(np.arctan((rad*pix_size)/sdd)/2)
```

GIXS Image

This button allows us to generate a publication-quality plot of our scattering image if

we did a grazing-incidence experiment. For this section, you can also utilize all the boxes below to control plot parameters such as the plot range, as described below:

1. **Q_{xy} and Q_z Min/Max** – Enter the range that you would like in your final plot. If there is not enough data for the full range, there will be blank space in this area of your final plot. The default values are 0 as the minimum and 2.5 as the maximum for both Q_{xy} and Q_z .
2. **Intensity** – These boxes should automatically fill once you load an image with the lowest and highest intensity pixel present in the image. You can edit this range to affect the contrast in your final image.
3. **Font** – This will list all of your system fonts that you can then use in your plot, and the box next to the font dropdown menu is the font size that will be used. The defaults for both of these will be “Arial” and size 16.
4. **Colormaps** – This is the list of the installed Python colormaps that you can use for your final image. If you want to see what these colormaps look like you can follow this link: [Matplotlib Colormaps](#).⁷ The default will be the first available colormap in alphabetical order (probably “Accent”). The colormaps `viridis`, `plasma`, `inferno`, `magma`, and `cividis` are all what are called “perceptually uniform”, meaning that the intensity of the colors in the range consistently increase from the first color to the last. The advantage of this over one of the typical colormaps like `jet` is that all colors go from “dark” to “light”, unlike `jet` which goes from a dark blue to a dark red. There is some more information about this topic [here](#) if you are interested.⁸
5. **Log Image?** – Checking this box will normalize the colors on the logarithmic scale rather than linear. The lowest value will be set to 0, but you can control the maximum

again. This can be used to maximize your desired contrast if you cannot easily see features on a linear scale.

6. **Ticks** – You can set the interval of the major and minor tick marks in your plot, the default values being 1.0 for major and 0.5 for minor.

Once you have edited all the parameters to your liking, clicking the “GIXS Image” button will generate a plot of your diffraction data with the correct geometric correction and display the plot, as in Figure 2.20. The program will also save a .png file, in the same location as the original image, of the plot with a resolution of 300 dots-per-inch, ideal for publication. The image we have used for this example is one of PBTTT (poly[2,5-bis(3-tetradecylthiophen-2-yl)thieno[3,2-b]thiophene]), collected at ALS 7.3.3.

To understand the reshaping of pixels to produce a geometrically-accurate grazing-incidence X-ray scattering image, Figure 2.21 illustrates the two angles of interest, θ and ϕ . We essentially need to take the image data from the flat detector and project it into spherical coordinates. Then, conversion from a spherical coordinate system into Cartesian coordinates that we can plot can be done using Equations 2.5, 2.6, and 2.7.

$$x = r\cos(\theta)\cos(\phi) \tag{2.5}$$

$$y = r\cos(\theta)\sin(\phi) \tag{2.6}$$

$$z = r\sin(\theta) \tag{2.7}$$

Since we have elastic X-ray scattering, the magnitude of our scattered X-ray is constant (not to be confused with the *scattering vector* \vec{q} , whose magnitude and direction *does* change), with $|k| = 2\pi/\lambda$, so this is the r in the equations above. Since the scattering vector is the

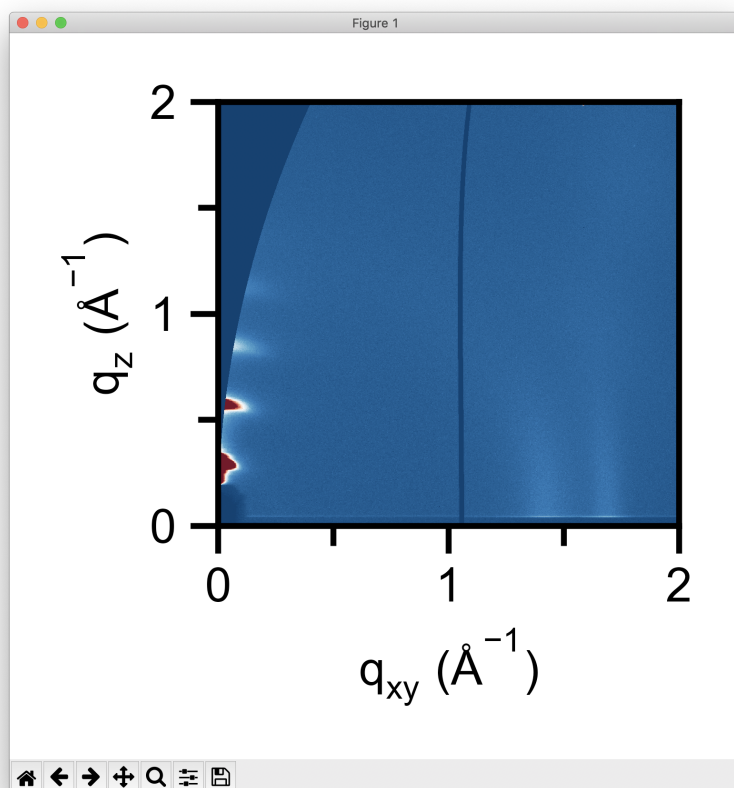


Figure 2.20: Geometrically-reshaped GIWAXS image of PBTTT collected at ALS Beamline 7.3.3.

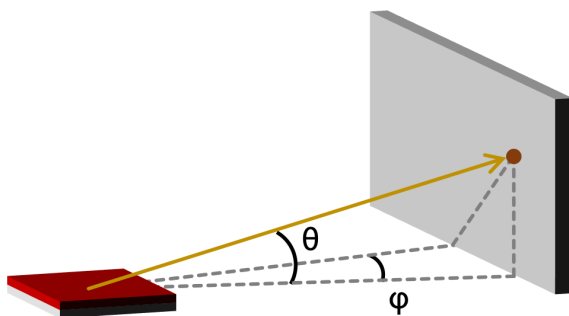


Figure 2.21: Schematic of grazing-incidence X-ray scattering experiment, with the angles θ and ϕ labeled.

difference between the outgoing and incoming X-rays, we can calculate the three components of \vec{q} as follows using incident angle ω , shown in Equations 2.8, 2.9, and 2.10 (note that the incoming X-ray only has components in the y and z directions).

$$q_x = (2\pi/\lambda)\cos(\theta)\cos(\phi) \quad (2.8)$$

$$q_y = (2\pi/\lambda)[\cos(\theta)\sin(\phi) - \cos(\omega)] \quad (2.9)$$

$$q_z = (2\pi/\lambda)[\sin(\theta) - \sin(\omega)] \quad (2.10)$$

Finally, since we are only measuring two-dimensional data, our in-plane data is actually q_{xy} , which is calculated as the magnitude of the vector of the sum of the q_x and q_y vectors, shown in Equation 2.11

$$q_{xy} = \sqrt{q_x^2 + q_y^2} \quad (2.11)$$

In-Plane Linecut

The “IP Linecut” button calculates an intensity cut along the q_{xy} axis and displays the data. In this example, we have again used the diffraction image of PBTTT shown in Figure 2.20. The resulting data is shown in a new window (Figure 2.22) and also saved as a .csv file in the same location of the original image file. In this example, we see the two $\pi - \pi$ stacking peaks along the in-plane cut. To improve the signal-to-noise of the intensity cut, we have utilized a 15-pixel averaging around the beam center y-pixel, allowing us to more clearly capture the peaks.

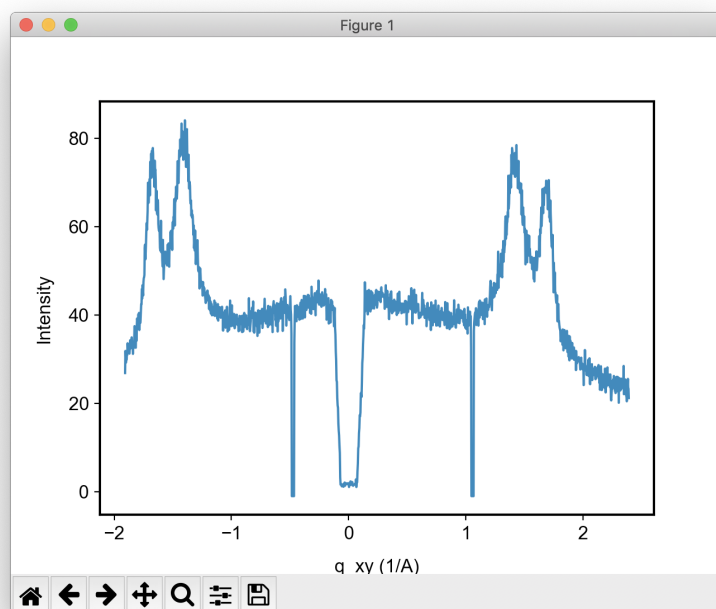


Figure 2.22: In-plane intensity cut of PBTTT measured at ALS Beamline 7.3.3, showing $\pi - \pi$ stacking peaks.

Out-of-Plane Linecut

The “OOP Linecut” button calculates an intensity cut along the q_z axis and displays the data. Again, using the same PBTTT example, the data will show in new window seen in Figure 2.23 and be saved as a .csv file in the same location. The data shown is on a linear scale, but if the y-axis is scaled to logarithmic, all the alkyl stacking peaks in PBTTT will become more apparent. Again, to improve the signal-to-noise, we have used an 11 pixel average around the central x-pixel. Since out-of-plane diffraction is so strong, this averaging is less necessary than in the in-plane case.

Using the scripts presented in the previous three sections, you should be able to process your synchrotron diffraction data and compare it to the expected diffraction from the solved crystal structures. The details of the calculations have also been presented in this and

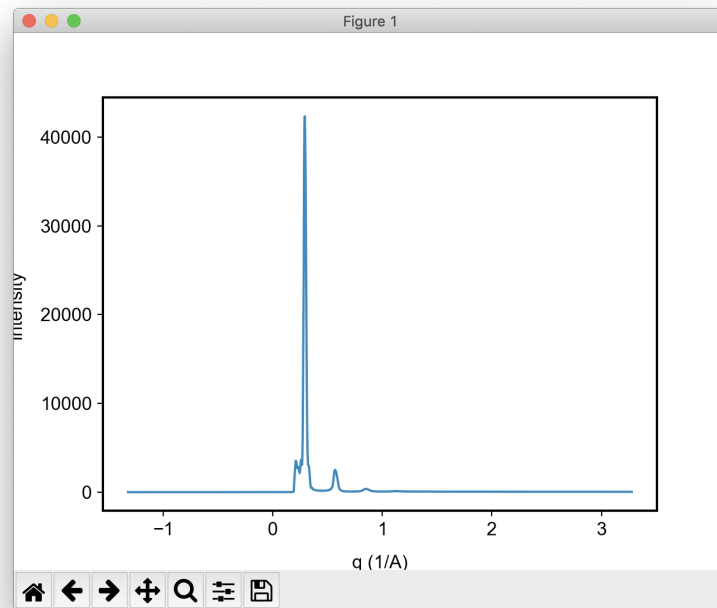


Figure 2.23: Out-of-plane intensity cut of PBTTT measured at ALS Beamline 7.3.3, showing alkyl stacking peaks. Peak contrast can be improved by re-plotting the data using a logarithmic y-axis.

other chapters if you wish to create your own script to process synchrotron diffraction data. All scripts are open-source and created in Python, so any improvements on the current implementations is welcomed and encouraged.

2.6 References

1. Birkholz, M. *Thin Film Analysis by X-Ray Scattering* (John Wiley & Sons, 2006).
2. Baker, J. L., Jimison, L. H., Mannsfeld, S., Volkman, S., Yin, S., Subramanian, V., Salleo, A., Alivisatos, A. P. & Toney, M. F. Quantification of Thin Film Crystallographic Orientation Using X-Ray Diffraction with an Area Detector. *Langmuir* **26**, 9146–9151 (2010).
3. Schlipf, J., Docampo, P., Schaffer, C. J., Körstgens, V., Bießmann, L., Hanusch, F., Giesbrecht, N., Bernstorff, S., Bein, T. & Müller-Buschbaum, P. A Closer Look into Two-Step Perovskite Conversion with X-Ray Scattering. *The Journal of Physical Chemistry Letters* **6**, 1265–1269 (2015).
4. Schlipf, J. & Müller-Buschbaum, P. Structure of Organometal Halide Perovskite Films as Determined with Grazing-Incidence X-Ray Scattering Methods. *Advanced Energy Materials*, 1700131 (2017).
5. Anaconda. *Anaconda Python/R Distribution - Free Download* Library Catalog: www.anaconda.com. 2020.
6. Momma, K. & Izumi, F. VESTA-3 for Three-Dimensional Visualization of Crystal, Volumetric and Morphology Data. *Journal of Applied Crystallography* **44**, 1272–1276 (2011).
7. Matplotlib. *Choosing Colormaps in Matplotlib* 2020.
8. Smith, N. & van der Walt, S. *Matplotlib Colormaps* <https://bids.github.io/colormap/>. 2020.

Chapter 3

Charge Transport in a Two-Dimensional Hybrid Metal Halide Thiocyanate Compound

3.1 Abstract

Solution-processable organic metal halide compounds, such as methylammonium lead iodide ($\text{CH}_3\text{NH}_3\text{PbI}_3$), possess unique optical and electronic properties such as long carrier lifetimes and high charge carrier mobility. Here we study a layered, two-dimensional hybrid halide compound: methylammonium lead thiocyanate iodide ($(\text{CH}_3\text{NH}_3)_2\text{Pb}(\text{SCN})_2\text{I}_2$). Films deposited from solution are observed to grow with strong preferential alignment of two-dimensional layers parallel to the substrate. The charge transport properties of carriers in the two-dimensional planes of $(\text{CH}_3\text{NH}_3)_2\text{Pb}(\text{SCN})_2\text{I}_2$ were measured using the contactless electronic characterization technique time-resolved microwave conductivity (TRMC). TRMC measurements show that the sum of the electron and hole charge carrier mobilities in $(\text{CH}_3\text{NH}_3)_2\text{Pb}(\text{SCN})_2\text{I}_2$ is above $1 \text{ cm}^2 \text{ V}^{-1} \text{ s}^{-1}$ and that the carrier lifetime is relatively

long.

3.2 Introduction

Solution-processable, earth-abundant organic metal halide materials possess optoelectronic properties that are, by many metrics, extraordinary.¹⁻¹⁶ Hybrid organic metal-halide, Pb-based compounds with the general perovskite formula ABX_3 are strong absorbers in the visible and near-infrared portion of the solar spectrum,^{7,17} have high charge-carrier mobilities,^{12,18} exhibit carrier-diffusion lengths on the order of microns,^{5,6} display an unusually low concentration^{7,19} of energetically shallow¹² electronic trap states, and demonstrate evidence of photon recycling.¹⁵ Lab-scale solar cells based on methylammonium lead iodide ($CH_3NH_3PbI_3$) (see Figure 3.1a) and other related compounds have been reported with certified power conversion efficiencies in excess of 22%;²⁰ fast approaching that of monocrystalline silicon,^{21,22} making them competitive with existing thin film materials such as CdTe.²³ Despite these breakthroughs and following intense research, questions related to the stability of these materials and their fundamental properties must be answered before widespread commercialization of these systems can take place.²⁴⁻²⁷ For this reason, the incentive to identify alternative materials with similar optoelectronic properties is considerable.²⁸⁻⁴¹

The range of three-dimensional hybrid-halide perovskites is relatively limited,²⁹⁻³² owing to the size constraint of the A-site, which facilitates just two organic cations (when the B site is Pb^{2+} , Sn^{2+}): methylammonium ($CH_3NH_3^+$) and formamidinium ($HC(NH_2)_2^+$), and inorganic counterions such as Cs^+ . However, there are now a number of notable reports of other hybrid-halide material classes with interesting properties, including “perovskite-like” structures such as defect perovskites,³³ double-perovskites,^{39,40} perovskite-related materials with bismuth and antimony,^{36,37} and hybrid-halide compounds utilizing functional

organic cations.⁴¹ It has been long known that by reducing the dimensionality of the corner-connected perovskite structure, the size constraint on the organic cation molecule can be relaxed, enabling a larger range of molecules to be employed.⁴² By controlling the number of perovskite layers^{35,43,44} or the orientation⁴⁵ in such layered compounds, a range of optical and electronic properties have been observed. Ruddlesden–Popper hybrid-halide compounds for example^{34,35,38} have shown remarkable stability and sustained performance in single junction solar cells due to preferential film growth orientation.³⁸

In this report, we study an alternative strategy to form two-dimensional hybrid-halide compounds. Instead of replacing the cation molecule, some of the halide atoms can be substituted with pseudo-halides, as in the case of the compound methylammonium lead thiocyanate iodide: $(\text{CH}_3\text{NH}_3)_2\text{Pb}(\text{SCN})_2\text{I}_2$ (see Figure 3.1b).^{46–56} This is a two-dimensional analog of $\text{CH}_3\text{NH}_3\text{PbI}_3$, where the halide anion I^- is substituted with the pseudo-halide thiocyanate $(\text{SCN})^-$ in the axial sites of the Pb octahedra. We employ time-resolved microwave conductivity (TRMC) to study the charge transport properties of $(\text{CH}_3\text{NH}_3)_2\text{Pb}(\text{SCN})_2\text{I}_2$. Because this compound is a layered two-dimensional structure rather than a three-dimensional perovskite, one can anticipate significant differences in the optical and charge-transport properties from $\text{CH}_3\text{NH}_3\text{PbI}_3$.^{44,51,56,57}

TRMC is a local technique that probes the combined charge-carrier generation and transport properties of a material, without the need for a continuous film,^{12,58–72} hence providing a probe of material properties independent of its behavior in a device. The extracted figure of merit $\phi \Sigma \mu$, and lifetime τ , serve as reliable proxies for potential charge-extraction performance in solar cells.^{12,73} By applying the TRMC technique to $(\text{CH}_3\text{NH}_3)_2\text{Pb}(\text{SCN})_2\text{I}_2$, we are able to identify long lived-carriers with mobilities of $\sim 1 \text{ cm}^2 \text{ V}^{-1} \text{ s}^{-1}$, as has previously been observed for fully-halogenated layered organic metal halides.⁴⁴

3.3 Results and Discussion

We grew films of $\text{CH}_3\text{NH}_3\text{PbI}_3$ and $(\text{CH}_3\text{NH}_3)_2\text{Pb}(\text{SCN})_2\text{I}_2$ on quartz substrates from solution *via* known solvent-annealing techniques.^{51,74,75} Optical micrographs are shown in Figure 3.1c and d for $\text{CH}_3\text{NH}_3\text{PbI}_3$ and $(\text{CH}_3\text{NH}_3)_2\text{Pb}(\text{SCN})_2\text{I}_2$, respectively, demonstrating the semi-continuous nature of the $(\text{CH}_3\text{NH}_3)_2\text{Pb}(\text{SCN})_2\text{I}_2$ films over large areas. Scanning electron microscope images of $\text{CH}_3\text{NH}_3\text{PbI}_3$ and $(\text{CH}_3\text{NH}_3)_2\text{Pb}(\text{SCN})_2\text{I}_2$ are shown in Figure 3.1e and f respectively. The lateral dimensions of the grains determined by image analysis are approximately 200 nm for $\text{CH}_3\text{NH}_3\text{PbI}_3$, comparable to films grown under similar conditions,⁷⁰ and 2 μm for $(\text{CH}_3\text{NH}_3)_2\text{Pb}(\text{SCN})_2\text{I}_2$. The size of grains in films of $\text{CH}_3\text{NH}_3\text{PbI}_3$ are known to be highly-dependent on growth conditions^{70,75,76} and we have not examined protocols to produce micron-sized⁷⁶ grains of $\text{CH}_3\text{NH}_3\text{PbI}_3$ for the purposes of this study.

The optical properties of the films were determined using ultraviolet-visible spectroscopy (see Figure 3.2). The absorption spectrum of $(\text{CH}_3\text{NH}_3)_2\text{Pb}(\text{SCN})_2\text{I}_2$ is clearly blue-shifted with respect to the three-dimensional perovskite, as expected for a two-dimensional analog.^{51,77} There is a clear exciton peak in the two-dimensional material at 554 nm (2.24 eV), and the spectrum is in general agreement with those previously reported.^{51,53} Photoluminescence spectroscopy measurements were also carried out on these films, again in agreement with previous reports⁵⁶ (see Section 3.5.5).

The structural purity and preferential alignment of $(\text{CH}_3\text{NH}_3)_2\text{Pb}(\text{SCN})_2\text{I}_2$ films were examined using X-ray diffraction. Figure 3.3a shows normalized experimental XRD patterns of $(\text{CH}_3\text{NH}_3)_2\text{Pb}(\text{SCN})_2\text{I}_2$ grown on a quartz substrate, scraped off the surface with a razor blade, then ground into a powder, and of a pristine $(\text{CH}_3\text{NH}_3)_2\text{Pb}(\text{SCN})_2\text{I}_2$ film. Calculated diffraction patterns of $(\text{CH}_3\text{NH}_3)_2\text{Pb}(\text{SCN})_2\text{I}_2$ with preferential orientation (isotropic) are additionally shown. We see that, as expected, the powder scraped off the substrate has a pattern closely matching that of isotropic $(\text{CH}_3\text{NH}_3)_2\text{Pb}(\text{SCN})_2\text{I}_2$. The diffraction pattern

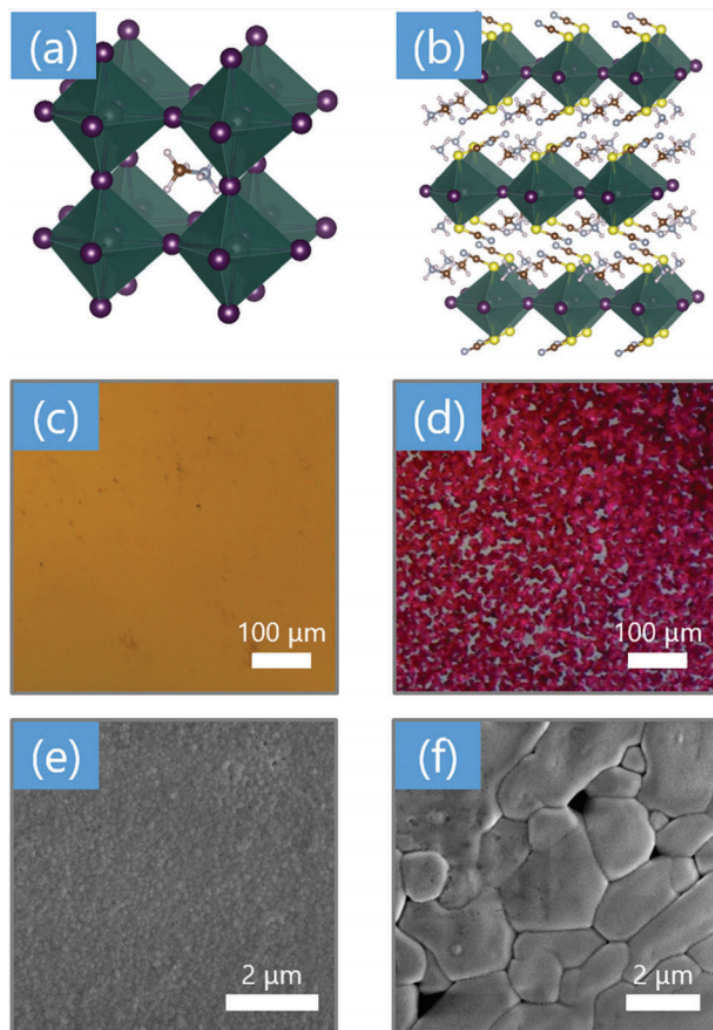


Figure 3.1: (a and b) Crystal structure of methylammonium lead iodide ($\text{CH}_3\text{NH}_3\text{PbI}_3$) and methylammonium lead thiocyanate iodide ($(\text{CH}_3\text{NH}_3)_2\text{Pb}(\text{SCN})_2\text{I}_2$) respectively. Purple spheres represent iodine atoms, green octahedra surround lead atoms, brown spheres represent carbon atoms, gray spheres nitrogen atoms, yellow spheres represent sulfur, and white spheres hydrogen atoms. (c and d) Optical microscope images of $\text{CH}_3\text{NH}_3\text{PbI}_3$ and $(\text{CH}_3\text{NH}_3)_2\text{Pb}(\text{SCN})_2\text{I}_2$ films deposited onto quartz substrates, respectively. (e and f) Scanning electron microscope images of $\text{CH}_3\text{NH}_3\text{PbI}_3$ and $(\text{CH}_3\text{NH}_3)_2\text{Pb}(\text{SCN})_2\text{I}_2$ film surfaces, respectively.

of the film of $(\text{CH}_3\text{NH}_3)_2\text{Pb}(\text{SCN})_2\text{I}_2$ appears to closely match that with preferential orientation in the $[100]$ direction, *i.e.* with two-dimensional planes parallel to the substrate. We do not observe the presence of $\text{CH}_3\text{NH}_3\text{PbI}_3$ in films of $(\text{CH}_3\text{NH}_3)_2\text{Pb}(\text{SCN})_2\text{I}_2$, and the same experimental data is plotted with a logarithmic y-axis scale in the Section 3.5.3 to

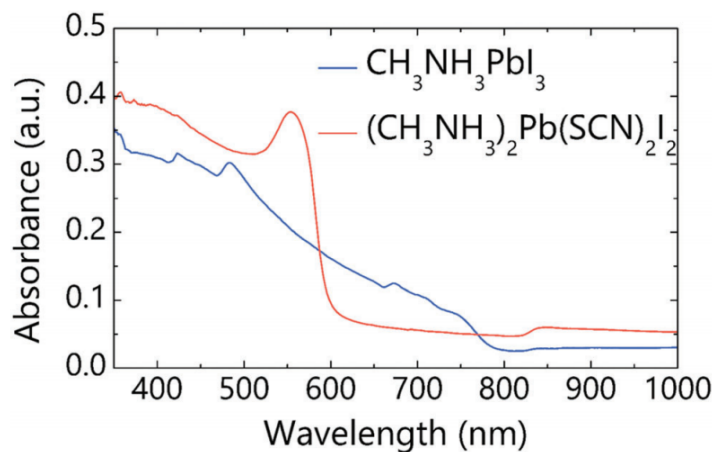


Figure 3.2: Optical absorption spectra of films of methylammonium lead iodide ($\text{CH}_3\text{NH}_3\text{PbI}_3$) and methylammonium lead thiocyanate iodide ($(\text{CH}_3\text{NH}_3)_2\text{Pb}(\text{SCN})_2\text{I}_2$).

illustrate purity.

Figure 3.3b shows a rocking curve taken at the 200 peak of $(\text{CH}_3\text{NH}_3)_2\text{Pb}(\text{SCN})_2\text{I}_2$. The full-width at half maximum of the rocking curve is 515 arcseconds, a value that is indicative of a polycrystalline film that is highly textured along the [100] direction.

When reducing the dimensionality of a system, one can generally expect to observe a wider bandgap in a two-dimensional system than its three-dimensional counterpart.^{57,77,78} The exact details of the electronic structure of $(\text{CH}_3\text{NH}_3)_2\text{Pb}(\text{SCN})_2\text{I}_2$ are currently under debate with respect to the experimentally observed optical absorption spectrum,^{50,51} but the band structure calculated by density functional theory (DFT) indicates the compound has a nearly direct bandgap of ~ 2.1 eV, with a marginally smaller indirect gap of ~ 2.05 eV.⁵¹ The band structure reported from DFT yields effective masses parallel to the two-dimensional sheets in $(\text{CH}_3\text{NH}_3)_2\text{Pb}(\text{SCN})_2\text{I}_2$ as $m_h^* = 0.99m_e$ and $m_e^* = 0.88m_e$ in the [010] direction and $m_h^* = 2.36m_e$ and $m_e^* = 0.34m_e$ in the [001] direction, where m_e is the rest mass of an electron *in vacuo*.⁵¹ For comparison, the effective masses of carriers in $\text{CH}_3\text{NH}_3\text{PbI}_3$ are reported to be between $0.1m_e$ and $0.3m_e$.⁷⁹ However, the band diagram is very flat in the [100] direction between layers in $(\text{CH}_3\text{NH}_3)_2\text{Pb}(\text{SCN})_2\text{I}_2$, suggesting that carriers are

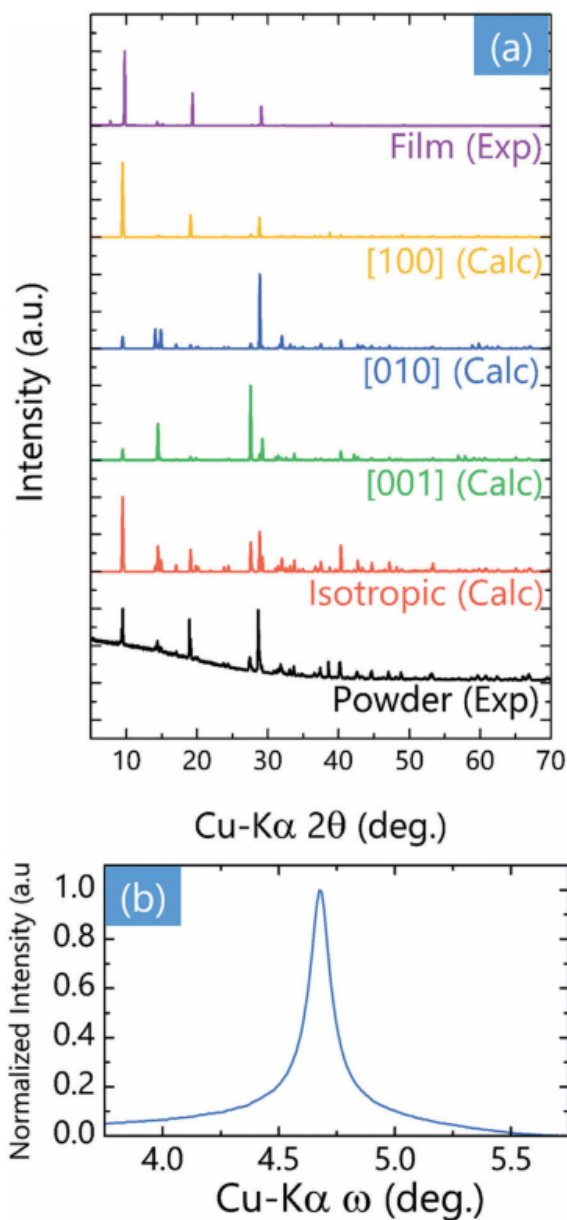


Figure 3.3: (a) Experimental and calculated XRD patterns of various forms of methylammonium lead thiocyanate iodide $((\text{CH}_3\text{NH}_3)_2\text{Pb}(\text{SCN})_2\text{I}_2)$. “Film (Exp)” labels the experimentally measured diffraction of a thin film, “[hkl] (Calc)” labels the calculated diffraction pattern with preferential growth in the labeled direction, “Isotropic (Calc)” labels the calculated diffraction pattern with no preferential growth direction and “Powder (Exp)” labels the diffraction pattern obtained experimentally from a powder scraped off a thin film and ground up. (b) Normalized rocking curve of 200 diffraction peak in $(\text{CH}_3\text{NH}_3)_2\text{Pb}(\text{SCN})_2\text{I}_2$ (along the plane stacking direction). The full-width at half-maximum was extracted to be 515 arcseconds.

highly confined to the two-dimensional planes and that transport between layers would occur by hopping conduction.

To study the electronic properties of this compound we employed time-resolved microwave conductivity (TRMC).^{58,64} The geometry of our TRMC system enables us to measure the mobility of charge carriers moving perpendicular to the propagation direction of the incident optical photons and hence in the plane of the film and, based on orientation extracted from XRD, in the planes of $(\text{CH}_3\text{NH}_3)_2\text{Pb}(\text{SCN})_2\text{I}_2$ layers. The energy of incident photons (2.33 eV) is in excess of the band gap of both $\text{CH}_3\text{NH}_3\text{PbI}_3$ (~ 1.5 eV)¹⁹ and $(\text{CH}_3\text{NH}_3)_2\text{Pb}(\text{SCN})_2\text{I}_2$ (~ 2.0 eV)⁵¹ so carriers are generated by band-to-band transitions in both systems. Thermalization of hot carriers is known to take place on the order of $\sim \text{ps}^6$ to $\sim 100 \text{ ps}^{80}$ in hybrid halide compounds, which, despite being slower than in organic bulk heterojunctions for example,^{81,82} is faster than the timescale of TRMC measurements, defined by the response of the cavity and width of the laser pulse ($\sim \text{ns}$). Hence, we can be confident that the values of $\phi \Sigma \mu$ extracted are representative of relaxed carriers. Our excitation energy is higher than the exciton binding energy of $(\text{CH}_3\text{NH}_3)_2\text{Pb}(\text{SCN})_2\text{I}_2$; therefore the initially formed electron-hole pairs can recombine to the ground state, or to form excitonic states upon relaxation. Nonetheless, we expect the carrier yield to be lower in $(\text{CH}_3\text{NH}_3)_2\text{Pb}(\text{SCN})_2\text{I}_2$ than in $\text{CH}_3\text{NH}_3\text{PbI}_3$.

The effective masses calculated for $(\text{CH}_3\text{NH}_3)_2\text{Pb}(\text{SCN})_2\text{I}_2$,⁵¹ while higher than $\text{CH}_3\text{NH}_3\text{PbI}_3$,⁷⁹ suggest that in-plane charge transport should result in a mobility comparable to other solution processable semiconductors. Figure 3.4 shows TRMC plots ($\phi \Sigma \mu$ as a function of time) for a film of $\text{CH}_3\text{NH}_3\text{PbI}_3$ and $(\text{CH}_3\text{NH}_3)_2\text{Pb}(\text{SCN})_2\text{I}_2$ at a high fluence of $1.6 \times 10^{14} \text{ photons cm}^{-2}$. The TRMC figure of merit ($\phi \Sigma \mu$) is the product of the charge-carrier generation efficiency ϕ , and the sum of the electron and hole mobilities: $\Sigma \mu = \mu_e + \mu_h$. At this fluence of $1.6 \times 10^{14} \text{ photons cm}^{-2}$, the maximum value of $\phi \Sigma \mu$ is approximately $0.8 \text{ cm}^2 \text{ V}^{-1} \text{ s}^{-1}$ for $\text{CH}_3\text{NH}_3\text{PbI}_3$ and $0.4 \text{ cm}^2 \text{ V}^{-1} \text{ s}^{-1}$ for

$(\text{CH}_3\text{NH}_3)_2\text{Pb}(\text{SCN})_2\text{I}_2$. Fig. 3.4c shows TRMC plots for $(\text{CH}_3\text{NH}_3)_2\text{Pb}(\text{SCN})_2\text{I}_2$ under various fluences, with a logarithmic y-axis scale.

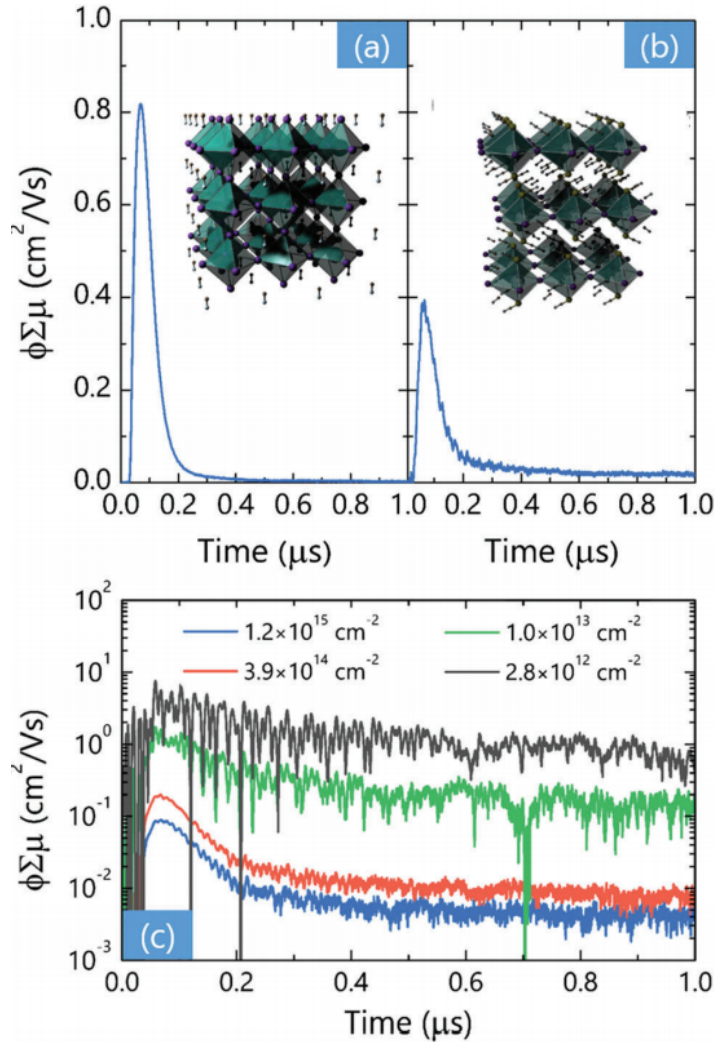


Figure 3.4: Example time-resolved microwave conductivity (TRMC) plots; $\phi \Sigma \mu$ as a function of time, for films of (a) methylammonium lead iodide ($\text{CH}_3\text{NH}_3\text{PbI}_3$) and (b) methylammonium lead thiocyanate iodide ($(\text{CH}_3\text{NH}_3)_2\text{Pb}(\text{SCN})_2\text{I}_2$) at a fluence of 1.6×10^{14} photons cm^{-2} . (c) Four example TRMC plots for $(\text{CH}_3\text{NH}_3)_2\text{Pb}(\text{SCN})_2\text{I}_2$ at various fluences, plotted with a logarithmic y-axis scale. The samples were illuminated with green light from a pulsed Nd:YAG laser with emission frequency of 532 nm and a full-width at half maximum of 5 ns. The films were measured in ambient air conditions at room temperature. The applied microwave power and frequency were 16 dBm and 8.35 GHz, respectively. Insets: structures of $\text{CH}_3\text{NH}_3\text{PbI}_3$ (a) and (b) $(\text{CH}_3\text{NH}_3)_2\text{Pb}(\text{SCN})_2\text{I}_2$.

Figure 3.5a shows peak values $\phi \Sigma \mu$ for $\text{CH}_3\text{NH}_3\text{PbI}_3$ and $(\text{CH}_3\text{NH}_3)_2\text{Pb}(\text{SCN})_2\text{I}_2$ at var-

ious fluences. A minimum fluence of $1.1 \times 10^{11} \text{ cm}^{-2}$ and $2.8 \times 10^{12} \text{ cm}^{-2}$ were studied for the $\text{CH}_3\text{NH}_3\text{PbI}_3$ and $(\text{CH}_3\text{NH}_3)_2\text{Pb}(\text{SCN})_2\text{I}_2$ films respectively. These values represent the respective instrument limits for the two films. Because the film coverage was better in the former case, the signal-to-noise ratio was higher, and the measurement range was larger. Extraction of the sum of the mobility of the carriers from the peak value of $\phi \Sigma \mu$ is dependent on knowledge of the number of carriers in the sample generated by the light pulse, and is affected by the yield and recombination prior to detection of the transient. The yield of carriers will depend on the exciton binding energy, and the yield is known to decrease with lower dimensionality in layered hybrid-halide compounds.⁴⁴ In the two-dimensional compound, $(\text{CH}_3\text{NH}_3)_2\text{Pb}(\text{SCN})_2\text{I}_2$, the exciton binding energy is reported to be approximately 200 meV,⁵³ while the value for the three-dimensional perovskite $\text{CH}_3\text{NH}_3\text{PbI}_3$ is known to be $\sim 5\text{--}60 \text{ meV}$.^{83–85} The relatively strong signal in our TRMC data is consistent with ionization of the carriers in $(\text{CH}_3\text{NH}_3)_2\text{Pb}(\text{SCN})_2\text{I}_2$. We can consider a simple model that the rate of ionization of excitons will vary with the exciton binding energy (E_b) as $\sim \nu_0 \exp(-E_b/k_b T)$ where ν_0 is an attempt frequency. At room temperature with the reported E_b of $\sim 200 \text{ meV}$,⁵³ the rate is expected to be $\sim 10^8$ to 10^9 s^{-1} assuming typical pre-factors of 10^{12} to 10^{13} s^{-1} . This frequency is much larger than the observed recombination rate of the carriers suggesting that ionization can be relatively facile or that there are long lived excitations in this material (*vide infra*).⁵⁶ Overall, we expect the room-temperature value of ϕ in the lower-dimensional $(\text{CH}_3\text{NH}_3)_2\text{Pb}(\text{SCN})_2\text{I}_2$ to be lower than that in $\text{CH}_3\text{NH}_3\text{PbI}_3$,⁴⁴ which would only increase the observed sum of the carrier mobilities.

The peak values of $\phi \Sigma \mu$ decrease with increasing fluence, a phenomenon widely observed in TRMC experiments.^{12,62,64,86–92} At higher fluence, and hence high charge-carrier densities, higher order (*e.g.* bimolecular and Auger) recombination processes during the $\sim \text{ns}$ laser pulse also affect the peak value of $\phi \Sigma \mu$ ($\phi \Sigma \mu_{\text{max}}$).^{88,93,94} A consequence of this recombination is a reduction in the observed value of $\phi \Sigma \mu_{\text{max}}$ with increas-

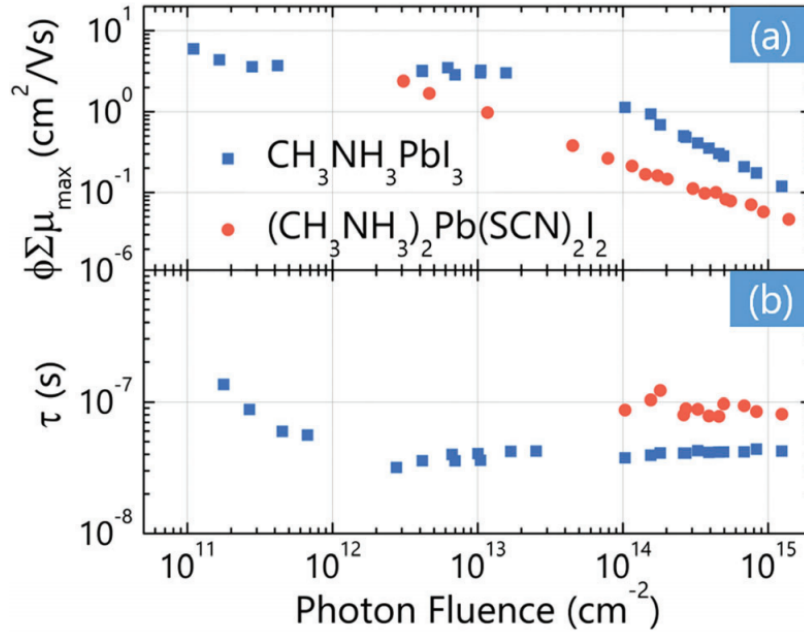


Figure 3.5: (a) Maximum value of $\phi \Sigma \mu_{\max}$ extracted from TRMC plots and (b) time constant obtained by taking a weighted average of two single exponential fits to two regions of the TRMC plots, as a function of fluence. The samples were illuminated with green light from a pulsed Nd:YAG laser with emission frequency of 532 nm and a full-width at half maximum of 5 ns. The films were measured in ambient air conditions at room temperature. The applied microwave power and frequency were 16 dBm and 8.35 GHz, respectively.

ing fluence.¹² Figure 3.5a shows $\phi \Sigma \mu_{\max}$ as a function of fluence for $\text{CH}_3\text{NH}_3\text{PbI}_3$ and $(\text{CH}_3\text{NH}_3)_2\text{Pb}(\text{SCN})_2\text{I}_2$, with values reaching $\sim 2 \text{ cm}^2 \text{ V}^{-1} \text{ s}^{-1}$ for the latter, at the lowest fluence examined. At low fluence (roughly $\leq 10^{13} \text{ cm}^{-2}$) higher order recombination processes (bimolecular and Auger) are no longer dominant, and a roughly fluence-independent $\phi \Sigma \mu_{\max}$ for $\text{CH}_3\text{NH}_3\text{PbI}_3$ is observed. It is anticipated that at a lower fluence (beyond that of our instrument resolution), $\phi \Sigma \mu_{\max}$ for $(\text{CH}_3\text{NH}_3)_2\text{Pb}(\text{SCN})_2\text{I}_2$ should also reach a maximum, fluence-independent, value. The difference in the incident fluence at which $\phi \Sigma \mu_{\max}$ makes the transition from being fluence-dependent to fluence-independent for $\text{CH}_3\text{NH}_3\text{PbI}_3$ and $(\text{CH}_3\text{NH}_3)_2\text{Pb}(\text{SCN})_2\text{I}_2$ is attributed to the differences in the bimolecular and Auger rate constants expected with dimensionality in hybrid halide compounds.⁴⁴

We observe that $\phi \Sigma \mu_{\max}$ for $(\text{CH}_3\text{NH}_3)_2\text{Pb}(\text{SCN})_2\text{I}_2$ is a factor of 2 to 4 lower than

that of a thin film of $\text{CH}_3\text{NH}_3\text{PbI}_3$ at fluences of $> 10^{13} \text{ cm}^{-2}$. We do not know the precise carrier density as a function of fluence because the carrier yield is likely lower in the layered compound,⁴⁴ precluding a direct comparison of the sum of the mobilities in the three-dimensional and layered compounds. Our values of $\phi \Sigma \mu_{\text{max}}$ as a function of fluence for $\text{CH}_3\text{NH}_3\text{PbI}_3$ agree relatively well with those reported in the literature for comparable grain size and incident fluence,^{12,71,95} and repeated measurements on separate films illustrate our techniques are consistent (see Section 3.5.5). The mobility in $\text{CH}_3\text{NH}_3\text{PbI}_3$ films has been shown to depend on the grain size and processing conditions,¹³ with a plateau in $\phi \Sigma \mu_{\text{max}}$ by TRMC, at large grain sizes and at low incident fluence.⁷⁰ The grain size between films formed of the two compounds here are significantly different (see Figure 3.1e and f). Our films of $(\text{CH}_3\text{NH}_3)_2\text{Pb}(\text{SCN})_2\text{I}_2$ have grain sizes comparable to those reported in the plateau region for the mobility of $\text{CH}_3\text{NH}_3\text{PbI}_3$, while our films of $\text{CH}_3\text{NH}_3\text{PbI}_3$ are lower than the reported plateau. For comparison, the reported value of $\phi \Sigma \mu$ for films of $\text{CH}_3\text{NH}_3\text{PbI}_3$ with micron scale grains is $\sim 25 \text{ cm}^2 \text{ V}^{-1} \text{ s}^{-1}$ at low fluence,⁷⁰ and ~ 11 to $25 \text{ cm}^2 \text{ V}^{-1} \text{ s}^{-1}$ from a different lab for 500 nm to micron scale grains at a fluence of $\sim 10^{12} \text{ cm}^{-2}$.⁹⁵ While our maximum value of $\phi \Sigma \mu$ for $(\text{CH}_3\text{NH}_3)_2\text{Pb}(\text{SCN})_2\text{I}_2$ is lower than this ($\sim 2 \text{ cm}^2 \text{ V}^{-1} \text{ s}^{-1}$), we have not completely eliminated the contribution of carrier recombination to the peak value. A comparable figure of merit ($\sim 1 \text{ cm}^2 \text{ V}^{-1} \text{ s}^{-1}$) was found for the fully halogenated layered compound, $(\text{C}_6\text{H}_5\text{C}_2\text{H}_4\text{NH}_3)_2\text{PbI}_4$ (phenethylammonium lead iodide) by THz spectroscopy.⁴⁴

We observe long-lived carriers in $(\text{CH}_3\text{NH}_3)_2\text{Pb}(\text{SCN})_2\text{I}_2$, similar to observations in $\text{CH}_3\text{NH}_3\text{PbI}_3$.¹² The lifetime τ , of carriers is determined by a number of processes (monomolecular, bimolecular, and Auger),⁸⁵ that have different relative contributions at different carrier concentrations. For this reason, unambiguously extracting a single decay parameter from TRMC transients is challenging.⁷¹ As described in the Section 3.5.4, we have here estimated the carrier lifetime by fitting single exponential functions to two re-

gions of the TRMC decay curves and taking a weighted average of the two, in an analogous approach to previous reports.⁷¹ Figure 3.5b shows the lifetime τ , of carriers in films of $\text{CH}_3\text{NH}_3\text{PbI}_3$ and $(\text{CH}_3\text{NH}_3)_2\text{Pb}(\text{SCN})_2\text{I}_2$. The value of τ is observed to be approximately constant with incident fluence at high values and increases at lower values for $\text{CH}_3\text{NH}_3\text{PbI}_3$ – indicative of the presence of higher-order processes at higher fluence. As is evident from Fig. 3.4c, there exists a very long-lifetime, signal in $(\text{CH}_3\text{NH}_3)_2\text{Pb}(\text{SCN})_2\text{I}_2$ that does not decay sufficiently on our experimentally accessible timescale to determine a decay constant. For this reason, and to avoid ambiguity in extracting parameters, we have only estimated τ for this compound at high fluence where bimolecular recombination is likely the dominant process, and the transient can be fit with confidence to an exponential decay. Our values are substantially longer than the monomolecular lifetime for $(\text{C}_6\text{H}_5\text{C}_2\text{H}_4\text{NH}_3)_2\text{PbI}_4$ found by THz spectroscopy of ~ 1 ns.⁴⁴ A key difference here, other than the change in coordination at the Pb atom, is the reduced layer spacing in $(\text{CH}_3\text{NH}_3)_2\text{Pb}(\text{SCN})_2\text{I}_2$. We attribute the existence of long-lived carriers to ionization of long-lived states, but whether the origin is the reduced layer spacing, which modifies the dielectric coupling between layers,⁹⁶ or the coordination of Pb is not clear at the present. There is evidence for long-lived states in $(\text{CH}_3\text{NH}_3)_2\text{Pb}(\text{SCN})_2\text{I}_2$ assigned to triplet states and we observed emission from our films in agreement with those observations (Figure 3.12).⁵⁶ A recent study has also suggested generation from edge states in fully halogenated layered materials.³⁸ In either case, the behavior here differs from that in previously examined two-dimensional layered organic metal halides.

3.4 Conclusion

In conclusion, we have studied the electronic properties of a two-dimensional layered hybrid-halide compound formed by halide substitution. We grew thin films of

the three-dimensional perovskite: methylammonium lead iodide ($\text{CH}_3\text{NH}_3\text{PbI}_3$) and the two-dimensional layered compound: methylammonium lead thiocyanate iodide ($(\text{CH}_3\text{NH}_3)_2\text{Pb}(\text{SCN})_2\text{I}_2$). Solution-deposited films of $(\text{CH}_3\text{NH}_3)_2\text{Pb}(\text{SCN})_2\text{I}_2$ were observed to form with layers highly-aligned parallel to the substrate. The yield-mobility product of charge-carriers moving in plane were observed to be comparable for $\text{CH}_3\text{NH}_3\text{PbI}_3$ and $(\text{CH}_3\text{NH}_3)_2\text{Pb}(\text{SCN})_2\text{I}_2$ and the carriers had relatively long lifetimes. This illustrates the potential promise of lower-dimensional hybrid-halide compounds. With respect to application in solar cells, the band gap (~ 2 eV) of $(\text{CH}_3\text{NH}_3)_2\text{Pb}(\text{SCN})_2\text{I}_2$ would likely limit its use to tandem or front cells. However, we anticipate $(\text{CH}_3\text{NH}_3)_2\text{Pb}(\text{SCN})_2\text{I}_2$ will be attractive for short-wavelength (blue/ultraviolet) lateral photodetector applications, and in thin-film transistors,^{79,97,98} where carriers largely travel parallel to the substrate. Thin-film transistors based on $\text{CH}_3\text{NH}_3\text{PbI}_3$ are known to be highly susceptible to ionic screening,⁹⁷ but the isolated layers in $(\text{CH}_3\text{NH}_3)_2\text{Pb}(\text{SCN})_2\text{I}_2$, could inhibit ionic screening mechanisms and potentially enable such devices to operate with high carrier mobilities at room temperature.^{99,100}

3.5 Appendix

3.5.1 Experimental Methods

Methylammonium iodide synthesis

Methylammonium iodide ($\text{CH}_3\text{NH}_3\text{I}$) was prepared following the common method¹⁰¹ by an acid-base reaction of HI with the amine CH_3NH_2 . For 2 g of product, HI (1.74 mL, 13.2 mmol, 1.05 eq., 57% in aqueous solution, 99.95%, Sigma-Aldrich) in anhydrous ethanol (2 mL, 99.5%, Sigma-Aldrich) was slowly dropped into a solution of CH_3NH_2 (1.57 mL, 12.6 mmol, 1.00 eq. 33% solution in absolute ethanol, 99%, Sigma-Aldrich) at 0 °C. After

stirring from 30 min at room temperature, the excess solvent was removed using a rotary evaporator. The remaining precipitation was recrystallized twice from a hot ethanol/water mixture and dried under vacuum at 60 °C for 1 hr to give white crystals. The phase purity was confirmed by powder X-ray diffraction (data not shown).

Lead thiocyanate synthesis

Lead thiocyanate was synthesized following reported procedure.¹⁰² Summarized, 500 mL of 1 M lead nitrate [Pb(NO₃)₂] (Sigma-Aldrich, 99.99%) was added in 50 mL aliquots with moderate stirring to 136 mL of 10 M ammonium thiocyanate (NH₄SCN) (Sigma-Aldrich, 99.99%). These reagent solutions were made at room temperature, filtered, then cooled in an ice bath prior to combining. This chilled combined solution was allowed to stir for 30 minutes. White precipitate settled out after mixing which was washed *via* decantation with ice cooled deionized (DI) water. The crude Pb(SCN)₂ was then dissolved in boiling DI water at a ratio of approximately 100 grams of lead thiocyanate to 3000 mL DI water, hot filtered, and then slowly cooled. White prismatic crystals were collected *via* vacuum filtration and then dried under vacuum overnight. This product was stored in a dry glovebox but can be kept in a desiccator with no issues.

Methylammonium lead iodide thin film preparation

Lead iodide (PbI₂) and CH₃NH₃I were mixed in a 1:1 molar ratio then dissolved in a mixture of dimethyl sulfoxide (DMSO) and γ -butyrolactone (GBL) (3:7 by volume). The solution was left stirring overnight at 60 °C before deposition. Films were spin-cast under atmospheric-pressure N₂ at 5000 rpm. In order to drive out solvent, chlorobenzene (CB) was applied to the sample a few seconds before the spin-casting procedure was complete, as reported elsewhere.^{74,75,97} The films were then annealed at 110 °C for 10 minutes under atmospheric-pressure N₂. CH₃NH₃I was synthesized as described above and PbI₂

was purchased from Sigma-Aldrich. All film preparation was conducted in an N₂-filled glovebox with sub-ppm oxygen and moisture levels.

Methylammonium lead thiocyanate iodide thin film preparation

A 2:1 molar ratio of methylammonium iodide (CH₃NH₃I) and lead thiocyanate (Pb(SCN)₂) were dissolved in *N,N*-dimethylformamide (DMF) at a concentration of 700 mg mL⁻¹. The resultant solution was left to stir at 60 °C for at least three hours prior to film deposition. Films were spin-cast at 2000 rpm with a subsequent drying spin of 5000 rpm. To ensure complete removal of DMF, diethyl ether (Et₂O) was applied to film at the conclusion of the final spin cycle, as reported earlier.⁵¹ Samples were annealed at room temperature for 30 minutes prior to any characterization measurements. Precursor materials (CH₃NH₃I and Pb(SCN)₂) were synthesized as described above; anhydrous DMF and Et₂O were purchased from Sigma-Aldrich. All film preparation was conducted in an N₂-filled glovebox with sub-ppm oxygen and moisture levels.

Film thickness measurements

The average thickness of spin-cast films of CH₃NH₃PbI₃ and (CH₃NH₃)₂Pb(SCN)₂I₂ were evaluated using a Bruker Dektak XT profilometer. Films were deposited as described above onto quartz substrates. Valleys were formed in the films by scratching with carbon-tipped tweezers. The film thickness was then measured in 20 different positions for each film. The average and standard deviations of each film were then evaluated to be: CH₃NH₃PbI₃: 120 ± 10 nm and (CH₃NH₃)₂Pb(SCN)₂I₂: 2.3 ± 1.9 μm.

Optical microscopy

Optical microscope images of films of CH₃NH₃PbI₃ and (CH₃NH₃)₂Pb(SCN)₂I₂ were taken using an Olympus BH2 optical microscope. Measurements were made in transmission

mode with various exposure times.

Scanning electron microscopy

Scanning electron microscope images were obtained using an FEI Nova NanoSEM 650, with a 10 keV beam and a spot size of 3.0. Films of $\text{CH}_3\text{NH}_3\text{PbI}_3$ and $(\text{CH}_3\text{NH}_3)_2\text{Pb}(\text{SCN})_2\text{I}_2$ were deposited onto polished, highly-doped (n^{++}) silicon.

X-ray diffraction

X-ray diffraction patterns were measured using a Panalytical Empyrean powder diffractometer with a copper $K\alpha$ source (films were of large enough thickness to measure adequate signal in Bragg–Brentano geometry). The rocking curve was measured on a Panalytical MRD PRO diffractometer ($\text{Cu-K}\alpha$) at the Bragg condition corresponding to the 200 peak of $(\text{CH}_3\text{NH}_3)_2\text{Pb}(\text{SCN})_2\text{I}_2$. Powder XRD patterns were simulated using the General Structure Analysis System (GSAS), with a calibration file specific to our instrument and structure factors taken from a solved single-crystal. Oriented diffraction patterns were simulated using March–Dollase preferred orientation correction factors of 0.5.¹⁰³

Ultraviolet-visible spectroscopy

Films of methylammonium lead iodide ($\text{CH}_3\text{NH}_3\text{PbI}_3$) and methylammonium lead thiocyanate iodide ($(\text{CH}_3\text{NH}_3)_2\text{Pb}(\text{SCN})_2\text{I}_2$) were grown as described above. Measurements were carried out using a Shimadzu UV-2600 ultraviolet-visible spectrophotometer.

Photoluminescence measurements

Films of methylammonium lead iodide ($\text{CH}_3\text{NH}_3\text{PbI}_3$) and methylammonium lead thiocyanate iodide ($(\text{CH}_3\text{NH}_3)_2\text{Pb}(\text{SCN})_2\text{I}_2$) were grown as described above. Photoluminescence measurements were carried out on a Horiba FluoroMax 4 spectrometer calibrated

using Milli-Q water. Films were loaded into a thin-film sample stage angled between the excitation and emission port.

Time-resolved microwave conductivity

A diagrammatic illustration of the time-resolved microwave conductivity (TRMC) system is shown in Figure 3.6. A microwave-frequency oscillatory electric signal is generated using a Sivers IMA VO4280X/00 voltage controlled oscillator (VCO). The signal has an approximate power of 16 dBm and a tunable frequency between 8 GHz and 15 GHz. The oscillatory signal is then directed through coaxial cables to port 1 of an electronic circulator (Fairview Microwave SFC0712). The circulator acts as uni-directional device in which signals entering from port 1 exit through port 2 and signals entering from port 2 exit through port 3. The signal exiting the circulator from port 2 is then fed into a SMA to X-band waveguide adapter (purchased on eBay but similar to Fairview Microwave part 90AC206). This antenna is coupled to X-band cavity (purchased on eBay) using a homebuilt coupling iris and tuning screw fabricated from a thin aluminum plate. The cavity is a TE_{103} mode formed by a short section of X-band waveguide and a homemade slotted copper plate (slots along the direction of current) that allows optical access to the sample. The antenna emits electromagnetic radiation (microwaves) which form a standing wave in the cavity. The tuning screw enabled over-, critical-, and undercoupling to the cavity and all experiments were performed in the under-coupled regime. The sample is mounted inside the cavity at a maximum of the electric-field component of the standing microwaves. Microwaves reflected from the cavity are then incident on port 2 of the circulator, exiting through port 3. Microwaves emitted from port 3 of the circulator – the power reflected from the cavity and sample – are then directed into a zero-bias Schottky diode detector (Fairview Microwave SMD0218 operating in the linear regime). The rectified signal is amplified by a homebuilt DC-coupled, wide-band amplifier built

around a Texas Instruments THS3091 operational amplifier (battery powered, three stages of amplification). We note that the microwave power is split at the source allowing a second detector and amplification stage to monitor/normalize the reflected power from the cavity. The amplified signal (and reference) is detected by a Textronix TDS 3032C digital oscilloscope. A Minilite Continuum pulsed Nd:YAG laser is used to illuminate the sample. The laser pulse has a wavelength of 532 nm, a full-width at half-maximum of approximately 5 nm and a maximum fluence of 10^{15} cm^{-2} . An external trigger link is employed to trigger the oscilloscope 50 ns before the laser fires. The area exposed to the incident optical pulse is approximately 10% of the cross-sectional area of the cavity. Changes in the detector voltage under illumination can then be used to extract the relevant TRMC parameters; $\phi\Sigma\mu$ and τ , as described in Section 3.5.2. The films were measured in ambient air conditions at room temperature, immediately after being removed from the glovebox. The total measurement time was ~ 2 hours for a fluence-dependent sweep. Carrying out the sweep from high to low fluence vs. low to high fluence, yielded no difference in behavior. This suggests that neither degradation in air over this period, nor damage due to the laser were significant in our study. TRMC measurements conducted on encapsulated films exhibited no significant difference from those carried out under ambient conditions.

3.5.2 Evaluation of time-resolved microwave conductivity figure of merit

A diagrammatic representation of the time-resolved microwave conductivity (TRMC) system employed in this study is shown in Figure 3.6 of the main text.

The microwave detectors employed in our system output a voltage that is linearly pro-

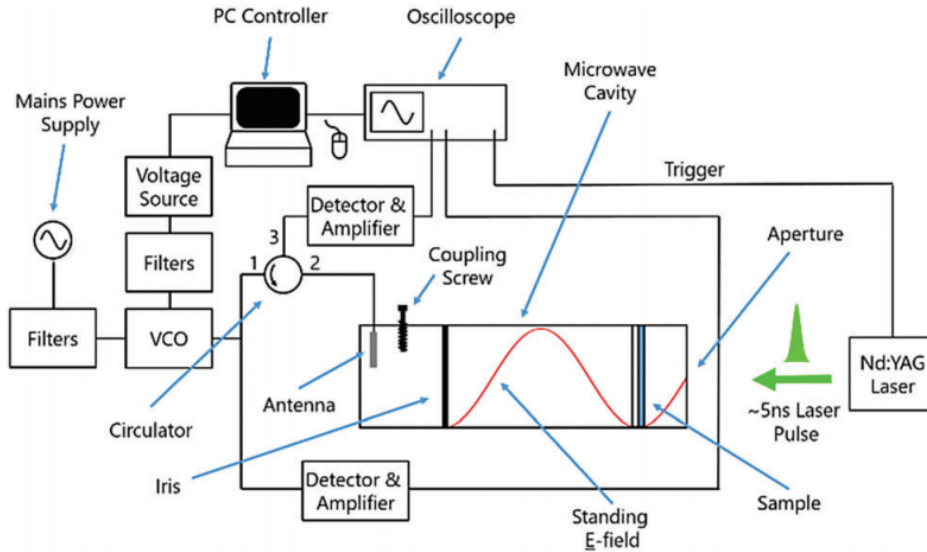


Figure 3.6: Schematic representation of time-resolved microwave conductivity (TRMC) system. A microwave-frequency ($\sim 8\text{--}9$ GHz) electrical signal is generated by voltage controlled oscillator (labeled VCO). The electrical signal is directed into port 1 of the circulator through coaxial cables. The incident signal exits the circulator via terminal 2 and enters the antenna in the microwave cavity. The oscillatory signal in antenna emits microwaves into the cavity which form a standing wave (electric field component only shown for clarity). A sample is placed into the cavity at one of the maxima of the standing electric field. Free carriers within the sample absorb microwaves, resulting in an attenuation in the reflected microwave signal. The reflected microwave-frequency electrical signal then exits the circulator from terminal 3, where it is directed into the detection circuit. Carriers are created in the sample using a pulsed Nd:YAG laser with emission frequency of 532 nm and full-width at half maximum of 5 ns.

portional to the incident microwave power P . The photoinduced change in the sample conductance ΔG , is related to the normalized change in microwave power ($\Delta P/P$) via Equation 3.1:^{12,60,64}

$$\Delta G(t) = -\frac{1}{K} \frac{\Delta P(t)}{P} \quad (3.1)$$

Since ΔG is dependent on the normalized change in microwave power $\Delta P/P$, it is not necessary to know the absolute values of microwave power, just the relative change under illumination. For this reason, with a knowledge of the detector voltage in the dark

V , and the change under illumination ΔV , it is possible to determine the photoinduced conductance from the signal voltage:

$$\Delta G(t) = -\frac{1}{K} \frac{\Delta V(t)}{V} \quad (3.2)$$

Here, K is the sensitivity factor of the cavity. Assuming the electric field in the cavity possesses an integer number of half-wavelengths (as is the case for TE/TEM modes) this parameter has been derived¹⁰⁴ for a cavity filled with a conducting medium to be:

$$K^{\text{full}} = -\frac{(1 + 1/\sqrt{R_0})Q}{\pi f_0 \epsilon_0 \epsilon_r L \beta} \quad (3.3)$$

The parameters in Equation 3.3 are as follows: R_0 is the reflectivity of the cavity to microwaves at the resonance frequency f_0 , ϵ_0 , and ϵ_r are the vacuum permittivity and the relative permittivity of the medium of the cavity, respectively. L is the length of the cavity. β is the ratio of the two remaining cavity dimensions, with the numerator/denominator depending on the polarization direction of the standing wave. In our case $\beta = 2.25$. Q is the cavity quality factor, expressed as the ratio of the resonance frequency f_0 , to the full-width at half-maximum ΔW :

$$Q = \frac{f_0}{\Delta W} \quad (3.4)$$

To account for the fact we are studying the change in conductance of a thin film of thickness d , rather than a homogeneous medium filling the length of the cavity L , we multiply K^{full} by a correction factor $g(L, d)$, to account for the difference in integrated electric field magnitude over the region of interest:

$$K = g(L, d)K^{\text{full}} \quad (3.5)$$

$$g(L, d) = \frac{\int_{z_0}^{z_0+d} \sin\left(\frac{\pi mz}{L}\right) dz}{\int_0^L \sin\left(\frac{\pi mz}{L}\right) dz} \quad (3.6)$$

Here z_0 is the position in the cavity where the sample is located and m is the integer number of half wavelengths of the electric field component in the cavity (which depends on the mode of the cavity). The sample position z_0 is chosen to be at a maxima of the magnitude of the electric field, hence: $z_0 = L(n + 1)/(2m)$ where $n \in \mathbb{Z}$. In the regime where $L \gg d$, as is the case in our experiment, the correction factor becomes the following for all $m \in \mathbb{Z}$, giving the following value for K :

$$g(L, d) = \frac{2d}{L} \quad (3.7)$$

$$K = -\frac{2Q(1 + 1/\sqrt{R_0})}{\pi f_0 \epsilon_0 \epsilon_r L \beta} \quad (3.8)$$

Since our measurements are carried out in air, and the sample thickness is typically $\sim 100 \text{ nm} - 1 \mu\text{m}$, we have here approximated $\epsilon_r = 1$. The relative permittivity of $\text{CH}_3\text{NH}_3\text{PbI}_3$ is known to be ~ 10 .⁹⁷ However, since the film is only $\sim 100 \text{ nm}$ to $\sim 1 \mu\text{m}$ thick and length of the cavity is $\sim 100 \text{ mm}$ (*i.e.* 10^5 to 10^6 times longer), the weighted average in the cavity can to a very good approximation be assumed to be unity. To determine R_0 , f_0 , and ΔW (and hence Q), the reflectivity of the cavity must be evaluated as a function of microwave frequency. To achieve this, we make use of the reference channel on our TRMC design (see Figure 3.6 main text). Microwaves directed through the reference channel do not enter the cavity and hence the ratio of the signal to the reference signals provides the reflectivity of the cavity. Figure 3.7 shows an example of the reflectivity of our loaded cavity as a function of microwave frequency, with approximate parameters extracted.

With the conductance ΔG determined, The TRMC figure of merit can then be evaluated

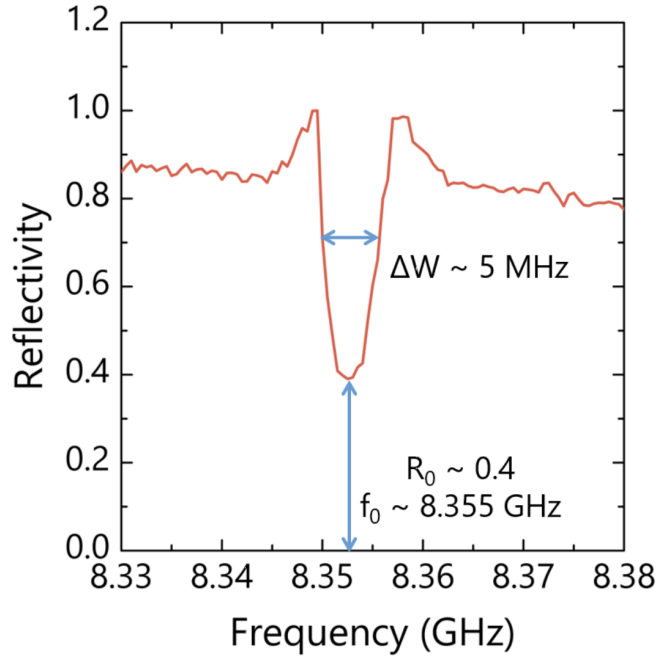


Figure 3.7: Frequency response of loaded microwave cavity, showing the detected reflectivity of the cavity as a function of incident frequency. The parameters f_0 , R_0 , and ΔW can all be extracted from this plot as shown.

using Equation 3.9:⁶⁴

$$\phi \Sigma \mu(t) = \frac{\Delta G(t)}{\beta e I_0 F_A M} \quad (3.9)$$

Here I_0 is the fluence of laser (photons/unit area/pulse), e is the magnitude of the fundamental unit of charge, and F_A ($\in [0, 1]$) is the fraction of photons absorbed in the sample at the excitation wavelength. The parameter F_A was extracted from the optical transmittance spectra from Figure 3.2 of the main text to be 0.41 for $\text{CH}_3\text{NH}_3\text{PbI}_3$ and 0.54 for $(\text{CH}_3\text{NH}_3)_2\text{Pb}(\text{SCN})_2\text{I}_2$. The parameter M ($\in [0, 1]$) is the fractional area of the sample in the cavity exposed to incident light; here evaluated *via* image analysis to be 0.101.

3.5.3 Purity of $(\text{CH}_3\text{NH}_3)_2\text{Pb}(\text{SCN})_2\text{I}_2$ films

Figure 3.8 shows the experimental XRD patterns of films of $(\text{CH}_3\text{NH}_3)_2\text{Pb}(\text{SCN})_2\text{I}_2$, with calculated powder patterns of isotropic $\text{CH}_3\text{NH}_3\text{PbI}_3$ and $[100]$ aligned $(\text{CH}_3\text{NH}_3)_2\text{Pb}(\text{SCN})_2\text{I}_2$. Comparison of calculated patterns with measured patterns indicates no peaks from $\text{CH}_3\text{NH}_3\text{PbI}_3$ in the thiocyanate-based film. Films of $\text{CH}_3\text{NH}_3\text{PbI}_3$ are typically textured with a preferential orientation of the $[110]$ direction; to account for the possibility of impurity domains in the thiocyanate film being randomly oriented with respect to the bulk, the isotropic powder pattern was used. The two peaks labeled with asterisks in the pattern of $(\text{CH}_3\text{NH}_3)_2\text{Pb}(\text{SCN})_2\text{I}_2$ represent peaks that are unaccounted for. The unaccounted peak at approximately 7° represents diffraction from a larger d -spacing than the $(\text{CH}_3\text{NH}_3)_2\text{Pb}(\text{SCN})_2\text{I}_2$ layer spacing. These peaks neither belong to $\text{CH}_3\text{NH}_3\text{PbI}_3$, nor PbI_2 . Because they appear at such a low concentration, we believe that this unknown low concentration impurity should not appreciably affect our TRMC measurements.

3.5.4 Analysis of TRMC decay constants

The lifetime τ , of carriers is determined by a number of processes (monomolecular, bimolecular, and Auger),⁸⁵ that have different relative contributions at different carrier concentrations. For this reason, unambiguously extracting a single decay parameter from TRMC transients is challenging.⁷¹ As illustrated by Figure 3.4c in the main text, the form of the decay is often complicated, and the time-dependence of the figure of merit cannot accurately be quantified by a small number of parameters. An approach previously taken to roughly quantify the decay is to fit a double exponential function and evaluate τ as a weighted average of these constants.⁷¹ To make comparison with the literature as simple as possible, we have here analyzed our data using a similar (but not identical) approach.

We have fitted the experimental data to a single exponential decay, in two separate

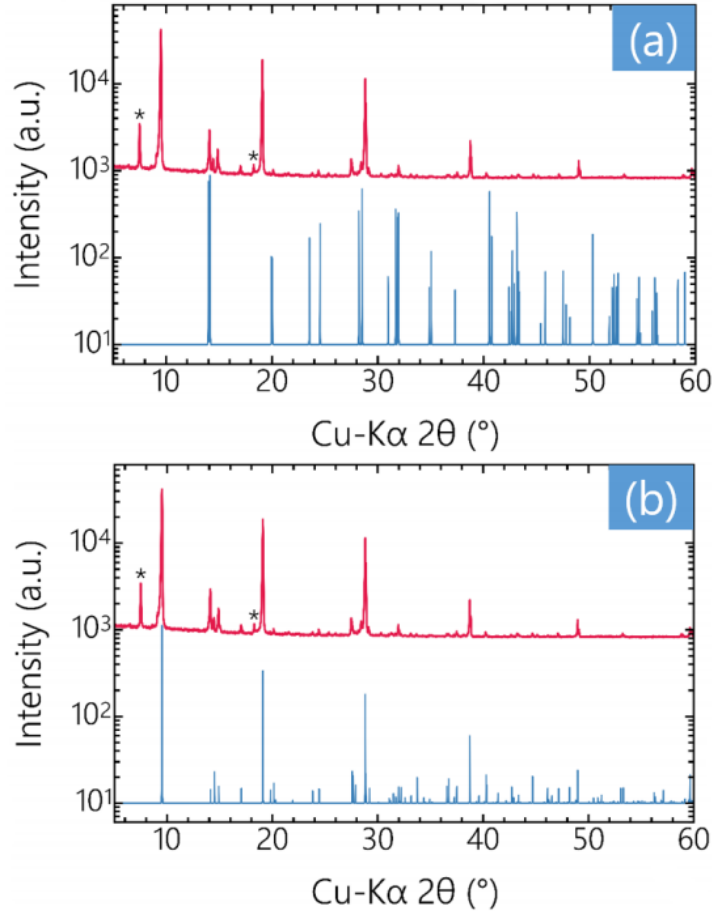


Figure 3.8: X-ray diffraction patterns of thin films of $(\text{CH}_3\text{NH}_3)_2\text{Pb}(\text{SCN})_2\text{I}_2$ (red) plotted against calculated patterns (blue) of (a) $\text{CH}_3\text{NH}_3\text{PbI}_3$ and (b) $[100]$ oriented $(\text{CH}_3\text{NH}_3)_2\text{Pb}(\text{SCN})_2\text{I}_2$ (planes parallel to the substrate), plotted on a logarithmic y-axis scale. Patterns were calculated as described in Section 3.5.1.

regions of each plot – roughly defined as the fast and slow regions. These decay rates are labeled here τ_1 and τ_2 , with y-axis intercepts of C_1 and C_2 respectively. The representative decay constant τ , is expressed as a weighted average of the two decays:

$$\tau = \frac{C_1\tau_1 + C_2\tau_2}{C_1 + C_2} \quad (3.10)$$

We have in this case not fitted directly to a double exponential function to avoid using 4 fitting parameters simultaneously per fit. Figure 3.9 shows example TRMC traces for

$\text{CH}_3\text{NH}_3\text{PbI}_3$ and $(\text{CH}_3\text{NH}_3)_2\text{Pb}(\text{SCN})_2\text{I}_2$ plotted with logarithmic y -axis scales, fitted to exponential functions in 2 regions of the plot. The values of τ plotted in Figure 3.5b of the main text are evaluated using the weighted average of the two from Equation 3.10. As shown in Figure 3.4c of the main text and in Figure 3.9, the $(\text{CH}_3\text{NH}_3)_2\text{Pb}(\text{SCN})_2\text{I}_2$ compound exhibits a very long-lived decay which cannot be accurately fitted using the techniques described here. For this reason, and to avoid ambiguity, values at lower fluence have not been included in the data in Figure 3.3e of the main text.

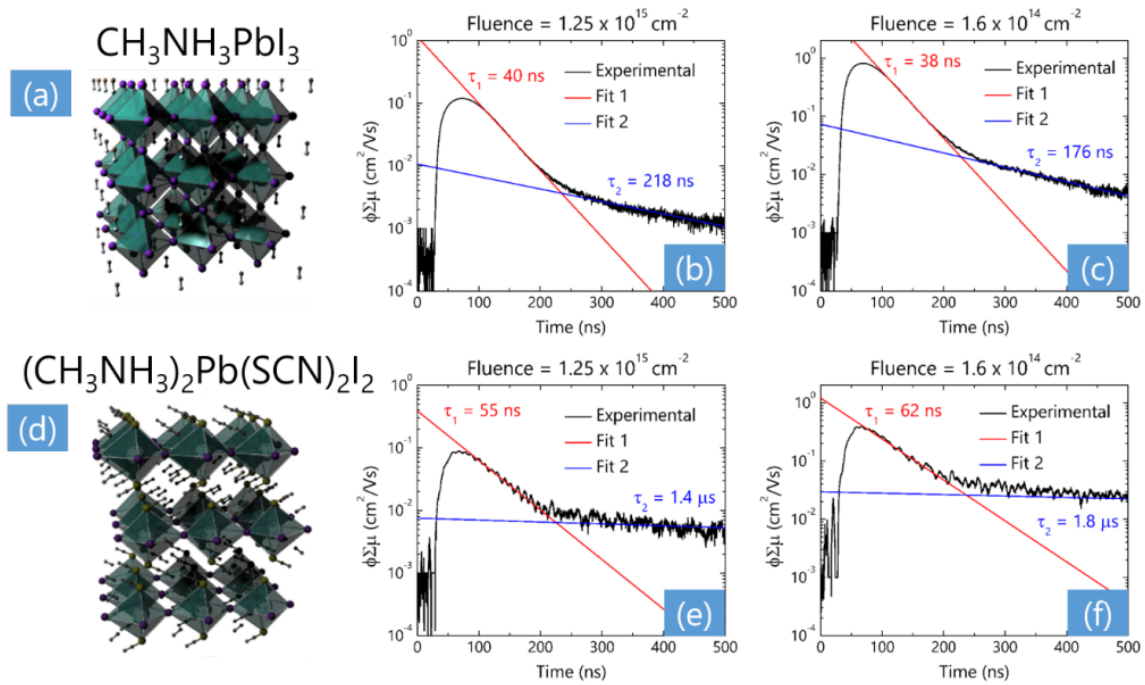


Figure 3.9: (a) Structure of methylammonium lead iodide ($\text{CH}_3\text{NH}_3\text{PbI}_3$). Time-resolved microwave conductivity data (TRMC) plot ($\phi \Sigma \mu$ as a function of time) of $\text{CH}_3\text{NH}_3\text{PbI}_3$ plotted on a logarithmic scale at a (b) high and (c) low fluence. (d) Structure of methylammonium lead thiocyanate iodide ($(\text{CH}_3\text{NH}_3)_2\text{Pb}(\text{SCN})_2\text{I}_2$). Time-resolved microwave conductivity data (TRMC) plot ($\phi \Sigma \mu$ as a function of time) of $(\text{CH}_3\text{NH}_3)_2\text{Pb}(\text{SCN})_2\text{I}_2$ plotted on a logarithmic scale at a (e) high and (f) low fluence.

3.5.5 Verification of TRMC figures of merit

We conducted a set of repeated measurements to ensure that our extracted figure of merit ($\phi\Sigma\mu$) is reliable and reproducible. Figure 3.10 shows the extracted maximum figure of merit ($\phi\Sigma\mu_{\max}$) for films of (a) $\text{CH}_3\text{NH}_3\text{PbI}_3$ and (b) $(\text{CH}_3\text{NH}_3)_2\text{Pb}(\text{SCN})_2\text{I}_2$ as a function of incident fluence from Figure 3.5a of the main text combined with a repeated set of measurements for a different film, prepared under identical conditions, on a different day. The data show broadly consistent values, indicative of a reliable and consistent measurement technique. The slight variations at low fluence are due to subjective ambiguity in extracting values of $\phi\Sigma\mu_{\max}$ from data with a low signal/noise ratio.

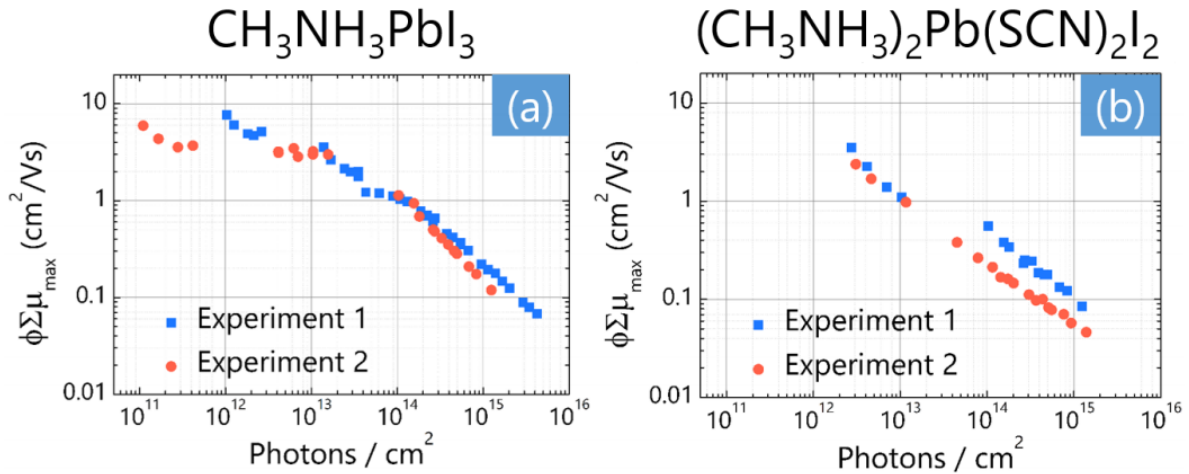


Figure 3.10: Extracted maximum time-resolved microwave conductivity (TRMC) figure of merit ($\phi\Sigma\mu$) as a function of incident optical fluence for two films of (a) $\text{CH}_3\text{NH}_3\text{PbI}_3$ and (b) $(\text{CH}_3\text{NH}_3)_2\text{Pb}(\text{SCN})_2\text{I}_2$, prepared and measured on different days.

To compare with previously measured values, Figure 3.11 shows the same data plotted with values extracted from a recent publication by Oga *et. al.*¹²

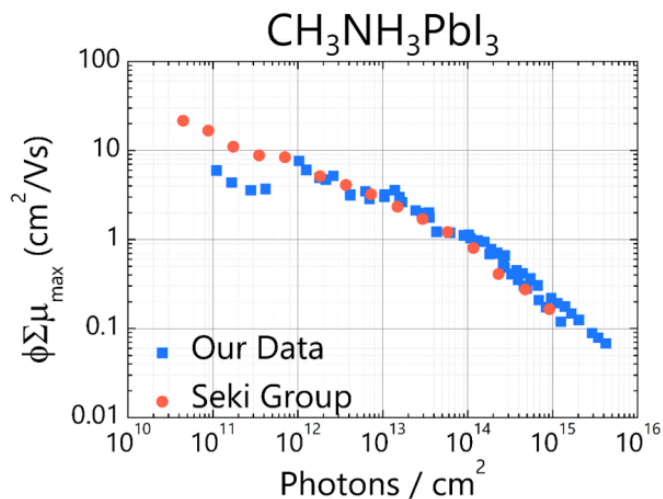


Figure 3.11: Extracted values of $\phi \Sigma \mu_{\max}$ as a function of incident optical fluence from both sets of data in Figure 3.10a plotted with previously reported values by the Seki group.¹²

3.5.6 Photoluminescence measurements

Photoluminescence measurements of $\text{CH}_3\text{NH}_3\text{PbI}_3$ and $(\text{CH}_3\text{NH}_3)_2\text{Pb}(\text{SCN})_2\text{I}_2$ were carried out as described in the main text. Absorbance and emission spectra as a function of wavelength and energy are shown for both compounds in Figure 3.12. In both cases, the excitation wavelength used was 450 nm. Both materials appear to emit at very similar energies, however the purity of the thiocyanate compound is confirmed by X-ray diffraction (Figure 3.8). The large energetic shift seen in the $(\text{CH}_3\text{NH}_3)_2\text{Pb}(\text{SCN})_2\text{I}_2$ optical data has recently been attributed to long-lived triplet states,⁵⁶ and may reconcile the long lifetimes seen in the TRMC data.

3.6 Acknowledgments

Defense Threat Reduction Agency (HDTRA1-15-1-0023) supported development of TRMC instrumentation and U.S. Department of Energy, Office of Science, Basic Energy

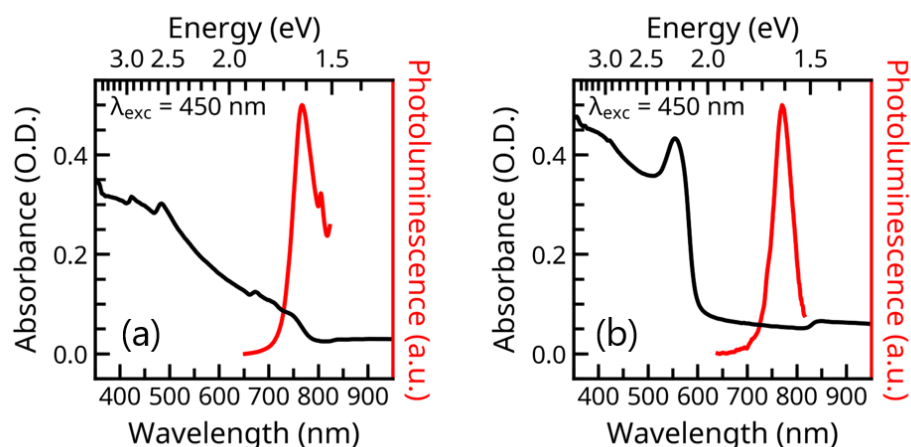


Figure 3.12: Absorbance and emission spectra of (a) $\text{CH}_3\text{NH}_3\text{PbI}_3$ and (b) $(\text{CH}_3\text{NH}_3)_2\text{Pb}(\text{SCN})_2\text{I}_2$ illustrating large energetic shift reported previously.

Sciences (DE-SC-0012541) supported materials synthesis. Use of the shared experimental facilities of the Materials Research Laboratory at UCSB was supported by the MRSEC Program of the National Science Foundation under Award No. DMR 1121053. J. G. L. gratefully acknowledges Virgil Elings and Betty Elings Wells for financial support through the Elings Fellowship Awards. We thank Dr. Garry Rumbles and Obadih Reid (NREL) for helpful discussions about the experimental details of TRMC.

3.7 Permissions and Attributions

The content of this chapter and appendix has been reprinted with permission from “Charge Transport in a Two-Dimensional Hybrid Metal Halide Thiocyanate Compound” by J. G. Labram *et al.*. Copyright © 2017 Royal Society of Chemistry.

3.8 References

1. Kojima, A., Teshima, K., Shirai, Y. & Miyasaka, T. Organometal Halide Perovskites as Visible-Light Sensitizers for Photovoltaic Cells. *Journal of the American Chemical Society* **131**, 6050–6051 (2009).
2. Lee, M. M., Teuscher, J., Miyasaka, T., Murakami, T. N. & Snaith, H. J. Efficient Hybrid Solar Cells Based on Meso-Superstructured Organometal Halide Perovskites. *Science* **338**, 643–647 (2012).
3. Snaith, H. J. Perovskites: The Emergence of a New Era for Low-Cost, High-Efficiency Solar Cells. *The Journal of Physical Chemistry Letters* **4**, 3623–3630 (2013).
4. Stoumpos, C. C., Malliakas, C. D. & Kanatzidis, M. G. Semiconducting Tin and Lead Iodide Perovskites with Organic Cations: Phase Transitions, High Mobilities, and Near-Infrared Photoluminescent Properties. *Inorganic Chemistry* **52**, 9019–9038 (2013).
5. Stranks, S. D., Eperon, G. E., Grancini, G., Menelaou, C., Alcocer, M. J. P., Leijtens, T., Herz, L. M., Petrozza, A. & Snaith, H. J. Electron-Hole Diffusion Lengths Exceeding 1 Micrometer in an Organometal Trihalide Perovskite Absorber. *Science* **342**, 341–344 (2013).
6. Xing, G., Mathews, N., Sun, S., Lim, S. S., Lam, Y. M., Grätzel, M., Mhaisalkar, S. & Sum, T. C. Long-Range Balanced Electron- and Hole-Transport Lengths in Organic-Inorganic $\text{CH}_3\text{NH}_3\text{PbI}_3$. *Science* **342**, 344–347 (2013).
7. De Wolf, S., Holovsky, J., Moon, S.-J., Löper, P., Niesen, B., Ledinsky, M., Haug, F.-J., Yum, J.-H. & Ballif, C. Organometallic Halide Perovskites: Sharp Optical Absorption Edge and Its Relation to Photovoltaic Performance. *The Journal of Physical Chemistry Letters* **5**, 1035–1039 (2014).
8. Frost, J. M., Butler, K. T., Brivio, F., Hendon, C. H., van Schilfgaarde, M. & Walsh, A. Atomistic Origins of High-Performance in Hybrid Halide Perovskite Solar Cells. *Nano Letters* **14**, 2584–2590 (2014).
9. Grätzel, M. The Light and Shade of Perovskite Solar Cells. *Nature Materials* **13**, 838–842 (2014).
10. Green, M. A., Ho-Baillie, A. & Snaith, H. J. The Emergence of Perovskite Solar Cells. *Nature Photonics* **8**, 506–514 (2014).
11. Kazim, S., Nazeeruddin, M. K., Grätzel, M. & Ahmad, S. Perovskite as Light Harvester: A Game Changer in Photovoltaics. *Angewandte Chemie International Edition* **53**, 2812–2824 (2014).
12. Oga, H., Saeki, A., Ogomi, Y., Hayase, S. & Seki, S. Improved Understanding of the Electronic and Energetic Landscapes of Perovskite Solar Cells: High Local Charge Carrier Mobility, Reduced Recombination, and Extremely Shallow Traps. *Journal of the American Chemical Society* **136**, 13818–13825 (2014).

13. de Quilettes, D. W., Vorpahl, S. M., Stranks, S. D., Nagaoka, H., Eperon, G. E., Ziffer, M. E., Snaith, H. J. & Ginger, D. S. Impact of Microstructure on Local Carrier Lifetime in Perovskite Solar Cells. *Science* **348**, 683–686 (2015).
14. Dong, Q., Fang, Y., Shao, Y., Mulligan, P., Qiu, J., Cao, L. & Huang, J. Electron-Hole Diffusion Lengths > 175 Mm in Solution-Grown CH₃NH₃PbI₃ Single Crystals. *Science* **347**, 967–970 (2015).
15. Pazos-Outón, L. M., Szumilo, M., Lamboll, R., Richter, J. M., Crespo-Quesada, M., Abdi-Jalebi, M., Beeson, H. J., Vručinić, M., Alsari, M. & Snaith, H. J. Photon Recycling in Lead Iodide Perovskite Solar Cells. *Science* **351**, 1430–1433 (2016).
16. Brenner, T. M., Egger, D. A., Kronik, L., Hodes, G. & Cahen, D. Hybrid Organic—Inorganic Perovskites: Low-Cost Semiconductors with Intriguing Charge-Transport Properties. *Nature Reviews Materials* **1**, 1–16 (2016).
17. Quarti, C., Mosconi, E., Ball, J. M., D’Innocenzo, V., Tao, C., Pathak, S., Snaith, H. J., Petrozza, A. & Angelis, F. D. Structural and Optical Properties of Methylammonium Lead Iodide across the Tetragonal to Cubic Phase Transition: Implications for Perovskite Solar Cells. *Energy & Environmental Science* **9**, 155–163 (2016).
18. Wehrenfennig, C., Eperon, G. E., Johnston, M. B., Snaith, H. J. & Herz, L. M. High Charge Carrier Mobilities and Lifetimes in Organolead Trihalide Perovskites. *Advanced Materials* **26**, 1584–1589 (2014).
19. Endres, J., Egger, D. A., Kulbak, M., Kerner, R. A., Zhao, L., Silver, S. H., Hodes, G., Rand, B. P., Cahen, D., Kronik, L. & Kahn, A. Valence and Conduction Band Densities of States of Metal Halide Perovskites: A Combined Experimental–Theoretical Study. *The Journal of Physical Chemistry Letters* **7**, 2722–2729 (2016).
20. Green, M. A., Emery, K., Hishikawa, Y., Warta, W., Dunlop, E. D., Levi, D. H. & Ho-Baillie, A. W. Y. Solar Cell Efficiency Tables (Version 49). *Progress in Photovoltaics: Research and Applications* **25**, 3–13 (2017).
21. Blakers, A., Zin, N., McIntosh, K. R. & Fong, K. High Efficiency Silicon Solar Cells. *Energy Procedia. PV Asia Pacific Conference 2012* **33**, 1–10 (2013).
22. Battaglia, C., Cuevas, A. & Wolf, S. D. High-Efficiency Crystalline Silicon Solar Cells: Status and Perspectives. *Energy & Environmental Science* **9**, 1552–1576 (2016).
23. Wu, X. High-Efficiency Polycrystalline CdTe Thin-Film Solar Cells. *Solar Energy. Thin Film PV* **77**, 803–814 (2004).
24. Fabini, D. Quantifying the Potential for Lead Pollution from Halide Perovskite Photovoltaics. *The Journal of Physical Chemistry Letters* **6**, 3546–3548 (2015).
25. Snaith, H. J., Abate, A., Ball, J. M., Eperon, G. E., Leijtens, T., Noel, N. K., Stranks, S. D., Wang, J. T.-W., Wojciechowski, K. & Zhang, W. Anomalous Hysteresis in Perovskite Solar Cells. *The Journal of Physical Chemistry Letters* **5**, 1511–1515 (2014).

26. Unger, E. L., Hoke, E. T., Bailie, C. D., Nguyen, W. H., Bowring, A. R., Heumüller, T., Christoforo, M. G. & McGehee, M. D. Hysteresis and Transient Behavior in Current–Voltage Measurements of Hybrid-Perovskite Absorber Solar Cells. *Energy & Environmental Science* **7**, 3690–3698 (2014).
27. Frost, J. M. & Walsh, A. What Is Moving in Hybrid Halide Perovskite Solar Cells? *Accounts of Chemical Research* **49**, 528–535 (2016).
28. Stoumpos, C. C. & Kanatzidis, M. G. Halide Perovskites: Poor Man’s High-Performance Semiconductors. *Advanced Materials* **28**, 5778–5793 (2016).
29. Eperon, G. E., Stranks, S. D., Menelaou, C., Johnston, M. B., Herz, L. M. & Snaith, H. J. Formamidinium Lead Trihalide: A Broadly Tunable Perovskite for Efficient Planar Heterojunction Solar Cells. *Energy & Environmental Science* **7**, 982–988 (2014).
30. Hao, F., Stoumpos, C. C., Cao, D. H., Chang, R. P. H. & Kanatzidis, M. G. Lead-Free Solid-State Organic–Inorganic Halide Perovskite Solar Cells. *Nature Photonics* **8**, 489–494 (2014).
31. Kumawat, N. K., Dey, A., Kumar, A., Gopinathan, S. P., Narasimhan, K. L. & Kabra, D. Band Gap Tuning of $\text{CH}_3\text{NH}_3\text{Pb}(\text{Br}_{1-x}\text{Cl}_x)_3$ Hybrid Perovskite for Blue Electroluminescence. *ACS Applied Materials & Interfaces* **7**, 13119–13124 (2015).
32. Protesescu, L., Yakunin, S., Bodnarchuk, M. I., Krieg, F., Caputo, R., Hendon, C. H., Yang, R. X., Walsh, A. & Kovalenko, M. V. Nanocrystals of Cesium Lead Halide Perovskites (CsPbX_3 , X= Cl, Br, and I): Novel Optoelectronic Materials Showing Bright Emission with Wide Color Gamut. *Nano Letters* **15**, 3692–3696 (2015).
33. Lee, B., Stoumpos, C. C., Zhou, N., Hao, F., Malliakas, C., Yeh, C.-Y., Marks, T. J., Kanatzidis, M. G. & Chang, R. P. H. Air-Stable Molecular Semiconducting Iodosalts for Solar Cell Applications: Cs_2SnI_6 as a Hole Conductor. *Journal of the American Chemical Society* **136**, 15379–15385 (2014).
34. Smith, I. C., Hoke, E. T., Solis-Ibarra, D., McGehee, M. D. & Karunadasa, H. I. A Layered Hybrid Perovskite Solar-Cell Absorber with Enhanced Moisture Stability. *Angewandte Chemie International Edition* **126**, 11414–11417 (2014).
35. Cao, D. H., Stoumpos, C. C., Farha, O. K., Hupp, J. T. & Kanatzidis, M. G. 2D Homologous Perovskites as Light-Absorbing Materials for Solar Cell Applications. *Journal of the American Chemical Society* **137**, 7843–7850 (2015).
36. Lehner, A. J., Wang, H., Fabini, D. H., Liman, C. D., Hébert, C.-A., Perry, E. E., Wang, M., Bazan, G. C., Chabynyc, M. L. & Seshadri, R. Electronic Structure and Photovoltaic Application of BiI_3 . *Applied Physics Letters* **107**, 131109 (2015).
37. Saparov, B., Hong, F., Sun, J.-P., Duan, H.-S., Meng, W., Cameron, S., Hill, I. G., Yan, Y. & Mitzi, D. B. Thin-Film Preparation and Characterization of $\text{Cs}_3\text{Sb}_2\text{I}_9$: A Lead-Free Layered Perovskite Semiconductor. *Chemistry of Materials* **27**, 5622–5632 (2015).

38. Tsai, H., Nie, W., Blancon, J.-C., Stoumpos, C. C., Asadpour, R., Harutyunyan, B., Neukirch, A. J., Verduzco, R., Crochet, J. J., Tretiak, S., Pedesseau, L., Even, J., Alam, M. A., Gupta, G., Lou, J., Ajayan, P. M., Bedzyk, M. J., Kanatzidis, M. G. & Mohite, A. D. High-Efficiency Two-Dimensional Ruddlesden-Popper Perovskite Solar Cells. *Nature* **536**, 312–316 (2016).
39. Slavney, A. H., Hu, T., Lindenberg, A. M. & Karunadasa, H. I. A Bismuth-Halide Double Perovskite with Long Carrier Recombination Lifetime for Photovoltaic Applications. *Journal of the American Chemical Society* **138**, 2138–2141 (2016).
40. McClure, E. T., Ball, M. R., Windl, W. & Woodward, P. M. Cs₂AgBiX₆ (X = Br, Cl): New Visible Light Absorbing, Lead-Free Halide Perovskite Semiconductors. *Chemistry of Materials* **28**, 1348–1354 (2016).
41. Evans, H. A., Lehner, A. J., Labram, J. G., Fabini, D. H., Barreda, O., Smock, S. R., Wu, G., Chabinye, M. L., Seshadri, R. & Wudl, F. (TTF)Pb₂I₅: A Radical Cation-Stabilized Hybrid Lead Iodide with Synergistic Optoelectronic Signatures. *Chemistry of Materials* **28**, 3607–3611 (2016).
42. Mitzi, D. B. Templating and Structural Engineering in Organic–Inorganic Perovskites. *Journal of the Chemical Society, Dalton Transactions*, 1–12 (2001).
43. Mitzi, D. B., Feild, C. A., Harrison, W. T. A. & Guloy, A. M. Conducting Tin Halides with a Layered Organic-Based Perovskite Structure. *Nature* **369**, 467–469 (1994).
44. Milot, R. L., Sutton, R. J., Eperon, G. E., Haghighirad, A. A., Martinez Hardigree, J., Miranda, L., Snaith, H. J., Johnston, M. B. & Herz, L. M. Charge-Carrier Dynamics in 2D Hybrid Metal-Halide Perovskites. *Nano Letters* **16**, 7001–7007 (2016).
45. Mitzi, D. B., Wang, S., Feild, C. A., Chess, C. A. & Guloy, A. M. Conducting Layered Organic-Inorganic Halides Containing <110>-Oriented Perovskite Sheets. *Science* **267**, 1473–1476 (1995).
46. Chen, Y., Li, B., Huang, W., Gao, D. & Liang, Z. Efficient and Reproducible CH₃NH₃PbI_{3-x}(SCN)_x Perovskite Based Planar Solar Cells. *Chemical Communications* **51**, 11997–11999 (2015).
47. Daub, M. & Hillebrecht, H. Synthesis, Single-Crystal Structure and Characterization of (CH₃NH₃)₂Pb(SCN)₂I₂. *Angewandte Chemie International Edition* **54**, 11016–11017 (2015).
48. Jiang, Q., Rebollar, D., Gong, J., Piacentino, E. L., Zheng, C. & Xu, T. Pseudohalide-Induced Moisture Tolerance in Perovskite CH₃NH₃Pb(SCN)₂I Thin Films. *Angewandte Chemie International Edition* **54**, 7617–7620 (2015).
49. Halder, A., Chulliyil, R., Subbiah, A. S., Khan, T., Chatteraj, S., Chowdhury, A. & Sarkar, S. K. Pseudohalide (SCN⁻)-Doped MAPbI₃ Perovskites: A Few Surprises. *The Journal of Physical Chemistry Letters* **6**, 3483–3489 (2015).

50. Ganose, A. M., Savory, C. N. & Scanlon, D. O. $(\text{CH}_3\text{NH}_3)_2\text{Pb}(\text{SCN})_2\text{I}_2$: A More Stable Structural Motif for Hybrid Halide Photovoltaics? *The Journal of Physical Chemistry Letters* **6**, 4594–4598 (2015).
51. Xiao, Z., Meng, W., Saparov, B., Duan, H.-S., Wang, C., Feng, C., Liao, W., Ke, W., Zhao, D., Wang, J., Mitzi, D. B. & Yan, Y. Photovoltaic Properties of Two-Dimensional $(\text{CH}_3\text{NH}_3)_2\text{Pb}(\text{SCN})_2\text{I}_2$ Perovskite: A Combined Experimental and Density Functional Theory Study. *The Journal of Physical Chemistry Letters* **7**, 1213–1218 (2016).
52. Tai, Q., You, P., Sang, H., Liu, Z., Hu, C., Chan, H. L. W. & Yan, F. Efficient and Stable Perovskite Solar Cells Prepared in Ambient Air Irrespective of the Humidity. *Nature Communications* **7**, 1–8 (2016).
53. Umeyama, D., Lin, Y. & Karunadasa, H. I. Red-to-Black Piezochromism in a Compressible Pb–I–SCN Layered Perovskite. *Chemistry of Materials* **28**, 3241–3244 (2016).
54. Yang, S., Liu, W., Zuo, L., Zhang, X., Ye, T., Chen, J., Li, C.-Z., Wu, G. & Chen, H. Thiocyanate Assisted Performance Enhancement of Formamidinium Based Planar Perovskite Solar Cells through a Single One-Step Solution Process. *Journal of Materials Chemistry A* **4**, 9430–9436 (2016).
55. Liu, J., Shi, J., Li, D., Zhang, F., Li, X., Xiao, Y. & Wang, S. Molecular Design and Photovoltaic Performance of a Novel Thiocyanate-Based Layered Organometal Perovskite Material. *Synthetic Metals* **215**, 56–63 (2016).
56. Younts, R., Duan, H.-S., Gautam, B., Saparov, B., Liu, J., Mongin, C., Castellano, F. N., Mitzi, D. B. & Gundogdu, K. Efficient Generation of Long-Lived Triplet Excitons in 2D Hybrid Perovskite. *Advanced Materials* **29**, 1604278 (2017).
57. Kamminga, M. E., Fang, H.-H., Filip, M. R., Giustino, F., Baas, J., Blake, G. R., Loi, M. A. & Palstra, T. T. M. Confinement Effects in Low-Dimensional Lead Iodide Perovskite Hybrids. *Chemistry of Materials* **28**, 4554–4562 (2016).
58. De Haas, M. P. & Warman, J. M. Photon-Induced Molecular Charge Separation Studied by Nanosecond Time-Resolved Microwave Conductivity. *Chemical Physics* **73**, 35–53 (1982).
59. Kunst, M. & Werner, A. Comparative Study of Time-Resolved Conductivity Measurements in Hydrogenated Amorphous Silicon. *Journal of Applied Physics* **58**, 2236–2241 (1985).
60. Kroeze, J. E., Savenije, T. J., Vermeulen, M. J. W. & Warman, J. M. Contactless Determination of the Photoconductivity Action Spectrum, Exciton Diffusion Length, and Charge Separation Efficiency in Polythiophene-Sensitized TiO_2 Bilayers. *The Journal of Physical Chemistry B* **107**, 7696–7705 (2003).
61. Schindler, K. M. & Kunst, M. Charge-Carrier Dynamics in Titania Powders. *The Journal of Physical Chemistry* **94**, 8222–8226 (1990).

62. Dayal, S., Reese, M. O., Ferguson, A. J., Ginley, D. S., Rumbles, G. & Kopidakis, N. The Effect of Nanoparticle Shape on the Photocarrier Dynamics and Photovoltaic Device Performance of Poly(3-Hexylthiophene):CdSe Nanoparticle Bulk Heterojunction Solar Cells. *Advanced Functional Materials* **20**, 2629–2635 (2010).
63. Saeki, A., Koizumi, Y., Aida, T. & Seki, S. Comprehensive Approach to Intrinsic Charge Carrier Mobility in Conjugated Organic Molecules, Macromolecules, and Supramolecular Architectures. *Accounts of Chemical Research* **45**, 1193–1202 (2012).
64. Savenije, T. J., Ferguson, A. J., Kopidakis, N. & Rumbles, G. Revealing the Dynamics of Charge Carriers in Polymer:Fullerene Blends Using Photoinduced Time-Resolved Microwave Conductivity. *The Journal of Physical Chemistry C* **117**, 24085–24103 (2013).
65. Tsutsui, Y., Schweicher, G., Chattopadhyay, B., Sakurai, T., Arlin, J.-B., Ruzié, C., Aliev, A., Ciesielski, A., Colella, S., Kennedy, A. R., Lemaur, V., Olivier, Y., Hadji, R., Sanguinet, L., Castet, F., Osella, S., Dudenko, D., Beljonne, D., Cornil, J., Samorì, P., Seki, S. & Geerts, Y. H. Unraveling Unprecedented Charge Carrier Mobility through Structure Property Relationship of Four Isomers of Didodecyl[1]Benzothieno[3,2-b][1]Benzothiophene. *Advanced Materials* **28**, 7106–7114 (2016).
66. Savenije, T. J., Nanu, M., Schoonman, J. & Goossens, A. A Time-Resolved Microwave Conductivity Study of the Optoelectronic Processes in $\text{TiO}_2|\text{In}_2\text{S}_3|\text{CuInS}_2$ Heterojunctions. *Journal of Applied Physics* **101**, 113718 (2007).
67. Friedrich, D. & Kunst, M. Analysis of Charge Carrier Kinetics in Nanoporous Systems by Time Resolved Photoconductance Measurements. *The Journal of Physical Chemistry C* **115**, 16657–16663 (2011).
68. Gélvez-Rueda, M. C., Cao, D. H., Patwardhan, S., Renaud, N., Stoumpos, C. C., Schatz, G. C., Hupp, J. T., Farha, O. K., Savenije, T. J., Kanatzidis, M. G. & Grozema, F. C. Effect of Cation Rotation on Charge Dynamics in Hybrid Lead Halide Perovskites. *The Journal of Physical Chemistry C* **120**, 16577–16585 (2016).
69. Oosterhout, S. D., Ferguson, A. J., Larson, B. W., Olson, D. C. & Kopidakis, N. Modeling the Free Carrier Recombination Kinetics in PTB7:PCBM Organic Photovoltaics. *The Journal of Physical Chemistry C* **120**, 24597–24604 (2016).
70. Reid, O. G., Yang, M., Kopidakis, N., Zhu, K. & Rumbles, G. Grain-Size-Limited Mobility in Methylammonium Lead Iodide Perovskite Thin Films. *ACS Energy Letters* **1**, 561–565 (2016).
71. Pascoe, A. R., Yang, M., Kopidakis, N., Zhu, K., Reese, M. O., Rumbles, G., Fekete, M., Duffy, N. W. & Cheng, Y.-B. Planar versus Mesoscopic Perovskite Microstructures: The Influence of $\text{CH}_3\text{NH}_3\text{PbI}_3$ Morphology on Charge Transport and Recombination Dynamics. *Nano Energy* **22**, 439–452 (2016).

72. Hutter, E. M., Gélvez-Rueda, M. C., Oshero, A., Bulović, V., Grozema, F. C., Stranks, S. D. & Savenije, T. J. Direct-Indirect Character of the Bandgap in Methylammonium Lead Iodide Perovskite. *Nature Materials* **16**, 115–120 (2017).
73. Foster, S., Deledalle, F., Mitani, A., Kimura, T., Kim, K.-B., Okachi, T., Kirchartz, T., Oguma, J., Miyake, K., Durrant, J. R., Doi, S. & Nelson, J. Electron Collection as a Limit to Polymer:PCBM Solar Cell Efficiency: Effect of Blend Microstructure on Carrier Mobility and Device Performance in PTB7:PCBM. *Advanced Energy Materials* **4**, 1400311 (2014).
74. Jung, J. W., Williams, S. T. & Jen, A. K.-Y. Low-Temperature Processed High-Performance Flexible Perovskite Solar Cells via Rationally Optimized Solvent Washing Treatments. *RSC Advances* **4**, 62971–62977 (2014).
75. Jeon, N. J., Noh, J. H., Kim, Y. C., Yang, W. S., Ryu, S. & Seok, S. I. Solvent Engineering for High-Performance Inorganic–Organic Hybrid Perovskite Solar Cells. *Nature Materials* **13**, 897–903 (2014).
76. Im, J.-H., Jang, I.-H., Pellet, N., Grätzel, M. & Park, N.-G. Growth of $\text{CH}_3\text{NH}_3\text{PbI}_3$ Cuboids with Controlled Size for High-Efficiency Perovskite Solar Cells. *Nature Nanotechnology* **9**, 927–932 (2014).
77. Umebayashi, T., Asai, K., Kondo, T. & Nakao, A. Electronic Structures of Lead Iodide Based Low-Dimensional Crystals. *Physical Review B* **67**, 155405 (2003).
78. Dingle, R., Wiegmann, W. & Henry, C. H. Quantum States of Confined Carriers in Very Thin $\text{Al}_x\text{Ga}_{1-x}\text{As}$ - GaAs - $\text{Al}_x\text{Ga}_{1-x}\text{As}$ Heterostructures. *Physical Review Letters* **33**, 827–830 (1974).
79. Chin, X. Y., Cortecchia, D., Yin, J., Bruno, A. & Soci, C. Lead Iodide Perovskite Light-Emitting Field-Effect Transistor. *Nature Communications* **6**, 8383 (2015).
80. Zhu, H., Miyata, K., Fu, Y., Wang, J., Joshi, P. P., Niesner, D., Williams, K. W., Jin, S. & Zhu, X.-Y. Screening in Crystalline Liquids Protects Energetic Carriers in Hybrid Perovskites. *Science* **353**, 1409–1413 (2016).
81. Jailaubekov, A. E., Willard, A. P., Tritsch, J. R., Chan, W.-L., Sai, N., Gearba, R., Kaake, L. G., Williams, K. J., Leung, K., Rossky, P. J. & Zhu, X.-Y. Hot Charge-Transfer Excitons Set the Time Limit for Charge Separation at Donor/Acceptor Interfaces in Organic Photovoltaics. *Nature Materials* **12**, 66–73 (2013).
82. Grancini, G., Maiuri, M., Fazzi, D., Petrozza, A., Egelhaaf, H.-J., Brida, D., Cerullo, G. & Lanzani, G. Hot Exciton Dissociation in Polymer Solar Cells. *Nature Materials* **12**, 29–33 (2013).
83. Miyata, A., Mitoglu, A., Plochocka, P., Portugall, O., Wang, J. T.-W., Stranks, S. D., Snaith, H. J. & Nicholas, R. J. Direct Measurement of the Exciton Binding Energy and Effective Masses for Charge Carriers in Organic-Inorganic Tri-Halide Perovskites. *Nature Physics* **11**, 582–587 (2015).

84. Galkowski, K., Mitioglu, A., Miyata, A., Plochocka, P., Portugall, O., E. Eperon, G., Tse-Wei Wang, J., Stergiopoulos, T., D. Stranks, S., J. Snaith, H. & J. Nicholas, R. Determination of the Exciton Binding Energy and Effective Masses for Methylammonium and Formamidinium Lead Tri-Halide Perovskite Semiconductors. *Energy & Environmental Science* **9**, 962–970 (2016).
85. Herz, L. M. Charge-Carrier Dynamics in Organic-Inorganic Metal Halide Perovskites. *Annual Review of Physical Chemistry* **67**, 65–89 (2016).
86. Wojciechowski, K., Stranks, S. D., Abate, A., Sadoughi, G., Sadhanala, A., Kopidakis, N., Rumbles, G., Li, C.-Z., Friend, R. H., Jen, A. K.-Y. & Snaith, H. J. Heterojunction Modification for Highly Efficient Organic–Inorganic Perovskite Solar Cells. *ACS Nano* **8**, 12701–12709 (2014).
87. Hutter, E. M., Eperon, G. E., Stranks, S. D. & Savenije, T. J. Charge Carriers in Planar and Meso-Structured Organic–Inorganic Perovskites: Mobilities, Lifetimes, and Concentrations of Trap States. *The Journal of Physical Chemistry Letters* **6**, 3082–3090 (2015).
88. Savenije, T. J., Kroeze, J. E., Wienk, M. M., Kroon, J. M. & Warman, J. M. Mobility and Decay Kinetics of Charge Carriers in Photoexcited PCBM/PPV Blends. *Physical Review B* **69**, 155205 (2004).
89. Piris, J., Kopidakis, N., Olson, D. C., Shaheen, S. E., Ginley, D. S. & Rumbles, G. The Locus of Free Charge-Carrier Generation in Solution-Cast $\text{Zn}_{1-x}\text{Mg}_x\text{O}$ /Poly(3-Hexylthiophene) Bilayers for Photovoltaic Applications. *Advanced Functional Materials* **17**, 3849–3857 (2007).
90. Reid, O. G., Malik, J. A. N., Latini, G., Dayal, S., Kopidakis, N., Silva, C., Stingelin, N. & Rumbles, G. The Influence of Solid-State Microstructure on the Origin and Yield of Long-Lived Photogenerated Charge in Neat Semiconducting Polymers. *Journal of Polymer Science Part B: Polymer Physics* **50**, 27–37 (2012).
91. Savenije, T. J., Kroeze, J. E., Yang, X. & Loos, J. The Formation of Crystalline P3HT Fibrils upon Annealing of a PCBM:P3HT Bulk Heterojunction. *Thin Solid Films. EMSR 2005 - Proceedings of Symposium F on Thin Film and Nanostructured Materials for Photovoltaics* **511**, 2–6 (2006).
92. Saeki, A., Tsuji, M. & Seki, S. Direct Evaluation of Intrinsic Optoelectronic Performance of Organic Photovoltaic Cells with Minimizing Impurity and Degradation Effects. *Advanced Energy Materials* **1**, 661–669 (2011).
93. Nelson, J. *The Physics of Solar Cells* (Imperial College Press, 2003).
94. Johnston, M. B. & Herz, L. M. Hybrid Perovskites for Photovoltaics: Charge-Carrier Recombination, Diffusion, and Radiative Efficiencies. *Accounts of Chemical Research* **49**, 146–154 (2016).

95. Guse, J. A., Soufiani, A. M., Jiang, L., Kim, J., Cheng, Y.-B., Schmidt, T. W., Ho-Baillie, A. & McCamey, D. R. Spectral Dependence of Direct and Trap-Mediated Recombination Processes in Lead Halide Perovskites Using Time Resolved Microwave Conductivity. *Physical Chemistry Chemical Physics* **18**, 12043–12049 (2016).
96. Muljarov, E. A., Tikhodeev, S. G., Gippius, N. A. & Ishihara, T. Excitons in Self-Organized Semiconductor/Insulator Superlattices: PbI-Based Perovskite Compounds. *Physical Review B* **51**, 14370–14378 (1995).
97. Labram, J. G., Fabini, D. H., Perry, E. E., Lehner, A. J., Wang, H., Glaudell, A. M., Wu, G., Evans, H., Buck, D., Cotta, R., Echegoyen, L., Wudl, F., Seshadri, R. & Chabiniy, M. L. Temperature-Dependent Polarization in Field-Effect Transport and Photovoltaic Measurements of Methylammonium Lead Iodide. *The Journal of Physical Chemistry Letters* **6**, 3565–3571 (2015).
98. Senanayak, S. P., Yang, B., Thomas, T. H., Giesbrecht, N., Huang, W., Gann, E., Nair, B., Goedel, K., Guha, S., Moya, X., McNeill, C. R., Docampo, P., Sadhanala, A., Friend, R. H. & Sringhaus, H. Understanding Charge Transport in Lead Iodide Perovskite Thin-Film Field-Effect Transistors. *Science Advances* **3**, e1601935 (2017).
99. Kagan, C. R., Mitzi, D. B. & Dimitrakopoulos, C. D. Organic-Inorganic Hybrid Materials as Semiconducting Channels in Thin-Film Field-Effect Transistors. *Science* **286**, 945–947 (1999).
100. Matsushima, T., Hwang, S., Sandanayaka, A. S. D., Qin, C., Terakawa, S., Fujihara, T., Yahiro, M. & Adachi, C. Solution-Processed Organic-Inorganic Perovskite Field-Effect Transistors with High Hole Mobilities. *Advanced Materials* **28**, 10275–10281 (2016).
101. Qiu, J., Qiu, Y., Yan, K., Zhong, M., Mu, C., Yan, H. & Yang, S. All-Solid-State Hybrid Solar Cells Based on a New Organometal Halide Perovskite Sensitizer and One-Dimensional TiO₂ Nanowire Arrays. *Nanoscale* **5**, 3245–3248 (2013).
102. Lambou, M. G. & Dollear, F. G. A Preparation of Lead Thiocyanate. *Oil & Soap* **23**, 97–101 (1946).
103. Dollase, W. A. Correction of Intensities for Preferred Orientation in Powder Diffraction: Application of the March Model. *Journal of Applied Crystallography* **19**, 267–272 (1986).
104. Infelta, P. P., de Haas, M. P. & Warman, J. M. The Study of the Transient Conductivity of Pulse Irradiated Dielectric Liquids on a Nanosecond Timescale Using Microwaves. *Radiation Physics and Chemistry* **10**, 353–365 (1977).

Chapter 4

Charge-Carrier Dynamics and Crystalline Texture of Layered Ruddlesden–Popper Hybrid Lead Iodide Perovskite Thin Films

4.1 Abstract

Solution-processable organic metal halide Ruddlesden–Popper phases have shown promise in optoelectronics because of their efficiencies in solar cells along with increased material stability relative to their three-dimensional counterparts ($\text{CH}_3\text{NH}_3\text{PbI}_3$). Here, we study the layered material butylammonium methylammonium lead iodide $(\text{C}_4\text{H}_9\text{NH}_3)_2(\text{CH}_3\text{NH}_3)_{n-1}\text{Pb}_n\text{I}_{3n+1}$ for values of n ranging from 1 to 4. Thin films cast from solution show a gradual change in the crystalline texture of the two-dimensional lead iodide layers from being parallel to the substrate to perpendicular with increasing n . Contactless time-resolved microwave conductivity measurements show that the average recombina-

tion rate order increases with n and that the yield-mobility products and carrier lifetimes of these thin films are much lower than that of $\text{CH}_3\text{NH}_3\text{PbI}_3$, along with increased higher-order recombination rate constants.

4.2 Introduction

Hybrid organic-inorganic perovskite (HOIP) materials are solution-processable semiconductors composed of inexpensive, earth abundant materials.¹⁻⁷ When used as the active material in photovoltaic cells, HOIPs based on methylammonium lead iodide ($\text{CH}_3\text{NH}_3\text{PbI}_3$) and formamidinium lead iodide ($\text{HC}(\text{NH}_2)_2\text{PbI}_3$) have shown a drastic increase in their power conversion efficiencies (PCE), from an initial value of 3.8%⁸ to 22.1%⁹, in less than a decade, making them competitive with thin film solar cell technologies such as CIGS, CdTe, and amorphous silicon.¹⁰ Despite this high performance in lab-based solar cells, HOIP photovoltaics are susceptible to degradation by heat and moisture, potentially limiting their long-term use.¹¹⁻¹³

Thin films of layered perovskites of the form $\text{A}'_2\text{A}_{n-1}\text{B}_n\text{X}_{3n+1}$, known as Ruddlesden-Popper phases,^{14,15} have been shown to produce efficient solar cells with increased stability.¹⁶⁻²¹ The introduction of large, hydrophobic cations in the A' site appears to improve their tolerance to moisture in comparison to films of $\text{CH}_3\text{NH}_3\text{PbI}_3$.²² These spacer ions, however, break the lead iodide octahedra into two-dimensional layers, making transport highly anisotropic because of weak electronic coupling between layers.^{23,24}

In this study, we report a quantitative optical, structural, and electronic characterization of thin films of butylammonium methylammonium lead iodide, $(\text{C}_4\text{H}_9\text{NH}_3)_2(\text{CH}_3\text{NH}_3)_{n-1}\text{Pb}_n\text{I}_{3n+1}$. Photovoltaic devices based on $(\text{C}_4\text{H}_9\text{NH}_3)_2(\text{CH}_3\text{NH}_3)_{n-1}\text{Pb}_n\text{I}_{3n+1}$ have previously exhibited PCE values of 12.5%,¹⁸ but their charge transport and structure are still not well-understood. Structural changes

are here quantified using a combination of X-ray diffraction and atomic force microscopy. By using contactless time-resolved microwave conductivity (TRMC) measurements, we can specifically probe in-plane mobility and relate film texturing to anisotropic charge transport.

4.3 Results and Discussion

Thin films of $(\text{C}_4\text{H}_9\text{NH}_3)_2(\text{CH}_3\text{NH}_3)_{n-1}\text{Pb}_n\text{I}_{3n+1}$ were synthesized for $n = 1$ to $n = 4$ from solutions in *N,N*-dimethylformamide (DMF) by spin-coating onto z-cut quartz substrates. For brevity, butylammonium is termed BA and methylammonium MA. Crystal structures at room temperature from the literature,²⁴ visualized along the $[10\bar{1}]$ crystallographic direction using VESTA,²⁵ are shown in Figure 4.1. In all cases, the structure is assigned such that the *b*-axis (along the $[010]$ direction) corresponds to the direction normal to the lead iodide layers, or the stacking direction.

The optical properties of thin films of $(\text{BA})_2(\text{MA})_{n-1}\text{Pb}_n\text{I}_{3n+1}$ match those reported in the literature and show differences from the optical spectra reported for bulk samples.^{18,21,24,26} Optical absorbance and photoluminescence data show distinct absorption and emission edges for each of the different phases, consistent with the different colors of the films (photographs shown as insets in Figure 4.1). Additionally, the single- ($n = 1$) and double-layer ($n = 2$) films exhibit strong excitonic behavior due to confinement effects, with features attributed to excitons at 2.43 and 2.20 eV, respectively. Previous studies have shown exciton binding energies ranging from 200 to 400 meV for single-layer lead iodide compounds with varying spacer lengths,^{27–29} while three-dimensional MAPbI_3 has a much lower value, in the range of 5–50 meV at room temperature.^{30–32} The lack of a sharp exciton feature in the absorbance spectra of the $n = 3$ and 4 phases suggests that there is a near convergence to bulk ($n = \infty$) optical properties, illustrated in Figure 4.7, where the photoluminescence

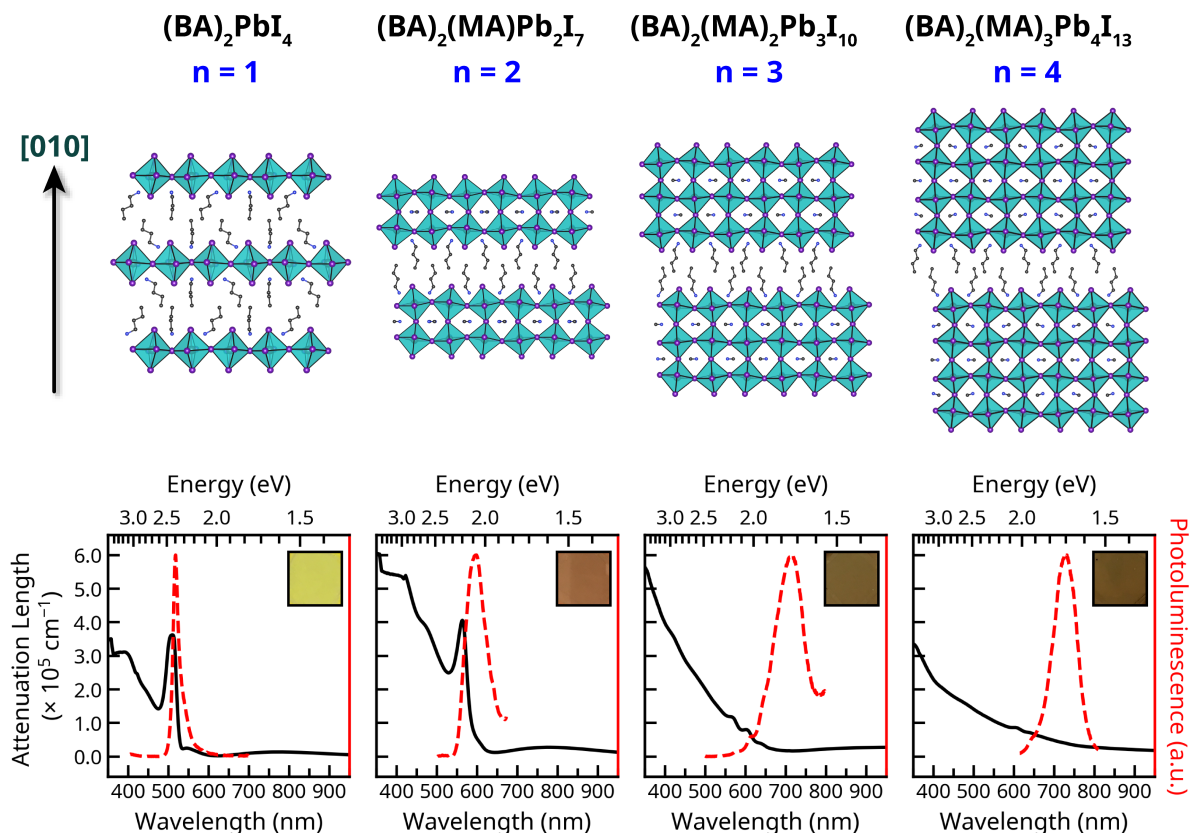


Figure 4.1: Crystal structures, viewed along the $[10\bar{1}]$ crystallographic direction, along with optical attenuation lengths and photoluminescence emission for the first four Ruddlesden-Popper phases. Insets in optical data show photographs of thin films on a white background to illustrate color. Crystal structures were taken from the literature, and attenuation lengths were calculated using film thicknesses extracted from X-ray reflectivity measurements.

peaks are plotted as a function of n . However, previous measurements of absorption and emission on exfoliated single crystals of these compounds have shown clear excitonic behavior in the $n = 3$ and $n = 4$ phases with blue-shifted optical edges compared to films. Therefore, this rapid convergence to apparent bulk properties appears to be specific to the thin films, and its origin is still to be fully determined, with one study attributing it to edge-state defects.²⁶

Because of the question of the origin of the change in optical properties, we examined the structure of the thin films in detail using X-ray scattering and found a gradual change in

texture of the crystallites as the lead iodide layer thickness (n) increases, as shown in Figure 4.2a. Diffraction data is presented in the form of the out-of-plane scattering vector, q_z , because the symmetric $\theta/2\theta$ scan results in scattering from lattice planes oriented parallel to the substrate surface. The assignment of the scattering peaks based on single-crystal structures reveals alignment of the lead iodide layers parallel to the substrate in the $n = 1$ compound, with an increasing population of perpendicularly aligned lead iodide sheets as the layer thickness increases (schematic in Figure 4.2b), as seen by the relative peak heights of the [010] and [101] textured domains. The proportion of parallel to perpendicular domains can be quantified because the integrated peak intensities are linearly proportional to the weight fraction of a phase.³³ As optical measurements suggest no obvious presence of MAPbI₃ inclusions, weight fractions represent the proportion of each textured population of the respective Ruddlesden–Popper phase. The fraction of domains textured along $[h'k'l']$ with respect to $[hkl]$ is given by Equation 4.1 (derivation in the Appendix section 4.5.6), where P_{hkl} is the peak height, θ_{hkl} the Bragg diffraction angle, and $|F_{hkl}|$ the structure factor for the (hkl) lattice plane (calculated from crystal structures). The main assumption of Equation 4.1 is the presence of only two distinct textures; this is valid as every peak in the diffraction patterns of the four phases can be indexed to texturing along [010] or [101], shown in Figure 4.8.

$$f_{(h'k'l')} = \left(\frac{P_{h'k'l'}}{P_{h'k'l'} + P_{hkl}} \right) \cdot \left(\frac{LP(\theta_{hkl})}{LP(\theta_{h'k'l'})} \right) \cdot \left(\frac{|F_{hkl}|}{|F_{h'k'l'}|} \right)^2 \quad (4.1)$$

Quantitative texture analysis shows that the single-layer ($n = 1$) phase is mainly textured along [010], with an increasing percentage of domains along [101] of 25%, 76%, and 94% for $n = 2, 3$, and 4, respectively. This gradual texture change with increasing n is shown in Figure 4.2c. Notably, MAPbI₃ thin films are also oriented along the same direction as $n = 4$ with respect to the unit cell (Figure 4.10). These diffraction data show that

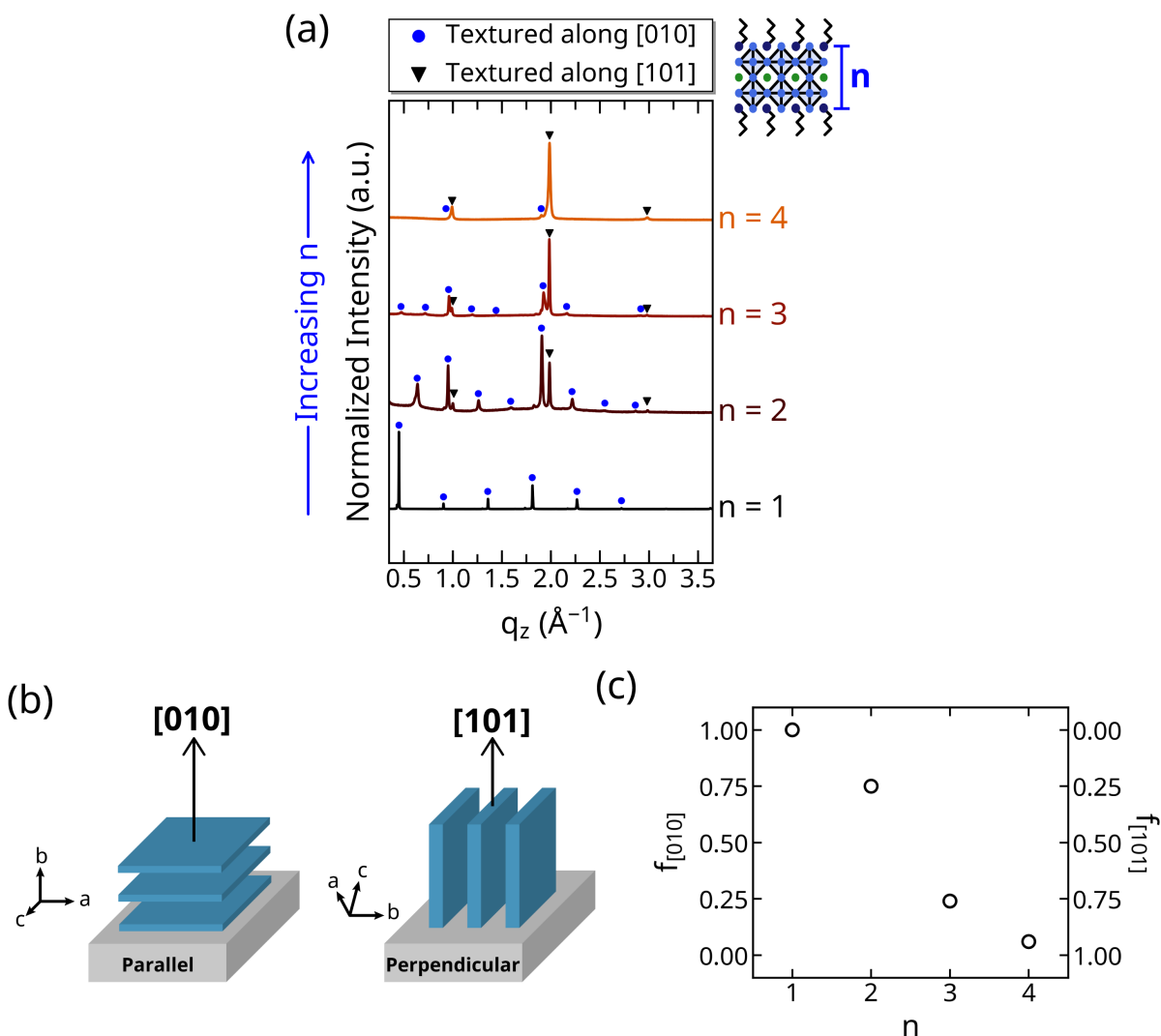


Figure 4.2: (a) Specular X-ray diffraction patterns of $(\text{BA})_2(\text{MA})_{n-1}\text{Pb}_n\text{I}_{3n+1}$ for $n = 1$ to 4, illustrating an increase in the fraction of crystals textured along $[101]$ with increasing n . (b) Schematic of parallel and perpendicular texturing of lead iodide sheets (blue layers) along with their respective crystallographic axes and (c) fraction of $[010]$ and $[101]$ textured domains for each of the four phases, calculated using Equation 4.1 and peak heights shown in Figure 4.9.

the orientation of crystallites in Ruddlesden–Popper thin films converge to the preferred orientation of the bulk, three-dimensional material.

To corroborate structural changes from X-ray diffraction, atomic force microscopy (AFM) micrographs were collected for each compound, showing marked differences in sur-

face film morphologies. In the single-layer ($n = 1$) compound, which was shown by XRD to texture entirely along [010], the surface appears to be smooth with grains on the order of 1 μm , but with regions of deep pinholes. The $n = 2$ phase, despite being dominantly textured along [010], appears rougher, with smaller domains on the order of 100 nm, likely because of the presence of [010] textured crystals that disturb growth of parallel lead iodide and limit domain size. The $n = 3$ and $n = 4$ films, which both contain a majority of [101] textured domains, have similar morphologies, where the small crystallites are representative of the perpendicular lead iodide domains, with smooth, slender grains attributed to the minority fraction of [010] textured crystals. The morphologies from AFM are therefore in agreement with the texture fractions calculated from XRD. Scanning electron microscopy (SEM) micrographs of each compound (see Figure 4.11) are also consistent with measurements from AFM.

The charge transport properties of these compounds were measured using time-resolved microwave conductivity, a method that has been previously used to measure carrier dynamics in hybrid perovskites.^{34–37} The sample is photoexcited with a laser pulse, creating free carriers and/or excitons; only the free carriers then interact with an applied, rapidly changing electric field of microwave frequency (8–9 GHz) in a cavity. Absorption of energy due to carrier drift results in an attenuation of the applied microwave signal, which can be used to calculate the transient photoconductance of the sample. This change in conductance provides the yield–mobility product, $\phi \Sigma \mu$, which is the product of the charge carrier yield (free carriers per incident photon) ϕ , and the sum of electron and hole mobilities, $\Sigma \mu = \mu_h + \mu_e$. Additionally, carrier motion is probed only in the direction of the electric field, which is perpendicular to the direction of wave propagation and therefore parallel to the substrate surface. Because TRMC is a local probe of carrier motion, despite both the deep-lying pinholes and small domain sizes (for larger n) seen from microscopy (Figures 4.3 and 4.11), measurements are possible without stringent process optimization (*i.e.*,

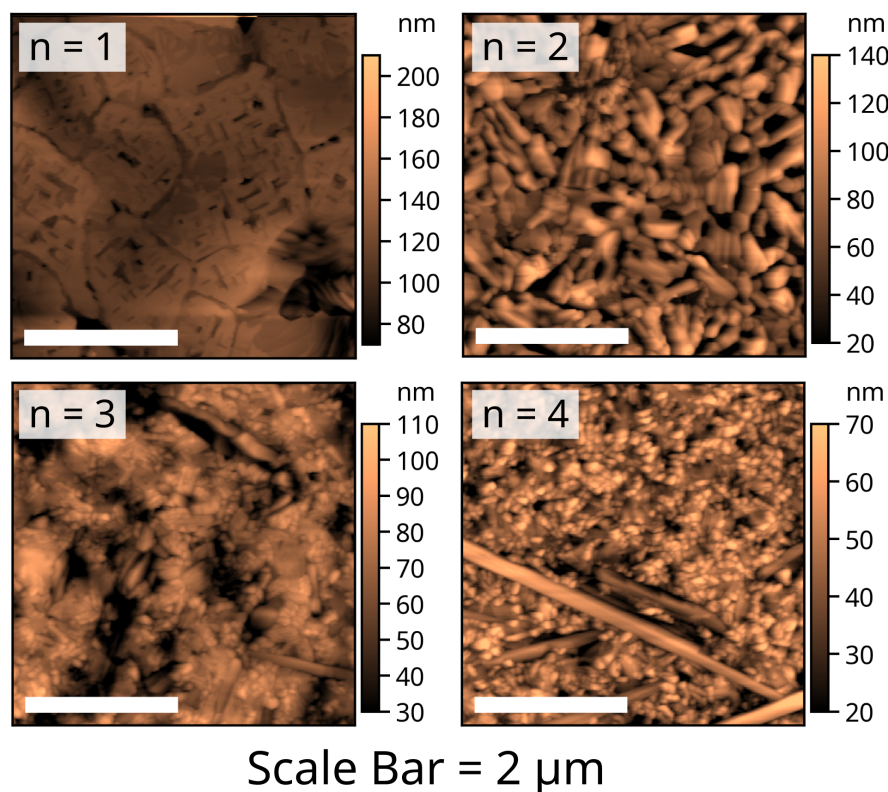


Figure 4.3: Topographical height retrace maps of $(\text{BA})_2(\text{MA})_{n-1}\text{Pb}_n\text{I}_{3n+1}$ measured using atomic force microscopy, illustrating different surface film morphologies in layered perovskite thin films. Microstructure is consistent with conclusions from X-ray diffraction regarding proportions of textured domains. All scale bars are 2 μm .

continuous films and large grains). A schematic of the TRMC setup, along with expected carrier motion based on lead iodide layer alignment, is shown in Figure 4.4. The lowest measurable laser fluence for each of the compounds was limited by the signal-to-noise of the instrument.

The structural analysis of the texture of the crystallites can be used to understand the resulting microwave conductivity of the films. The maximum values of $\phi\Sigma\mu$ with varying incident laser fluence are presented in Figure 4.5, showing similar values for all four compounds at low power, with increasingly stronger dependence on incident optical power as n goes from 1 to 4. All plots have negative slopes as extracted $\phi\Sigma\mu$ values from TRMC commonly exhibit a strong dependence on fluence.^{34,38-42} We expect that a larger fraction

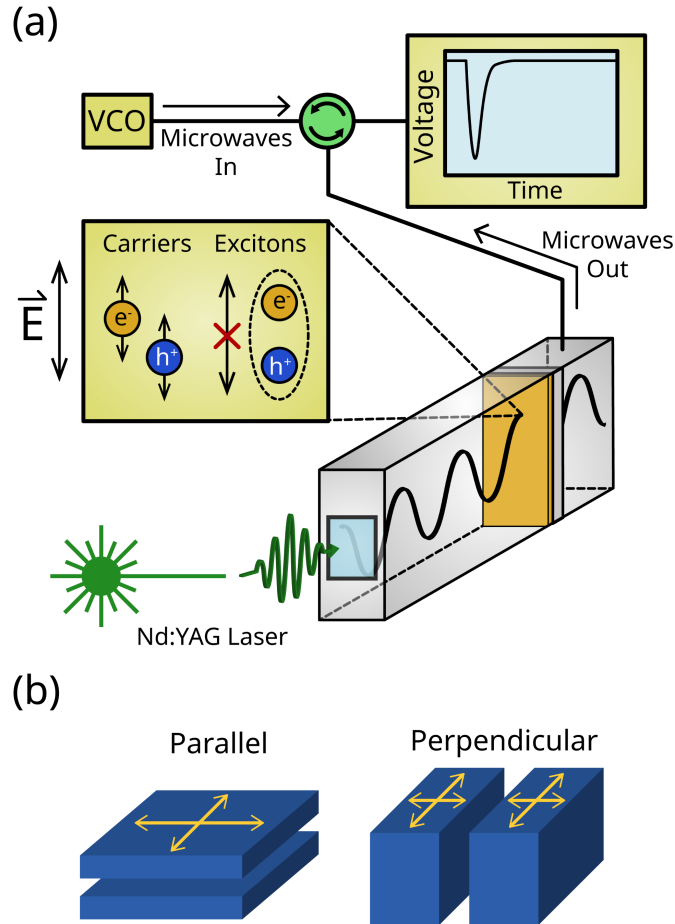


Figure 4.4: (a) Schematic of time-resolved microwave conductivity setup, with a detailed description of the experimental setup presented in Appendix section 4.5.1. (b) Parallel and perpendicular lead iodide layers (layer thickness representative of the value of n) within crystalline regions, respectively, showing expected carrier motion along the in-plane electric field from the microwave source. Parallel domains have unrestricted motion in-plane, while perpendicular domains have restricted motion in the layer-stacking direction because of confinement by the butylammonium spacers.

of perpendicularly oriented lead iodide sheets would decrease the measured value of $\phi \Sigma \mu$. The decrease is expected because the signal contains contributions from carrier motion along the confined, layer-stacking direction, in which previous electronic structure calculations have shown no dispersion.^{18,24} Although transport along this direction is not bandlike, charge hopping between lead iodide sheets is still possible, and we expect that there could be an increasing contribution within the sheets as their thickness increases. By $n = 4$,

the lead iodide layers are approximately 2.5 nm thick; therefore, motion of the confined carrier may be measurable by TRMC. Because of fiber-texturing of the small (~ 100 nm) crystallites in the films from spin-coating, these perpendicular lead iodide sheets are randomly oriented in-plane. In all of the films examined, the yield-mobility products from TRMC represent in-plane, rotationally averaged values. Optically, the charge carrier yield (ϕ) should increase with the lead iodide layer thickness because of the decreasing exciton binding energy, reducing the measured values of $\phi \Sigma \mu$ at lower values of n . Combining these opposing contributions from structural and optical effects, we can expect that in-plane mobility is higher for films with a larger fraction of parallel lead iodide sheets. Previous optical-pump terahertz-probe (THz) measurements on a similar layered system with a phenethylammonium ($\text{C}_6\text{H}_5\text{C}_2\text{H}_4\text{NH}_3^+$) spacer cation suggest yield-mobility products that vary within 1 order of magnitude, generally increasing with layer thickness (n), and in the range of $1\text{--}11 \text{ cm}^2 \text{ V}^{-1} \text{ s}^{-1}$.⁴³ These measurements, like ours, are also normalized by carrier yield and are still susceptible to attenuation due to poor exciton dissociation in the lower n phases. The microwave cavity response also introduces a delay into acquisition by TRMC, so peak $\phi \Sigma \mu$ values are decreased by signal decay prior to measurement, explaining consistently smaller values than in THz, as our values are in the range of $0.03\text{--}0.04 \text{ cm}^2 \text{ V}^{-1} \text{ s}^{-1}$ at a similar incident laser power.⁴⁴

TRMC shows that carriers in films of these layered compounds show significant recombination losses compared to MAPbI_3 . To gain insight into the nature of carrier recombination in these systems, power-law fits were made to the TRMC data in Figure 4.5 and have slopes of -0.6 , -0.65 , -0.7 , and -0.8 for $n = 1, 2, 3$, and 4 , respectively. The total rate of recombination is governed by the sum of the rates of all recombination pathways, $\sum k_m \cdot n^m$, where n is the carrier concentration and k_m is the rate constant of the m th order process. The recombination pathways of interest are for $m \leq 3$, or monomolecular (single-exciton and trap-assisted recombination), bimolecular (free-carrier and two-exciton recombina-

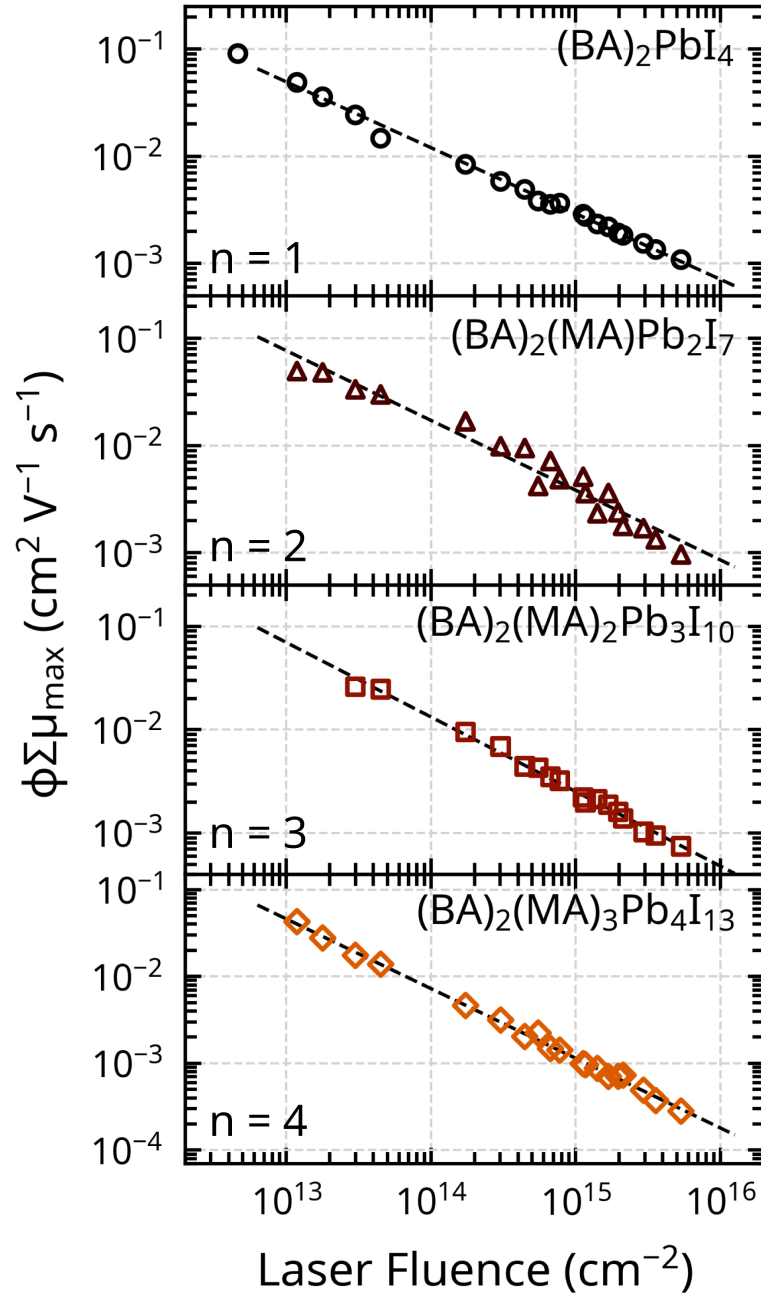


Figure 4.5: Maximum values of TRMC figure-of-merit $\phi \Sigma \mu$ over a range of incident laser fluences, with dashed lines indicating power-law fits to the data. Values of $\phi \Sigma \mu$ decrease at higher fluences because of increased recombination at larger carrier concentration, decreasing the apparent value of ϕ . Samples were pulsed with a Nd:YAG laser with a full-width at half-maximum of 5 ns and an emission wavelength of 532 nm and were measured at room temperature in ambient.

tion), and trimolecular (Auger recombination).^{32,45} The monomolecular rate constant, k_1 , represents a limit on the initial yield-mobility product, because this recombination pathway is mediated by the trap density of a material.^{32,43,45–47}

As the laser fluence (and therefore carrier concentration) increases, bimolecular and Auger pathways become more active. This leads to appreciable recombination during the excitation pulse, reducing the apparent carrier yield and subsequently $\phi \Sigma \mu$ at high laser fluences.⁴⁸ Previous TRMC measurements on MAPbI₃ show that at laser fluences below $\sim 10^{14}$ cm⁻², the dependence of mobility on incident laser power becomes minimal because of low trap density and long carrier lifetimes.^{34,38,49} The four layered compounds, however, clearly do not reach this threshold where trap-assisted recombination is the dominant pathway, shown by the monotonic increase in $\phi \Sigma \mu$ with decreasing laser fluence over our measurable range; it is expected that we would see this behavior at low enough fluences (below the resolution of our instrument). Defect densities in the Ruddlesden–Popper phases should be large because of the number of interfaces between the inorganic material and organic spacer units, suggesting large values of k_2 and k_3 relative to MAPbI₃, which have been found in the literature to be in the ranges of $0.8\text{--}20 \times 10^{-10}$ cm³ s⁻¹ and $0.2\text{--}10 \times 10^{-28}$ cm⁶ s⁻¹, respectively.^{34,46,47,50–59} Because bimolecular and Auger recombination are dependent on higher powers of the carrier concentration, we can conclude that the more negative slopes in power-law fits to TRMC data represent, on average, higher-order recombination.

In all four materials, there appears to be appreciable higher-order recombination, and the decrease in slope with n can be explained by the confinement of carriers. In lower n phase films, we expect significant monomolecular recombination from undissociated excitons, lowering the overall average recombination order. Additionally, in the higher n phase films, because there are many inorganic/organic interfaces parallel to the substrate, we expect a higher defect density and an increase in trap-assisted recombination. The decreasing

slope, however, shows that the lessening confinement effects promote increased free carrier formation and bimolecular recombination, compensating for this increased defect density. Although excitons in thin films of the $n = 3$ and 4 compounds have been hypothesized to relax into lower-energy edge-states,²⁶ which are inherently defects, these do not appear to increase the monomolecular character of the average recombination.

Despite large reported PCE values for the $n = 3$ and 4 layered compounds, the yield–mobility product is lower than that of methylammonium lead iodide. Previous TRMC studies of MAPbI₃ have shown mobilities at room temperature on the order of $10 \text{ cm}^2 \text{ V}^{-1} \text{ s}^{-1}$ (assuming $\phi = 1$),^{34,36,49} with the value having shown to be sensitive to the grain size in the film.⁶⁰ At the lowest measurable fluence, all four materials show $\phi \Sigma\mu$ values at least 2 orders of magnitude below this value. The $n = 1$ and 2 phases are excitonic and likely have low ϕ , leading to higher mobility; however, the texturing of these films is not ideal for the vertical charge transport required in a photovoltaic. Previous THz measurements on the same $n = 4$ system report a large in-plane mobility of $1.88 \text{ cm}^2 \text{ V}^{-1} \text{ s}^{-1}$, inconsistent with the [101] texturing seen in this study.⁶¹ However, THz measurements on an analogous system show similar results, although the thin film texture was not quantitatively characterized, making a direct comparison with this work difficult.⁴³

To compare carrier lifetimes, photoconductance transients at large fluence (highest signal-to-noise) are shown in Figure 4.13 and suggest faster decays in the layered compounds than in MAPbI₃. These, along with the dominant higher-order recombination seen in Figure 4.5, indicate that there is not a large population of long-lived carriers (see Appendix section 4.5.12). Time-resolved photoluminescence (TRPL) measurements on these compounds have also shown lifetimes on the order of $\sim 10 \text{ ns}$.^{20,26} Although TRPL lifetimes have shown to significantly underestimate lifetime compared to TRMC for MAPbI₃ bulk crystals because of surface recombination,⁶² our decays from TRMC (Figure 4.13) appear to be consistent with measured PL lifetimes. Despite similar fluence dependence, the single-

layer compound $(\text{MA})_2\text{Pb}(\text{SCN})_2\text{I}_2$ has shown long lifetimes, which has been attributed to either intersystem crossing into triplet exciton states^{23,63} or Rashba splitting;⁶⁴ however, TRMC transients clearly show slower decays.⁴⁹ While shorter lifetimes than those of MAPbI_3 can still lead to efficient photovoltaic cells, they still limit the thickness of the absorber layer, as seen by the peak in PCE value at intermediate thicknesses in $(\text{BA})_2(\text{MA})_3\text{Pb}_4\text{I}_{13}$.¹⁸

4.4 Conclusion

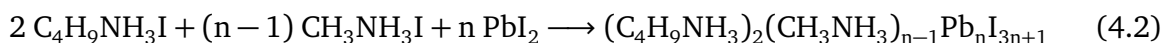
In conclusion, thin films of four Ruddlesden–Popper phases of $(\text{BA})_2(\text{MA})_{n-1}\text{Pb}_n\text{I}_{3n+1}$ were grown from solution and characterized. X-ray diffraction reveals a gradual change in thin film texturing, where lead iodide layers are preferentially aligned parallel to the substrate in the single layer ($n = 1$) compound and are nearly entirely perpendicular in the $n = 4$ compound; this change is confirmed by microscopy measurements. Finally, despite large measured PCEs for the $n = 3$ and 4 compounds in previous literature, TRMC measurements indicate yield-mobility products 2 orders of magnitude lower than MAPbI_3 , with no clear evidence of longer than average carrier lifetime. The highly controlled film texturing, however, makes these materials promising for a wide array of optoelectronic applications beyond photovoltaics, such as lateral photodetectors and thin-film transistors, and the increased stability of these layered materials also makes them viable for long-term use in ambient environments.

4.5 Appendix

4.5.1 Experimental Methods

Butylammonium methylammonium lead iodide thin film synthesis

Stoichiometric ratios according to Equation 4.2 of *n*-butylammonium iodide (BAI), methylammonium iodide (MAI), and lead (II) iodide (PbI₂) were mixed in anhydrous *N,N*-dimethylformamide (DMF) to a solution concentration of 150 mg/mL. All solutions were allowed to stir at 70° and 300 rpm for at least three hours prior to film deposition by spin-coating onto either glass (X-ray diffraction measurements) or z-cut quartz (all other characterizations) substrates cleaned with soap water, deionized water, acetone, and isopropanol, followed by a 10-minute plasma clean to improve surface wetting. Solutions were spun at 4000 rpm for 1 minute and subsequently annealed at 100° for 30 minutes prior to measurements. BAI and MAI precursors were purchased from GreatCell Solar, PbI₂ and anhydrous DMF were purchased from Sigma Aldrich. All synthesis was conducted in a N₂-filled glovebox with sub-ppm oxygen and moisture levels.



Methylammonium lead iodide thin film synthesis

Methylammonium lead iodide thin-films were spun from solutions of a 1:1 molar ratio of MAI and PbI₂ in a 3:7 (volume/volume) mixture of dimethylsulfoxide (DMSO) and γ -butyrolactone (GBL) at a concentration of 1 M. Solutions were stirred at 70°C and 300 rpm for at least three hours prior to deposition. Films were deposited on glass and z-cut quartz that were cleaned as described in the previous section and spun at 5000 rpm with a two-step solvent-annealing procedure; chlorobenzene (CB) was used as antisolvent 5

seconds prior to the end of the spin cycle. Samples were then annealed at 100°C for 5 minutes before any characterization measurements. GBL, anhydrous DMSO, and CB were all purchased from Sigma Aldrich. All synthesis was conducted in a N₂-filled glovebox with sub-ppm oxygen and moisture levels.

X-ray diffraction measurements

Specular X-ray diffraction (XRD) was measured on a Panalytical Empyrean powder diffractometer in reflection mode with a Cu-K α source, operating with an accelerating voltage of 45 kV and beam current of 40 mA. Due to fiber-textured nature of spincoated films, in which diffraction patterns are invariant to rotation, samples were rotated to increase the signal-to-noise ratio of collected patterns. Simulated patterns were calculated using the General Structure Analysis System (GSAS), with a calibration file specific to our instrument and structure factors from previously-solved single-crystals. For simulated patterns with preferred orientation, March-Dollase correction factors were utilized during calculation.

Scanning electron microscope measurements

Scanning electron microscope (SEM) micrographs of thin-films were collected using an FEI Nova NanoSEM 650 in secondary electron mode, operating with an accelerating voltage of 5 kV and a spot size of 3.0. Films were deposited on z-cut quartz and coated with a thin (~nm) conductive layer of a gold/palladium alloy to prevent charging during imaging.

Atomic force microscope measurements

Atomic force microscope (AFM) micrographs of thin-films were collected with an Asylum Research MFP-3D Standard System in tapping mode. Films were deposited on z-cut quartz, the surface was cleaned with a pressurized N₂ gun, and measured in ambient pressure air.

X-ray reflectivity measurements

X-ray reflectivity (XRR) measurements were collected using a Rigaku Smartlab Diffractometer with a Cu-K α source, operating with an accelerating voltage of 45 kV and beam current of 40 mA. Films were deposited on z-cut quartz instead of glass since reflectivity angles are far below those of scattering peaks from quartz.

UV-Vis Absorption Spectroscopy

Films were deposited on z-cut quartz as described above and absorption measurements were performed using a Shimadzu UV-2600 ultraviolet-visible spectrophotometer at room temperature in ambient conditions.

Photoluminescence Measurements

Films were deposited on z-cut quartz as described above and photoluminescence measurements were carried out on a Horiba FluoroMax 4 spectrometer calibrated using Milli-Q water. Films were loaded into a thin-film sample stage angled at 60° between the excitation and emission port. All measurements were performed with an excitation wavelength of 450 nm. In order to limit effects of Rayleigh scattering at long wavelengths, a long-pass filter slightly above the excitation wavelength (455 nm) was placed in front of the emission port.

Time-resolved microwave conductivity measurements

Time-resolved microwave conductivity measurements were conducted using a setup described in previous studies. A microwave frequency oscillatory electric signal is generated using a Sivers IMA VO4280X/00 voltage controlled oscillator (VCO). The signal has an approximate power of 16 dBm and a tunable frequency between 8 GHz and 15 GHz. The oscillatory signal is then directed through coaxial cables to port 1 of an electronic circulator

(Fairview Microwave SFC0712). The circulator acts as a unidirectional device in which signals entering from port 1 exit through port 2 and signals entering from port 2 exit through port 3. The signal exiting the circulator from port 2 is then fed into a SMA to X-band waveguide adapter (purchased on eBay but similar to Fairview Microwave part 90AC206). This antenna is coupled to X-band cavity (purchased on eBay) using a homebuilt coupling iris and tuning screw fabricated from a thin aluminum plate. The cavity is a TE_{103} mode formed by a short section of X-band waveguide and a homemade slotted copper plate (slots along the direction of current) that allows optical access to the sample. The antenna emits electromagnetic radiation (microwaves) which form a standing wave in the cavity. The tuning screw enables over, critical, and undercoupling to the cavity and all experiments were performed in the undercoupled regime. The sample is mounted inside the cavity at a maximum of the electric-field component of the standing microwaves. Microwaves reflected from the cavity are then incident on port 2 of the circulator, exiting through port 3. Microwaves emitted from port 3 of the circulator are then directed into a zero-bias Schottky diode detector (Fairview Microwave SMD0218 operating in the linear regime). The rectified signal is amplified by a homebuilt DC-coupled, wide-band amplifier built around a Texas Instruments THS3091 operational amplifier (battery-powered, three stages of amplification). We note that the microwave power is split at the source, allowing a second detector and amplification stage to monitor/normalize the reflected power from the cavity. The amplified signal (and reference) is detected by a Tektronix TDS 3032C digital oscilloscope. The system used in these experiments has a cavity response of approximately 60 ns, comparable to previously reported systems. By illuminating the sample with a light from a Continuum Minilite pulsed Nd:YAG 532 nm laser with a FWHM of ~ 5 ns, free carriers are generated in the semiconducting sample (which should have a low carrier concentration at room temperature and in the dark). Any free carriers in the film move under the influence of the standing wave, with a velocity proportional to their mobility: $\vec{v} = \mu\vec{E}$. The change

in reflected microwave intensity can then be used to determine the TRMC figure of merit: $\phi \Sigma \mu$ at each fluence.

4.5.2 Determination of thickness from X-ray reflectivity

Reflectivity data was collected in $\theta/2\theta$ geometry at angles ranging from 0° – 3° from a Cu-K α source. Data from XRR measurements are shown in Figure 4.6, with an inset showing X-ray critical angle values. The critical angle was taken to be the angle at which the intensity drops to half of its value at total external reflection. The positions of the minima of the thickness fringes were fit to Equation 4.3 to calculate film thickness, where θ_m is the angle of the m th thickness fringe, θ_c is the X-ray critical angle, λ is the wavelength of the X-ray source (0.154 nm), and t is the thickness. Thicknesses and critical angles are tabulated below the XRR plots.

$$\sqrt{\theta_m^2 - \theta_c^2} = m \frac{\lambda}{2t} \quad (4.3)$$

Table 4.1: X-ray critical angles and thicknesses of Ruddlesden-Popper thin-films.

Material	X-Ray Critical Angle ($^\circ$)	Thickness (nm)
$(\text{BA})_2\text{PbI}_4$	0.200	104.5
$(\text{BA})_2\text{MAPb}_2\text{I}_7$	0.235	69.7
$(\text{BA})_2(\text{MA})_2\text{Pb}_3\text{I}_{10}$	0.225	68.1
$(\text{BA})_2(\text{MA})_3\text{Pb}_4\text{I}_{13}$	0.255	56.0

4.5.3 Calculation of optical attenuation lengths

The Beer-Lambert Law, shown in Equation 4.4, can be rearranged to calculate linear optical attenuation lengths using UV-Vis and thickness data from XRR. This is shown in

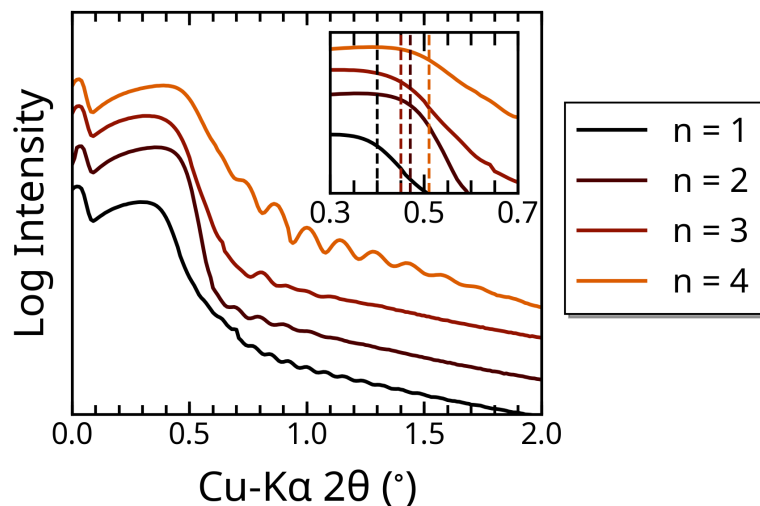


Figure 4.6: X-ray reflectivity (XRR) measurements of thin-films of $(\text{BA})_2(\text{MA})_{n-1}\text{Pb}_n\text{I}_{3n+1}$ of varying lead iodide layer thicknesses, indicated by n . Vertical offset between traces was arbitrarily added for ease of visualization. Inset shows zoomed-in total external reflection region, showing X-ray critical angles ($2\theta_c$) of each phase, calculated as the angle at which intensity is half of that at total reflection.

Equation 4.5, where T is the transmittance of the sample (blank subtracted), t is the film thickness, and μ is the optical attenuation length.

$$\frac{I}{I_0} = T = \exp(-\mu t) \quad (4.4)$$

$$\mu = \frac{-\log_e T}{t} \quad (4.5)$$

4.5.4 Comparison of optical properties of R-P series

The absorbance and emission of $\text{CH}_3\text{NH}_3\text{PbI}_3$ along with a comparison of the photoluminescence emission edges of the layered compounds and $\text{CH}_3\text{NH}_3\text{PbI}_3$ are presented in Figure 4.7.

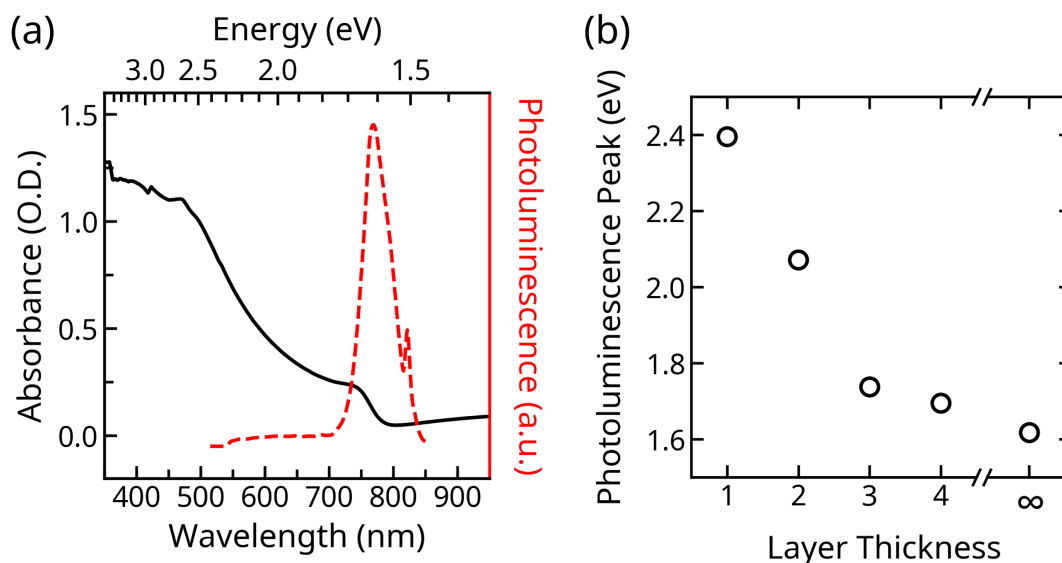


Figure 4.7: (a) Optical absorbance and photoluminescence measurements of $\text{CH}_3\text{NH}_3\text{PbI}_3$ thin films on quartz and (b) position of peak emission as a function of layer thickness, showing quick convergence to bulk ($n = \infty$) values.

4.5.5 Indexing of XRD patterns of layered perovskites

Figure 4.8 shows each of the four experimental specular X-ray diffraction patterns along with simulated patterns of isotropic, [010], and [101] textured films. All the diffraction peaks from experimental patterns are accounted for by the textured simulations, validating the assumption made in the derivation of Equation 4.1 that only two distinct texture populations are present.

4.5.6 Derivation of equation quantifying texture

The integrated peak intensity, as measured by specular X-ray diffraction, is proportional to the product of four terms, shown in Equation 4.6: the square of the structure factor (F_{hkl}), the Lorentz-polarization correction factor ($LP(\theta)$), the multiplicity of a particular lattice

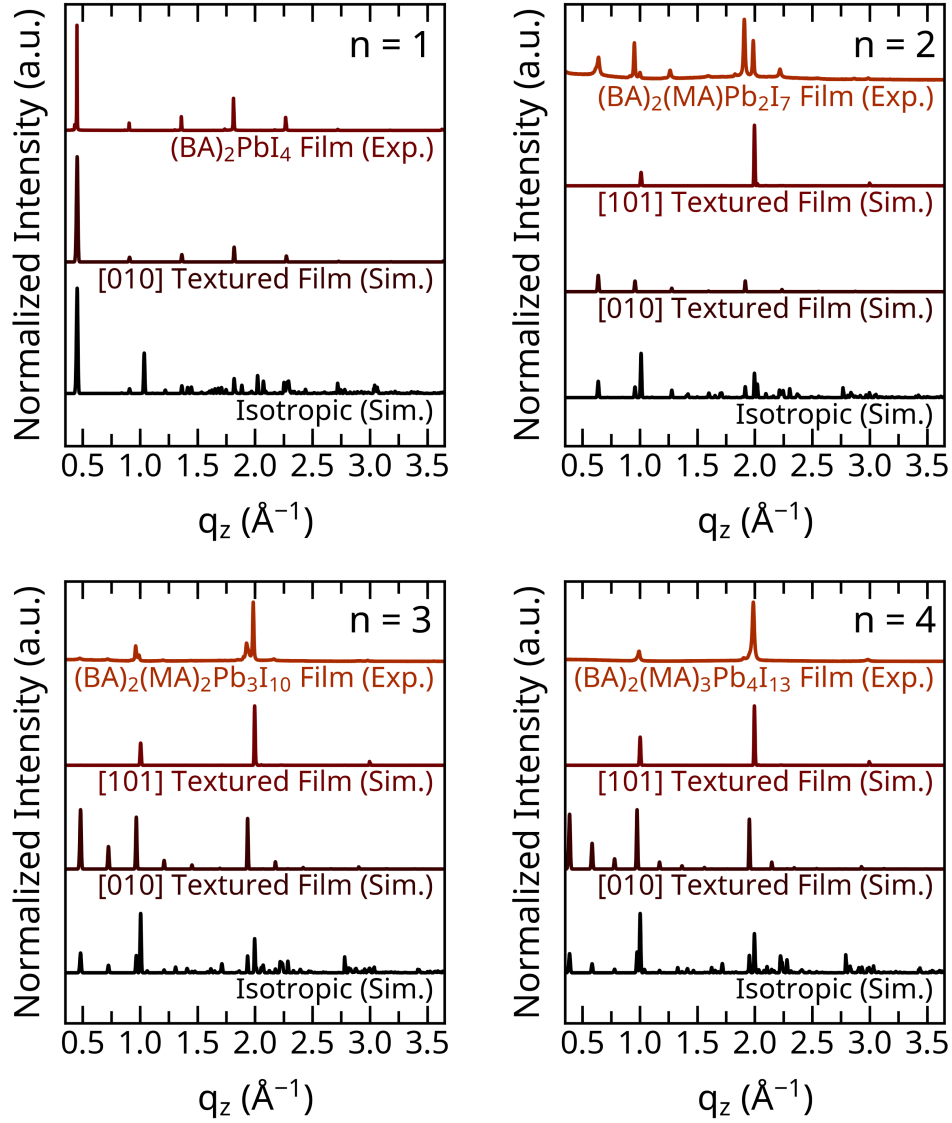


Figure 4.8: Experimental and simulated diffraction patterns of layered perovskite thin films of $(\text{BA})_2(\text{MA})_{n-1}\text{Pb}_n\text{I}_{3n+1}$, illustrating that films are a linear combination of [010] and [101] textured domains since all diffraction peaks are accounted for by the simulated patterns.

plane family (M_{hkl}), and the Debye-Waller thermal correction factor ($DW(\theta)$).

$$I \propto |F_{hkl}|^2 \cdot LP(\theta) \cdot M_{hkl} \cdot DW(\theta) \quad (4.6)$$

The peaks used for texture analysis for each of the compounds were the $(0k0)$ and $(h0h)$

lattice plane peaks in the vicinity of 2.0 \AA^{-1} in the specular XRD pattern, shown in Figure 4.9. Both peaks were assumed to be fit by a Gaussian function, allowing integrated peak intensity to be replaced by peak heights. The temperature correction factor is only appreciable at large angles; regardless, since the scattering angles of the two peaks of interest are within 1° of each other (raw data measured in 2θ from a Cu-K α source), this factor was assumed to be a constant for both. Additionally, due to strong out-of-plane orientation in the thin-films, the multiplicity of lattice planes measured *via* specular diffraction should be equal to unity. Therefore, the only relevant correction factor for calculation is the Lorentz-polarization correction, shown in Equation 4.7.

$$LP(\theta) = \frac{1 + \cos^2(2\theta)}{2\sin^2(\theta)\cos^2(\theta)} \quad (4.7)$$

Using both this correction factor and the structure factors from previously solved structures, the ratio of peak heights is weighted to calculate the fraction of each texture, shown in Equation 4.8 (also Equation 4.1 above).

$$f_{(h'k'l')} = \left(\frac{P_{h'k'l'}}{P_{h'k'l'} + P_{hkl}} \right) \cdot \left(\frac{LP(\theta_{hkl})}{LP(\theta_{h'k'l'})} \right) \cdot \left(\frac{|F_{hkl}|}{|F_{h'k'l'}|} \right)^2 \quad (4.8)$$

4.5.7 Calculation of fraction of textured populations

In all the mixed texture phases ($n > 1$), there are two peaks between 1.9 and 2.0 \AA^{-1} in reciprocal space, one characteristic of a lattice plane from the $\{010\}$ family of planes and one from $\{101\}$. This is shown in Figure 4.9 below, which is just the same data from Figure 4.2 but over a smaller range. Shaded regions show the gradual increase in the $\{101\}$ peak intensity with respect to $\{010\}$. Bragg angles and peak intensities were extracted from the data shown in Figure 4.9 and used with Equation 4.8 to calculate texture fractions.

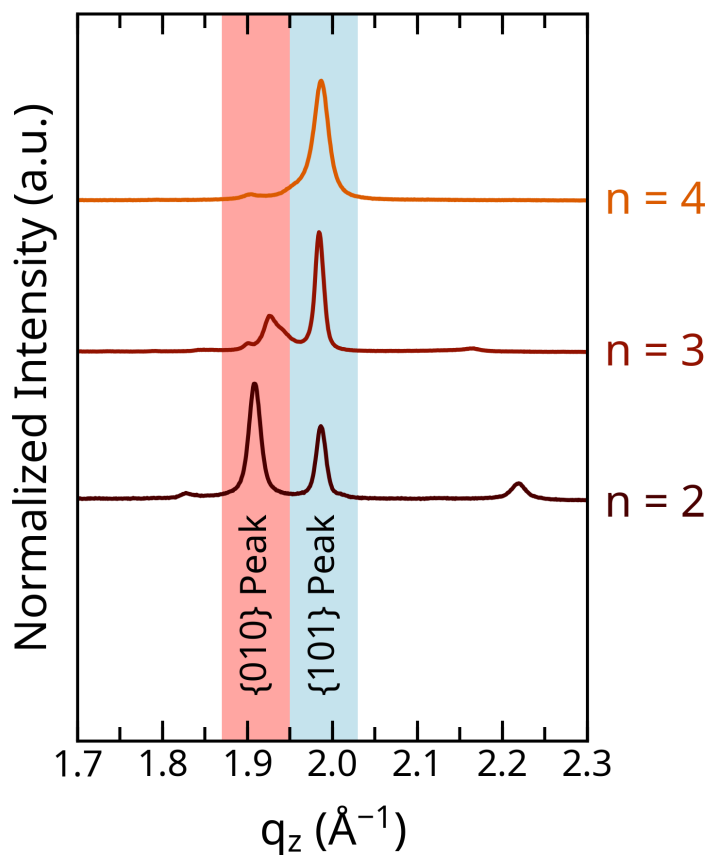


Figure 4.9: XRD patterns of $n = 2$ to 4 of $(\text{BA})_2(\text{MA})_{n-1}\text{Pb}_n\text{I}_{3n+1}$ thin films spun on glass, illustrating characteristic peaks corresponding to texturing along $[010]$ and $[101]$ crystallographic directions. Relative peak heights were used, along with Equation 4.8, to calculate the fraction of textured populations.

Table 4.2: Fractions of texture populations in Ruddlesden–Popper thin films

n	$f_{[010]}$ (parallel)	$f_{[101]}$ (perpendicular)
1	1.00	0.00
2	0.75	0.25
3	0.24	0.76
4	0.06	0.94

4.5.8 XRD and preferred orientation of $\text{CH}_3\text{NH}_3\text{PbI}_3$

An X-ray diffraction pattern of methylammonium lead iodide was collected as described in Section 4.5.1 and is shown in Figure 4.10, along with simulated patterns of an isotropic powder of $\text{CH}_3\text{NH}_3\text{PbI}_3$ and one with texturing along the $[101]$ crystallographic direction. The crystal structure of methylammonium lead iodide is also shown, with a red plane corresponding to the $[101]$ direction, consistent with the texturing of lead iodide planes in the higher n Ruddlesden–Popper thin-films.

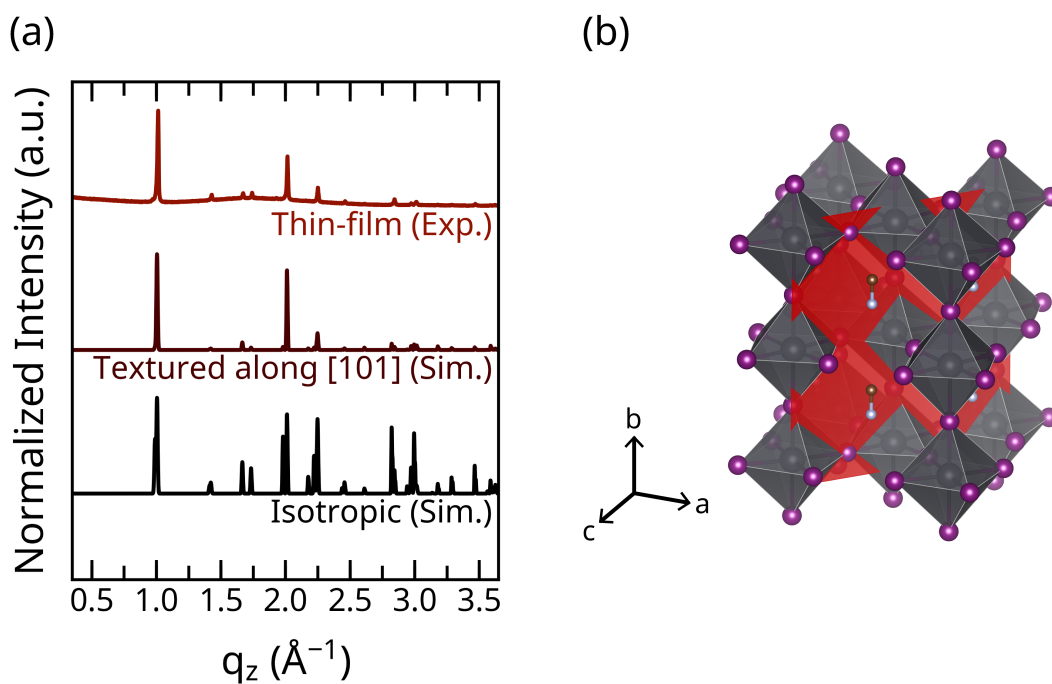


Figure 4.10: (a) Specular X-ray diffraction pattern of a thin-film of methylammonium lead iodide ($\text{CH}_3\text{NH}_3\text{PbI}_3$), along with simulated patterns of an isotropic sample and one textured along the $[101]$ crystallographic direction. (b) Crystal structure of $\text{CH}_3\text{NH}_3\text{PbI}_3$ along with red plane corresponding to the (101) lattice plane, consistent with the majority texturing in the $n = 4$ sample.

4.5.9 SEM micrographs of Ruddlesden–Popper thin films

Scanning electron microscope (SEM) micrographs were collected as described in methods in Section 4.5.1 and are presented in Figure 4.11. White spots on film surfaces are nanoparticles of the gold/palladium alloy used for the conductive coating.

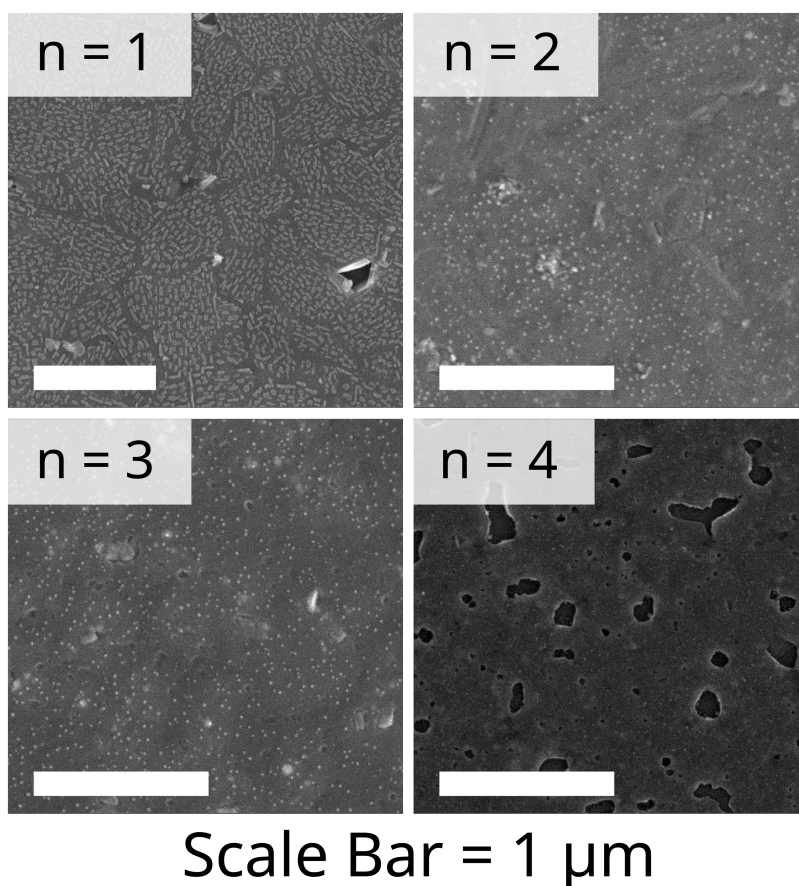


Figure 4.11: Scanning electron microscope (SEM) micrographs of thin films of $n = 1$ to 4 coated on z-cut quartz, illustrating the same microstructure as the AFM micrographs presented in the main text. Films were coated with an alloy of gold/palladium and imaged with an accelerating voltage of 5 kV and a spot size of 3.0.

4.5.10 Fluence-dependent TRMC data on $\text{CH}_3\text{NH}_3\text{PbI}_3$

Fluence-dependent TRMC data for thin films of methylammonium lead iodide (spun on quartz as described in Section 4.5.1) is shown in Figure 4.12, along with a power-law fit to the points above which higher-order recombination pathways become more active, for comparison with layered phases. The more negative slope of the trace in comparison with the four Ruddlesden-Popper phases is due to mostly bimolecular recombination as seen in previous literature, while the layered materials have a large degree of monomolecular recombination. This is primarily due to the volume of interfaces between the inorganic lead iodide layers and the organic butylammonium spacer cations that act as recombination centers. Additionally, the increased excitonic behavior due to confinement effects results in increased recombination by single-exciton decay, also a monomolecular process.

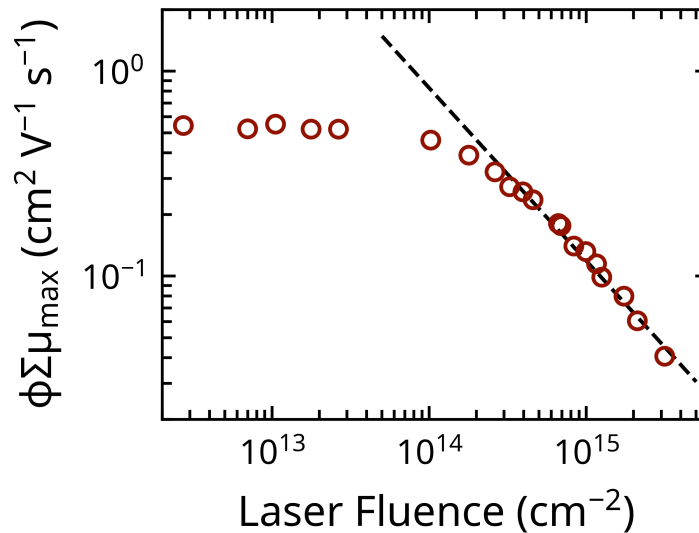


Figure 4.12: Fluence-dependent TRMC measurements of the maximum value of $\phi \Sigma \mu$ for three-dimensional methylammonium lead iodide ($\text{CH}_3\text{NH}_3\text{PbI}_3$), illustrating the clear roll-off in the lower fluence regime to nearly constant values due to dominant monomolecular recombination. The dashed line represents a power-law fit to the data and has a slope of -0.84 , more negative than the $n = 4$ compound as presented in the main text. This is due to increased bimolecular character of the recombination at high fluences in $\text{CH}_3\text{NH}_3\text{PbI}_3$, a result consistent with previous literature.

4.5.11 High-fluence TRMC transients

Time-resolved microwave conductivity transients at high fluences ($5.35 \times 10^{15} \text{ cm}^{-2}$ for layered compounds and $3.16 \times 10^{15} \text{ cm}^{-2}$ for $\text{CH}_3\text{NH}_3\text{PbI}_3$) are shown in Figure 4.13

4.5.12 Quantification of recombination rate constants

From TRMC data on methylammonium lead iodide, we know that monomolecular recombination is the dominant pathway below incident laser fluences of approximately 10^{14} cm^{-3} . Due to confinement effects, we expect the Ruddlesden-Popper phases to have higher exciton binding energies and, therefore, lower carrier yields (ϕ) than in MAPbI_3 . The recombination rate constants in planar thin films of MAPbI_3 have been previously quantified by the THz spectroscopy, with values listed below.

$$k_1 = 1.50 \times 10^7 \text{ s}^{-1}$$

$$k_2 = 1.05 \times 10^{-11} \text{ cm}^3 \text{ s}^{-1}$$

$$k_3 = 5.75 \times 10^{-27} \text{ cm}^6 \text{ s}^{-1}$$

Assuming $\phi \approx 1$ in MAPbI_3 , we can say monomolecular recombination is dominant at carrier concentrations of 10^{14} cm^{-3} . Since carrier yields are lower in the layered phases, we know that at the same laser fluence, there is actually a lower carrier concentration. Despite this, the slope in the fluence-dependent TRMC plots are all negative. Therefore, even if we assume the same values of k_1 for all compounds, the higher order rate constants must be larger to show this behavior, and all four layered phases have substantial higher-order recombination and no obviously evident long-lived carriers.

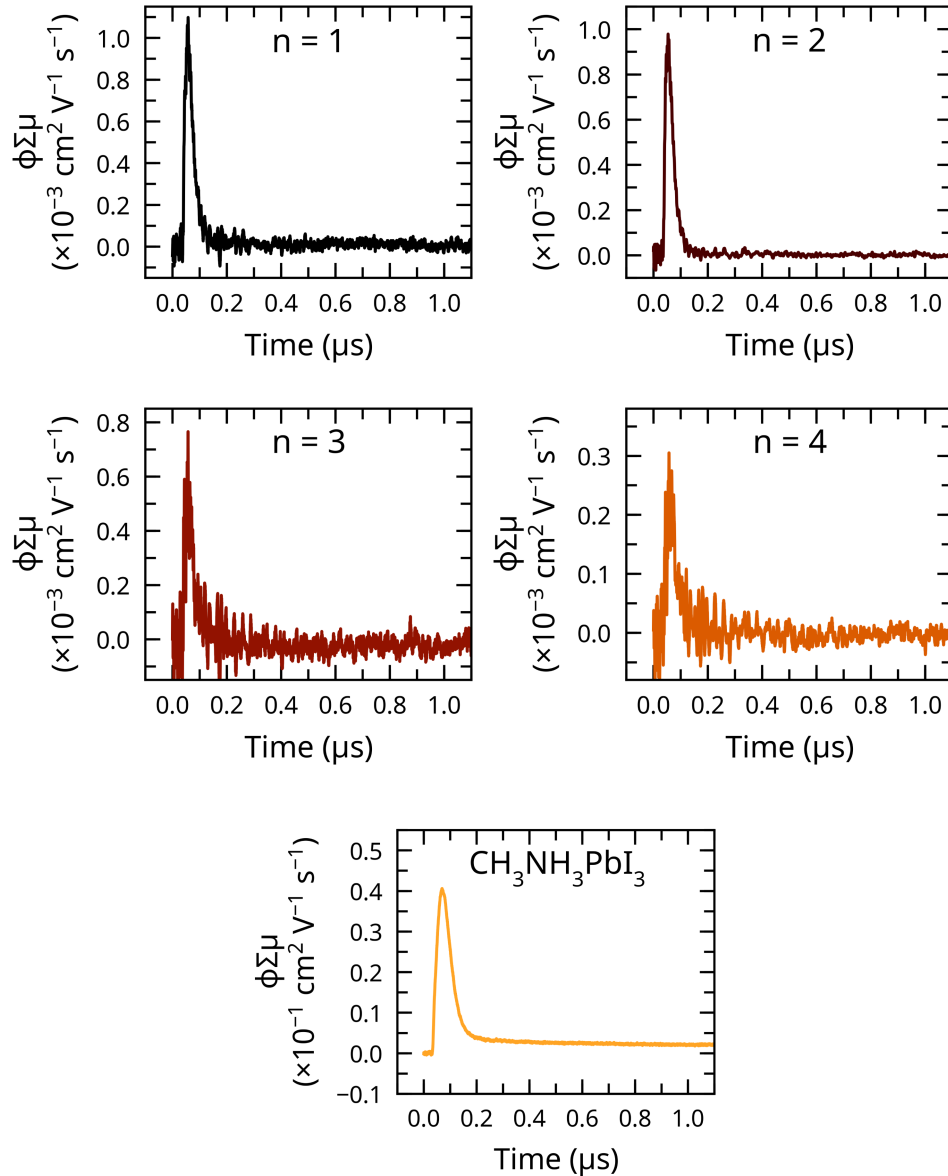


Figure 4.13: Transient TRMC traces of $n = 1$ to 4 of $(\text{BA})_2(\text{MA})_{n-1}\text{Pb}_n\text{I}_{3n+1}$ Ruddlesden–Popper phases (fluence of $5.35 \times 10^{15} \text{ cm}^{-2}$), along with methylammonium lead iodide, $\text{CH}_3\text{NH}_3\text{PbI}_3$ (fluence of $3.16 \times 10^{15} \text{ cm}^{-2}$), illustrating peak $\phi\Sigma\mu$ values. Peak values are lower than at lower fluence since higher-order recombination is appreciable at high carrier concentrations. The layered compounds all have $\phi\Sigma\mu_{\text{max}}$ approximately two orders of magnitude lower than the three-dimensional compound. Additionally, the carrier lifetime, as inferred from the TRMC decay, is larger in $\text{CH}_3\text{NH}_3\text{PbI}_3$ as seen by the curve having values greater than zero through the duration of the experiment.

4.6 Acknowledgments

Development of the microwave conductivity instrument was supported by the Defense Threat Reduction Agency under Award Number HDTRA1-15-1-0023. Materials synthesis and structural characterization was supported by the U.S. Department of Energy, Office of Science, Basic Energy Sciences, under Award Number DE-SC-0012541. The research reported here made use of shared facilities of the UCSB MRSEC (NSF DMR 1720256), a member of the Materials Research Facilities Network (www.mrfn.org). J.G.L. gratefully acknowledges Virgil Elings and Betty Elings Wells for financial support through the Elings Fellowship Awards.

4.7 Permissions and Attributions

The content of this chapter and appendix has been reprinted with permission from “Charge-Carrier Dynamics and Crystalline Texture of Layered Ruddlesden–Popper Hybrid Lead Iodide Perovskite Thin Films” by N. R. Venkatesan *et al.*. Copyright © 2018 American Chemical Society.

4.8 References

1. Mitzi, D. B., Chondroudis, K. & Kagan, C. R. Organic-Inorganic Electronics. *IBM Journal of Research and Development* **45**, 29–45 (2001).
2. Berry, J., Buonassisi, T., Egger, D. A., Hodes, G., Kronik, L., Loo, Y.-L., Lubomirsky, I., Marder, S. R., Mastai, Y., Miller, J. S., Mitzi, D. B., Paz, Y., Rappe, A. M., Riess, I., Rybtchinski, B., Stafsudd, O., Stevanovic, V., Toney, M. F., Zitoun, D., Kahn, A., Ginley, D. & Cahen, D. Hybrid Organic-Inorganic Perovskites (HOIPs): Opportunities and Challenges. *Advanced Materials* **27**, 5102–5112 (2015).
3. Kagan, C. R., Mitzi, D. B. & Dimitrakopoulos, C. D. Organic-Inorganic Hybrid Materials as Semiconducting Channels in Thin-Film Field-Effect Transistors. *Science* **286**, 945–947 (1999).
4. Saparov, B. & Mitzi, D. B. Organic–Inorganic Perovskites: Structural Versatility for Functional Materials Design. *Chemical Reviews* **116**, 4558–4596 (2016).
5. Papavassiliou, G. C., Mousdis, G. A. & Koutselas, I. B. Some New Organic–Inorganic Hybrid Semiconductors Based on Metal Halide Units: Structural, Optical and Related Properties†. *Advanced Materials for Optics and Electronics* **9**, 265–271 (1999).
6. Snaith, H. J. Perovskites: The Emergence of a New Era for Low-Cost, High-Efficiency Solar Cells. *The Journal of Physical Chemistry Letters* **4**, 3623–3630 (2013).
7. Zhang, W., Eperon, G. E. & Snaith, H. J. Metal Halide Perovskites for Energy Applications. *Nature Energy* **1**, 16048 (2016).
8. Kojima, A., Teshima, K., Shirai, Y. & Miyasaka, T. Organometal Halide Perovskites as Visible-Light Sensitizers for Photovoltaic Cells. *Journal of the American Chemical Society* **131**, 6050–6051 (2009).
9. Yang, W. S., Park, B.-W., Jung, E. H., Jeon, N. J., Kim, Y. C., Lee, D. U., Shin, S. S., Seo, J., Kim, E. K., Noh, J. H. & Seok, S. I. Iodide Management in Formamidinium-Lead-Halide-Based Perovskite Layers for Efficient Solar Cells. *Science* **356**, 1376–1379 (2017).
10. Green, M. A., Emery, K., Hishikawa, Y., Warta, W., Dunlop, E. D., Levi, D. H. & Ho-Baillie, A. W. Y. Solar Cell Efficiency Tables (Version 49). *Progress in Photovoltaics: Research and Applications* **25**, 3–13 (2017).
11. Aristidou, N., Sanchez-Molina, I., Chotchuangchutchaval, T., Brown, M., Martinez, L., Rath, T. & Haque, S. A. The Role of Oxygen in the Degradation of Methylammonium Lead Trihalide Perovskite Photoactive Layers. *Angewandte Chemie International Edition* **54**, 8208–8212 (2015).
12. Zhao, L., Kerner, R. A., Xiao, Z., Lin, Y. L., Lee, K. M., Schwartz, J. & Rand, B. P. Redox Chemistry Dominates the Degradation and Decomposition of Metal Halide Perovskite Optoelectronic Devices. *ACS Energy Letters* **1**, 595–602 (2016).

13. Leijtens, T., Eperon, G. E., Noel, N. K., Habisreutinger, S. N., Petrozza, A. & Snaith, H. J. Stability of Metal Halide Perovskite Solar Cells. *Advanced Energy Materials* **5**, 1500963 (2015).
14. Ruddlesden, S. N. & Popper, P. New Compounds of the K_2NiF_4 Type. *Acta Crystallographica* **10**, 538–539 (1957).
15. Ruddlesden, S. N. & Popper, P. The Compound $Sr_3Ti_2O_7$ and Its Structure. *Acta Crystallographica* **11**, 54–55 (1958).
16. Smith, I. C., Hoke, E. T., Solis-Ibarra, D., McGehee, M. D. & Karunadasa, H. I. A Layered Hybrid Perovskite Solar-Cell Absorber with Enhanced Moisture Stability. *Angewandte Chemie International Edition* **126**, 11414–11417 (2014).
17. Quan, L. N., Yuan, M., Comin, R., Voznyy, O., Beauregard, E. M., Hoogland, S., Buin, A., Kirmani, A. R., Zhao, K., Amassian, A., Kim, D. H. & Sargent, E. H. Ligand-Stabilized Reduced-Dimensionality Perovskites. *Journal of the American Chemical Society* **138**, 2649–2655 (2016).
18. Tsai, H., Nie, W., Blancon, J.-C., Stoumpos, C. C., Asadpour, R., Harutyunyan, B., Neukirch, A. J., Verduzco, R., Crochet, J. J., Tretiak, S., Pedesseau, L., Even, J., Alam, M. A., Gupta, G., Lou, J., Ajayan, P. M., Bedzyk, M. J., Kanatzidis, M. G. & Mohite, A. D. High-Efficiency Two-Dimensional Ruddlesden-Popper Perovskite Solar Cells. *Nature* **536**, 312–316 (2016).
19. Pedesseau, L., Saponi, D., Traore, B., Robles, R., Fang, H.-H., Loi, M. A., Tsai, H., Nie, W., Blancon, J.-C., Neukirch, A., Tretiak, S., Mohite, A. D., Katan, C., Even, J. & Kepenekian, M. Advances and Promises of Layered Halide Hybrid Perovskite Semiconductors. *ACS Nano* **10**, 9776–9786 (2016).
20. Zhang, X., Wu, G., Yang, S., Fu, W., Zhang, Z., Chen, C., Liu, W., Yan, J., Yang, W. & Chen, H. Vertically Oriented 2D Layered Perovskite Solar Cells with Enhanced Efficiency and Good Stability. *Small* **13**, 1700611 (2017).
21. Cao, D. H., Stoumpos, C. C., Farha, O. K., Hupp, J. T. & Kanatzidis, M. G. 2D Homologous Perovskites as Light-Absorbing Materials for Solar Cell Applications. *Journal of the American Chemical Society* **137**, 7843–7850 (2015).
22. Chen, Y., Sun, Y., Peng, J., Tang, J., Zheng, K. & Liang, Z. 2D Ruddlesden–Popper Perovskites for Optoelectronics. *Advanced Materials* **30**, 1703487 (2017).
23. Xiao, Z., Meng, W., Saparov, B., Duan, H.-S., Wang, C., Feng, C., Liao, W., Ke, W., Zhao, D., Wang, J., Mitzi, D. B. & Yan, Y. Photovoltaic Properties of Two-Dimensional $(CH_3NH_3)_2Pb(SCN)_2I_2$ Perovskite: A Combined Experimental and Density Functional Theory Study. *The Journal of Physical Chemistry Letters* **7**, 1213–1218 (2016).
24. Stoumpos, C. C., Cao, D. H., Clark, D. J., Young, J., Rondinelli, J. M., Jang, J. I., Hupp, J. T. & Kanatzidis, M. G. Ruddlesden–Popper Hybrid Lead Iodide Perovskite 2D Homologous Semiconductors. *Chemistry of Materials* **28**, 2852–2867 (2016).

25. Momma, K. & Izumi, F. VESTA-3 for Three-Dimensional Visualization of Crystal, Volumetric and Morphology Data. *Journal of Applied Crystallography* **44**, 1272–1276 (2011).
26. Blancon, J.-C., Tsai, H., Nie, W., Stoumpos, C. C., Pedesseau, L., Katan, C., Kepenekian, M., Soe, C. M. M., Appavoo, K., Sfeir, M. Y., Tretiak, S., Ajayan, P. M., Kanatzidis, M. G., Even, J., Crochet, J. J. & Mohite, A. D. Extremely Efficient Internal Exciton Dissociation through Edge States in Layered 2D Perovskites. *Science* **355**, 1288–1292 (2017).
27. Umeyama, D., Lin, Y. & Karunadasa, H. I. Red-to-Black Piezochromism in a Compressible Pb–I–SCN Layered Perovskite. *Chemistry of Materials* **28**, 3241–3244 (2016).
28. Umebayashi, T., Asai, K., Kondo, T. & Nakao, A. Electronic Structures of Lead Iodide Based Low-Dimensional Crystals. *Physical Review B* **67**, 155405 (2003).
29. Hirasawa, M., Ishihara, T., Goto, T., Uchida, K. & Miura, N. Magnetoabsorption of the Lowest Exciton in Perovskite-Type Compound $(\text{CH}_3\text{NH}_3)\text{PbI}_3$. *Physica B: Condensed Matter* **201**, 427–430 (1994).
30. Miyata, A., Mitioglu, A., Plochocka, P., Portugall, O., Wang, J. T.-W., Stranks, S. D., Snaith, H. J. & Nicholas, R. J. Direct Measurement of the Exciton Binding Energy and Effective Masses for Charge Carriers in Organic-Inorganic Tri-Halide Perovskites. *Nature Physics* **11**, 582–587 (2015).
31. Galkowski, K., Mitioglu, A., Miyata, A., Plochocka, P., Portugall, O., E. Eperon, G., Tse-Wei Wang, J., Stergiopoulos, T., D. Stranks, S., J. Snaith, H. & J. Nicholas, R. Determination of the Exciton Binding Energy and Effective Masses for Methylammonium and Formamidinium Lead Tri-Halide Perovskite Semiconductors. *Energy & Environmental Science* **9**, 962–970 (2016).
32. Herz, L. M. Charge-Carrier Dynamics in Organic-Inorganic Metal Halide Perovskites. *Annual Review of Physical Chemistry* **67**, 65–89 (2016).
33. Birkholz, M. *Thin Film Analysis by X-Ray Scattering* (John Wiley & Sons, 2006).
34. Oga, H., Saeki, A., Ogomi, Y., Hayase, S. & Seki, S. Improved Understanding of the Electronic and Energetic Landscapes of Perovskite Solar Cells: High Local Charge Carrier Mobility, Reduced Recombination, and Extremely Shallow Traps. *Journal of the American Chemical Society* **136**, 13818–13825 (2014).
35. Savenije, T. J., Ponseca, C. S., Kunneman, L., Abdellah, M., Zheng, K., Tian, Y., Zhu, Q., Canton, S. E., Scheblykin, I. G., Pullerits, T., Yartsev, A. & Sundström, V. Thermally Activated Exciton Dissociation and Recombination Control the Carrier Dynamics in Organometal Halide Perovskite. *The Journal of Physical Chemistry Letters* **5**, 2189–2194 (2014).

36. Hutter, E. M., Gélvez-Rueda, M. C., Oshero, A., Bulović, V., Grozema, F. C., Stranks, S. D. & Savenije, T. J. Direct-Indirect Character of the Bandgap in Methylammonium Lead Iodide Perovskite. *Nature Materials* **16**, 115–120 (2017).
37. Ponseca, C. S., Savenije, T. J., Abdellah, M., Zheng, K., Yartsev, A., Pascher, T., Harlang, T., Chabera, P., Pullerits, T., Stepanov, A., Wolf, J.-P. & Sundström, V. Organometal Halide Perovskite Solar Cell Materials Rationalized: Ultrafast Charge Generation, High and Microsecond-Long Balanced Mobilities, and Slow Recombination. *Journal of the American Chemical Society* **136**, 5189–5192 (2014).
38. Ishida, N., Wakamiya, A. & Saeki, A. Quantifying Hole Transfer Yield from Perovskite to Polymer Layer: Statistical Correlation of Solar Cell Outputs with Kinetic and Energetic Properties. *ACS Photonics* **3**, 1678–1688 (2016).
39. Savenije, T. J., Kroeze, J. E., Wienk, M. M., Kroon, J. M. & Warman, J. M. Mobility and Decay Kinetics of Charge Carriers in Photoexcited PCBM/PPV Blends. *Physical Review B* **69**, 155205 (2004).
40. Reid, O. G., Malik, J. A. N., Latini, G., Dayal, S., Kopidakis, N., Silva, C., Stingelin, N. & Rumbles, G. The Influence of Solid-State Microstructure on the Origin and Yield of Long-Lived Photogenerated Charge in Neat Semiconducting Polymers. *Journal of Polymer Science Part B: Polymer Physics* **50**, 27–37 (2012).
41. Savenije, T. J., Kroeze, J. E., Yang, X. & Loos, J. The Formation of Crystalline P3HT Fibrils upon Annealing of a PCBM:P3HT Bulk Heterojunction. *Thin Solid Films. EMSR 2005 - Proceedings of Symposium F on Thin Film and Nanostructured Materials for Photovoltaics* **511**, 2–6 (2006).
42. Saeki, A., Tsuji, M. & Seki, S. Direct Evaluation of Intrinsic Optoelectronic Performance of Organic Photovoltaic Cells with Minimizing Impurity and Degradation Effects. *Advanced Energy Materials* **1**, 661–669 (2011).
43. Milot, R. L., Sutton, R. J., Eperon, G. E., Haghighirad, A. A., Martinez Hardigree, J., Miranda, L., Snaith, H. J., Johnston, M. B. & Herz, L. M. Charge-Carrier Dynamics in 2D Hybrid Metal-Halide Perovskites. *Nano Letters* **16**, 7001–7007 (2016).
44. Savenije, T. J., Ferguson, A. J., Kopidakis, N. & Rumbles, G. Revealing the Dynamics of Charge Carriers in Polymer:Fullerene Blends Using Photoinduced Time-Resolved Microwave Conductivity. *The Journal of Physical Chemistry C* **117**, 24085–24103 (2013).
45. Herz, L. M. Charge-Carrier Mobilities in Metal Halide Perovskites: Fundamental Mechanisms and Limits. *ACS Energy Letters* **2**, 1539–1548 (2017).
46. Johnston, M. B. & Herz, L. M. Hybrid Perovskites for Photovoltaics: Charge-Carrier Recombination, Diffusion, and Radiative Efficiencies. *Accounts of Chemical Research* **49**, 146–154 (2016).

47. Wehrenfennig, C., Eperon, G. E., Johnston, M. B., Snaith, H. J. & Herz, L. M. High Charge Carrier Mobilities and Lifetimes in Organolead Trihalide Perovskites. *Advanced Materials* **26**, 1584–1589 (2014).
48. Labram, J. G. & Chabinyc, M. L. Recombination at High Carrier Density in Methylammonium Lead Iodide Studied Using Time-Resolved Microwave Conductivity. *Journal of Applied Physics* **122**, 065501 (2017).
49. Labram, J. G., Venkatesan, N. R., Takacs, C. J., Evans, H. A., Perry, E. E., Wudl, F. & Chabinyc, M. L. Charge Transport in a Two-Dimensional Hybrid Metal Halide Thiocyanate Compound. *Journal of Materials Chemistry C* **5**, 5930–5938 (2017).
50. Stranks, S. D., Eperon, G. E., Grancini, G., Menelaou, C., Alcocer, M. J. P., Leijtens, T., Herz, L. M., Petrozza, A. & Snaith, H. J. Electron-Hole Diffusion Lengths Exceeding 1 Micrometer in an Organometal Trihalide Perovskite Absorber. *Science* **342**, 341–344 (2013).
51. Yamada, Y., Yamada, T., Phuong, L. Q., Maruyama, N., Nishimura, H., Wakamiya, A., Murata, Y. & Kanemitsu, Y. Dynamic Optical Properties of $\text{CH}_3\text{NH}_3\text{PbI}_3$ Single Crystals As Revealed by One- and Two-Photon Excited Photoluminescence Measurements. *Journal of the American Chemical Society* **137**, 10456–10459 (2015).
52. D’innocenzo, V., Grancini, G., Alcocer, M. J. P., Kandada, A. R. S., Stranks, S. D., Lee, M. M., Lanzani, G., Snaith, H. J. & Petrozza, A. Excitons versus Free Charges in Organo-Lead Tri-Halide Perovskites. *Nature Communications* **5**, 3586 (2014).
53. Milot, R. L., Eperon, G. E., Snaith, H. J., Johnston, M. B. & Herz, L. M. Temperature-Dependent Charge-Carrier Dynamics in $\text{CH}_3\text{NH}_3\text{PbI}_3$ Perovskite Thin Films. *Advanced Functional Materials* **25**, 6218–6227 (2015).
54. de Quilettes, D. W., Vorpahl, S. M., Stranks, S. D., Nagaoka, H., Eperon, G. E., Ziffer, M. E., Snaith, H. J. & Ginger, D. S. Impact of Microstructure on Local Carrier Lifetime in Perovskite Solar Cells. *Science* **348**, 683–686 (2015).
55. Saba, M., Cadelano, M., Marongiu, D., Chen, F., Sarritzu, V., Sestu, N., Figus, C., Aresti, M., Piras, R., Lehmann, A. G., Cannas, C., Musinu, A., Quochi, F., Mura, A. & Bongiovanni, G. Correlated Electron–Hole Plasma in Organometal Perovskites. *Nature Communications* **5**, 6049 (2014).
56. Xing, G., Mathews, N., Sun, S., Lim, S. S., Lam, Y. M., Grätzel, M., Mhaisalkar, S. & Sum, T. C. Long-Range Balanced Electron- and Hole-Transport Lengths in Organic-Inorganic $\text{CH}_3\text{NH}_3\text{PbI}_3$. *Science* **342**, 344–347 (2013).
57. Nie, W., Tsai, H., Asadpour, R., Blancon, J.-C., Neukirch, A. J., Gupta, G., Crochet, J. J., Chhowalla, M., Tretiak, S., Alam, M. A., Wang, H.-L. & Mohite, A. D. High-Efficiency Solution-Processed Perovskite Solar Cells with Millimeter-Scale Grains. *Science* **347**, 522–525 (2015).

58. Guo, Z., Manser, J. S., Wan, Y., Kamat, P. V. & Huang, L. Spatial and Temporal Imaging of Long-Range Charge Transport in Perovskite Thin Films by Ultrafast Microscopy. *Nature Communications* **6**, 8471 (2015).
59. Manser, J. S. & Kamat, P. V. Band Filling with Free Charge Carriers in Organometal Halide Perovskites. *Nature Photonics* **8**, 737–743 (2014).
60. Reid, O. G., Yang, M., Kopidakis, N., Zhu, K. & Rumbles, G. Grain-Size-Limited Mobility in Methylammonium Lead Iodide Perovskite Thin Films. *ACS Energy Letters* **1**, 561–565 (2016).
61. Chen, Y., Sun, Y., Peng, J., Zhang, W., Su, X., Zheng, K., Pullerits, T. & Liang, Z. Tailoring Organic Cation of 2D Air-Stable Organometal Halide Perovskites for Highly Efficient Planar Solar Cells. *Advanced Energy Materials* **7**, 1700162 (2017).
62. Bi, Y., Hutter, E. M., Fang, Y., Dong, Q., Huang, J. & Savenije, T. J. Charge Carrier Lifetimes Exceeding 15 μs in Methylammonium Lead Iodide Single Crystals. *The Journal of Physical Chemistry Letters* **7**, 923–928 (2016).
63. Younts, R., Duan, H.-S., Gautam, B., Saparov, B., Liu, J., Mongin, C., Castellano, F. N., Mitzi, D. B. & Gundogdu, K. Efficient Generation of Long-Lived Triplet Excitons in 2D Hybrid Perovskite. *Advanced Materials* **29**, 1604278 (2017).
64. Tang, G., Yang, C., Stroppa, A., Fang, D. & Hong, J. Revealing the Role of Thiocyanate Anion in Layered Hybrid Halide Perovskite $(\text{CH}_3\text{NH}_3)_2\text{Pb}(\text{SCN})_2\text{I}_2$. *The Journal of Chemical Physics* **146**, 224702 (2017).

Chapter 5

Phase Intergrowth and Structural Defects in Organic Metal Halide Ruddlesden–Popper Thin Films

5.1 Abstract

Organic metal halide Ruddlesden–Popper layered perovskite phases combine the excellent optoelectronic properties of three-dimensional, bulk hybrid perovskites with superior material stability under ambient conditions. However, the thin film structure of these layered perovskites is still poorly understood, as phase purity is typically determined solely by specular X-ray diffraction. The thin film structure of these Ruddlesden–Popper phases was examined by increasingly local characterization techniques. From the comparison of grazing-incidence wide-angle X-ray scattering patterns of cast films to the expected scattering from single-crystal structures, significant in-plane disorder was observed. Spatially localized photoluminescence measurements show that films do not phase separate on the micrometer scale. Selected area electron diffraction measurements show the intergrowth

of different phases within the same thin film, consistent with previous observations seen in epitaxially grown Ruddlesden–Popper complex oxides. Despite the presence of phase impurities that would typically be detrimental for device performance, fits to photothermal deflection spectroscopy measurements show relatively low Urbach energies of 33 meV for $(\text{C}_4\text{H}_9\text{NH}_3)_2(\text{CH}_3\text{NH}_3)_2\text{Pb}_3\text{I}_{10}$ and 32 meV for $(\text{C}_4\text{H}_9\text{NH}_3)_2(\text{CH}_3\text{NH}_3)_3\text{Pb}_4\text{I}_{13}$, indicating that the electronic properties are insensitive to the phase impurities.

5.2 Introduction

Hybrid halide perovskites have shown great promise as cost-effective, solution-processable semiconductors because of their remarkable optoelectronic properties.^{1–7} Although they possess modest carrier mobilities in comparison to those of other inorganic semiconductors, hybrid perovskites have significantly long carrier lifetimes,^{8,9} the origin of which is still highly debated.^{10–14} The power conversion efficiencies of laboratory-scale solar cells made with mixed cation and anion perovskite alloys have reached values near 23%,¹⁵ making perovskites competitive with existing, established thin film solar cell technologies.¹⁶ More recently, perovskite alloys have also been found to have desirable emission properties, ranging from monochromatic light for light-emitting diode (LED) applications,^{17–19} to broadband white light emission.^{20–22} The stability of perovskite-based absorbers in the ambient environment is still a major concern, because degradation from moisture and heat is extremely detrimental to device performance.^{23–25}

To improve the environmental stability of perovskites, great research efforts have been put into Ruddlesden–Popper phases, layered analogues of the three-dimensional perovskite structure.^{26,27} Extensively studied in the field of complex oxides,^{28,29} Ruddlesden–Popper phases have an overall stoichiometry of $\text{A}'_2\text{A}_{n-1}\text{B}_n\text{X}_{3n+1}$, where n defines the size of the perovskite-like sheets that are spatially separated by the A' moieties. Formation of these

phases has been achieved in hybrid perovskites through the use of a large organic (typically alkylammonium) cation as a spacer.³⁰ These spacer cations have also been utilized to produce single-crystal perovskite nanoparticles and nanoplatelets, which, because of their increased quantum confinement and phase purity, have narrow emission line widths with large ($\sim 90\%$) photoluminescence quantum efficiencies.³¹⁻³³ Photovoltaic devices employing Ruddlesden–Popper phases have shown increases in their lifetimes relative to those of their three-dimensional counterparts.^{34,35} However, the thin film structures of these layered perovskite films are poorly understood. Previous studies suggested that the layered hybrid halide thin films naturally form highly crystalline, oriented domains upon spin coating, but optical and electronic transport measurements appear to show high defect densities that contribute to high recombination rates.^{36,37} A thorough understanding of crystalline structure within these thin films should lead to improvements in the performance of optoelectronic devices.

In this study, we characterized the thin film structure of the $n = 3$ and 4 Ruddlesden–Popper phases butylammonium methylammonium lead iodide, $(\text{C}_4\text{H}_9\text{NH}_3)_2(\text{CH}_3\text{NH}_3)_{n-1}\text{Pb}_n\text{I}_{3n+1}$, over varying length scales. Grazing-incidence X-ray scattering measurements were used to probe the average composition of thin films. Micrometer-scale structure was then evaluated by analyzing spatially resolved photoluminescence maps. Transmission electron microscopy (TEM) was then used to deduce the nanoscale, local structure. Using all of the structural characterization techniques, a generalized structure for Ruddlesden–Popper thin films was proposed. Finally, the impact of film structure on electronic properties was assessed by measuring the absorption coefficient with photothermal deflection spectroscopy (PDS) and fitting the absorption edges to extract the Urbach energies.

5.3 Results and Discussion

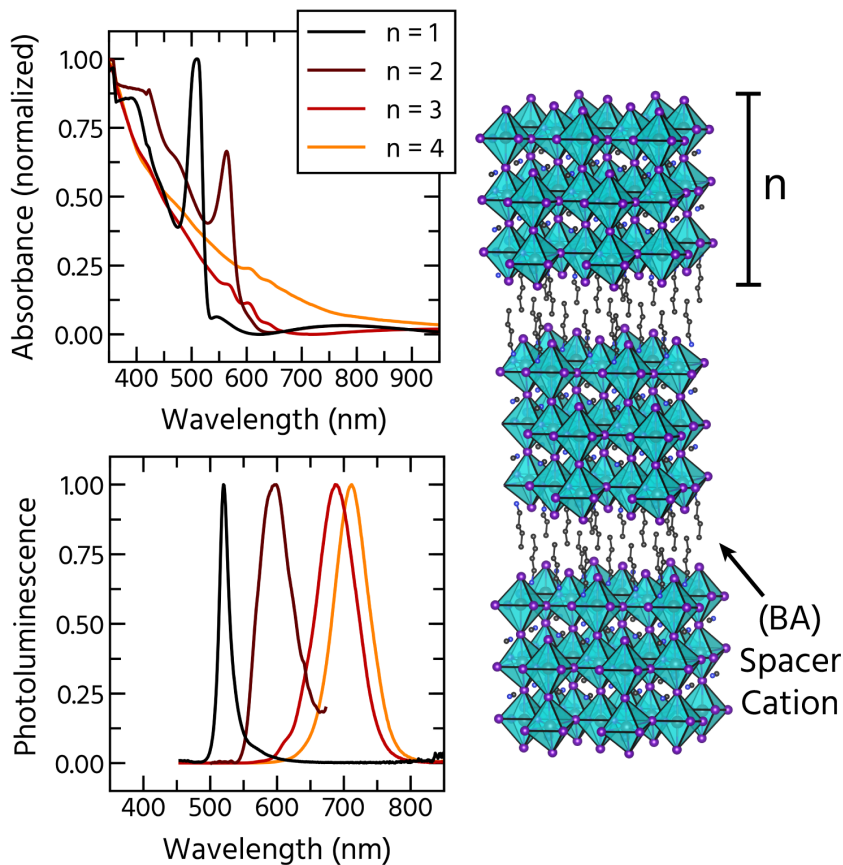


Figure 5.1: Normalized optical absorbance and photoluminescence for thin films of Ruddlesden–Popper phases with $n = 1–4$, illustrating rapid red-shifting of the emission peak and a vanishing excitonic absorption onset. A schematic of general Ruddlesden–Popper crystal structure with n values is shown on the right.

To study the structure of mixed butylammonium/methylammonium (BA/MA) Ruddlesden–Popper thin films, samples were cast from solutions in *N,N*-dimethylformamide (DMF) by spin-coating onto cleaned, z-cut quartz substrates. Further details of growth conditions are presented in Section 5.5.1. Previous studies have utilized a hotcasting technique,^{34,38–40} in which the substrate is heated prior to spinning; however, all samples here were deposited and annealed after spinning, consistent with our previous study.³⁶ A schematic depicting the general hybrid halide Ruddlesden–Popper

structure (with n -butylammonium spacers), along with absorbance and emission data, is shown in Figure 5.1. The exact absorption edges in the $n = 3$ and 4 films are difficult to discern because of scattering of long wavelength light in the measurement. The optical properties of these thin films suggest a rapid convergence to the absorbance and emission of the three-dimensionally connected MAPbI₃ for values of $n > 2$, despite the expected quantum confinement from the thickness of the lead iodide layers in the structure; in the $n = 4$ phase, the inorganic layers within the structure are only approximately 2.5 nm thick. The results in Figure 5.1 are consistent with previously reported spectra for solution-cast thin films.^{36,38} Because measurements of exfoliated single crystals clearly show excitonic effects and expected changes in emission with n , the origin of this optical behavior in thin films is still not well understood and has been attributed to defects at the edges of crystals.³⁸

To characterize bulk thin film structure in the $n = 3$ and 4 phases, grazing-incidence wide-angle X-ray scattering (GIWAXS) images of Ruddlesden–Popper thin films were collected and quantitatively analyzed. By utilizing a shallow incidence angle (schematic in Figure 5.2a), scattering from the underlying substrate is eliminated. Additionally, collection of the signal by an image plate detector allows for rapid reciprocal space mapping (RSM), a technique often used on inorganic semiconductors to measure strain and lattice mismatch.^{41,42} Most importantly, the in-plane and off-specular diffraction peaks provide information about misorientation and thin film structure. GIWAXS images for (BA)₂(MA)₂Pb₃I₁₀ and (BA)₂(MA)₃Pb₄I₁₃ are presented in panels c and d of Figure 5.2, respectively. Because of the fixed angle of incidence, the projection of the scattering cones onto a planar detector results in the loss of specular information, which is represented by the missing wedge of intensity along q_z , the out-of-plane scattering vector. These GIWAXS images can therefore be used in conjunction with the specular XRD patterns (Figure 5.8) to map reciprocal space.

To determine whether obtained X-ray scattering patterns match expected structure, GI-

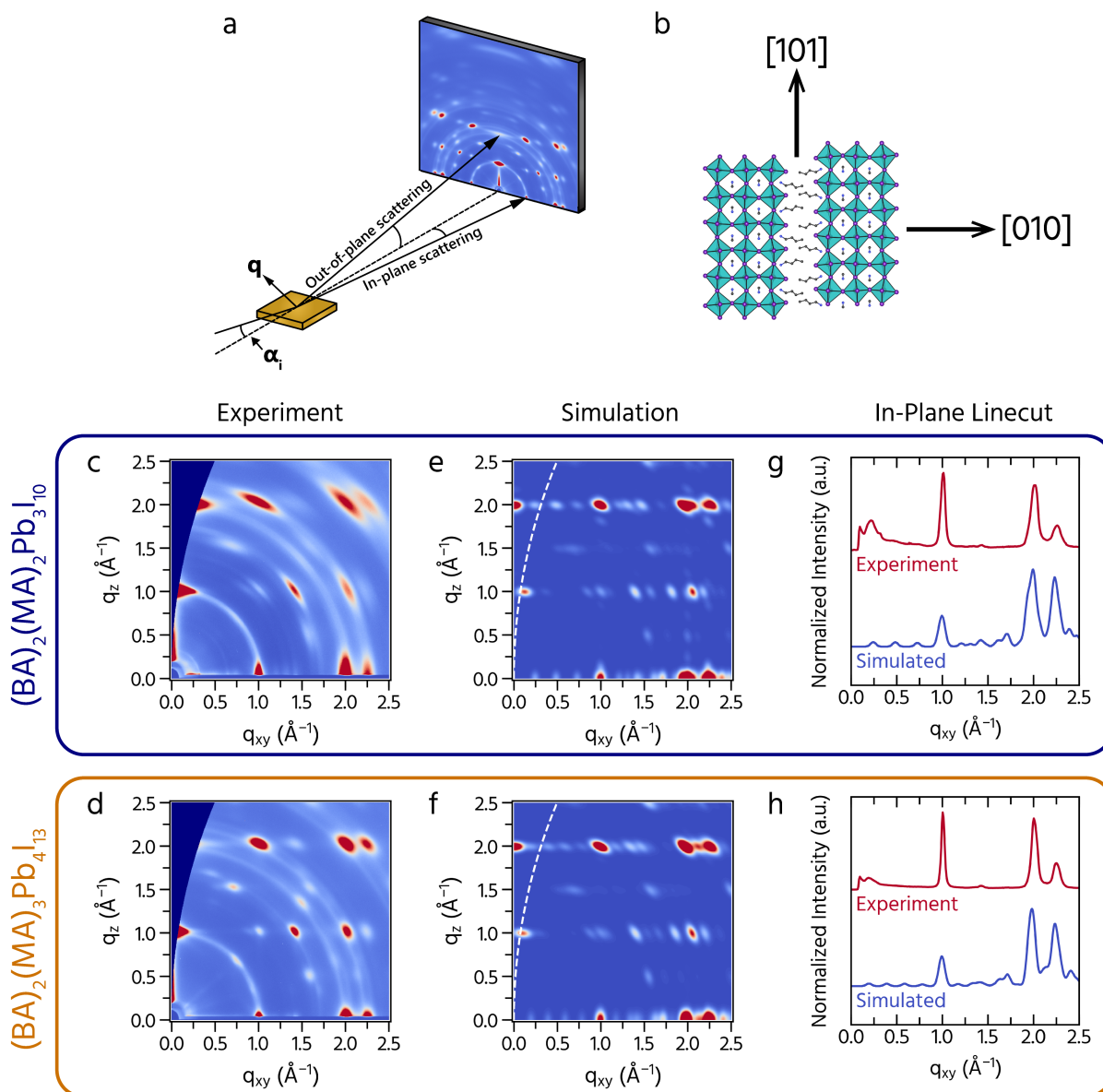


Figure 5.2: (a) Schematic of the grazing-incidence wide-angle X-ray scattering (GIWAXS) experimental setup with an image plate detector, where α_i represents the fixed, incidence angle. (b) Representative crystal structure of hybrid Ruddlesden–Popper phases ($n = 3$), showing important crystallographic directions. (c and d) Experimentally collected and (e and f) simulated GIWAXS patterns (with peak broadening based on experimental results) of $(\text{BA})_2(\text{MA})_2\text{Pb}_3\text{I}_{10}$ and $(\text{BA})_2(\text{MA})_3\text{Pb}_4\text{I}_{13}$, respectively, along with (g and h) line cuts of scattering intensity along the q_{xy} axis.

WAXS patterns were simulated and are shown in panels e and f of Figure 5.2. Peak positions were determined from previously determined single-crystal structures,⁴³ and the intensi-

ties of peaks were set to the square of the structure factor ($I_{hkl} = |F_{hkl}^2|$) for a particular lattice plane. Detailed descriptions of simulated calculations are provided in the Appendix section 5.5.3. Additionally, peak broadening from crystals in the films was introduced to match experimental results; unbroadened patterns from a perfect crystal are presented in the Appendix section 5.5.4. For films exhibiting a mixture of crystalline textures, final simulated images were calculated as a linear combination of GIWAXS images corresponding to each preferred orientation direction, weighted by the associated texture fraction.

The Ruddlesden–Popper phases show differing structural disorder based on the value of n . The experimental $n = 3$ and 4 GIWAXS patterns presented here are consistent with measurements in the literature on the same system.^{34,44} For comparison, measured and simulated GIWAXS patterns of the pure $n = 1$ phase are shown in the Appendix section 5.5.5, displaying agreement between the two images. However, in the $n = 3$ and 4 phases, it appears that many reflections are missing in the experimental patterns, noticeably along the q_{xy} direction at fixed values of q_z . To better understand the origin of these missing peaks, the schematic in Figure 5.2b illustrated important crystallographic directions in the structure of these Ruddlesden–Popper phases. Previous diffraction measurements have shown that the majority of the $(\text{BA})_2(\text{MA})_2\text{Pb}_3\text{I}_{10}$ and $(\text{BA})_2(\text{MA})_3\text{Pb}_4\text{I}_{13}$ align along the [101] crystallographic direction or with lead iodide sheets oriented perpendicular to the substrate.^{34,36} This implies that the measured in-plane scattering is primarily due to Bragg reflections along the [010] direction, or b axis, corresponding to the direction along which lead iodide sheets stack in the crystal structure. The presence of strong scattering peaks at both $q_{xy} = 1.0 \text{ \AA}^{-1}$ and $q_{xy} = 2.0 \text{ \AA}^{-1}$ is consistent with those in the simulated patterns; however, the less intense $0k0$ peaks that are missing in the experimental pattern should be observable considering the intensity of the visible peaks.

To make these absences easier to observe, line cuts of the in-plane scattering intensity were taken for both the experimental and simulated patterns and are shown in panels g

and h of Figure 5.2. The large spike in intensity near $q_{xy} = 0$ in the experimental pattern is due to beamstop scattering. Comparison of the expected and collected diffraction line cuts confirms the in-plane disorder seen in the two-dimensional scattering patterns, suggestive of defects in the perovskite layer stacking, possibly because of stacking faults. Quantitative fits of the scattering peaks are difficult for these thin films because broadening from crystallites causes many of the scattering peaks to overlap with each other. For the purpose of analysis, the full width at half-maximum (fwhm) of the in-plane peak at $q_{xy} = 1.0 \text{ \AA}^{-1}$ is taken as a combination of two peaks as shown in the Appendix section 5.5.6. The scattering peak at this location was chosen as the ideal candidate for fitting as it results from the overlap of only two peaks, unlike other strong reflections that results from the overlap of three or more (Figure 5.11). Fits of the peaks show an approximate fwhm value of 0.03 \AA^{-1} for both $n = 3$ and 4 , indicating a minimum lateral domain size of 20.9 nm from Scherrer broadening based on our sample size and detector resolution.

Determination of the phase purity in thin films of Ruddlesden–Popper compounds from GIWAXS is also difficult because of overlap between peaks from different phases. The issue is clear from the simulated GIWAXS pattern of three-dimensional MAPbI_3 (Figure 5.13) that shows overlap in this strong diffraction peaks with those in the layered phases due to the similarity in structure. Additionally, because of the similarities in the value of the a and c lattice constants in all phases, indexing of peaks with components along the b axis becomes the only method for clearly distinguishing between the different phases by diffraction. The similarity of the lattice constants makes it difficult to identify phases with larger n values in a dominantly lower n sample. Measurements at very small diffraction angles may make the differences in reflections from the layer stacking distance more apparent; however, disorder-induced peak broadening makes this challenging as in-plane peaks fade into the background. Previous work explored the growth kinetics of Ruddlesden–Popper thin films from solution, showing characteristic diffraction peaks associated with the differ-

ent n values.^{45,46} If the phase fractions of the impurities are small, it still makes it difficult to identify in the final thin film. Therefore, X-ray scattering cannot be solely used as the means of assessing phase purity of lead iodide-based layered perovskite thin films.

Because X-ray scattering provides only a measure of the average thin film structure, we used a combination of optical microscopy and spatially resolved photoluminescence measurements to observe the micrometer-scale structure and determined that there is no phase separation on this length scale. Panels a and b of Figure 5.3 show transmission optical microscope images of $n = 3$ and 4 thin films, respectively, illustrating distinct film morphologies. The $n = 3$ film appears to possess a higher concentration of smaller grains (~ 500 nm), while the $n = 4$ film has more slender grains ($2\text{--}3\ \mu\text{m}$) in a larger matrix of smaller (~ 500 nm) grains. To quantitatively characterize the structure, we measured the spatial dependence of the photoluminescence. Using a custom-built setup (described in Section 5.5.1), the localized emission from 72 square subregions each $7\ \mu\text{m} \times 7\ \mu\text{m}$ in size (optical microscope images show a fraction of the total area) was measured. These spatial emission measurements are presented in panels b and c of Figure 5.3, where the average photoluminescence spectrum based on the emission from all 72 regions is shown along with the peak emission energies for both films. The average photoluminescence spectra are consistent with bulk steady-state emission measurements on films (shown in Figure 5.1), also confirmed by taking the difference between the normalized steady-state spectrum and the average spectrum, shown in Figure 5.14. The shoulders in the emission spectra also suggest local compositional deviations that cannot be clearly resolved by this technique. In both cases, the peak emission energies of our thin films are blue-shifted by 90 meV in $n = 3$ films and 40 meV in $n = 4$ films from those presented in the earlier study,³⁸ in which both $n = 3$ and 4 films emit at 1.7 eV. Despite this discrepancy, which could be attributed to not using a hot-casting process to form the films, the diffraction patterns (both specular and GIWAXS) are consistent with previous studies utilizing hot-casting,^{34,44} so we are confident

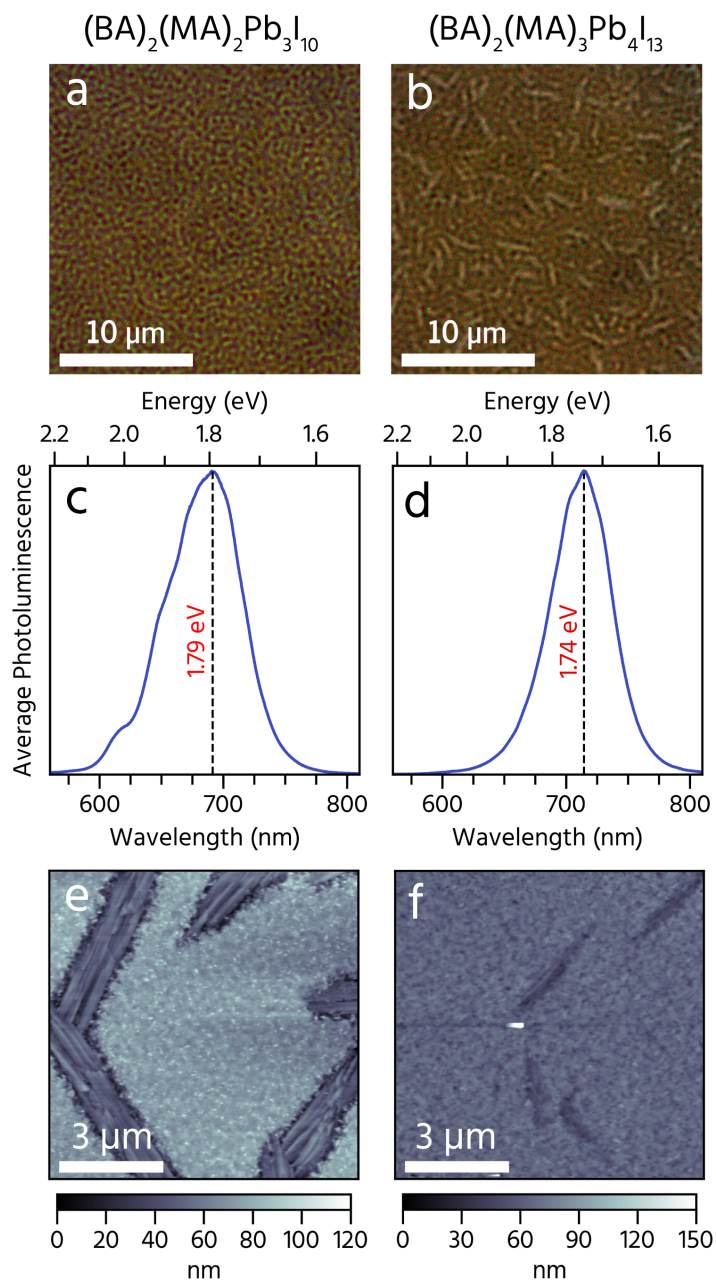


Figure 5.3: (a and b) Optical microscope images, (c and d) average of spatial photoluminescence spectra and peak energies, and (e and f) atomic force microscope (AFM) micrographs of thin films of $(\text{BA})_2(\text{MA})_2\text{Pb}_3\text{I}_{10}$ and $(\text{BA})_2(\text{MA})_3\text{Pb}_4\text{I}_{13}$, respectively. Spatial photoluminescence spectra were collected by measuring local emission of 72 regions each $7\ \mu\text{m} \times 7\ \mu\text{m}$ in size. Average emission spectra match those from steady-state photoluminescence measurements. AFM micrographs are also consistent with previous measurements.

our thin films are structurally similar over the length scale of these optical measurements. Additionally, fitting the emission profiles to Gaussian functions (Appendix section 5.5.9) shows that although the overall fwhm of the $n = 3$ film appears larger than that of the $n = 4$ film, when decomposed into contributions from different emitters, the fwhm's of the thin film states are nearly equal (0.14 eV in the $n = 3$ film and 0.15 eV in the $n = 4$ film). Finally, atomic force microscope (AFM) micrographs of the two films are presented in panels e and f of Figure 5.3, illustrating microscale morphologies consistent with previously reported measurements.³⁶ The micrometer-scale spatial photoluminescence measurements therefore show no clearly resolved phase separation in the Ruddlesden–Popper thin films.

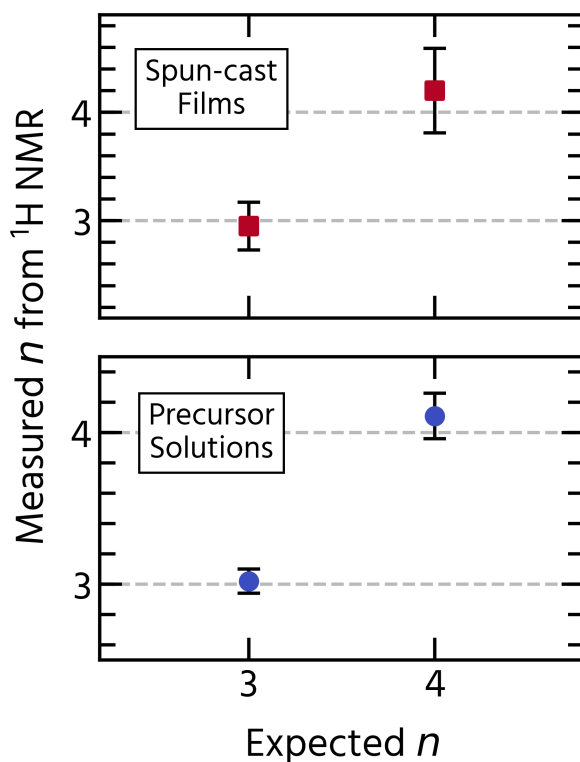


Figure 5.4: Experimentally measured n values of precursor solutions and spin-cast thin films of $(\text{BA})_2(\text{MA})_2\text{Pb}_3\text{I}_{10}$ ($n = 3$) and $(\text{BA})_2(\text{MA})_3\text{Pb}_4\text{I}_{13}$ ($n = 4$) from results of ^1H nuclear magnetic resonance (NMR). Error bars were determined by the standard deviation based on comparison of signals from different BA and MA protons.

The ambiguity in assessing phase purity from X-ray scattering and spatial emission mea-

measurements motivated the need to determine the effective stoichiometry of the final thin films. ^1H nuclear magnetic resonance (NMR) spectra were collected for both the precursor solutions and deposited films (Appendix section 5.5.11), a technique that has been previously used to assess the actual stoichiometry of perovskite thin films.^{47,48} NMR spectra for the spin-coated films were obtained by scraping off material from the substrate with a razor blade and dissolving the material into deuterated dimethyl sulfoxide ($\text{DMSO-}d_6$). Analysis of the integrations of characteristic NMR peaks results in a measured stoichiometry of $n = 2.95 \pm 0.22$ for the $n = 3$ film and $n = 4.20 \pm 0.39$ for the $n = 4$ film (Figure 5.4), so we are confident that on average, stoichiometrically, our thin films are representative of the specific layered phases. However, because some off-stoichiometric values of n are within error of our measurement, it is possible that defects of smaller and larger n values exist within our films, an assertion that has previously been suggested for phenethylammonium-based Ruddlesden–Popper halides.⁴⁹ Additionally, because the spacer cation is limiting to the formation of these structures, inclusions of bulk methylammonium lead iodide ($I4/mcm$ at room temperature⁵⁰) are possible when butylammonium is undersupplied.

The nanometer-scale structure of the Ruddlesden–Popper thin films was characterized by TEM and suggests that films contain inclusions of different n values and three-dimensional methylammonium lead iodide. To ensure consistency in the growth kinetics for TEM samples and to avoid introducing defects from utilizing a focused ion beam (FIB), we used a transfer process to examine the composition (Figure 5.5a). The precursor solution was first spun onto z-cut quartz substrates, and the resulting films were then annealed and scraped off using a razor blade. These flakes were deposited onto TEM grids for electron microscopy measurements, similar to methods used in previous studies.^{51,52} Because this scraping method does not quantitatively preserve out-of-plane crystalline texturing, we focused only on the composition of the films on a local scale rather than on the texture. Real space TEM micrographs along with inset selected area electron diffraction (SAED)

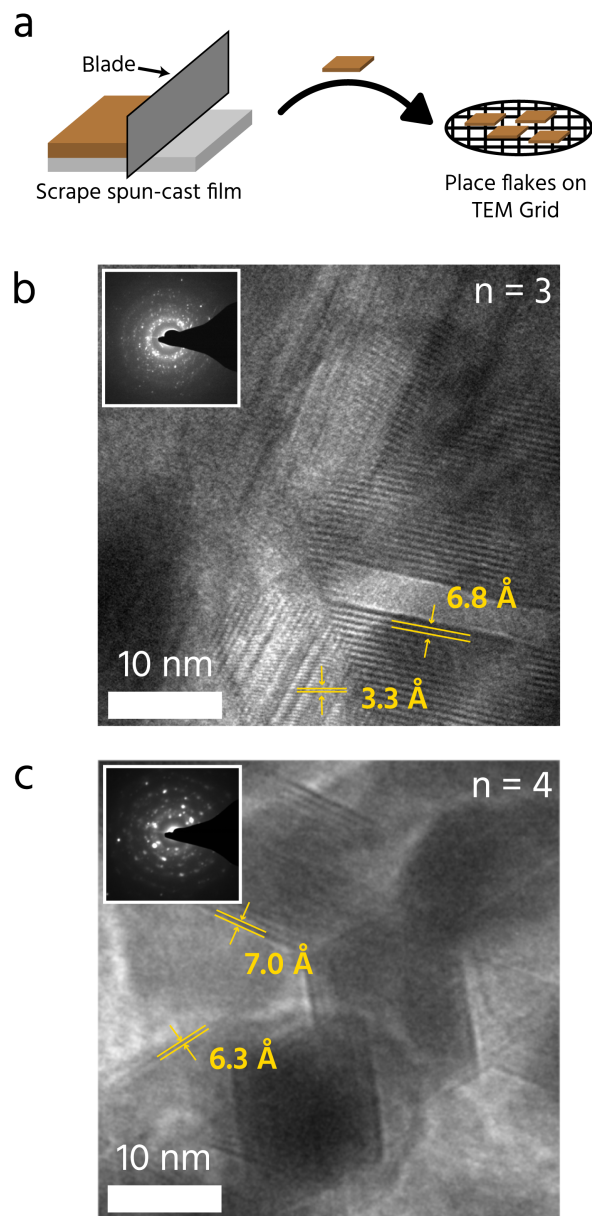


Figure 5.5: (a) Schematic illustrating sample preparation for transmission electron microscopy (TEM) measurements of Ruddlesden–Popper thin films and real space TEM micrographs of (b) $(\text{BA})_2(\text{MA})_2\text{Pb}_3\text{I}_{10}$ ($n = 3$) and (c) $(\text{BA})_2(\text{MA})_3\text{Pb}_4\text{I}_{13}$ ($n = 4$), with selected area electron diffraction (SAED) patterns shown as insets. Distinct lattice fringe spacings are indicated on real space micrographs.

patterns for thin films of the $n = 3$ and 4 phases are shown in panels b and c of Figure 5.5. The spacing of distinct sets of lattice fringes is labeled in the real space micrographs.

In the $n = 3$ film, the measured d spacing of 6.8 Å is within error of the 0 4 0 reflection of $(\text{BA})_2\text{PbI}_4$ (6.91 Å), while 3.3 Å is very similar to the spacing of the strong reflections 0 12 0 (3.28 Å), 0 16 0 (3.25 Å), and 0 20 0 (3.22 Å) in $(\text{BA})_2\text{MAPb}_2\text{I}_7$, $(\text{BA})_2(\text{MA})_2\text{Pb}_3\text{I}_{10}$, and $(\text{BA})_2(\text{MA})_3\text{Pb}_4\text{I}_{13}$, respectively. Similarly, in the $n = 4$ film, there are characteristic d spacings of different phases. The 7.0 Å spacing is again similar to that of 0 4 0 in $(\text{BA})_2\text{PbI}_4$, and 6.3 Å corresponds to the 1 1 1 reflections in $(\text{BA})_2\text{MAPb}_2\text{I}_7$ (6.22 Å), $(\text{BA})_2(\text{MA})_2\text{Pb}_3\text{I}_{10}$ (6.25 Å), and $(\text{BA})_2(\text{MA})_3\text{Pb}_4\text{I}_{13}$ (6.27 Å), as well as 1 1 0 in MAPbI_3 (6.25 Å). This mixed phase behavior is further confirmed from indexing the SAED patterns (Appendix section 5.5.12). Although distinct spots are visible, the diffraction patterns are fit with rings because solution growth from spin-coating results in thin films with fiber texture; there is a strong out-of-plane orientation, but crystallites are randomly rotated in-plane. Because the measured area for SAED is small, not enough grains are sampled to produce continuous rings of diffraction, but we would expect this to be true if a large area were measured. These results indicate that these films are certainly not phase pure at the nanoscale and that inclusions of lower- and higher-value Ruddlesden–Popper phases are clearly forming adjacent to each other. The defects seen from TEM are also not predominantly at the crystal edges, as suggested previously for measurements on exfoliated single-crystals.³⁸ Although these literature measurements are at a much larger length scale, the nanoscale defects are also consistent with the spatial photoluminescence. With majority [101] texturing, the surface of our thin films would be made up of the edges of the Pb–I sheets, so at small emission angles, we would expect primarily edge photoluminescence. However, the oil immersion objective in our instrument allows us to collect emission over large angles, and large contributions from the single-crystal emission energies (Section 5.5.10) are still not present. Increased emission at the edges of the exfoliated crystals could therefore be due to phase impurities introduced by mechanical damage from the exfoliation process. Finally, the diffuse rings of intensity seen in the SAED background can be attributed to some amount of

disordered phase in the films, consistent with the arcing of Bragg spots seen in GIWAXS images.

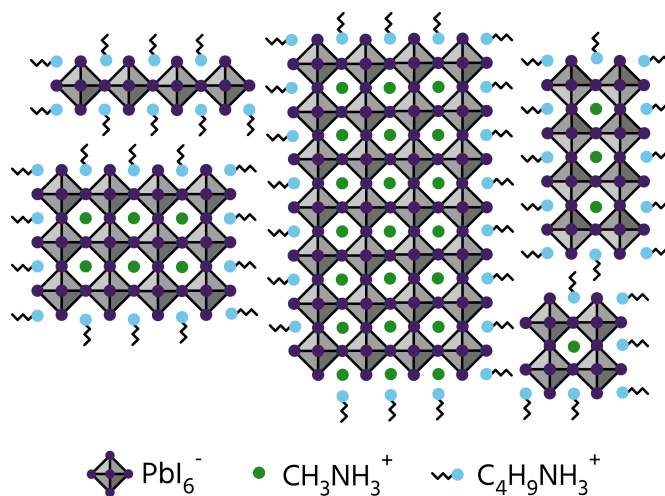


Figure 5.6: Schematic of the proposed morphology of Ruddlesden–Popper thin films, where regions appear to have structures corresponding to $n = 1 - 4$, as well as small inclusions that appear to be like nanoparticles of three-dimensional methylammonium lead iodide. Phase impurities are consistent with spatial photoluminescence and TEM, while the stacking faults are consistent with the missing in-plane peaks seen in GIWAXS.

A proposed general structure of the crystalline regions of the Ruddlesden–Popper thin films is shown in Figure 5.6 and contains regions that correspond to the $n = 1 - 4$ phases, along with areas that are like nanoparticles of bulk MAPbI_3 . This structure is a schematic of the film morphology that is consistent with both the local deviations seen in spatial photoluminescence measurements and the indexing of multiple phases from TEM. These defects are also in agreement with planar faults previously seen in epitaxially grown inorganic Ruddlesden–Popper oxides.^{53,54} Irregular packing of the different phases is also responsible for the missing in-plane diffraction peaks from GIWAXS, because inclusions of other phases limit the long-range order. Therefore, the in-plane Bragg reflections are broadened and fade into the background. The large amount of structural disorder suggests that devices fabricated with the films should not operate efficiently, so a measure of electronic disorder is useful for comparison.

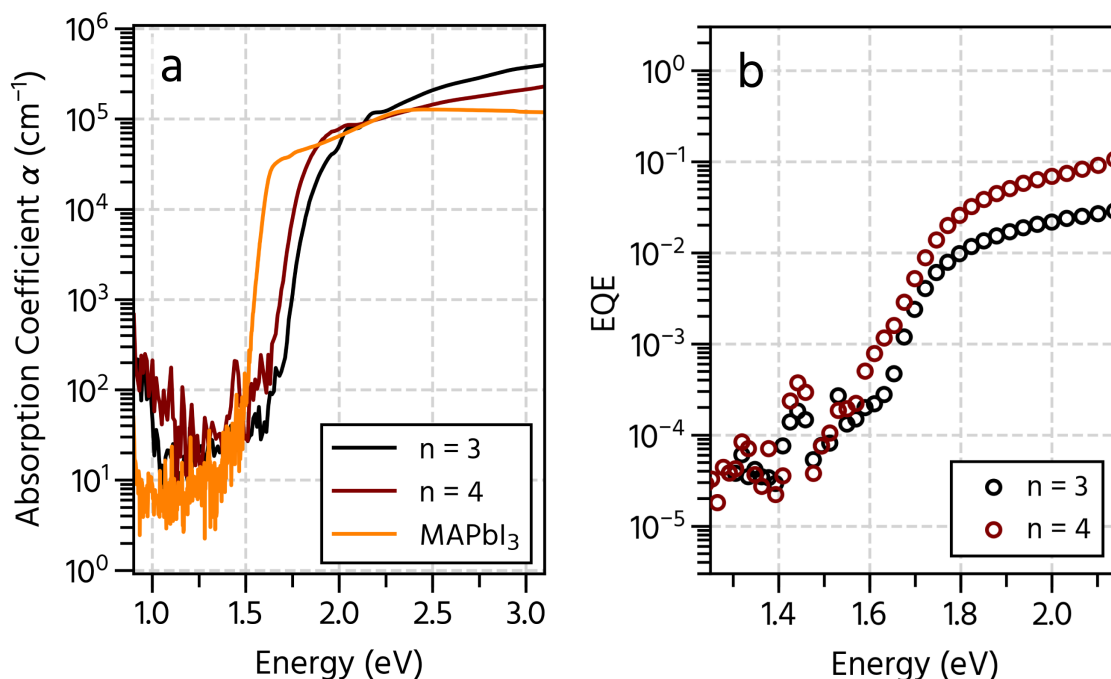


Figure 5.7: (a) Photothermal deflection spectroscopy (PDS) spectra of $n = 3$ and 4 Ruddlesden–Popper thin films, along with bulk methylammonium lead iodide, illustrating exponential tails at the absorption edges. (b) External quantum efficiency (EQE) spectra of devices fabricated with $n = 3$ and 4 thin films, also showing exponential tailing. Slopes of these tails are indicative of the Urbach energy and degree of electronic disorder, providing information about trap states at the band edges. The red-shifted EQE with respect to the PDS is due to the presence of MAPbI₃ nanoparticles which generate charge efficiently.

To assess the effect of structural defects and inhomogeneities on the electronic properties, high-resolution absorption spectra were collected using photothermal deflection spectroscopy (PDS) and suggest low electronic disorder in both $n = 3$ and 4 layered compounds. Because PDS uses localized heating to measure absorbance, it is nearly insensitive to scattering effects often seen in transmission measurements and therefore allows us to accurately measure low absorption coefficients over a wide magnitude range.^{55,56} PDS spectra of (BA)₂(MA)₂Pb₃I₁₀, (BA)₂(MA)₃Pb₄I₁₃, and bulk MAPbI₃ thin films are shown in Figure 5.7a. At the absorption onset, the slope of the exponential region called the Urbach tail is used as a metric to measure the amount of electronic and/or compositional disorder in semiconductors.⁵⁷ Optically accessible disorder in the density of states is captured in the

slope of the true absorption onset (Urbach tail); increased disorder results in a shallower onset and thus an increased Urbach disorder energy. Urbach tails were fit with exponentials and are shown in Section 5.5.13, giving an Urbach energy of 17 meV for MAPbI₃, consistent with the value of 15 meV previously measured by PDS.⁵⁸ Despite appreciable structural disorder, Urbach energies of the $n = 3$ and 4 Ruddlesden–Popper films are only 33 and 32 meV, respectively, values still indicative of a reasonably large degree of electronic order. For comparison with PDS results, photovoltaic devices were fabricated to measure the external quantum efficiency (EQE), shown in Figure 5.7b. Assuming efficient charge extraction at the band edge, the EQE spectrum of the device should match the absorbance of the active layer and can also be fit to extract the Urbach energy. In both $n = 3$ and 4 films, however, the EQE is red-shifted with respect to the PDS and Urbach energies are larger, with values of 46 and 41 meV, respectively (Appendix section 5.5.14).

The discrepancy between PDS and EQE measurements can be understood from the structural picture in Figure 5.6. Thin films are predominantly composed of the targeted n value phase; this composition is evident from both the distinct absorption edges in the optical data in Figure 5.1 and average n values from NMR measurements. Inclusions of higher n phases, because of their lower optical band gaps, would therefore act as funnels for photogenerated charge carriers. The transfer of excitons, or charge carriers, from smaller to larger n values has been observed in Ruddlesden–Popper thin films with a phenethylammonium spacer cation.^{18,48,59,60} Because TEM suggests the presence of nanoscale MAPbI₃ domains, excitations would eventually migrate to this phase during their lifetime prior to emission; this process is likely the cause of the red-shifted emission in thin films of $n = 3$ and 4. The difference in the peak positions of photoluminescence between $n = 3$ (1.8 eV) and $n = 4$ (1.74 eV) is likely from nanoscale confinement effects of the MAPbI₃ inclusions. This energy difference depends on the size of the nanoparticles, as increased quantum confinement effects blue-shift the emission. Because a larger amount of methylammonium is

supplied in the growth of the higher- n value phases, the nanoparticle domains of MAPbI₃ are on average larger in $n = 4$ films, explaining the lower-energy emission in comparison to that of $n = 3$ films. Measurements of PDS and EQE differ in that the former is sensitive to all absorbing species in a sample while the latter is dominated by the regions that generate charge efficiently from photoexcitation. In the PDS spectra presented in Figure 5.7, there is a low-intensity signal at 1.5 eV in both the $n = 3$ and 4 traces that corresponds to a small amount of absorbing MAPbI₃ moieties. The EQE measurements are therefore biased by the presence of these MAPbI₃ nanoparticles, resulting in a red-shifted absorption. Additionally, because of the irregular distribution of these nanoparticle domains in the film, more electronic disorder is expected and is captured in the shallower slopes of the Urbach tails from the EQE. Although the stand-alone thin film (PDS) and device (EQE) behavior could differ due to substrate effects, GIWAXS measurements of films spun on PEDOT:PSS (Figure 5.25) indicate that there is no appreciable structural variation between the neat thin films and those cast for device measurements. Therefore, it appears that device performance is highly dependent on the MAPbI₃ inclusions present. Furthermore, it is evident from the low Urbach energy values in PDS that the different perovskite phases present in the thin films are relatively well-isolated from each other.

5.4 Conclusion

In conclusion, the thin film structure of $n = 3$ and 4 Ruddlesden–Popper phases butylammonium methylammonium lead iodide, $(C_4H_9NH_3)_2(CH_3NH_3)_{n-1}Pb_nI_{3n+1}$, indicates significant structural disorder. GIWAXS shows a significant number of missing in-plane diffraction peaks, corresponding to disorder in the stacking of the lead iodide sheets. Additionally, micrometer-scale spatial mapping of photoluminescence shows no large-scale phase separation, with only small local deviations in emission energy. To understand the

source of disorder in scattering, the local structure was probed by transmission electron microscopy and shows the intergrowth of different Ruddlesden–Popper phases, as well as methylammonium lead iodide. Finally, the electronic disorder was assessed by photothermal deflection spectroscopy, showing low Urbach energies of 33 and 32 meV in $(\text{BA})_2(\text{MA})_2\text{Pb}_3\text{I}_{10}$ and $(\text{BA})_2(\text{MA})_3\text{Pb}_4\text{I}_{13}$, respectively. The large amount of structural disorder suggests that lead iodide domains are electronically isolated from each other. The results suggest that studies of devices, such as solar cells and LEDs, of Ruddlesden–Popper phases should account for the presence of multiple phases in the interpretation of their optoelectronic properties. Direct control over phase purity is therefore an essential goal for optimization of devices with layered perovskites.

5.5 Appendix

5.5.1 Experimental Methods

Perovskite and Ruddlesden–Popper Thin Film Preparation

Thin films of both the mixed methylammonium/butylammonium Ruddlesden–Popper phases and methylammonium lead iodide were prepared according to a previous study³⁶ and deposited on z-cut quartz substrates.

Specular X-Ray Diffraction

Specular X-ray diffraction (XRD) was measured on a Panalytical Empyrean powder diffractometer in reflection mode with a $\text{Cu-K}\alpha$ source, operating with an accelerating voltage of 45 kV and a beam current of 40 mA. Due to fiber-textured nature of spin-coated films, in which diffraction patterns are invariant to rotation, samples were rotated to increase the signal-to-noise ratio of collected patterns. All simulated specular diffraction

patterns were calculated using the General Structure Analysis System (GSAS), with a calibration file specific to our instrument and structure factors from previously solved crystal structures.^{43,61} For simulated patterns with preferred orientation, March–Dollase correction factors were utilized during calculation.⁶²

Grazing-Incidence Wide-Angle X-Ray Scattering

Grazing-incidence diffraction was measured at Stanford Synchrotron Radiation Lightsource (SSRL), on Experimental Station 11-3. The beamline is a 12.7 keV wiggler side-station equipped with a two-dimensional Rayonix MX225 CCD detector. Source-to-detector distances were calibrated using a standard sample of lanthanum hexaboride (LaB₆). All raw images were geometrically corrected using GIXSGUI.⁶³ Grazing-incidence angles were chosen based on previously-measured X-ray critical angles.³⁶

UV-Vis Spectroscopy

Films were deposited on z-cut quartz and absorption measurements were performed using a Shimadzu UV-2600 ultraviolet-visible spectrophotometer at room temperature in ambient conditions.

Photoluminescence Measurements

Films were deposited on z-cut quartz and photoluminescence measurements were carried out on a Horiba FluoroMax 4 spectrometer calibrated using Milli-Q water. Films were loaded into a thin film sample stage angled at 80° between the excitation and emission port. All measurements were performed with an excitation wavelength of 450 nm. In order to limit the effects of Rayleigh scattering at long wavelengths, a long-pass filter slightly above the excitation wavelength (455 nm) was placed in front of the emission port.

Spatial Photoluminescence Measurements

Spatially-resolved photoluminescence measurements were performed by focusing the 505 nm output of a fiber-coupled coherent white light source (NKT Photonics SuperK EXTREME) to the image plane at the rear port of a Nikon Ti-U inverted microscope. The excitation spot was optically coupled to the thin film samples through an oil-immersion objective (Nikon, 100x, NA 1.3, Plan Fluor) at normal incidence, producing a focal spot with a width of $\tilde{2} \mu\text{m}$. Various spots were excited by spatially translating the excitation point across the image plane, and thus the sample. The incident light was filtered via a 532 nm short-pass filter and reflected off a 532 nm dichroic to remove overlap with the emission wavelengths. Photoluminescence was collected through the same objective and transmitted through the same dichroic as well as a 532 nm long-pass filter. Total illumination intensities were kept below $1 \mu\text{W}$. Spectra were collected with an imaging spectrometer (Princeton Instruments IsoPlane SCT 320) with a 1.5 second integration time.

Atomic Force Microscope Measurements

Atomic force microscope (AFM) micrographs of thin films were collected with an Asylum Research MFP-3D Standard System in tapping mode. Films were deposited on z-cut quartz as previously described, the surface was cleaned with a pressurized N_2 gun, and measured in ambient pressure air.

^1H Nuclear Magnetic Resonance Measurements

The solution samples were prepared by collecting a $50 \mu\text{L}$ sample of precursor solution and evaporating the *N,N*-dimethylformamide (DMF) solvent, first by heating in a glovebox at 85°C for 10 minutes, and then pumping down on the precipitate under vacuum for 10 minutes. The precipitate was then re-dissolved in $650 \mu\text{L}$ of deuterated dimethylsulfoxide (DMSO-*d*6) and transferred to a 500 MHz NMR tube. To roughly compare the absolute

concentrations of precursors between samples, 10 μL of tetramethylsilane (TMS) was added to the sample solution. All ^1H nuclear magnetic resonance (NMR) spectra were obtained with a Bruker AVANCE500 spectrometer operating at 11.7 T (^1H Larmor frequency of 500.13 MHz). 1D ^1H spectra were acquired with a 30° pulse, 20.7 ppm spectral width and 5 second recycling time delay for a total acquisition time of about 20 minutes. Spectra were processed using the TopSpin software.

Transmission Electron Microscope Measurements

Ruddlesden–Popper perovskite films were deposited on z-cut quartz substrates as described above, and scraped onto TEM grids (Ted Pella No. 01824, ultrathin C film on holey carbon support film, 400 mesh, Cu) using a razor blade. Transmission electron microscopy (TEM) images were obtained using an FEI Tecnai G2 Sphera operating at 200keV.

Photothermal Deflection Spectroscopy Measurements

Photothermal deflection spectroscopy (PDS) measurements were performed on a home-built set-up described by Vandewal *et al.*^{64,65} Measurements were taken using a mechanically chopped (2Hz) monochromatic light source using both a 150 W Xenon and 100 W halogen pump lamp with 5nm spectral resolution focused onto the sample. Degassed and filtered perflourohexane (C_6F_{14} , 3M Flourinert FC-72) was used as the deflection medium. Thin films were made in a glovebox prepared *vide supra* by spincoating on quartz substrates in a nitrogen environment with sub-ppm levels of oxygen. The sample was aligned with maximal overlap between the pump beam and thin film. Samples were normalized for extinction above gap via procedure described previously.⁶⁶

External Quantum Efficiency Measurements

The external quantum efficiencies (EQEs) were analyzed using a fully computerized mea-

surement system consisting of a 300 W xenon lamp (Newport), a monochromator (Newport CS130), a chopper controller (Newport), two current preamplifiers (SRS SR570), and two lock-in amplifiers (SRS SR810).

5.5.2 Specular X-ray diffraction of thin films

Specular X-ray diffraction patterns were collected for the Ruddlesden–Popper thin films as described in Section 5.5.1 and are shown in Figure 5.8. Simulated isotropic and textured diffraction patterns were also produced as described in Section 5.5.1 and are shown for comparison.

5.5.3 Simulations of GIWAXS patterns

Grazing-incidence wide angle X-ray scattering (GIWAXS) patterns were simulated from previously solved crystal structures in literature.⁴³ Structure factors and d-spacings were exported using VESTA⁶⁷ and imported into a custom script written in Python. Peak positions in the q_{xy} – q_z plane were calculated assuming a fiber-texture geometry; due to in-plane rotational invariance in thin films, off-specular Bragg peaks become scattering cones, as illustrated in Figure 5.9 below. This in-plane rotational symmetry allows peak positions to be determined by calculating the angle between the normal (out-of-plane preferred orientation direction) and the desired scattering peak. The out-of-plane direction has been measured by specular diffraction in a previous study and was found to vary smoothly between [010] and [101] as the value of n increases.³⁶ In $n = 3$, 76% of domains are along [101] and 24% along [010], while for $n = 4$, 96% of domains are along [101] and 4% along [010]. For these mixed-texture films, a linear combination of simulated GIWAXS images along each preferred orientation direction was used for the final image.

To calculate peak positions, Equation 5.1 was used to find the angle between two lattice

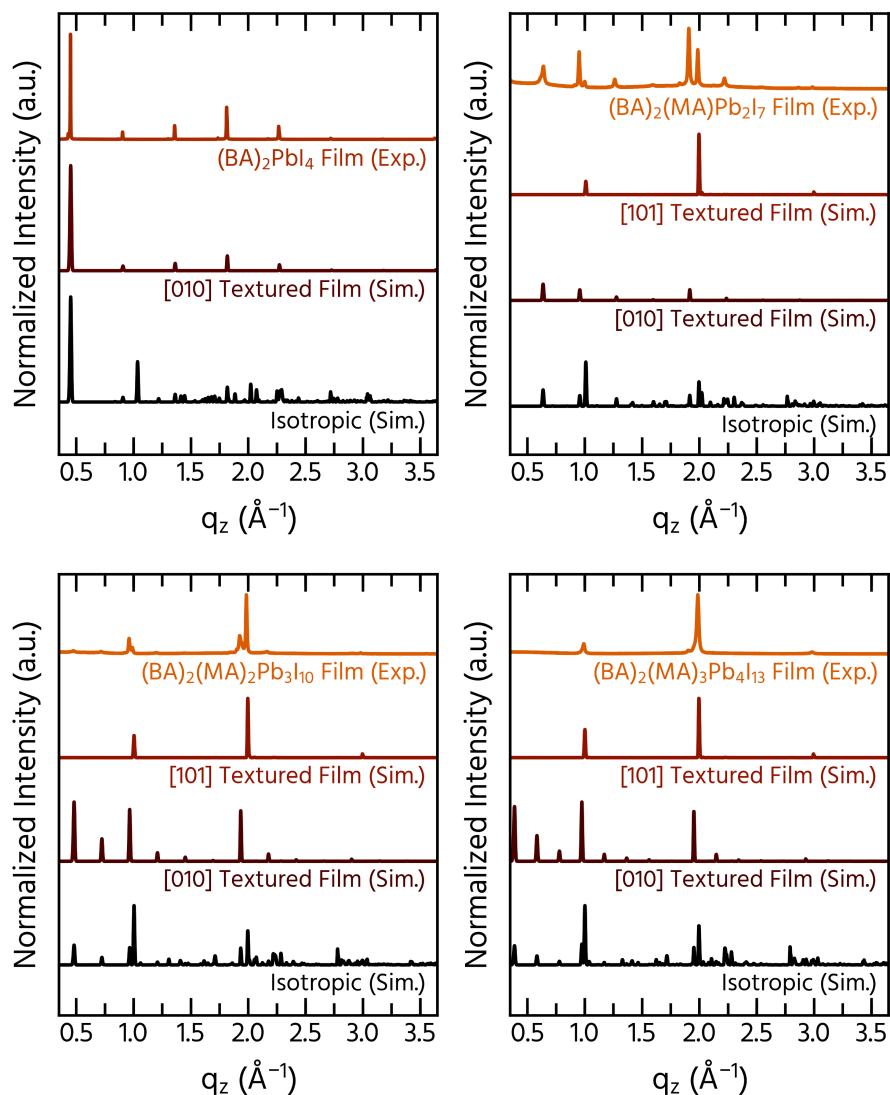


Figure 5.8: Specular X-ray diffraction of first four Ruddlesden–Popper thin films. Due to geometry, scattering vectors are entirely along q_z so data is complementary to GIWAXS images shown in main text, as data lies inside of the missing wedge. Simulated isotropic and textured diffraction patterns are also shown for comparison.

planes.⁶⁸ By iterating through the list of Bragg reflections, all possible peak positions were

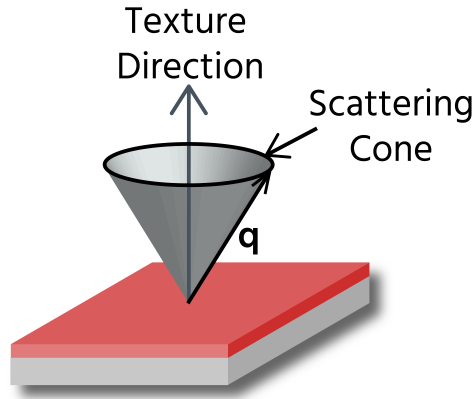


Figure 5.9: Scattering cone formed due to fiber texturing of thin film. Rotational invariance from spin-coating causes scattering vector \vec{q} to trace out a cone in reciprocal space.

calculated and plotted.

$$\begin{aligned} \cos(\phi) = & d_{hkl} d_{h'k'l'} [hh'a^{*2} + kk'b^{*2} + ll'c^{*2} + (kl' + lk')b^*c^* \cos(\alpha^*) \\ & + (hl' + lh')a^*c^* \cos(\beta^*) + (hk' + kh')a^*b^* \cos(\gamma^*)] \end{aligned} \quad (5.1)$$

Plotting of simulated diffraction image was done by creating a meshgrid of points in the q_{xy} - q_z plane and iterating through calculated peak positions. Diffraction peaks were approximated as elliptical Gaussian functions centered at (x_0, y_0) , with variance in both x (σ_x) and y (σ_y), along with rotation (θ). The general functional form used for the peaks is shown in Equation 5.2, with the equation parameters shown in Equations 5.3 – 5.5 below.⁶⁹ The angle θ corresponds to a clockwise rotation of the elliptical Gaussian, an approximation for the arcing seen in actual diffraction spots in experiment. The height associated with the peak was given by the square of the structure factor ($I_{hkl} = |F_{hkl}^2|$) for a given Bragg reflection, represented by the pre-factor A in Equation 5.2. After summing contributions

from all Gaussian functions, the resultant image is the final simulated diffraction pattern.

$$f(x, y) = A \cdot \exp[-(a(x - x_0)^2 + 2b(x - x_0)(y - y_0) + c(y - y_0)^2)] \quad (5.2)$$

$$a = \frac{\cos^2(\theta)}{2\sigma_x^2} + \frac{\sin^2(\theta)}{2\sigma_y^2} \quad (5.3)$$

$$b = -\frac{\sin(2\theta)}{4\sigma_x^2} + \frac{\sin(2\theta)}{4\sigma_y^2} \quad (5.4)$$

$$c = \frac{\sin^2(\theta)}{2\sigma_x^2} + \frac{\cos^2(\theta)}{2\sigma_y^2} \quad (5.5)$$

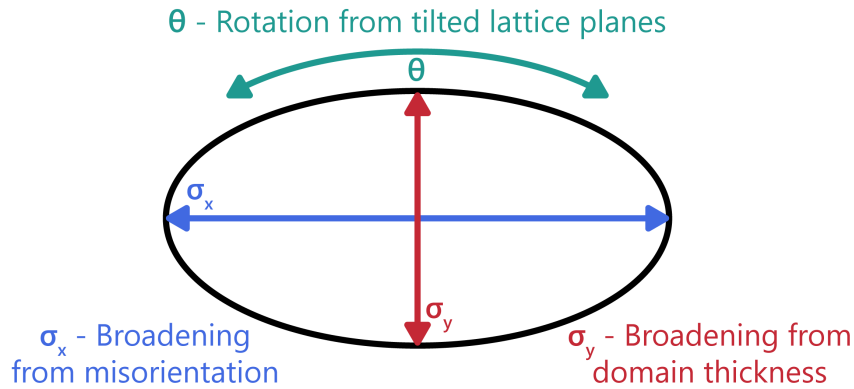


Figure 5.10: Cross section of base of elliptical Gaussian function, illustrating the effect of changing the parameters σ_x , σ_y , and θ on the shape of peaks.

5.5.4 Unbroadened simulated GIWAXS patterns

To determine peak broadening due to crystallite size, in-plane linecuts of measured GIWAXS patterns were fit to find the full-width at half maximum (fwhm) of diffraction peaks. However, since many peaks in the diffraction pattern overlap with each other, a strategic choice of peak was made for fitting. Figure 5.11 presents simulated GIWAXS

patterns of the $n = 3$ and 4 phases without any broadening due to misorientation or domain size, along with their associated in-plane linecuts.

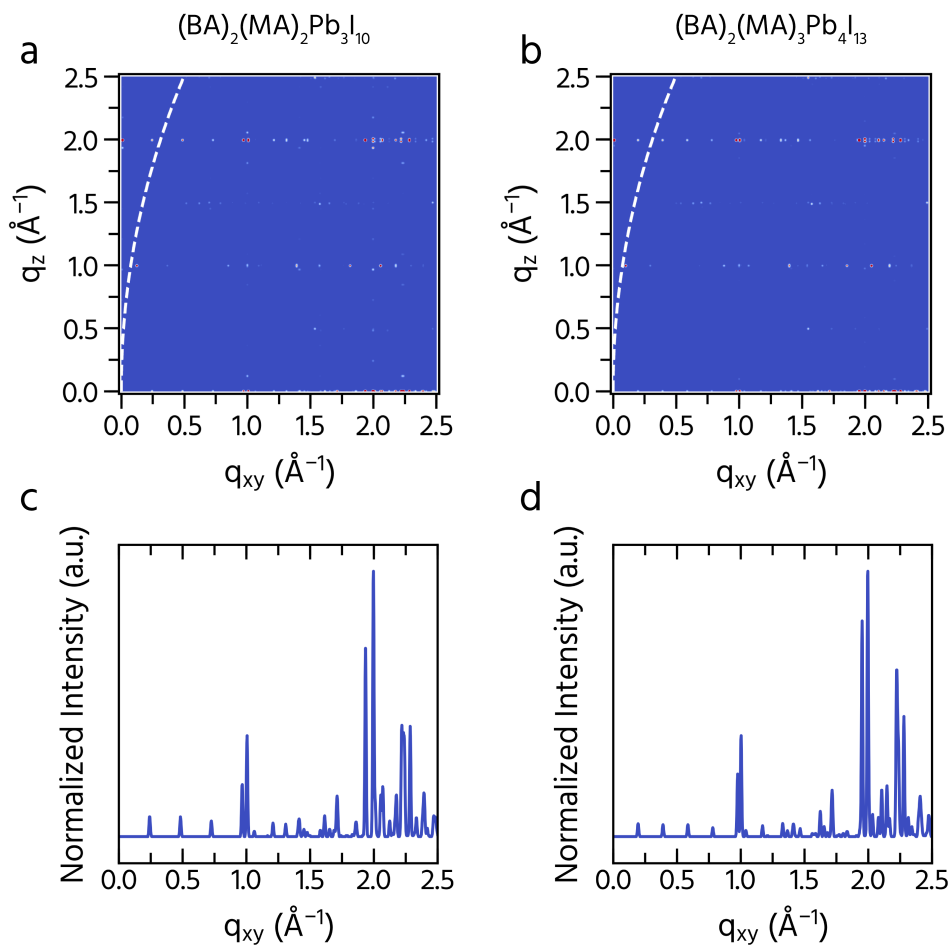


Figure 5.11: (a)-(b) Simulated GIWAXS patterns of $(\text{BA})_2(\text{MA})_2\text{Pb}_3\text{I}_{10}$ and $(\text{BA})_2(\text{MA})_3\text{Pb}_4\text{I}_{13}$ with no line broadening and (c)-(d) associated in-plane intensity linecuts.

5.5.5 GIWAXS simulation of $(\text{BA})_2\text{PbI}_4$ ($n = 1$)

Figure 5.12 shows both the simulated and experimental GIWAXS pattern of the $n = 1$ Ruddlesden–Popper film, $(\text{BA})_2\text{PbI}_4$, showing excellent agreement between the two images and confirming the validity of the GIWAXS simulation code.

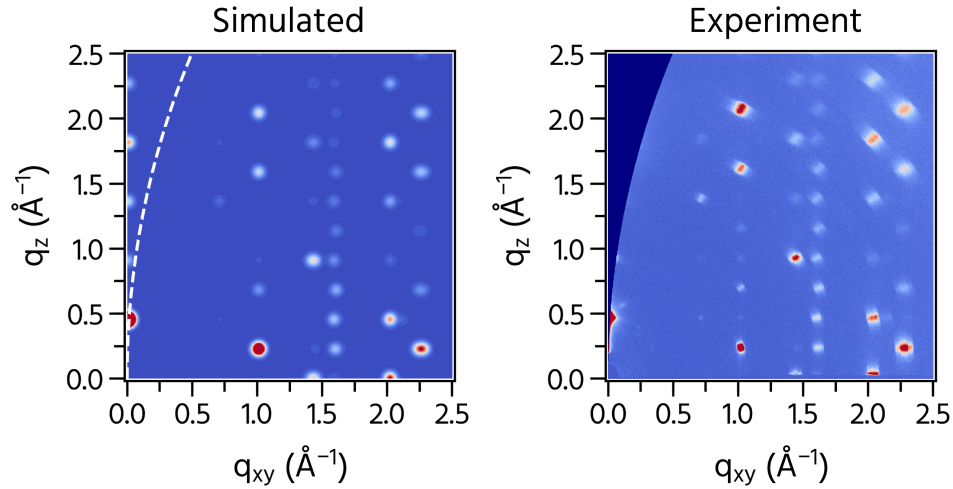


Figure 5.12: Simulated and experimental GIWAXS patterns of $(\text{BA})_2\text{PbI}_4$ ($n = 1$), showing good agreement and phase purity

5.5.6 Fitting of in-plane diffraction peaks

To fit the peak widths of the measured diffraction patterns, due to the missing in-plane scattering peaks, the region around 1.0 \AA^{-1} was chosen for fitting. In the actual measured pattern, the two peaks present at this location overlap, so the fitting was done assuming two different peaks. The results of the fitting for both $n = 3$ and 4 are shown below in Table 5.1. Differences in the peak location are systematic and likely due to substrate effects. Additionally, Table 5.2 lists the structure factors for all strong in-plane diffraction peaks in both the $n = 3$ and 4 compounds.

Table 5.1: Results of multipeak fitting of diffraction peak at $1.0 \text{ \AA}^{-1} q_{xy}$ for both $n = 3$ and $n = 4$ Ruddlesden–Popper thin films.

	$(\text{BA})_2(\text{MA})_2\text{Pb}_3\text{I}_{10}$		$(\text{BA})_2(\text{MA})_3\text{Pb}_4\text{I}_{13}$	
	$0\ 8\ 0$ Peak	$\bar{1}\ 1\ 1$ Peak	$0\ 10\ 0$ Peak	$1\ 1\ 1$ Peak
Peak Location (\AA^{-1})	1.00	1.02	1.00	1.02
FWHM (\AA^{-1})	0.04	0.03	0.03	0.03

Table 5.2: Structure factors and locations of in-plane diffraction peaks for both $n = 3$ and $n = 4$ Ruddlesden–Popper thin films, with blue shaded rows indicating peaks used for fitting.

Lattice Plane	$(\text{BA})_2(\text{MA})_2\text{Pb}_3\text{I}_{10}$		$(\text{BA})_2(\text{MA})_3\text{Pb}_4\text{I}_{13}$	
	q_{xy} (\AA^{-1})	$ F _{\text{hkl}}$	q_{xy} (\AA^{-1})	$ F _{\text{hkl}}$
0 4 0	0.48	645.26	0.39	638.44
0 6 0	0.73	585.32	0.59	637.15
0 8 0	0.97	1070.28	0.78	539.12
0 10 0	1.21	534.45	0.98	1446.92
$\bar{1}$ 1 1	1.01	1010.15	1.00	1287.60
0 12 0	1.45	383.49	1.17	593.16
0 14 0	1.69	241.58	1.37	442.68
0 16 0	1.94	2016.94	1.56	331.65
0 18 0	2.18	937.50	1.76	73.43
0 20 0	2.42	403.36	1.95	2673.96
0 22 0	2.66	323.63	2.15	1175.95
$\bar{2}$ 0 2	2.00	2164.08	2.00	2880.72

5.5.7 GIWAXS simulation of $\text{CH}_3\text{NH}_3\text{PbI}_3$

Figure 5.13 shows a $[110]$ -textured GIWAXS simulation of methylammonium lead iodide ($I4/mcm$ crystal structure at room temperature) along with an associated simulated in-plane linecut.

5.5.8 Comparison of bulk and spatially averaged emission

Spatial photoluminescence was measured by collecting emission from 72 tiled regions, each with a size of $7 \mu\text{m} \times 7 \mu\text{m}$. Each of these localized spectra were first normalized and used to find an average spectrum for the film. To confirm agreement between the averaged spectra and those measured by steady-state photoluminescence, the difference between the

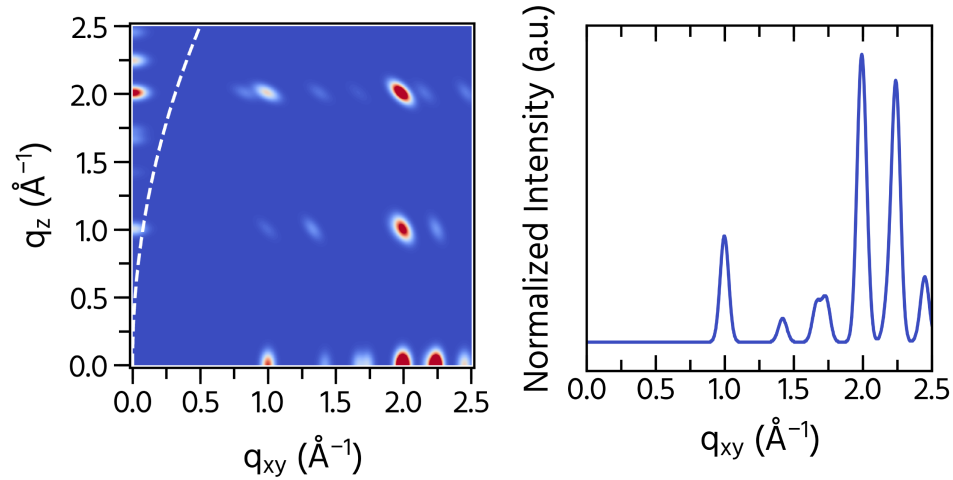


Figure 5.13: Simulated GIWAXS pattern (left) and in-plane intensity linecut (right) for $I4/mcm$ (room temperature crystal structure) of methylammonium lead iodide.

two was taken and is shown in Figure 5.14. While there are some small peaks and valleys seen in the plot, these differences are minimal and the peak emission energies are the same in both cases.

5.5.9 Fitting of spatial photoluminescence spectra

The spatial photoluminescence spectra presented in Figures 5.3c and d in the main text are fit to Gaussian functions in Figure 5.15 and the results of the peak positions and full-width at half maximum (fwhm) are tabulated in Table 5.3.

Table 5.3: Tabulated values of the peak positions and FWHM values of Gaussian functions based on fits shown in Figure 5.15.

	$(BA)_2(MA)_2Pb_3I_{10}$		$(BA)_2(MA)_3Pb_4I_{13}$	
	Location (eV)	fwhm (eV)	Location (eV)	fwhm (eV)
Peak 1	2.02	0.07	1.74	0.14
Peak 2	1.91	0.03	–	–
Peak 3	1.79	0.15	–	–

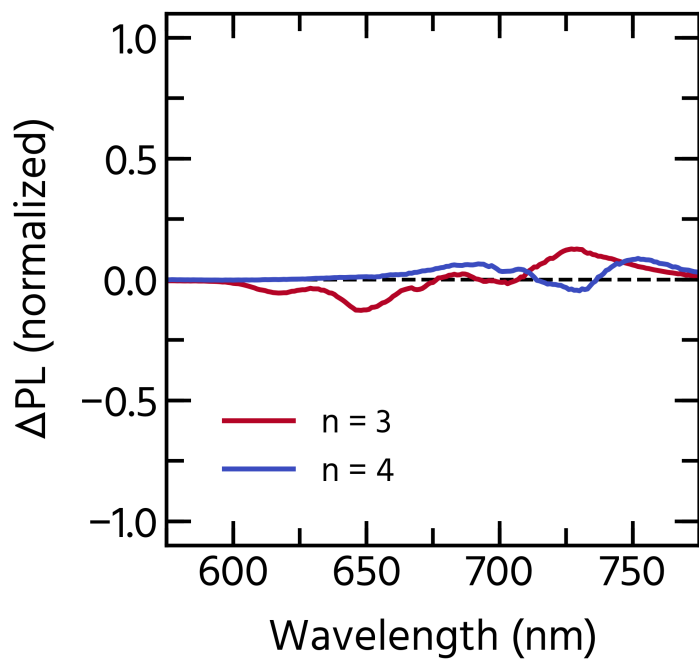


Figure 5.14: Difference between the normalized bulk, steady-state emission and spatially averaged photoluminescence measurements for $n = 3$ and 4 Ruddlesden–Popper thin films.

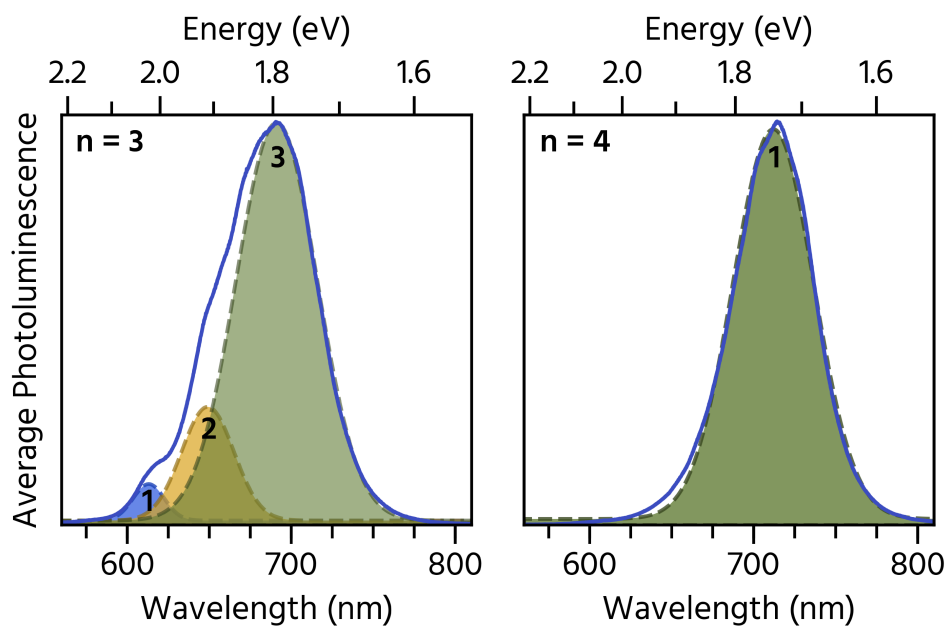


Figure 5.15: Fits of Gaussian functions to the photoluminescence peaks of $(\text{BA})_2(\text{MA})_2\text{Pb}_3\text{I}_{10}$ ($n = 3$) and $(\text{BA})_2(\text{MA})_3\text{Pb}_4\text{I}_{13}$ ($n = 4$).

5.5.10 Emission peak energies of crystals and thin films

Table 5.4 lists the expected emission from thin films of $(\text{BA})_2(\text{MA})_{n-1}\text{Pb}_n\text{I}_{3n+1}$ and exfoliated single-crystals was compiled from data previously published by Blancon *et al.*³⁸

Table 5.4: Emission energies for Ruddlesden–Popper thin films and exfoliated single-crystals.

<i>n</i> value	Exfoliated Crystals		Thin Films	
	Wavelength (nm)	Energy (eV)	Wavelength (nm)	Energy (eV)
1	528	2.35	534	2.32
2	585	2.12	608	2.04
3	617	2.01	729	1.70
4	653	1.90	729	1.70

5.5.11 ¹H NMR of precursor solutions and thin films

The effective stoichiometry of spincoated films and precursor solutions were measured with ¹H nuclear magnetic resonance (NMR) spectroscopy. The thin film samples were prepared as described previously in Section 5.5.1; however, to obtain a sufficient amount of sample for analysis, the films were prepared by spincoating onto a cleaned, glass substrate at 1000 rpm instead of 4000 rpm. The spincoated films were then annealed at 100°C for 10 minutes in a glovebox. The resulting films were then scraped off and dissolved in DMSO-*d*₆, and transferred to a 500 MHz NMR tube.

The butylammonium (BA)/methylammonium (MA) stoichiometric ratio was calculated by integrating the ¹H NMR peaks. An average peak integral was calculated from the multiple protons associated with each molecule, and the error in the resulting *n* value was taken as the standard deviation in the calculated BA/MA ratio.

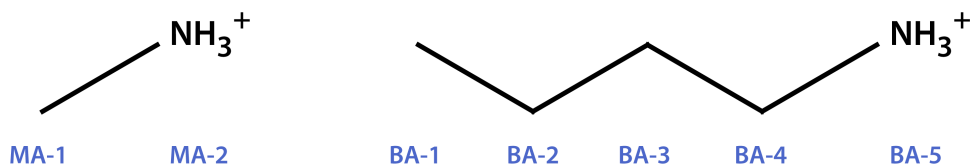


Figure 5.16: Molecular structures of methylammonium and *n*-butylammonium with associated labeled protons.

Table 5.5: Chemical shifts for methylammonium (CH_3NH_3).

Methylammonium (MA)		
Proton Label	MA-1	MA-2
Chemical Shift (ppm)	2.39	7.53

Table 5.6: Chemical shifts for *n*-butylammonium ($\text{C}_4\text{H}_9\text{NH}_3$).

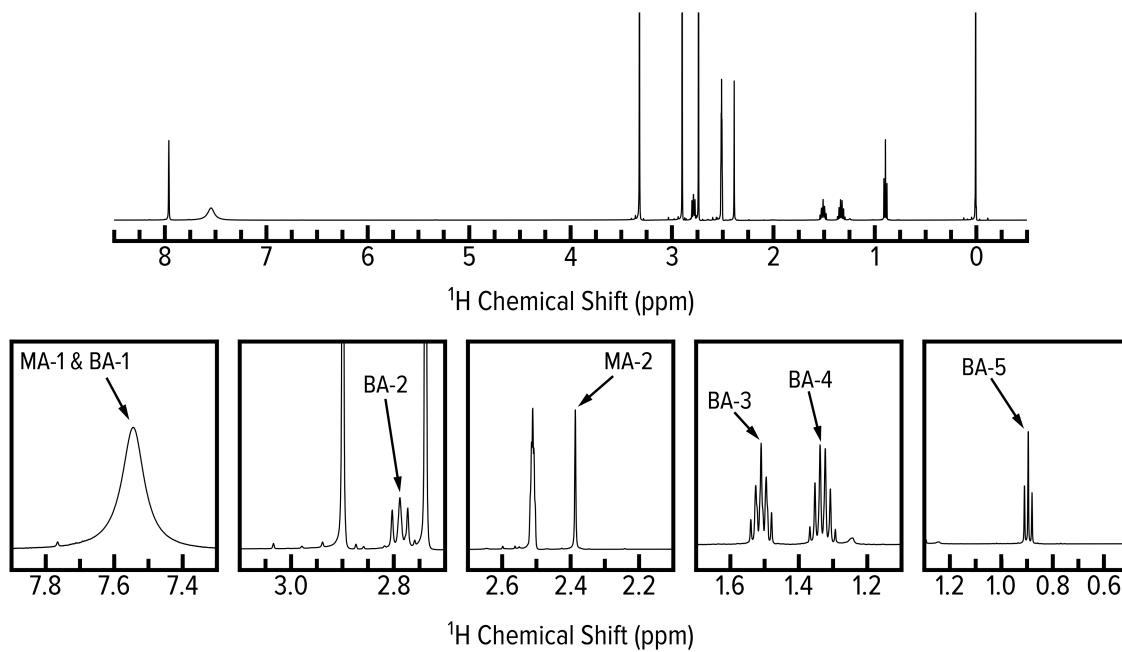
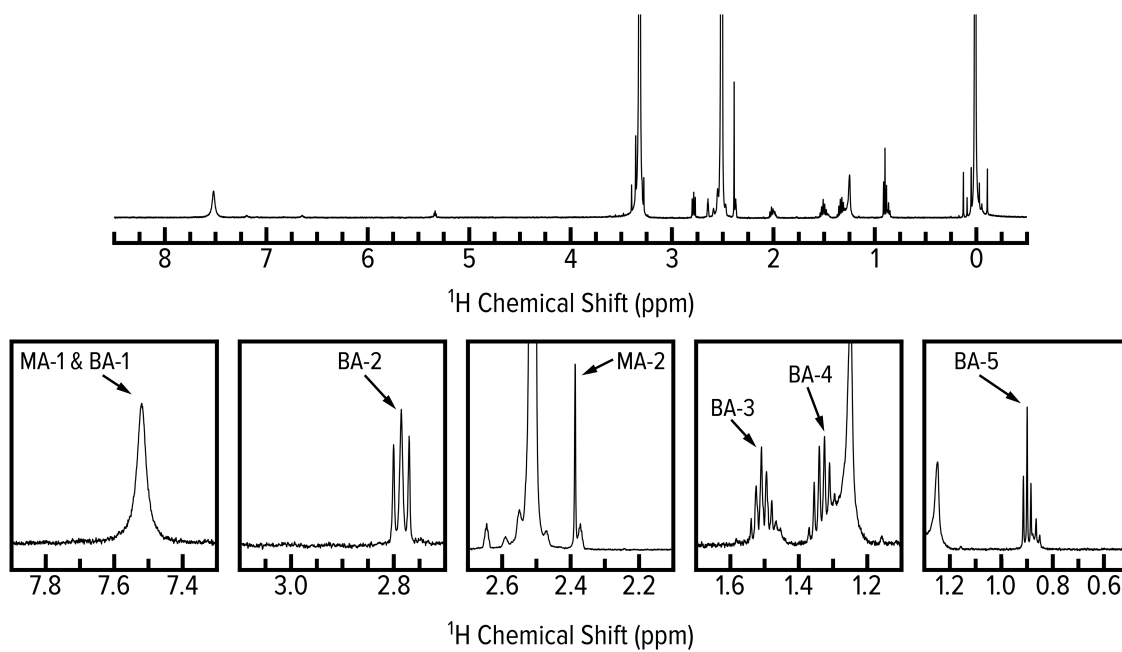
Butylammonium (BA)					
Proton Label	BA-1	BA-2	BA-3	BA-4	BA-5
Chemical Shift (ppm)	0.90	1.33	1.51	2.79	7.53

Table 5.7: Integrations of NMR protons for $n = 3$ and $n = 4$ solutions and thin films.

	MA-1/BA-1	MA-2	BA-2	BA-3	BA-4	BA-5
$n = 3$						
Solution	0.68	0.34	0.32	0.34	0.35	0.34
Film	0.33	0.16	0.15	0.19	0.15	0.18
$n = 4$						
Solution	0.80	0.47	0.31	0.31	0.31	0.31
Film	0.30	0.18	0.11	0.11	0.11	0.13

5.5.12 Diffraction fitting of SAED patterns

Single-crystal structures were used to calculate d spacings of intense Bragg reflections in the $n = 1-4$ Ruddlesden–Popper phases and methylammonium lead iodide and overlaid

Figure 5.17: ^1H NMR spectrum of $(\text{BA})_2(\text{MA})_2\text{Pb}_3\text{I}_{10}$ precursor solution.Figure 5.18: ^1H NMR spectrum of $(\text{BA})_2(\text{MA})_2\text{Pb}_3\text{I}_{10}$ thin film.

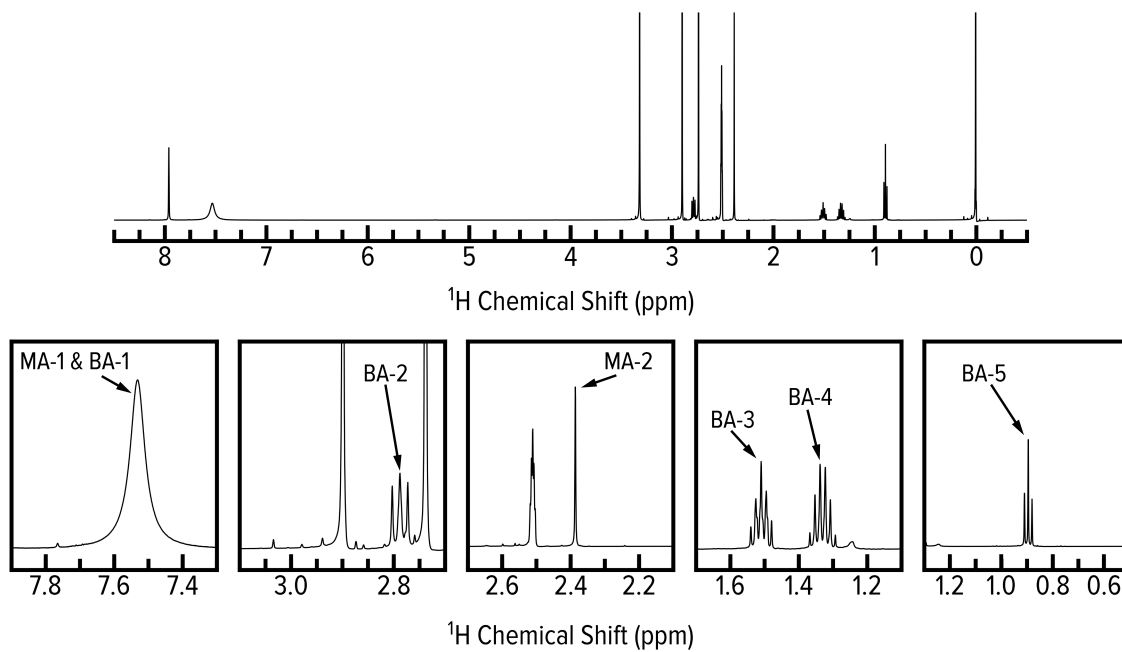
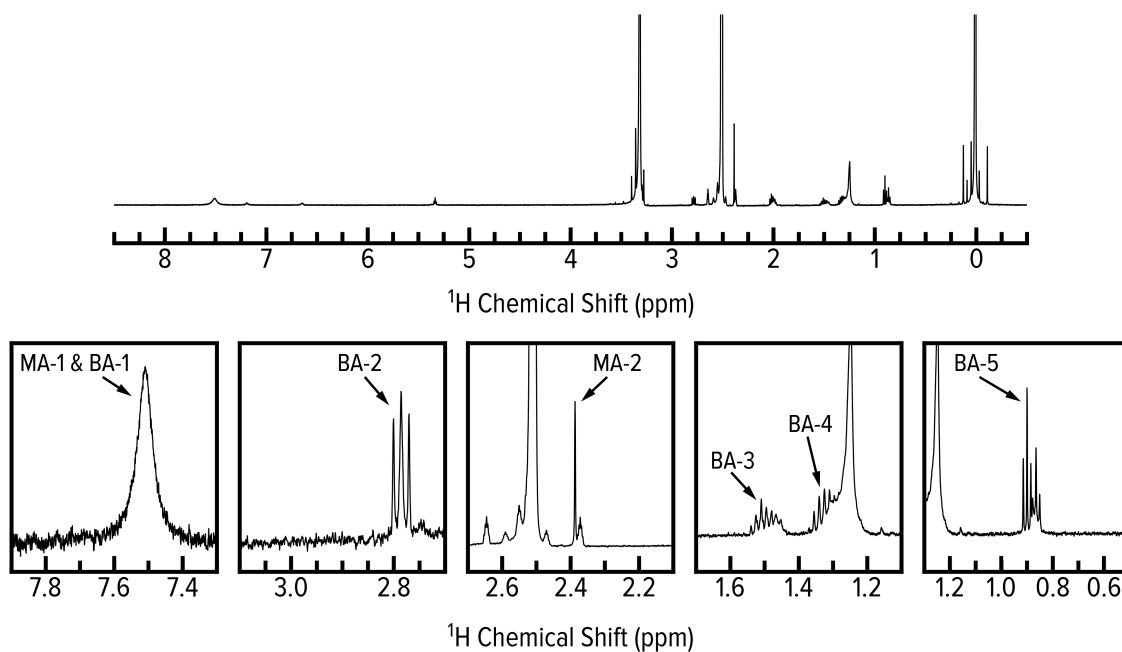
Figure 5.19: ^1H NMR spectrum of $(\text{BA})_2(\text{MA})_3\text{Pb}_4\text{I}_{13}$ precursor solution.Figure 5.20: ^1H NMR spectrum of $(\text{BA})_2(\text{MA})_3\text{Pb}_4\text{I}_{13}$ thin film.

Table 5.8: Calculated n values of Ruddlesden–Popper solutions and thin films.

	MA/BA Ratio	n
$n = 3$		
Solution	1.01 ± 0.04	3.02 ± 0.08
Film	0.98 ± 0.11	2.95 ± 0.22
$n = 4$		
Solution	1.55 ± 0.08	4.11 ± 0.15
Film	1.60 ± 0.19	4.20 ± 0.39

as rings on the selected area electron diffraction (SAED) patterns. Intersection of spots in the SAED patterns with overlaid rings is indicative of presence of that particular phase in the thin film. In both the cases of $n = 3$ and 4, there appear to be overlaid rings from all of the compounds that intersect reflections in the electron diffraction pattern. A summary of the reflections for each of the compounds is tabulated in Table 5.9. Reflections that are superscripted with a symbol are indistinguishable in reciprocal space and appear as one ring in the indexed patterns.

5.5.13 Fitting of Urbach energies for layered perovskites

Exponential fits to the Urbach tails of photothermal deflection data were done and shown in Figure 5.23. The slope of these lines on a logarithmic scale gives the Urbach energies of the layered phases, presented in Table 5.10.

5.5.14 External quantum efficiency measurements

Photovoltaic devices were fabricated with the $n = 3$ and 4 phases as active layers, using poly(3,4-ethylenedioxythiophene) polystyrene sulfonate (PEDOT:PSS) as a hole transport material and [6,6]-phenyl-C₆₁-butyric acid methyl ester (PCBM) as the electron transport

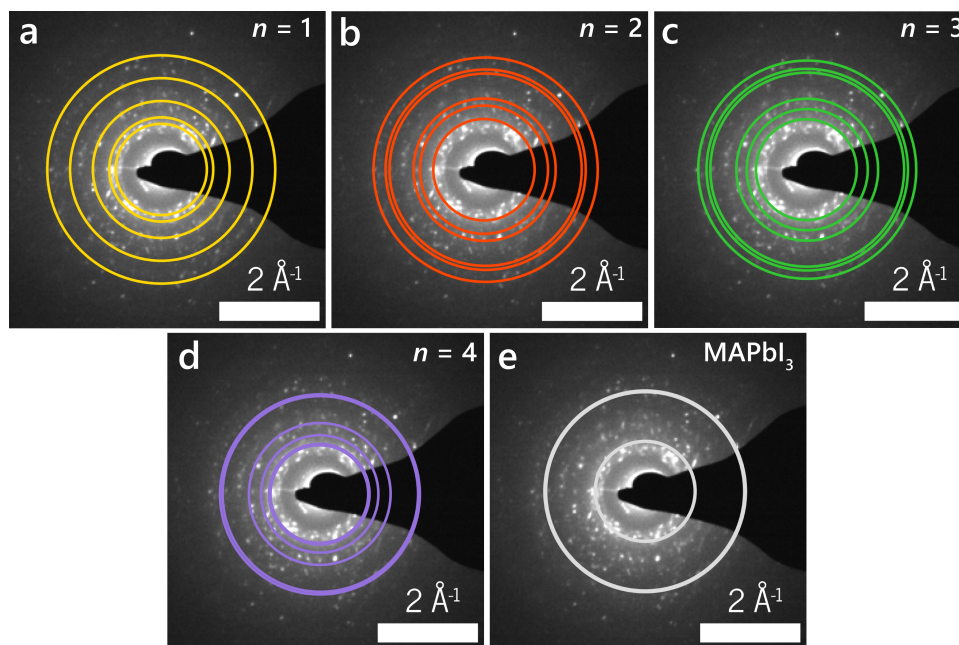


Figure 5.21: . Selected area electron diffraction (SAED) pattern of $(\text{BA})_2(\text{MA})_2\text{Pb}_3\text{I}_{10}$, along with overlaid diffraction rings from crystal structures for (a) $(\text{BA})_2\text{PbI}_4$, (b) $(\text{BA})_2\text{MAPb}_2\text{I}_7$, (c) $(\text{BA})_2(\text{MA})_2\text{Pb}_3\text{I}_{10}$, (d) $(\text{BA})_2(\text{MA})_3\text{Pb}_4\text{I}_{13}$, and (e) MAPbI_3 , displaying phase impurities present in thin film.

layer. The EQE measurements were conducted as described in Section 5.5.1 above and the results are shown in Figure 5.24 with a comparison to the absorption coefficient measurements by PDS. The exponential tails were fit to extract Urbach energies and are tabulated in Table 5.11.

5.5.15 GIWAXS images of thin films cast on PEDOT:PSS

GIWAXS images were collected for $n = 3$ and $n = 4$ thin films cast on PEDOT:PSS in order to characterize structural differences that may be present in device fabrication compared to those in the neat films on quartz. The images are presented in Figure 5.25 and show no appreciable difference between those shown in Figure 5.2.

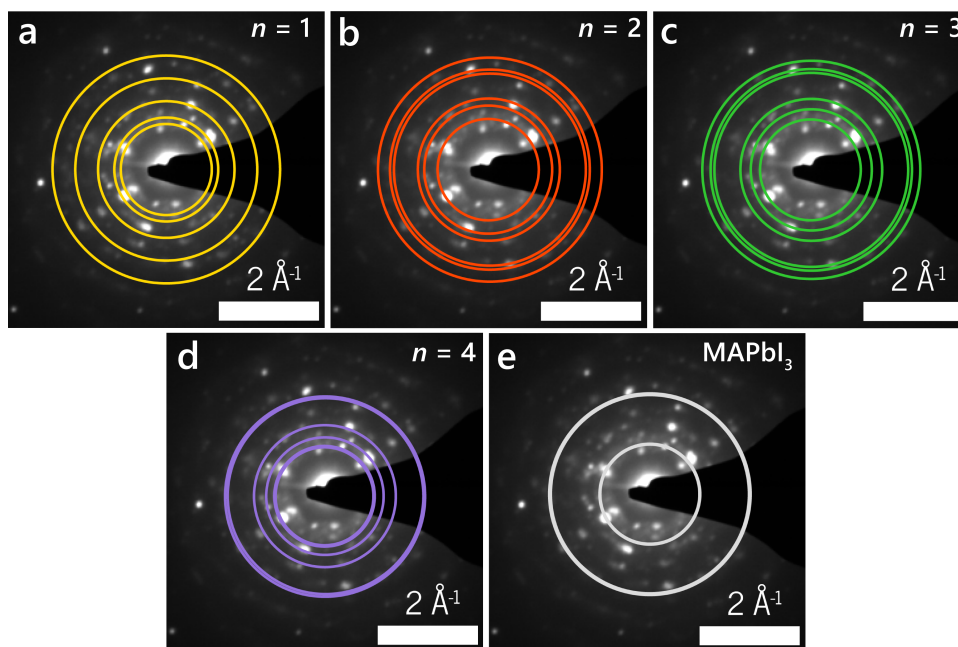


Figure 5.22: Selected area electron diffraction (SAED) pattern of $(\text{BA})_2(\text{MA})_3\text{Pb}_4\text{I}_{13}$, along with overlaid diffraction rings from crystal structures for (a) $(\text{BA})_2\text{PbI}_4$, (b) $(\text{BA})_2\text{MAPb}_2\text{I}_7$, (c) $(\text{BA})_2(\text{MA})_2\text{Pb}_3\text{I}_{10}$, (d) $(\text{BA})_2(\text{MA})_3\text{Pb}_4\text{I}_{13}$, and (e) MAPbI_3 , displaying phase impurities present in thin film.

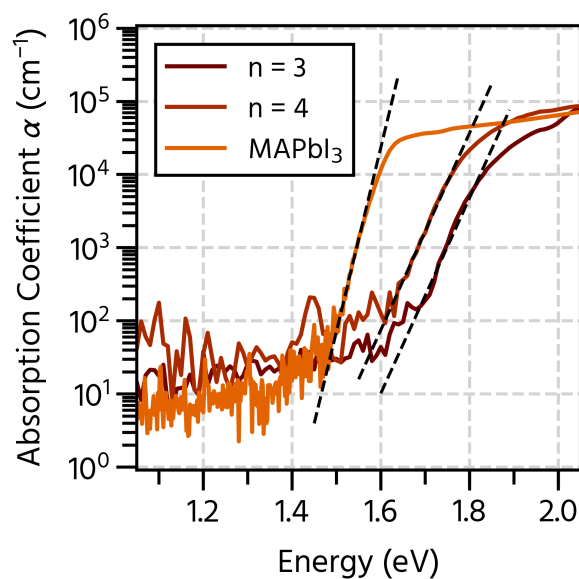


Figure 5.23: Exponential fitting of Urbach energies of MAPbI_3 , $(\text{BA})_2(\text{MA})_2\text{Pb}_3\text{I}_{10}$, and $(\text{BA})_2(\text{MA})_3\text{Pb}_4\text{I}_{13}$, showing extremely sharp tails, despite structural disorder seen from X-ray and electron diffraction.

Table 5.9: List of reflections and d spacings, listed in order of increasing scattering vector \vec{q} (increasing ring radius). Superscripted reflections are too close to each other in reciprocal space to distinguish.

(BA)₂PbI₄						
Reflection (hkl)	0 4 0	1 1 1	0 6 0	0 8 0	0 10 0	–
d spacing (Å)	6.91	6.06	4.61	3.46	2.77	–
(BA)₂MAPb₂I₇						
Reflection (hkl)	1 1 1	0 8 0	0 0 2	0 12 0	2 0 2	0 14 0
d spacing (Å)	6.22	4.92	4.43	3.28	3.15	2.81
(BA)₂MA₂Pb₃I₁₀						
Reflection (hkl)	1 1 1	0 10 0	0 0 2	0 16 0	2 0 2	0 18 0
d spacing (Å)	6.25	5.20	4.44	3.25	3.15	2.89
(BA)₂MA₃Pb₄I₁₃						
Reflection (hkl)	0 10 0*	1 1 1*	0 12 0	0 0 2	0 20 0 [#]	2 0 2 [#]
d spacing (Å)	6.44	6.27	5.37	4.44	3.22	3.15
MAPbI₃						
Reflection (hkl)	0 0 2*	1 1 0*	0 0 4 [#]	2 2 0 [#]	–	–
d spacing (Å)	6.35	6.25	3.17	3.13	–	–

Table 5.10: Urbach energies extracted from exponential fits of photothermal deflection spectroscopy data.

Material	Urbach Energy (meV)
MAPbI ₃	17
(BA) ₂ (MA) ₂ Pb ₃ I ₁₀	33
(BA) ₂ (MA) ₃ Pb ₄ I ₁₃	32

Table 5.11: Urbach energies extracted from exponential fits of external quantum efficiency data.

Material	Urbach Energy (meV)
(BA) ₂ (MA) ₂ Pb ₃ I ₁₀	46
(BA) ₂ (MA) ₃ Pb ₄ I ₁₃	41

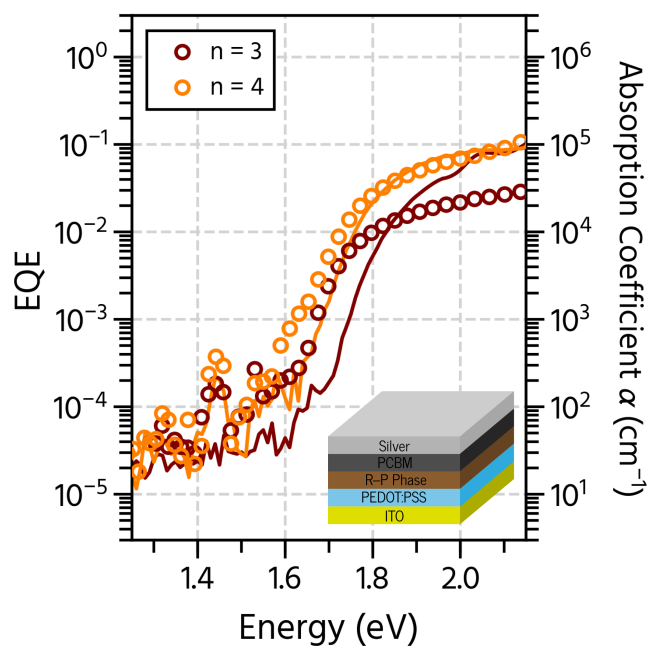


Figure 5.24: Comparison of external quantum efficiency (open circles) and absorption coefficients measured by photothermal deflection (solid lines) for $n = 3$ and $n = 4$ Rudlesden–Popper thin films. Device EQE data were fit to exponential functions at the band edge to extract Urbach energies, tabulated in Table 5.11.

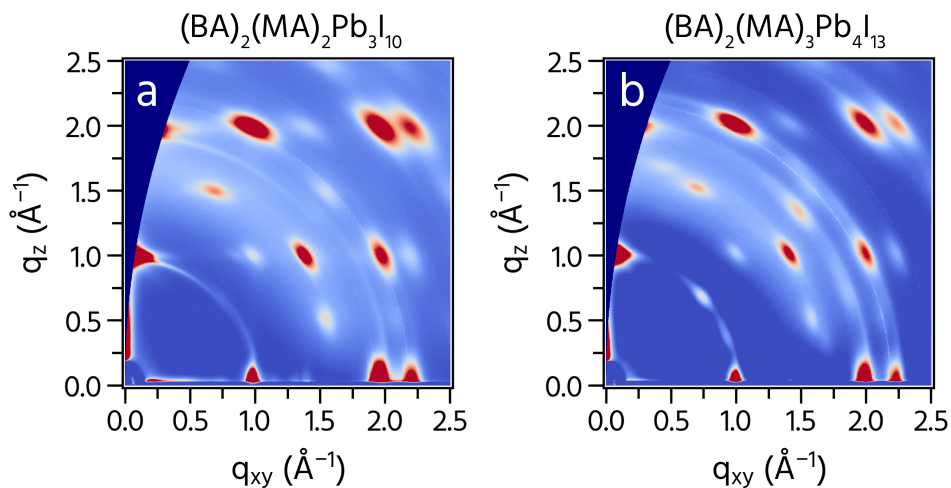


Figure 5.25: GIWAXS images of (a) $(\text{BA})_2(\text{MA})_2\text{Pb}_3\text{I}_{10}$ and (b) $(\text{BA})_2(\text{MA})_3\text{Pb}_4\text{I}_{13}$ spun-coat on PEDOT:PSS (hole transport layer in device), illustrating no structural differences from the neat films spun on quartz presented in Figure 5.2.

5.6 Acknowledgments

Materials synthesis and structural characterization were supported by the U.S. Department of Energy, Office of Science, Basic Energy Sciences, under Award DE-SC-0012541. Work on devices was supported by the Defense Threat Reduction Agency under Award HDTRA1-15-1-0023. Use of the Stanford Synchrotron Radiation Lightsource, SLAC National Accelerator Laboratory, is supported by U.S. Department of Energy, Office of Science, Basic Energy Sciences, under Contract DE-AC02-76SF00515. The research reported here also made use of the shared facilities of the UCSB MRSEC (National Science Foundation DMR 1720256), a member of the Materials Research Facilities Network (www.mrfn.org). R.M.K. gratefully acknowledges the National Defense Science and Engineering Graduate Fellowship for financial support. R.A.D. and J.A.S. acknowledge support from a National Science Foundation CAREER Award, under Award DMR-1454260. N.R.V. gratefully appreciates the help from D. Hanifi and Prof. A. Salleo with running and help with analysis of PDS.

5.7 Permissions and Attributions

The content of this chapter and appendix has been reprinted with permission from “Phase Intergrowth and Structural Defects in Organic Metal Halide Ruddlesden–Popper Thin Films” by N. R. Venkatesan *et al.*. Copyright © 2018 American Chemical Society.

5.8 References

1. Mitzi, D. B., Chondroudis, K. & Kagan, C. R. Organic-Inorganic Electronics. *IBM Journal of Research and Development* **45**, 29–45 (2001).
2. Berry, J., Buonassisi, T., Egger, D. A., Hodes, G., Kronik, L., Loo, Y.-L., Lubomirsky, I., Marder, S. R., Mastai, Y., Miller, J. S., Mitzi, D. B., Paz, Y., Rappe, A. M., Riess, I., Rybtchinski, B., Stafsudd, O., Stevanovic, V., Toney, M. F., Zitoun, D., Kahn, A., Ginley, D. & Cahen, D. Hybrid Organic-Inorganic Perovskites (HOIPs): Opportunities and Challenges. *Advanced Materials* **27**, 5102–5112 (2015).
3. Kagan, C. R., Mitzi, D. B. & Dimitrakopoulos, C. D. Organic-Inorganic Hybrid Materials as Semiconducting Channels in Thin-Film Field-Effect Transistors. *Science* **286**, 945–947 (1999).
4. Saparov, B. & Mitzi, D. B. Organic–Inorganic Perovskites: Structural Versatility for Functional Materials Design. *Chemical Reviews* **116**, 4558–4596 (2016).
5. Papavassiliou, G. C., Mousdis, G. A. & Koutselas, I. B. Some New Organic–Inorganic Hybrid Semiconductors Based on Metal Halide Units: Structural, Optical and Related Properties†. *Advanced Materials for Optics and Electronics* **9**, 265–271 (1999).
6. Snaith, H. J. Perovskites: The Emergence of a New Era for Low-Cost, High-Efficiency Solar Cells. *The Journal of Physical Chemistry Letters* **4**, 3623–3630 (2013).
7. Zhang, W., Eperon, G. E. & Snaith, H. J. Metal Halide Perovskites for Energy Applications. *Nature Energy* **1**, 16048 (2016).
8. Wehrenfennig, C., Eperon, G. E., Johnston, M. B., Snaith, H. J. & Herz, L. M. High Charge Carrier Mobilities and Lifetimes in Organolead Trihalide Perovskites. *Advanced Materials* **26**, 1584–1589 (2014).
9. Bi, Y., Hutter, E. M., Fang, Y., Dong, Q., Huang, J. & Savenije, T. J. Charge Carrier Lifetimes Exceeding 15 μ s in Methylammonium Lead Iodide Single Crystals. *The Journal of Physical Chemistry Letters* **7**, 923–928 (2016).
10. Yu, Z.-G. The Rashba Effect and Indirect Electron-Hole Recombination in Hybrid Organic–Inorganic Perovskites. *Physical Chemistry Chemical Physics* **19**, 14907–14912 (2017).
11. Mosconi, E., Etienne, T. & De Angelis, F. Rashba Band Splitting in Organohalide Lead Perovskites: Bulk and Surface Effects. *The Journal of Physical Chemistry Letters* **8**, 2247–2252 (2017).
12. Zheng, F., Tan, L. Z., Liu, S. & Rappe, A. M. Rashba Spin–Orbit Coupling Enhanced Carrier Lifetime in $\text{CH}_3\text{NH}_3\text{PbI}_3$. *Nano Letters* **15**, 7794–7800 (2015).
13. Ivanovska, T., Dionigi, C., Mosconi, E., De Angelis, F., Liscio, F., Morandi, V. & Ruani, G. Long-Lived Photoinduced Polarons in Organohalide Perovskites. *The Journal of Physical Chemistry Letters* **8**, 3081–3086 (2017).

14. Zhu, X.-Y. & Podzorov, V. Charge Carriers in Hybrid Organic–Inorganic Lead Halide Perovskites Might Be Protected as Large Polarons. *The Journal of Physical Chemistry Letters* **6**, 4758–4761 (2015).
15. Yang, W. S., Park, B.-W., Jung, E. H., Jeon, N. J., Kim, Y. C., Lee, D. U., Shin, S. S., Seo, J., Kim, E. K., Noh, J. H. & Seok, S. I. Iodide Management in Formamidinium–Lead–Halide–Based Perovskite Layers for Efficient Solar Cells. *Science* **356**, 1376–1379 (2017).
16. Polman, A., Knight, M., Garnett, E. C., Ehrler, B. & Sinke, W. C. Photovoltaic Materials: Present Efficiencies and Future Challenges. *Science* **352**, aad4424 (2016).
17. Xiao, Z., Kerner, R. A., Zhao, L., Tran, N. L., Lee, K. M., Koh, T.-W., Scholes, G. D. & Rand, B. P. Efficient Perovskite Light-Emitting Diodes Featuring Nanometre-Sized Crystallites. *Nature Photonics* **11**, 108–115 (2017).
18. Yuan, M., Quan, L. N., Comin, R., Walters, G., Sabatini, R., Voznyy, O., Hoogland, S., Zhao, Y., Beauregard, E. M., Kanjanaboos, P., Lu, Z., Kim, D. H. & Sargent, E. H. Perovskite Energy Funnels for Efficient Light-Emitting Diodes. *Nature Nanotechnology* **11**, 872–877 (2016).
19. Tsai, H., Nie, W., Blancon, J.-C., Stoumpos, C. C., Soe, C. M. M., Yoo, J., Crochet, J., Tretiak, S., Even, J., Sadhanala, A., Azzellino, G., Brenes, R., Ajayan, P. M., Bulović, V., Stranks, S. D., Friend, R. H., Kanatzidis, M. G. & Mohite, A. D. Stable Light-Emitting Diodes Using Phase-Pure Ruddlesden–Popper Layered Perovskites. *Advanced Materials* **30**, 1704217 (2018).
20. Smith, M. D., Jaffe, A., Dohner, E. R., Lindenberg, A. M. & Karunadasa, H. I. Structural Origins of Broadband Emission from Layered Pb–Br Hybrid Perovskites. *Chemical Science* **8**, 4497–4504 (2017).
21. Hu, T., Smith, M. D., Dohner, E. R., Sher, M.-J., Wu, X., Trinh, M. T., Fisher, A., Corbett, J., Zhu, X.-Y., Karunadasa, H. I. & Lindenberg, A. M. Mechanism for Broadband White-Light Emission from Two-Dimensional (110) Hybrid Perovskites. *The Journal of Physical Chemistry Letters* **7**, 2258–2263 (2016).
22. Smith, M. D. & Karunadasa, H. I. White-Light Emission from Layered Halide Perovskites. *Accounts of Chemical Research* **51**, 619–627 (2018).
23. Aristidou, N., Sanchez-Molina, I., Chotchuangchutchaval, T., Brown, M., Martinez, L., Rath, T. & Haque, S. A. The Role of Oxygen in the Degradation of Methylammonium Lead Trihalide Perovskite Photoactive Layers. *Angewandte Chemie International Edition* **54**, 8208–8212 (2015).
24. Zhao, L., Kerner, R. A., Xiao, Z., Lin, Y. L., Lee, K. M., Schwartz, J. & Rand, B. P. Redox Chemistry Dominates the Degradation and Decomposition of Metal Halide Perovskite Optoelectronic Devices. *ACS Energy Letters* **1**, 595–602 (2016).

25. Leijtens, T., Eperon, G. E., Noel, N. K., Habisreutinger, S. N., Petrozza, A. & Snaith, H. J. Stability of Metal Halide Perovskite Solar Cells. *Advanced Energy Materials* **5**, 1500963 (2015).
26. Ruddlesden, S. N. & Popper, P. New Compounds of the K_2NiF_4 Type. *Acta Crystallographica* **10**, 538–539 (1957).
27. Ruddlesden, S. N. & Popper, P. The Compound $Sr_3Ti_2O_7$ and Its Structure. *Acta Crystallographica* **11**, 54–55 (1958).
28. Haeni, J. H., Theis, C. D., Schlom, D. G., Tian, W., Pan, X. Q., Chang, H., Takeuchi, I. & Xiang, X.-D. Epitaxial Growth of the First Five Members of the $Sr_{n+1}Ti_nO_{3n+1}$ Ruddlesden–Popper Homologous Series. *Applied Physics Letters* **78**, 3292–3294 (2001).
29. Battle, P. D., Green, M. A., Laskey, N. S., Millburn, J. E., Murphy, L., Rosseinsky, M. J., Sullivan, S. P. & Vente, J. F. Layered Ruddlesden–Popper Manganese Oxides: Synthesis and Cation Ordering. *Chemistry of Materials* **9**, 552–559 (1997).
30. Chen, Y., Sun, Y., Peng, J., Tang, J., Zheng, K. & Liang, Z. 2D Ruddlesden–Popper Perovskites for Optoelectronics. *Advanced Materials* **30**, 1703487 (2017).
31. Akkerman, Q. A., D’Innocenzo, V., Accornero, S., Scarpellini, A., Petrozza, A., Prato, M. & Manna, L. Tuning the Optical Properties of Cesium Lead Halide Perovskite Nanocrystals by Anion Exchange Reactions. *Journal of the American Chemical Society* **137**, 10276–10281 (2015).
32. Protesescu, L., Yakunin, S., Bodnarchuk, M. I., Krieg, F., Caputo, R., Hendon, C. H., Yang, R. X., Walsh, A. & Kovalenko, M. V. Nanocrystals of Cesium Lead Halide Perovskites ($CsPbX_3$, X= Cl, Br, and I): Novel Optoelectronic Materials Showing Bright Emission with Wide Color Gamut. *Nano Letters* **15**, 3692–3696 (2015).
33. Weidman, M. C., Goodman, A. J. & Tisdale, W. A. Colloidal Halide Perovskite Nanoplatelets: An Exciting New Class of Semiconductor Nanomaterials. *Chemistry of Materials* **29**, 5019–5030 (2017).
34. Tsai, H., Nie, W., Blancon, J.-C., Stoumpos, C. C., Asadpour, R., Harutyunyan, B., Neukirch, A. J., Verduzco, R., Crochet, J. J., Tretiak, S., Pedesseau, L., Even, J., Alam, M. A., Gupta, G., Lou, J., Ajayan, P. M., Bedzyk, M. J., Kanatzidis, M. G. & Mohite, A. D. High-Efficiency Two-Dimensional Ruddlesden–Popper Perovskite Solar Cells. *Nature* **536**, 312–316 (2016).
35. Liao, Y., Liu, H., Zhou, W., Yang, D., Shang, Y., Shi, Z., Li, B., Jiang, X., Zhang, L., Quan, L. N., Quintero-Bermudez, R., Sutherland, B. R., Mi, Q., Sargent, E. H. & Ning, Z. Highly Oriented Low-Dimensional Tin Halide Perovskites with Enhanced Stability and Photovoltaic Performance. *Journal of the American Chemical Society* **139**, 6693–6699 (2017).
36. Venkatesan, N. R., Labram, J. G. & Chabinyk, M. L. Charge-Carrier Dynamics and Crystalline Texture of Layered Ruddlesden–Popper Hybrid Lead Iodide Perovskite Thin Films. *ACS Energy Letters* **3**, 380–386 (2018).

37. Labram, J. G., Venkatesan, N. R., Takacs, C. J., Evans, H. A., Perry, E. E., Wudl, F. & Chabynyc, M. L. Charge Transport in a Two-Dimensional Hybrid Metal Halide Thiocyanate Compound. *Journal of Materials Chemistry C* **5**, 5930–5938 (2017).
38. Blancon, J.-C., Tsai, H., Nie, W., Stoumpos, C. C., Pedesseau, L., Katan, C., Kepenekian, M., Soe, C. M. M., Appavoo, K., Sfeir, M. Y., Tretiak, S., Ajayan, P. M., Kanatzidis, M. G., Even, J., Crochet, J. J. & Mohite, A. D. Extremely Efficient Internal Exciton Dissociation through Edge States in Layered 2D Perovskites. *Science* **355**, 1288–1292 (2017).
39. Nie, W., Tsai, H., Asadpour, R., Blancon, J.-C., Neukirch, A. J., Gupta, G., Crochet, J. J., Chhowalla, M., Tretiak, S., Alam, M. A., Wang, H.-L. & Mohite, A. D. High-Efficiency Solution-Processed Perovskite Solar Cells with Millimeter-Scale Grains. *Science* **347**, 522–525 (2015).
40. Liao, H.-C., Guo, P., Hsu, C.-P., Lin, M., Wang, B., Zeng, L., Huang, W., Soe, C. M. M., Su, W.-F., Bedzyk, M. J., Wasielewski, M. R., Facchetti, A., Chang, R. P. H., Kanatzidis, M. G. & Marks, T. J. Enhanced Efficiency of Hot-Cast Large-Area Planar Perovskite Solar Cells/Modules Having Controlled Chloride Incorporation. *Advanced Energy Materials* **7**, 1601660 (2017).
41. Pereira, S., Correia, M. R., Pereira, E., O'Donnell, K. P., Alves, E., Sequeira, A. D., Franco, N., Watson, I. M. & Deatcher, C. J. Strain and Composition Distributions in Wurtzite InGaN/GaN Layers Extracted from x-Ray Reciprocal Space Mapping. *Applied Physics Letters* **80**, 3913–3915 (2002).
42. Saito, K., Ulyanenko, A., Grossmann, V., Röss, H., Brüggemann, L., Ohta, H., Kurosawa, T., Ueki, S. & Funakubo, H. Structural Characterization of BiFeO₃ Thin Films by Reciprocal Space Mapping. *Japanese Journal of Applied Physics* **45**, 7311–7314 (2006).
43. Stoumpos, C. C., Cao, D. H., Clark, D. J., Young, J., Rondinelli, J. M., Jang, J. I., Hupp, J. T. & Kanatzidis, M. G. Ruddlesden–Popper Hybrid Lead Iodide Perovskite 2D Homologous Semiconductors. *Chemistry of Materials* **28**, 2852–2867 (2016).
44. Chen, Y., Sun, Y., Peng, J., Zhang, W., Su, X., Zheng, K., Pullerits, T. & Liang, Z. Tailoring Organic Cation of 2D Air-Stable Organometal Halide Perovskites for Highly Efficient Planar Solar Cells. *Advanced Energy Materials* **7**, 1700162 (2017).
45. Zhang, X., Munir, R., Xu, Z., Liu, Y., Tsai, H., Nie, W., Li, J., Niu, T., Smilgies, D.-M., Kanatzidis, M. G., Mohite, A. D., Zhao, K., Amassian, A. & Liu, S. F. Phase Transition Control for High Performance Ruddlesden–Popper Perovskite Solar Cells. *Advanced Materials* **30**, 1707166 (2018).
46. Quintero-Bermudez, R., Gold-Parker, A., Proppe, A. H., Munir, R., Yang, Z., Kelley, S. O., Amassian, A., Toney, M. F. & Sargent, E. H. Compositional and Orientational Control in Metal Halide Perovskites of Reduced Dimensionality. *Nature Materials*, 1 (2018).

47. Pareja-Rivera, C., Solís-Cambero, A. L., Sánchez-Torres, M., Lima, E. & Solis-Ibarra, D. On the True Composition of Mixed-Cation Perovskite Films. *ACS Energy Letters* **3**, 2366–2367 (2018).
48. Proppe, A. H., Quintero-Bermudez, R., Tan, H., Voznyy, O., Kelley, S. O. & Sargent, E. H. Synthetic Control over Quantum Well Width Distribution and Carrier Migration in Low-Dimensional Perovskite Photovoltaics. *Journal of the American Chemical Society* **140**, 2890–2896 (2018).
49. Smith, I. C., Hoke, E. T., Solis-Ibarra, D., McGehee, M. D. & Karunadasa, H. I. A Layered Hybrid Perovskite Solar-Cell Absorber with Enhanced Moisture Stability. *Angewandte Chemie International Edition* **126**, 11414–11417 (2014).
50. Whitfield, P. S., Herron, N., Guise, W. E., Page, K., Cheng, Y. Q., Milas, I. & Crawford, M. K. Structures, Phase Transitions and Tricritical Behavior of the Hybrid Perovskite Methyl Ammonium Lead Iodide. *Scientific Reports* **6**, 35685 (2016).
51. Li, M., Wang, Z.-K., Zhuo, M.-P., Hu, Y., Hu, K.-H., Ye, Q.-Q., Jain, S. M., Yang, Y.-G., Gao, X.-Y. & Liao, L.-S. Pb–Sn–Cu Ternary Organometallic Halide Perovskite Solar Cells. *Advanced Materials* **30**, 1800258 (2018).
52. Wang, W., Ma, Y. & Qi, L. High-Performance Photodetectors Based on Organometal Halide Perovskite Nanonets. *Advanced Functional Materials* **27**, 1603653 (2017).
53. Suzuki, T., Nishi, Y. & Fujimoto, M. Ruddlesden–Popper Planar Faults and Nanotwins in Heteroepitaxial Nonstoichiometric Barium Titanate Thin Films. *Journal of the American Ceramic Society* **83**, 3185–3195 (2000).
54. Suzuki, T., Nishi, Y. & Fujimoto, M. Defect Structure in Homoepitaxial Non-Stoichiometric Strontium Titanate Thin Films. *Philosophical Magazine A* **80**, 621–637 (2000).
55. Boccara, A. C., Fournier, D., Jackson, W. & Amer, N. M. Sensitive Photothermal Deflection Technique for Measuring Absorption in Optically Thin Media. *Optics Letters* **5**, 377–379 (1980).
56. Jackson, W. B., Amer, N. M., Boccara, A. C. & Fournier, D. Photothermal Deflection Spectroscopy and Detection. *Applied Optics* **20**, 1333–1344 (1981).
57. Johnson, S. R. & Tiedje, T. Temperature Dependence of the Urbach Edge in GaAs. *Journal of Applied Physics* **78**, 5609–5613 (1995).
58. De Wolf, S., Holovsky, J., Moon, S.-J., Löper, P., Niesen, B., Ledinsky, M., Haug, F.-J., Yum, J.-H. & Ballif, C. Organometallic Halide Perovskites: Sharp Optical Absorption Edge and Its Relation to Photovoltaic Performance. *The Journal of Physical Chemistry Letters* **5**, 1035–1039 (2014).
59. Williams, O. F., Guo, Z., Hu, J., Yan, L., You, W. & Moran, A. M. Energy Transfer Mechanisms in Layered 2D Perovskites. *The Journal of Chemical Physics* **148**, 134706 (2018).

60. Shang, Q., Wang, Y., Zhong, Y., Mi, Y., Qin, L., Zhao, Y., Qiu, X., Liu, X. & Zhang, Q. Unveiling Structurally Engineered Carrier Dynamics in Hybrid Quasi-Two-Dimensional Perovskite Thin Films toward Controllable Emission. *The Journal of Physical Chemistry Letters* **8**, 4431–4438 (2017).
61. Toby, B. H. & Von Dreele, R. B. GSAS-II: The Genesis of a Modern Open-Source All Purpose Crystallography Software Package. *Journal of Applied Crystallography* **46**, 544–549 (2013).
62. Dollase, W. A. Correction of Intensities for Preferred Orientation in Powder Diffraction: Application of the March Model. *Journal of Applied Crystallography* **19**, 267–272 (1986).
63. Jiang, Z. GIXSGUI: A MATLAB Toolbox for Grazing-Incidence X-Ray Scattering Data Visualization and Reduction, and Indexing of Buried Three-Dimensional Periodic Nanostructured Films. *Journal of Applied Crystallography* **48**, 917–926 (2015).
64. Vandewal, K., Albrecht, S., Hoke, E. T., Graham, K. R., Widmer, J., Douglas, J. D., Schubert, M., Mateker, W. R., Bloking, J. T., Burkhard, G. F., Sellinger, A., Fréchet, J. M. J., Amassian, A., Riede, M. K., McGehee, M. D., Neher, D. & Salleo, A. Efficient Charge Generation by Relaxed Charge-Transfer States at Organic Interfaces. *Nature Materials* **13**, 63–68 (2014).
65. Vandewal, K., Goris, L., Haenen, K., Geerts, Y. & Manca, J. V. Highly Sensitive Spectroscopic Characterization of Inorganic and Organic Heterojunctions for Solar Cells. *The European Physical Journal Applied Physics* **36**, 281–283 (2006).
66. Buchaca-Domingo, E., Vandewal, K., Fei, Z., Watkins, S. E., Scholes, F. H., Bannock, J. H., de Mello, J. C., Richter, L. J., DeLongchamp, D. M., Amassian, A., Heeney, M., Salleo, A. & Stingelin, N. Direct Correlation of Charge Transfer Absorption with Molecular Donor:Acceptor Interfacial Area via Photothermal Deflection Spectroscopy. *Journal of the American Chemical Society* **137**, 5256–5259 (2015).
67. Momma, K. & Izumi, F. VESTA-3 for Three-Dimensional Visualization of Crystal, Volumetric and Morphology Data. *Journal of Applied Crystallography* **44**, 1272–1276 (2011).
68. Kelly, A. & Knowles, K. M. *Crystallography and Crystal Defects* (John Wiley & Sons, 2012).
69. Weisstein, E. W. *Gaussian Function* <http://mathworld.wolfram.com/GaussianFunction.html>.

Chapter 6

Enhanced Yield-Mobility Products in Hybrid Halide Ruddlesden–Popper Compounds with Aromatic Ammonium Spacers

6.1 Abstract

Hybrid halide Ruddlesden–Popper compounds are related to three-dimensional hybrid AMX_3 perovskites (*e.g.* where A is a monovalent cation, M is a divalent metal cation, and X is a halogen) with the general formula $L_2A_{n-1}M_nX_{3n+1}$ where L is a monovalent spacer cation. The crystal structure comprises perovskite-like layers separated by organic cation spacers. Here two Ruddlesden–Popper compounds with a conjugated cation, 2-(4-biphenyl)ethylammonium (BPEA) prepared by solvothermal and solvent evaporation techniques are reported. The structures of the two compounds: $(BPEA)_2PbI_4$ and $(BPEA)_2(CH_3NH_3)Pb_2I_7$, were solved by X-ray crystallography. The aromatic rings of the

BPEA groups are well-separated in the organic layers leading to optical properties comparable to $n = 1$ and 2 hybrid halide Ruddlesden–Popper compounds with simpler alkylammonium cations. The ambient stability of both compounds over time was also confirmed by powder X-ray diffraction. Finally, the transient photoconductance, measured by time-resolved microwave conductivity, show that the compounds have maximum yield-mobility products respectively of $0.07 \text{ cm}^2 \text{ V}^{-1} \text{ s}^{-1}$ and $1.11 \text{ cm}^2 \text{ V}^{-1} \text{ s}^{-1}$ for $(\text{BPEA})_2\text{PbI}_4$ and $(\text{BPEA})_2(\text{CH}_3\text{NH}_3)\text{Pb}_2\text{I}_7$, both slightly enhanced over what has been measured for compounds with *n*-butylammonium spacer cations.

6.2 Introduction

Hybrid organic-inorganic perovskites (HOIPs) are solution-processable semiconductors with a diversity of structures allowed by the combination of organic and inorganic groups.^{1–7} The power conversion efficiency (PCE) of photovoltaic devices composed of hybrid perovskite alloys (based on $\text{CH}_3\text{NH}_3\text{PbI}_3$ and $\text{HC}(\text{NH}_2)_2\text{PbI}_3$) has increased to 23.7% very quickly,⁸ competitive with other thin film technologies such as CIGS and CdTe.^{9,10} Additionally, HOIPs have shown great synthetic tunability, allowing control of emission energies, making them promising for light emission applications.^{11–20} However, three-dimensional hybrid perovskites have been shown to be susceptible to degradation from heat, light, and moisture, hampering their long-term device stability.^{21–26}

The class of two-dimensional layered perovskite compounds known as Ruddlesden–Popper (R–P) compounds, have been synthesized using organic ammonium and main group cations and halide anions. These compounds usually display enhanced stability in ambient conditions.^{27–30} The R–P compounds have a general stoichiometric formula of $\text{L}_2(\text{CH}_3\text{NH}_3)_{n-1}\text{Pb}_n\text{I}_{3n+1}$, where L represents a large organic cation that serves to break up the three-dimensional connectivity of the perovskite crystal structure and *n* represents the

number of lead iodide octahedra in the inorganic layer.^{31,32} The enhanced stability of R–P perovskites has been attributed to the increased hydrophobicity from the organic layer by the L cations.^{33–35} The addition of this organic layer, however, leads to highly anisotropic charge transport, and devices based on two-dimensional perovskites have only achieved PCE values close to 15%.^{28,36} The wider band gaps of two-dimensional perovskites relative to three-dimensional perovskites does provide the benefit of tuning the emission in light emitting diodes.^{14,15,17} Recent efforts to embed two-dimensional perovskite moieties into the overall three-dimensional perovskite matrix have also yielded efficiencies closer to that of champion devices, with some increased stability.^{37–39} The majority of studies have focused on alkylammonium L cations, and these compounds have resulted in the highest photovoltaic efficiencies to date for two-dimensional perovskite compounds.^{28,33,40–42} Various conjugated ions have also been incorporated into the Ruddlesden–Popper structure,^{12,43,44} including thiophenes,^{45,46} and the single phenyl analog of the structures reported here, phenethylammonium.^{27,47} Finally, recent efforts have embraced other layered perovskite motifs such as Dion–Jacobson compounds.^{48,49} Controlling the properties of lower dimensional perovskites by varying the L cation is desirable for tuning the electronic properties of the materials system either in pure systems or in composites.

We report here two Ruddlesden–Popper compounds using the aromatic organic cation 2-(4-biphenyl)ethylammonium (BPEA), resulting in the compounds $(\text{BPEA})_2\text{PbI}_4$ ($n = 1$) and $(\text{BPEA})_2(\text{CH}_3\text{NH}_3)\text{Pb}_2\text{I}_7$ ($n = 2$). These compounds were synthesized by solvothermal and solvent evaporation techniques, and the resulting crystal structures were solved from X-ray crystallography. Structural measurements after aging in ambient conditions show that both compounds are stable without encapsulation. The optical absorbance was measured with ultraviolet-visible spectroscopy, and the charge transport was characterized by time-resolved microwave conductivity (TRMC). By utilizing TRMC, carrier dynamics in the synthesized powders could be measured without device formation.

6.3 Results and Discussion

The structures of $(\text{BPEA})_2\text{PbI}_4$ and $(\text{BPEA})_2(\text{CH}_3\text{NH}_3)\text{Pb}_2\text{I}_7$, solved from single-crystal X-ray diffraction at 100 K, are shown in Figure 6.1, visualized along the [010] crystallographic direction for $(\text{BPEA})_2\text{PbI}_4$ and [001] for $(\text{BPEA})_2(\text{CH}_3\text{NH}_3)\text{Pb}_2\text{I}_7$ using VESTA.⁵⁰ The parameters of the structure solutions of each compound are shown in Table 6.1, and single-crystal diffraction images are presented in Section 6.5.2. Both compounds have orthorhombic unit cells and the diffraction data were fit best by non-centrosymmetric space groups. The organic BPEA moieties form symmetric bilayers in both compounds, while the inorganic framework in the two perovskites consists of corner-sharing lead iodide octahedra. The organic bilayer formed between the lead iodide sheets is consistent with previously reported hybrid halide Ruddlesden–Popper structures with other organic cation spacers.^{28,45,47,51,52} The BPEA moieties from subsequent layers do not interdigitate, preventing π - π interactions between L groups on each lead iodide layer. If we consider that the *n*-butylammonium cation would fit into a cylinder with a diameter of ~ 1.5 Å and it forms a bilayer structure rather than interdigitating, it is unsurprising that 2-(4-biphenyl)ethylammonium which packs with a closest C-C distance between phenyl rings of ~ 3.4 Å also forms separate layers. The widest region of the phenyl ring has a diameter of ~ 4 Å, so this aromatic packing distance is required when accounting for bond rotations. The separation distance between the lead iodide layers is ~ 15 Å in $(\text{BPEA})_2\text{PbI}_4$ and $(\text{BPEA})_2(\text{CH}_3\text{NH}_3)\text{Pb}_2\text{I}_7$, compared to ~ 10 Å in $(\text{PEA})_2\text{PbI}_4$ and $(\text{PEA})_2(\text{CH}_3\text{NH}_3)\text{Pb}_2\text{I}_7$.^{44,52} There is a slight difference in the layer spacing between the BPEA $n = 1$ (15.0 Å) and $n = 2$ (14.7 Å) that may be due to slightly more efficient packing in the $n = 2$ compound; regardless, the organic layers appear to be consistent in size. Geometric details of both crystal structures, including bond lengths and angles are tabulated in Table 6.2. The octahedra in the lead iodide layers in both $(\text{BPEA})_2\text{PbI}_4$ and $(\text{BPEA})_2(\text{CH}_3\text{NH}_3)\text{Pb}_2\text{I}_7$ are highly tilted in

plane, with equatorial Pb-I-Pb bond angles of approximately 155° in both structures. The measured bond lengths in both compounds are consistent (*i.e.* independent of L cation used) with previous observations in other hybrid halide Ruddlesden–Popper compounds, however the out of plane tilt between connected Pb-I octahedra (in the $n = 2$) are much stiffer (179.2°) compared to $(\text{BA})_2(\text{CH}_3\text{NH}_3)\text{Pb}_2\text{I}_7$ (165.6°).

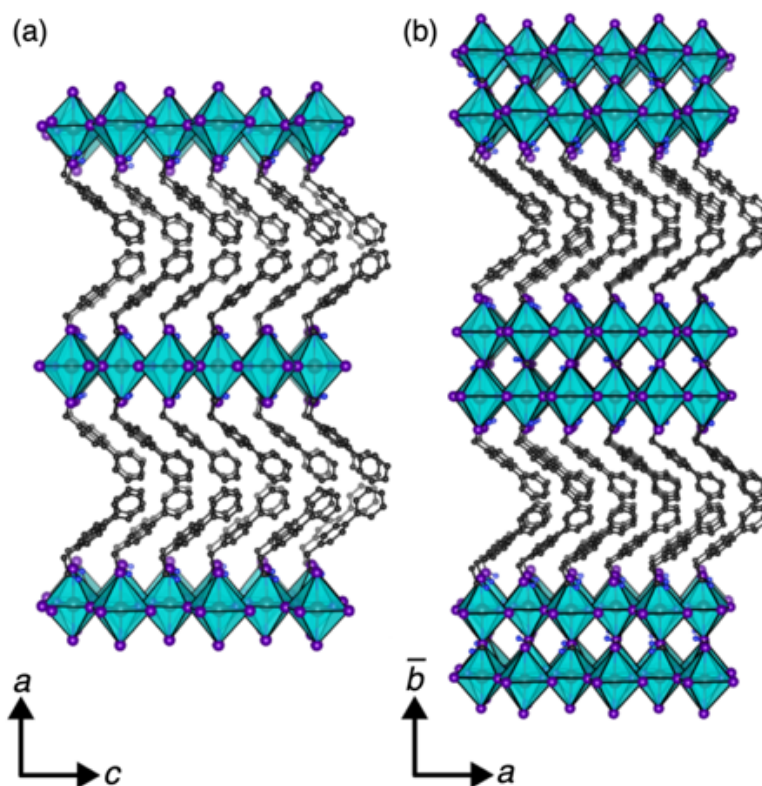


Figure 6.1: (a) Crystal structures of $(\text{BPEA})_2\text{PbI}_4$ and (b) $(\text{BPEA})_2(\text{CH}_3\text{NH}_3)\text{Pb}_2\text{I}_7$ solved by single-crystal X-ray diffraction, projected down the b and c crystallographic axes, respectively. The BPEA cations pack diagonally, are eclipsed with each other, and do not interdigitate.

Because bulk characterization measurements were carried out on powders consisting of crushed single-crystals, solved crystal structures were used to simulate powder X-ray diffraction (PXRD) patterns for comparison. Simulated diffraction patterns were generated as described in Section 6.5.1. Figure 6.2 shows PXRD measurements of crushed crystals of $(\text{BPEA})_2\text{PbI}_4$ and $(\text{BPEA})_2(\text{CH}_3\text{NH}_3)\text{Pb}_2\text{I}_7$ both immediately after preparation and

Table 6.1: Crystallographic Data for (BPEA)₂PbI₄ and (BPEA)₂(CH₃NH₃)Pb₂I₇ at 100 K.

Empirical Formula	(BPEA) ₂ PbI ₄	(BPEA) ₂ (CH ₃ NH ₃)Pb ₂ I ₇
Crystal Habit and Color	plate, orange	plate, red
Crystal System	orthorhombic	orthorhombic
Space Group (#)	<i>Cmc</i> 2 ₁ (36)	<i>Ab</i> a2 (41)
Volume (Å³)	3250.8(8)	4199.5(6)
Temperature (K)	100(2)	100(2)
<i>a</i> (Å)	42.920(6)	8.7633(8)
<i>b</i> (Å)	8.7431(11)	55.030(5)
<i>c</i> (Å)	8.6629(14)	8.7081(7)
<i>α</i> (°)	90	90
<i>β</i> (°)	90	90
<i>γ</i> (°)	90	90
Z	4	4
<i>ρ</i> (g mol⁻¹)	1107.32	1731.30
Dens. (g cm⁻³)	2.263	2.738
Abs. (mm⁻¹)	9.007	13.176
<i>F</i>₀₀₀	2016	3072
Reflections	10433 (2500)	9269 (3551)
<i>R</i>_{int}	0.0927	0.0861
<i>R</i>₁	0.0533	0.0653
<i>wR</i>₂	0.0892	0.1471
<i>∂F</i> (e Å⁻³)	2.612 & -1.446	4.473 & -5.449
GOF	1.436	1.095

after five weeks of aging in ambient conditions, along with their simulated diffraction patterns. To capture the correct structural behavior in (BPEA)₂(CH₃NH₃)Pb₂I₇, the simulated diffraction pattern included texturing along the [010] crystallographic direction, which is the lead iodide layer stacking direction (Figure 6.1). It is possible that due to the ten-

dency of these $n = 2$ crystals to grow as anisotropic flakes, the resulting powder retains some crystalline texture. If the slow growth direction during preparation was along this stacking direction (due to the incorporation of the BPEA layer), it is consistent with the flake-like crystals. This is evident when compared to a simulation of an isotropic sample of $(\text{BPEA})_2(\text{CH}_3\text{NH}_3)\text{Pb}_2\text{I}_7$, in which the relative peak height intensities do not match well with our measurement (Figure 6.7). In both the $n = 1$ and $n = 2$ compounds, the position and intensities of peaks in the diffraction patterns show no change after five weeks of aging. This suggests that $(\text{BPEA})_2(\text{CH}_3\text{NH}_3)_{n-1}\text{Pb}_n\text{I}_{3n+1}$ possesses increased stability relative to three-dimensionally connected perovskites, a property that has been widely observed in layered perovskite compounds.^{27,28,53} The subtle differences in relative peak heights between the as-synthesized and aged samples is likely due to the slight variations in the overall crystalline texturing from the loading of the powder samples for measurement. Ultimately, the structural measurements on both compounds show no formation of PbI_2 (Figure 6.8) and no other degradation upon aging in ambient conditions.

The optical absorbances of both layered perovskite compounds were measured and are presented in Figure 6.3, showing expected behavior. Due to the large optical density of both powder samples, absorbances were measured by taking diffuse reflectance data and transforming them according to the Kubelka-Munk equations.⁵⁴ In both cases, clear excitonic features are visible at the optical absorbance onset, consistent with the quantum confined structure of the Ruddlesden–Popper compounds. In $(\text{BPEA})_2\text{PbI}_4$, the peak attributed to excitonic absorption occurs at 2.4 eV, while in $(\text{BPEA})_2(\text{CH}_3\text{NH}_3)\text{Pb}_2\text{I}_7$, it appears at 2.2 eV. Both of these energies are equal to previously measured exciton energies in Ruddlesden–Popper systems containing both butylammonium and phenethylammonium spacer groups.^{47,55}

The charge carrier dynamics of these two compounds were analyzed using time-resolved microwave conductivity (TRMC).^{55–63} Excitation of the compounds with a pulse

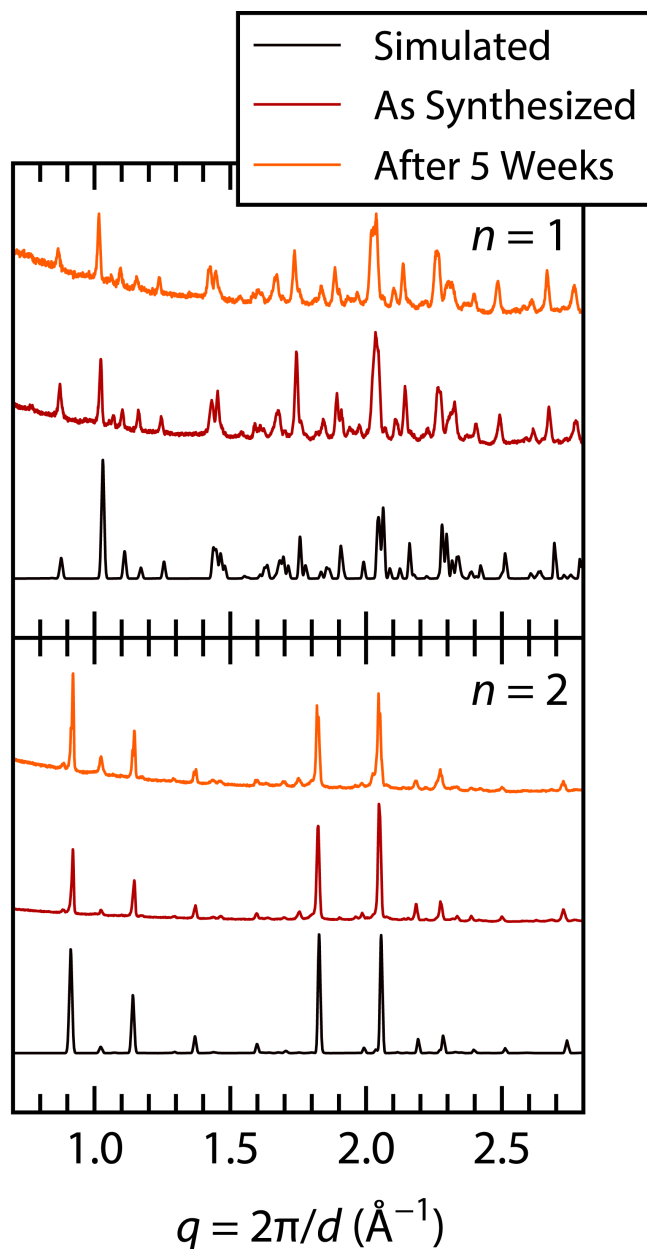


Figure 6.2: Powder X-ray diffraction (PXRD) spectra of $(\text{BPEA})_2\text{PbI}_4$ ($n = 1$) and $(\text{BPEA})_2(\text{CH}_3\text{NH}_3)\text{Pb}_2\text{I}_7$ ($n = 2$) both after preparation and after five weeks of aging in ambient conditions, along with simulated PXRD patterns of solved structures shown in Figure 6.1.

of light with energy above the band gap creates free carriers and excitons. Only the free carriers then interact with the microwave electric field (frequency range of 8 – 9 GHz) and the attenuation of this applied microwave signal, caused by carrier drift, can be then used

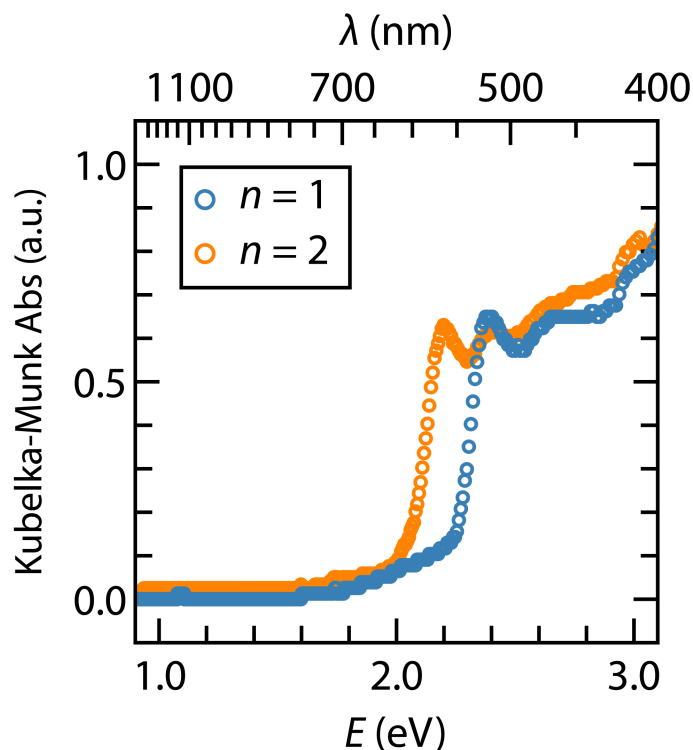


Figure 6.3: Optical absorbance of $(\text{BPEA})_2\text{PbI}_4$ ($n = 1$) and $(\text{BPEA})_2(\text{CH}_3\text{NH}_3)\text{Pb}_2\text{I}_7$ ($n = 2$) measured from diffuse reflectance of powder samples. Reflectance data were converted into absorbance values using the Kubelka-Munk equations and show excitonic features at 2.4 eV and 2.2 eV for $n = 1$ and 2, respectively.

to calculate the transient photoconductance in the sample. Using these photoconductance measurements, a value of $\phi \Sigma \mu$ can be determined, which is the figure-of-merit for TRMC – $\phi \Sigma \mu$ is the product of ϕ (the yield of free carriers per incident photon) and the sum of the electron and hole mobilities, $\Sigma \mu = \mu_e + \mu_h$. The value of $\phi \Sigma \mu$ at short times after the excitation pulse typically exhibit strong laser fluence dependence due to recombination of electron hole pairs.^{57,64} Fluence-dependent measurements of $\phi \Sigma \mu$ were therefore collected for both $(\text{BPEA})_2\text{PbI}_4$ and $(\text{BPEA})_2(\text{CH}_3\text{NH}_3)\text{Pb}_2\text{I}_7$ and are shown in Figure 6.4, along with previously measured values for $(\text{BA})_2\text{PbI}_4$ and $(\text{BA})_2(\text{CH}_3\text{NH}_3)\text{Pb}_2\text{I}_7$.⁵⁵ The lowest measurable fluence for both compounds was set by the signal-to-noise of our instrument. The peak yield-mobility products, $\phi \Sigma \mu_{\text{max}}$, for the $n = 1$ and 2 compounds are $0.07 \text{ cm}^2 \text{ V}^{-1} \text{ s}^{-1}$ (at

2.25×10^{13} photons cm^{-2}) and $1.11 \text{ cm}^2 \text{ V}^{-1} \text{ s}^{-1}$ (at 5.93×10^{12} photons cm^{-2}), respectively.

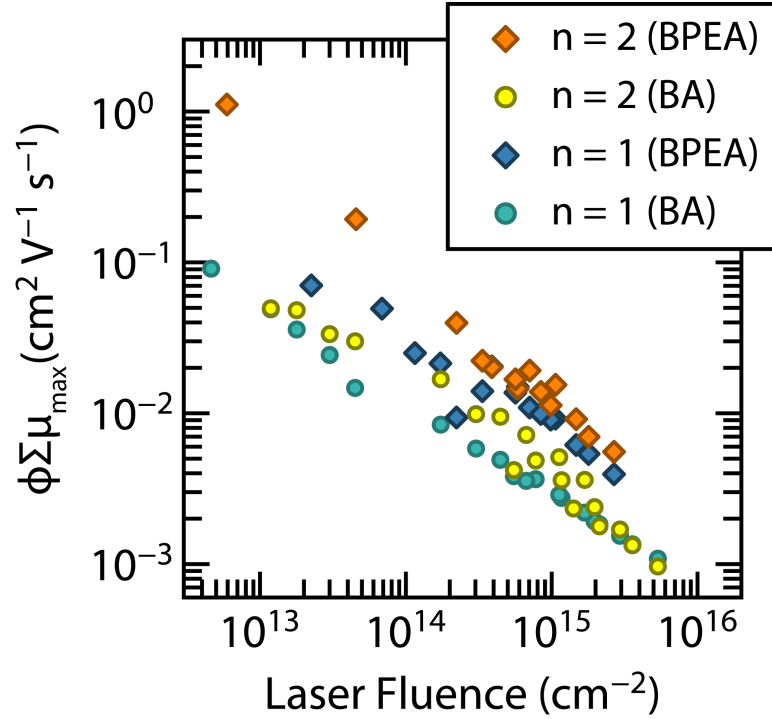


Figure 6.4: Maximum value of the TRMC figure-of-merit $\phi \Sigma \mu$ over a wide range of excitation laser fluences for $(\text{BPEA})_2\text{PbI}_4$ ($n = 1$) and $(\text{BPEA})_2(\text{CH}_3\text{NH}_3)\text{Pb}_2\text{I}_7$ ($n = 2$), along with TRMC data of $(\text{BA})_2\text{PbI}_4$ and $(\text{BA})_2(\text{CH}_3\text{NH}_3)\text{Pb}_2\text{I}_7$ from reference 55. Monotonic increases seen with decreasing fluence are characteristic of shorter carrier lifetimes and larger recombination rate coefficients compared to MAPbI_3 .

To understand the TRMC data, we must consider the different charge recombination pathways in both compounds. Charge recombination in semiconductors is governed by the rate equation $R = k_1 n(t) + k_2 n(t)^2 + k_3 n(t)^3$, where $n(t)$ is the instantaneous carrier concentration and k_1 , k_2 , and k_3 are the rate constants of monomolecular, bimolecular, and trimolecular or Auger recombination, respectively.^{55,56,65} By changing the incident laser fluence, we can change the initial carrier concentration and observe the effects of recombination at short times, *i.e.* if there is significant recombination during the excitation pulse width (~ 5 ns) and response time of the cavity (~ 60 ns). Therefore, at low initial carrier concentrations, it is expected that the recombination dynamics are dominated by

monomolecular recombination – since the recombination rate is linear with $n(t)$ in this regime, we would expect the TRMC plot to have a very shallow slope on a logarithmic scale because little recombination occurs at short times. Such behavior is observed in TRMC data of methylammonium lead iodide at low laser fluences.^{55–57} As the laser fluence and carrier concentration increases, both bimolecular and Auger recombination pathways become more active and the dependence of $\phi \Sigma \mu$ becomes increasingly more negative. We see an overall monotonic increase in $\phi \Sigma \mu$ for both compounds with decreasing laser fluence and do not see a plateau characteristic of monomolecular recombination. This dependence has been observed in previous TRMC measurements of layered hybrid halides and has been attributed to larger higher order recombination rate coefficients.^{55,56}

The electronic properties of layered R–P phases are highly anisotropic and the details of the physical properties of the samples must be considered to understand the TRMC results. The carrier mobilities within the Pb–I sheets (in-plane) are much higher than between subsequent Pb–I sheets (out-of-plane) because the electronic coupling between layers in R–P compounds through the L cation is weak.^{28,66–68} It is therefore important to understand the orientation of the crystals with respect to the microwave field to interpret the magnitude of the figure of merit. TRMC measurements on $n = 1$ and 2 were done on powders whereas those of $(\text{BA})_2\text{PbI}_4$ and $(\text{BA})_2(\text{CH}_3\text{NH}_3)\text{Pb}_2\text{I}_7$ were performed on thin films. However, these films were found to be highly textured – the phase fractions corresponding to lead iodide layers being oriented in-plane (parallel to substrate surface) were $f = 1.0$ in $n = 1$ and $f = 0.75$ in $n = 2$, respectively.⁵⁵ Therefore, the thin film measurements should also yield values that are highly biased towards the in-plane mobilities. In the $(\text{BPEA})_2\text{PbI}_4$ compound, the laser excitation consists of photons with energy (2.33 eV) slightly below the excitonic peak energy (2.4 eV) due to limitations in our experimental setup, but there is still reasonable absorbance, as shown in Figure 6.3. This results in a small value of ϕ in both $(\text{BPEA})_2\text{PbI}_4$ and $(\text{BA})_2\text{PbI}_4$ since the excitation is in a region where absorbance increases

steeply with energy, the latter also having an onset of 2.4 eV, making a direct comparison between the two compounds difficult. However, we do observe that the TRMC data for the BPEA $n = 1$ compound are consistently higher than that of the corresponding BA compound (Figure 6.4). The $n = 2$ (BPEA)₂(CH₃NH₃)Pb₂I₇ compound on the other hand, has a much larger value of $\phi \Sigma \mu_{\max}$ (0.19 cm² V⁻¹ s⁻¹ at 4.56×10^{13} photons per cm²), than the corresponding (BA)₂(CH₃NH₃)Pb₂I₇ at a comparable fluence (0.03 cm² V⁻¹ s⁻¹ at 4.49×10^{13} photons per cm²). It is difficult to make a direct comparison without knowing the value of ϕ , but we can speculate that the origin of the increased TRMC signal is due to decreased dielectric confinement. The majority (75%) of Pb-I sheets in (BA)₂(CH₃NH₃)Pb₂I₇ film are oriented in-plane, so even a powder sample of (BPEA)₂(CH₃NH₃)Pb₂I₇ with entirely in-plane Pb-I sheets would not solely account for the order of magnitude difference in $\phi \Sigma \mu_{\max}$, assuming similar carrier yields and mobilities. Factors that could therefore have larger influence on this value are grain size, defect density, and the dielectric environment induced by the spacer cation. Yield-mobility products measured from TRMC can be affected by the grain size, which is $\sim \mu\text{m}$ scale for the BPEA powders and was ~ 100 nm in the BA films, however, this effect has been shown to be minimal above 100 nm in CH₃NH₃PbI₃.⁶⁹ Slower solvothermal crystal growth could result in BPEA crystals with a lower defect concentration than faster growth during spin-coating of the BA thin films, but the monotonic increase in $\phi \Sigma \mu_{\max}$ with decreasing laser fluence suggests comparable recombination rate constants.⁵⁵ The increased TRMC signal in both BPEA compounds can be attributed to increased charge screening effects due to a larger dielectric constant, allowing easier dissociation of excitons into free carriers. This difference in the effective dielectric environment could also influence carrier mobility within the lead iodide sheets, accounting for some of the increase. Therefore, when considering all the factors affecting $\phi \Sigma \mu_{\max}$, it appears that the use of aromatic ammonium cations improves carrier transport relative to that of a straight alkyl chain. Our result suggests that using a higher dielectric constant group in

the spacer molecule in Ruddlesden–Popper compounds can improve the overall transport properties.

6.4 Conclusion

Two hybrid Ruddlesden–Popper compounds with a 2-(4-biphenyl)ethylammonium cationic spacer were prepared using solvothermal and solvent evaporation techniques. The two structures, $(\text{BPEA})_2\text{PbI}_4$ and $(\text{BPEA})_2(\text{CH}_3\text{NH}_3)\text{Pb}_2\text{I}_7$, were solved by X-ray crystallography and correspond to the $n = 1$ and 2 compounds of the general formula $(\text{BPEA})_2(\text{MA})_{n-1}\text{Pb}_n\text{I}_{3n+1}$. Both compounds form in the expected Ruddlesden–Popper structures with a bilayer of the larger organic cations separating the lead iodide inorganic layers. Structural measurements from X-ray diffraction on the as-synthesized and aged powders showed material stability in ambient conditions. Optical properties of both compounds were measured by diffuse reflectance and show highly excitonic absorption and optical bandgaps consistent with other $n = 1$ and $n = 2$ layered R–P compounds. Finally, time-resolved microwave conductivity was used to measure the charge transport properties. The contactless TRMC technique allowed us to directly measure carrier dynamics of the perovskite powders without the need to cast films or prepare devices. The yield-mobility products measured by TRMC were compared to those from the $(\text{BA})_2(\text{CH}_3\text{NH}_3)_{n-1}\text{Pb}_n\text{I}_{3n+1}$ R–P series and were found to possess comparable values in the $n = 1$ compounds but are an order of magnitude higher in $n = 2$. It is unclear whether this increase is directly due to the presence of the aromatic groups in the organic spacer cations, but it appears that the use of a higher dielectric constant organic spacer can improve the transport properties of Ruddlesden–Popper perovskite materials.

6.5 Appendix

6.5.1 Experimental Methods

(BPEA)₂PbI₄ Preparation

Single crystals of (BPEA)₂PbI₄ were prepared through solvothermal methods. A stoichiometric ratio of lead (II) iodide (PbI₂, 100 mg), 2-(4-biphenyl)ethylamine (BPEA, 85.6 mg), and aqueous (57 wt% in H₂O) hydroiodic acid (HI, 1 mL) were added to a pressure vessel (23 mL PTFE-lined stainless steel Parr autoclave). The temperature of the reaction vessel was ramped to 150°C over 2 hours, held for 8 hours, and then allowed to cool to room temperature over 2 hours. Resulting crystals were then washed with diethyl ether ((C₂H₅)₂O) and dried under vacuum for one day. Solvothermal synthesis of (BPEA)₂PbI₄ was required to produce single-crystals of sufficient size for X-ray crystallography.

(BPEA)₂(CH₃NH₃)Pb₂I₇ Preparation

Single crystals of (BPEA)₂(CH₃NH₃)Pb₂I₇ were prepared *via* solvent evaporation – a stoichiometric ratio of previously synthesized (BPEA)₂PbI₄ (30 mg), PbI₂ (24.9 mg), and methylammonium iodide (CH₃NH₃I, 8.6 mg) were dissolved in a 2:1 mixture (volume/volume) of acetone and nitromethane (15 mL). The mixture was stirred and heated at 90°C to form a pale-yellow solution. The solvent was allowed to evaporate at room temperature over six days, yielding bright, red crystals.

Single-Crystal X-Ray Diffraction

Single-crystal X-ray diffraction (SC-XRD) data was collected for each of the two Ruddlesden–Popper compounds with a Bruker KAPPA APEX II diffractometer equipped with an APEX II CCD detector utilizing a TRIUMPH monochromator and a Mo-K α X-ray

source ($\lambda = 0.71073 \text{ \AA}$). The crystals were mounted on a cryoloop with Paratone-N oil. The multi-scan method, SADABS, was used for absorption correction of the data.⁷⁰ Further calculations were done using SHELXTL.⁷¹ The low bond precision in carbon bonds is due to the disorder and poor contrast near to heavier elements. Structures were determined using direct methods,⁷² and the graphical depictions of crystal structures shown were created with VESTA.⁵⁰

Powder X-Ray Diffraction

Powder X-ray diffraction (PXRD) was measured using a Panalytical Empyrean powder diffractometer in reflection mode with a Cu-K α source, operating with an accelerating voltage of 45 kV and a beam current of 40 mA. Simulated diffraction patterns were calculated using the General Structure Analysis System (GSAS).⁷³ For simulated diffraction patterns containing preferred orientation, March–Dollase orientational correction factors were used.⁷⁴

Ultraviolet-Visible Spectroscopy

Absorption spectra were determined by grinding crystals into powders and measuring diffuse reflectance with a Shimadzu UV-2600 ultraviolet-visible spectrophotometer equipped with an integrating sphere. Reflectance data were converted to absorbance using the Kubelka-Munk equations.⁵⁴

Time-Resolved Microwave Conductivity

TRMC measurements were conducted with an experimental setup described previously.^{55,56,65} A Sivers IMA VO4280X/00 voltage-controlled oscillator (VCO) (approximate power of 16 dBm and a tunable frequency range of 8–15 GHz) was used to generate a microwave frequency signal. The signal was then directed into a Fairview Microwave SFC0712

electronic circulator, a three-port device that rotates signals from port 1 to port 2 and signals from port 2 to port 3. The signal from port 2 was then fed into a Fairview Microwave 90AC206 SMA to X-band waveguide and is coupled to an X-band cavity with homebuilt coupling iris and tuning screw. The cavity operates in TE_{103} mode, and a homemade copper plate with slots along direction of microwave current allows optical access to the sample. The microwaves form standing waves and the tuning screw allows for over coupling, critical coupling, and under coupling to the cavity – all experiments reported were performed in the under coupled regime. The powder samples were mounted to the inside of the cavity with double-sided tape and placed at the maximum of the microwave electric field. Reflected microwaves are directed to a Fairview Microwave SMD0218 zero-bias Schottky diode detector, operating in the linear regime. The rectified signal was amplified by a three stage, DC-coupled wide-band amplifier consisting of Texas Instruments THS3091 operational amplifiers. For the reference signal, the microwave signal was split at the source to normalize the reflected power from the cavity. The amplified signal and reference were detected using a Tektronix TDS 3032C digital oscilloscope. Free carriers are generated in the powder samples through illumination with a Continuum Minilite pulsed Nd:YAG 532 nm laser (FWHM of ~ 5 ns), which drift under the influence of the microwave signal with a velocity proportional to their mobility ($\vec{v} = \mu \vec{E}$). The change in reflected microwave intensity is then used to determine the transient photoconductance which, in turn, is used to calculate the TRMC figure-of-merit: $\phi \Sigma \mu$ (yield-mobility product) at each fluence.⁷⁵

6.5.2 Single-crystal X-ray diffraction patterns

Single-crystal X-ray diffraction data was collected using a Bruker KAPPA APEX II diffractometer equipped with an APEX II CCD detector utilizing a TRIUMPH monochromator and a Mo-K α X-ray source ($\lambda = 0.71703$ Å). Diffraction images are shown below in Figures 6.5

and 6.6.

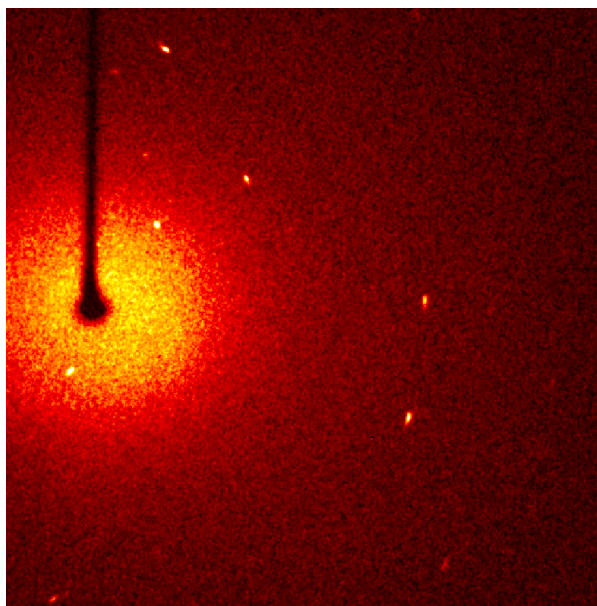


Figure 6.5: Sample X-ray diffraction image of (BPEA)₂PbI₄ obtained from grown single-crystals.

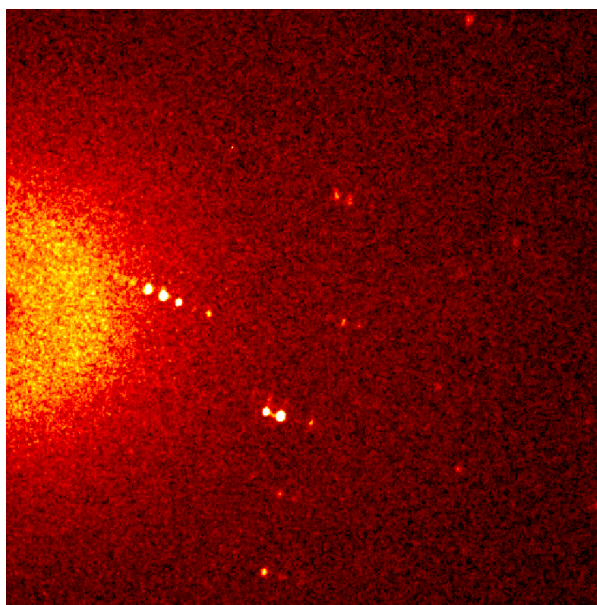


Figure 6.6: Sample X-ray diffraction image of (BPEA)₂(MA)Pb₂I₇ obtained from grown single-crystals.

6.5.3 Observed bond angles and distances in $(\text{BPEA})_2\text{PbI}_4$ and $(\text{BPEA})_2(\text{CH}_3\text{NH}_3)\text{Pb}_2\text{I}_7$

Structural details of $(\text{BPEA})_2\text{PbI}_4$ and $(\text{BPEA})_2(\text{CH}_3\text{NH}_3)\text{Pb}_2\text{I}_7$ are tabulated in Table 6.2. Bond distances for the four equatorial and two axial iodides, along with all I-Pb-I and Pb-I-Pb (if applicable) bond angles are presented. For comparison, the bond lengths and angles from $(\text{BA})_2\text{PbI}_4$ and $(\text{BA})_2(\text{CH}_3\text{NH}_3)\text{Pb}_2\text{I}_7$ are listed in Table 6.3.

Table 6.2: Structural details of $(\text{BPEA})_2\text{PbI}_4$ and $(\text{BPEA})_2(\text{CH}_3\text{NH}_3)\text{Pb}_2\text{I}_7$.

	$(\text{BPEA})_2\text{PbI}_4$	$(\text{BPEA})_2(\text{CH}_3\text{NH}_3)\text{Pb}_2\text{I}_7$
Bond Distances		
Pb-I_{axial} (1) (Å)	3.2073(14)	3.131(3)
Pb-I_{axial} (2) (Å)	3.2073(14)	3.2617(12)
Pb-I_{axial} (3) (Å)	N/A	3.2617(12)
Pb-I_{axial} (4) (Å)	N/A	3.131(3)
Pb-I_{equatorial} (1) (Å)	3.108(5)	3.141(4)
Pb-I_{equatorial} (2) (Å)	3.174(5)	3.179(3)
Pb-I_{equatorial} (3) (Å)	3.222(5)	3.191(4)
Pb-I_{equatorial} (4) (Å)	3.154(5)	3.157(4)
Bond Angles		
I-Pb-I_{axial} (1) (°)	176.4(3)	176.38(9)
I-Pb-I_{axial} (2) (°)	N/A	176.38(9)
I-Pb-I_{equatorial} (1) (°)	179.25(14)	176.31(8)
I-Pb-I_{equatorial} (2) (°)	178.18(16)	176.28(9)
Pb-I-Pb_{axial} (°)	N/A	179.2(3)
Pb-I-Pb_{equatorial} (°)	152.49(15)	154.52(11)

Table 6.3: Structural details of $(\text{BA})_2\text{PbI}_4$ and $(\text{BA})_2(\text{CH}_3\text{NH}_3)\text{Pb}_2\text{I}_7$.

	$(\text{BA})_2\text{PbI}_4$	$(\text{BA})_2(\text{CH}_3\text{NH}_3)\text{Pb}_2\text{I}_7$
Bond Distances		
Pb-I_{axial}(1) (Å)	3.201(16)	3.08(3)
Pb-I_{axial}(2) (Å)	3.213(13)	3.28(3)
Pb-I_{axial}(3) (Å)	N/A	3.25(3)
Pb-I_{axial}(4) (Å)	N/A	3.08(3)
Pb-I_{equatorial}(1) (Å)	3.164(7)	3.171(4)
Pb-I_{equatorial}(2) (Å)	3.212(8)	3.169(5)
Pb-I_{equatorial}(3) (Å)	3.191(6)	3.169(5)
Pb-I_{equatorial}(4) (Å)	3.160(7)	3.171(4)
Bond Angles		
I-Pb-I_{axial}(1) (°)	178.6(3)	177.3(3)
I-Pb-I_{axial}(2) (°)	N/A	177.3(3)
I-Pb-I_{equatorial}(1) (°)	179.2(5)	175.5(9)
I-Pb-I_{equatorial}(2) (°)	179.1(5)	175.5(9)
Pb-I-Pb_{axial} (°)	N/A	165.64(16)
Pb-I-Pb_{equatorial} (°)	155.1(3)	164.2(10)

6.5.4 Qualitative comparison of $(\text{BPEA})_2(\text{CH}_3\text{NH}_3)\text{Pb}_2\text{I}_7$ with isotropic and textured XRD simulations

The single-crystal structures of $(\text{BPEA})_2\text{PbI}_4$ and $(\text{BPEA})_2(\text{CH}_3\text{NH}_3)\text{Pb}_2\text{I}_7$ were used to simulate powder diffraction patterns and compared with actual measurements. Figure 6.7 shows the comparison of $(\text{BPEA})_2(\text{CH}_3\text{NH}_3)\text{Pb}_2\text{I}_7$ to a completely isotropic, untextured simulation of powder diffraction, showing poor agreement (isotropic $(\text{BPEA})_2\text{PbI}_4$ is presented as the simulation in Figure 6.2 of the main text). When texturing along the layer stacking direction ($[010]$) is added, the agreement between simulation and experiment is clear.

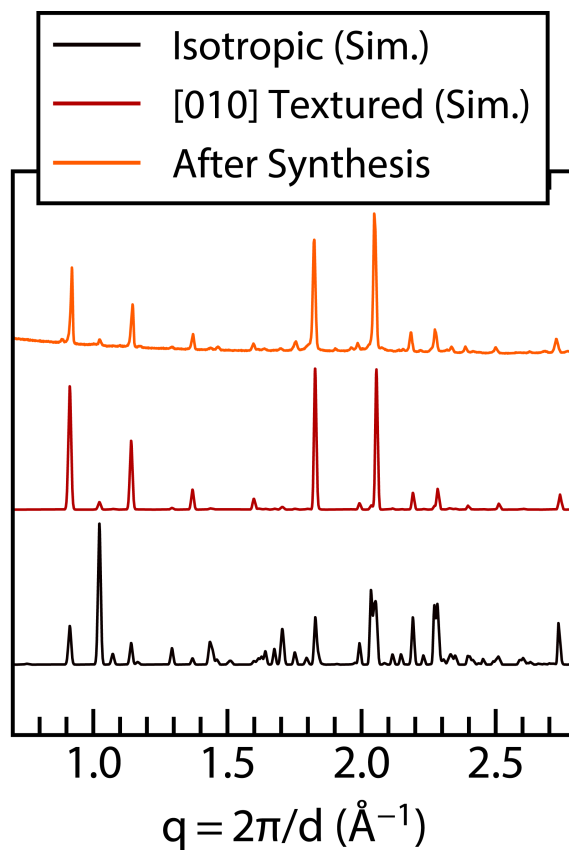


Figure 6.7: Powder X-ray diffraction of synthesized powder of $(\text{BPEA})_2(\text{CH}_3\text{NH}_3)\text{Pb}_2\text{I}_7$ compared to simulated diffraction patterns of an isotropic sample and a [010]-textured sample, illustrating structural agreement with the latter.

6.5.5 PXRD of aged powders compared to PbI_2

The aged (5 weeks in ambient) powders of $(\text{BPEA})_2\text{PbI}_4$ and $(\text{BPEA})_2(\text{CH}_3\text{NH}_3)\text{Pb}_2\text{I}_7$ were compared to the expected diffraction pattern of PbI_2 to show that there was no material degradation after exposure to ambient conditions.

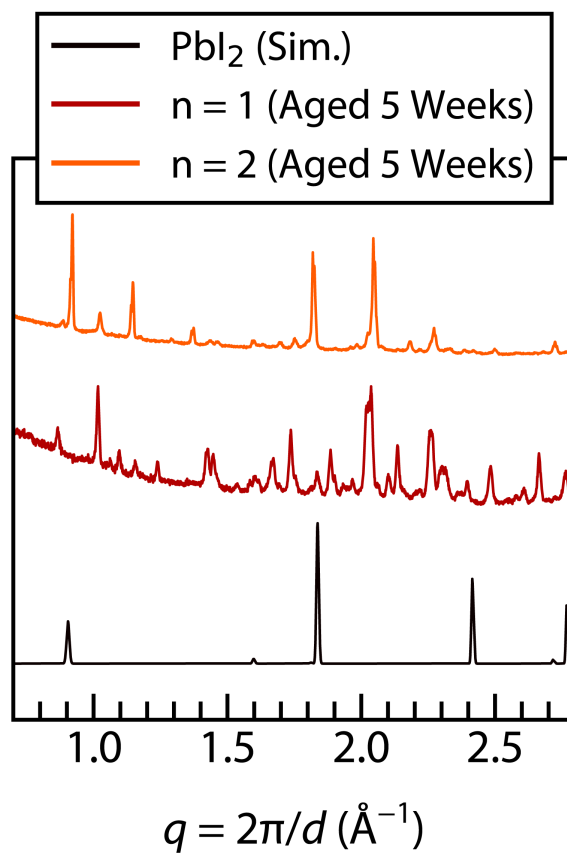


Figure 6.8: Powder X-ray diffraction patterns of $(\text{BPEA})_2\text{PbI}_4$ and $(\text{BPEA})_2(\text{MA})\text{Pb}_2\text{I}_7$ powders aged for five weeks in ambient conditions, along with simulated diffraction pattern of PbI_2 . Comparison with the simulated pattern illustrates no degradation of Ruddlesden–Popper phases into lead iodide.

6.6 Acknowledgments

The authors thank Emily Levin for assistance with initial stages of the manuscript, and Dr. Clayton Dahlman, Rhys Kennard, and Ryan DeCrescent for insightful discussions. This work was supported by the U.S. Department of Energy, Office of Science, Basic Energy Sciences under award number DE-SC-0012541. Development of the microwave conductivity instrument was supported by the Defense Threat Reduction Agency under Award Number HDTRA1-15-0023. The research reported here made use of the shared facilities of the Materials Research Science and Engineering Center (MRSEC) at UC Santa Barbara through NSF DMR 1720256. The UC Santa Barbara MRSEC is a member of the Materials Research Facilities Network (www.mrfn.org).

6.7 Permissions and Attributions

The content of this chapter and appendix has been reprinted with permission from “Enhanced Yield-Mobility Products in Hybrid Halide Ruddlesden–Popper Compounds with Aromatic Ammonium Spacers” by N. R. Venkatesan *et al.* Copyright © 2019 Royal Society of Chemistry.

6.8 References

1. Papavassiliou, G. C., Mousdis, G. A. & Koutselas, I. B. Some New Organic–Inorganic Hybrid Semiconductors Based on Metal Halide Units: Structural, Optical and Related Properties†. *Advanced Materials for Optics and Electronics* **9**, 265–271 (1999).
2. Saparov, B. & Mitzi, D. B. Organic–Inorganic Perovskites: Structural Versatility for Functional Materials Design. *Chemical Reviews* **116**, 4558–4596 (2016).
3. Berry, J., Buonassisi, T., Egger, D. A., Hodes, G., Kronik, L., Loo, Y.-L., Lubomirsky, I., Marder, S. R., Mastai, Y., Miller, J. S., Mitzi, D. B., Paz, Y., Rappe, A. M., Riess, I., Rybtchinski, B., Stafsudd, O., Stevanovic, V., Toney, M. F., Zitoun, D., Kahn, A., Ginley, D. & Cahen, D. Hybrid Organic-Inorganic Perovskites (HOIPs): Opportunities and Challenges. *Advanced Materials* **27**, 5102–5112 (2015).
4. Zhang, W., Eperon, G. E. & Snaith, H. J. Metal Halide Perovskites for Energy Applications. *Nature Energy* **1**, 16048 (2016).
5. Mitzi, D. B., Chondroudis, K. & Kagan, C. R. Organic-Inorganic Electronics. *IBM Journal of Research and Development* **45**, 29–45 (2001).
6. Mitzi, D. B., Kosbar, L. L., Murray, C. E., Copel, M. & Afzali, A. High-Mobility Ultrathin Semiconducting Films Prepared by Spin Coating. *Nature* **428**, 299–303 (2004).
7. Mitzi, D. B., Feild, C. A., Harrison, W. T. A. & Guloy, A. M. Conducting Tin Halides with a Layered Organic-Based Perovskite Structure. *Nature* **369**, 467–469 (1994).
8. Yang, W. S., Park, B.-W., Jung, E. H., Jeon, N. J., Kim, Y. C., Lee, D. U., Shin, S. S., Seo, J., Kim, E. K., Noh, J. H. & Seok, S. I. Iodide Management in Formamidinium-Lead-Halide-Based Perovskite Layers for Efficient Solar Cells. *Science* **356**, 1376–1379 (2017).
9. Polman, A., Knight, M., Garnett, E. C., Ehrler, B. & Sinke, W. C. Photovoltaic Materials: Present Efficiencies and Future Challenges. *Science* **352**, aad4424 (2016).
10. Green, M. A., Emery, K., Hishikawa, Y., Warta, W., Dunlop, E. D., Levi, D. H. & Ho-Baillie, A. W. Y. Solar Cell Efficiency Tables (Version 49). *Progress in Photovoltaics: Research and Applications* **25**, 3–13 (2017).
11. Yuan, M., Quan, L. N., Comin, R., Walters, G., Sabatini, R., Voznyy, O., Hoogland, S., Zhao, Y., Beauregard, E. M., Kanjanaboos, P., Lu, Z., Kim, D. H. & Sargent, E. H. Perovskite Energy Funnels for Efficient Light-Emitting Diodes. *Nature Nanotechnology* **11**, 872–877 (2016).
12. Wang, N., Cheng, L., Ge, R., Zhang, S., Miao, Y., Zou, W., Yi, C., Sun, Y., Cao, Y. & Yang, R. Perovskite Light-Emitting Diodes Based on Solution-Processed Self-Organized Multiple Quantum Wells. *Nature Photonics* **10**, 699 (2016).
13. Lin, K., Xing, J., Quan, L. N., de Arquer, F. P. G., Gong, X., Lu, J., Xie, L., Zhao, W., Zhang, D. & Yan, C. Perovskite Light-Emitting Diodes with External Quantum Efficiency Exceeding 20 per Cent. *Nature* **562**, 245 (2018).

14. Xiao, Z., Kerner, R. A., Zhao, L., Tran, N. L., Lee, K. M., Koh, T.-W., Scholes, G. D. & Rand, B. P. Efficient Perovskite Light-Emitting Diodes Featuring Nanometre-Sized Crystallites. *Nature Photonics* **11**, 108–115 (2017).
15. Kovalenko, M. V., Protesescu, L. & Bodnarchuk, M. I. Properties and Potential Optoelectronic Applications of Lead Halide Perovskite Nanocrystals. *Science* **358**, 745–750 (2017).
16. Protesescu, L., Yakunin, S., Bodnarchuk, M. I., Krieg, F., Caputo, R., Hendon, C. H., Yang, R. X., Walsh, A. & Kovalenko, M. V. Nanocrystals of Cesium Lead Halide Perovskites (CsPbX₃, X= Cl, Br, and I): Novel Optoelectronic Materials Showing Bright Emission with Wide Color Gamut. *Nano Letters* **15**, 3692–3696 (2015).
17. Weidman, M. C., Goodman, A. J. & Tisdale, W. A. Colloidal Halide Perovskite Nanoplatelets: An Exciting New Class of Semiconductor Nanomaterials. *Chemistry of Materials* **29**, 5019–5030 (2017).
18. Smith, M. D. & Karunadasa, H. I. White-Light Emission from Layered Halide Perovskites. *Accounts of Chemical Research* **51**, 619–627 (2018).
19. Smith, M. D., Jaffe, A., Dohner, E. R., Lindenberg, A. M. & Karunadasa, H. I. Structural Origins of Broadband Emission from Layered Pb–Br Hybrid Perovskites. *Chemical Science* **8**, 4497–4504 (2017).
20. Kennard, R. M., Dahlman, C. J., Nakayama, H., DeCrescent, R. A., Schuller, J. A., Seshadri, R., Mukherjee, K. & Chabynyc, M. L. Phase Stability and Diffusion in Lateral Heterostructures of Methyl Ammonium Lead Halide Perovskites. *ACS Applied Materials & Interfaces* **11**, 25313–25321 (2019).
21. Divitini, G., Cacovich, S., Matteocci, F., Cinà, L., Di Carlo, A. & Ducati, C. *In Situ* Observation of Heat-Induced Degradation of Perovskite Solar Cells. *Nature Energy* **1**, 15012 (2016).
22. Mosconi, E., Azpiroz, J. M. & De Angelis, F. Ab Initio Molecular Dynamics Simulations of Methylammonium Lead Iodide Perovskite Degradation by Water. *Chemistry of Materials* **27**, 4885–4892 (2015).
23. Li, Y., Xu, X., Wang, C., Ecker, B., Yang, J., Huang, J. & Gao, Y. Light-Induced Degradation of CH₃NH₃PbI₃ Hybrid Perovskite Thin Film. *The Journal of Physical Chemistry C* **121**, 3904–3910 (2017).
24. Aristidou, N., Sanchez-Molina, I., Chotchuangchutchaval, T., Brown, M., Martinez, L., Rath, T. & Haque, S. A. The Role of Oxygen in the Degradation of Methylammonium Lead Trihalide Perovskite Photoactive Layers. *Angewandte Chemie International Edition* **54**, 8208–8212 (2015).
25. Abraha Berhe, T., Su, W.-N., Chen, C.-H., Pan, C.-J., Cheng, J.-H., Chen, H.-M., Tsai, M.-C., Chen, L.-Y., Aregahegn Dubale, A. & Hwang, B.-J. Organometal Halide Perovskite Solar Cells: Degradation and Stability. *Energy & Environmental Science* **9**, 323–356 (2016).

26. Zhao, X. & Park, N.-G. Stability Issues on Perovskite Solar Cells. *Photonics* **2**, 1139–1151 (2015).
27. Smith, I. C., Hoke, E. T., Solis-Ibarra, D., McGehee, M. D. & Karunadasa, H. I. A Layered Hybrid Perovskite Solar-Cell Absorber with Enhanced Moisture Stability. *Angewandte Chemie International Edition* **126**, 11414–11417 (2014).
28. Tsai, H., Nie, W., Blancon, J.-C., Stoumpos, C. C., Asadpour, R., Harutyunyan, B., Neukirch, A. J., Verduzco, R., Crochet, J. J., Tretiak, S., Pedesseau, L., Even, J., Alam, M. A., Gupta, G., Lou, J., Ajayan, P. M., Bedzyk, M. J., Kanatzidis, M. G. & Mohite, A. D. High-Efficiency Two-Dimensional Ruddlesden-Popper Perovskite Solar Cells. *Nature* **536**, 312–316 (2016).
29. Pedesseau, L., Saponi, D., Traore, B., Robles, R., Fang, H.-H., Loi, M. A., Tsai, H., Nie, W., Blancon, J.-C., Neukirch, A., Tretiak, S., Mohite, A. D., Katan, C., Even, J. & Kepenekian, M. Advances and Promises of Layered Halide Hybrid Perovskite Semiconductors. *ACS Nano* **10**, 9776–9786 (2016).
30. Zhang, X., Wu, G., Yang, S., Fu, W., Zhang, Z., Chen, C., Liu, W., Yan, J., Yang, W. & Chen, H. Vertically Oriented 2D Layered Perovskite Solar Cells with Enhanced Efficiency and Good Stability. *Small* **13**, 1700611 (2017).
31. Ruddlesden, S. N. & Popper, P. New Compounds of the K_2NiF_4 Type. *Acta Crystallographica* **10**, 538–539 (1957).
32. Ruddlesden, S. N. & Popper, P. The Compound $Sr_3Ti_2O_7$ and Its Structure. *Acta Crystallographica* **11**, 54–55 (1958).
33. Chen, Y., Sun, Y., Peng, J., Tang, J., Zheng, K. & Liang, Z. 2D Ruddlesden–Popper Perovskites for Optoelectronics. *Advanced Materials* **30**, 1703487 (2017).
34. Chen, Y., Yu, S., Sun, Y. & Liang, Z. Phase Engineering in Quasi-2D Ruddlesden–Popper Perovskites. *The Journal of Physical Chemistry Letters* **9**, 2627–2631 (2018).
35. Koh, T. M., Febriansyah, B. & Mathews, N. Ruddlesden-Popper Perovskite Solar Cells. *Chem* **2**, 326–327 (2017).
36. Chen, Y., Sun, Y., Peng, J., Zhang, W., Su, X., Zheng, K., Pullerits, T. & Liang, Z. Tailoring Organic Cation of 2D Air-Stable Organometal Halide Perovskites for Highly Efficient Planar Solar Cells. *Advanced Energy Materials* **7**, 1700162 (2017).
37. Liu, Y., Akin, S., Pan, L., Uchida, R., Arora, N., Milić, J. V., Hinderhofer, A., Schreiber, F., Uhl, A. R., Zakeeruddin, S. M., Hagfeldt, A., Dar, M. I. & Grätzel, M. Ultrahydrophobic 3D/2D Fluoroarene Bilayer-Based Water-Resistant Perovskite Solar Cells with Efficiencies Exceeding 22%. *Science Advances* **5**, eaaw2543 (2019).
38. Wang, Z., Lin, Q., Chmiel, F. P., Sakai, N., Herz, L. M. & Snaith, H. J. Efficient Ambient-Air-Stable Solar Cells with 2D–3D Heterostructured Butylammonium-Caesium-Formamidinium Lead Halide Perovskites. *Nature Energy* **6**, nenergy2017135 (2017).

39. Lee, J.-W., Dai, Z., Han, T.-H., Choi, C., Chang, S.-Y., Lee, S.-J., Marco, N. D., Zhao, H., Sun, P., Huang, Y. & Yang, Y. 2D Perovskite Stabilized Phase-Pure Formamidinium Perovskite Solar Cells. *Nature Communications* **9**, 3021 (2018).
40. Hamaguchi, R., Yoshizawa-Fujita, M., Miyasaka, T., Kunugita, H., Ema, K., Takeoka, Y. & Rikukawa, M. Formamidine and Cesium-Based Quasi-Two-Dimensional Perovskites as Photovoltaic Absorbers. *Chemical Communications* **53**, 4366–4369 (2017).
41. Yu, D., Cao, F., Shen, Y., Liu, X., Zhu, Y. & Zeng, H. Dimensionality and Interface Engineering of 2D Homologous Perovskites for Boosted Charge-Carrier Transport and Photodetection Performances. *The Journal of Physical Chemistry Letters* **8**, 2565–2572 (2017).
42. Weidman, M. C., Seitz, M., Stranks, S. D. & Tisdale, W. A. Highly Tunable Colloidal Perovskite Nanoplatelets through Variable Cation, Metal, and Halide Composition. *ACS Nano* **10**, 7830–7839 (2016).
43. Chen, Z., Zhang, C., Jiang, X.-F., Liu, M., Xia, R., Shi, T., Chen, D., Xue, Q., Zhao, Y.-J., Su, S., Yip, H.-L. & Cao, Y. High-Performance Color-Tunable Perovskite Light Emitting Devices through Structural Modulation from Bulk to Layered Film. *Advanced Materials* **29**, 1603157 (2017).
44. Du, K.-z., Tu, Q., Zhang, X., Han, Q., Liu, J., Zauscher, S. & Mitzi, D. B. Two-Dimensional Lead(II) Halide-Based Hybrid Perovskites Templated by Acene Alkylamines: Crystal Structures, Optical Properties, and Piezoelectricity. *Inorganic Chemistry* **56**, 9291–9302 (2017).
45. Mitzi, D. B. Templating and Structural Engineering in Organic–Inorganic Perovskites. *Journal of the Chemical Society, Dalton Transactions*, 1–12 (2001).
46. Mitzi, D. B., Chondroudis, K. & Kagan, C. R. Design, Structure, and Optical Properties of Organic-Inorganic Perovskites Containing an Oligothiophene Chromophore. *Inorganic Chemistry* **38**, 6246–6256 (1999).
47. Milot, R. L., Sutton, R. J., Eperon, G. E., Haghighirad, A. A., Martinez Hardigree, J., Miranda, L., Snaith, H. J., Johnston, M. B. & Herz, L. M. Charge-Carrier Dynamics in 2D Hybrid Metal-Halide Perovskites. *Nano Letters* **16**, 7001–7007 (2016).
48. Mao, L., Ke, W., Pedesseau, L., Wu, Y., Katan, C., Even, J., Wasielewski, M. R., Stoumpos, C. C. & Kanatzidis, M. G. Hybrid Dion–Jacobson 2D Lead Iodide Perovskites. *Journal of the American Chemical Society* **140**, 3775–3783 (2018).
49. Li, Y., Milić, J. V., Ummadisingu, A., Seo, J.-Y., Im, J.-H., Kim, H.-S., Liu, Y., Dar, M. I., Zakeeruddin, S. M. & Wang, P. Bifunctional Organic Spacers for Formamidinium-Based Hybrid Dion–Jacobson Two-Dimensional Perovskite Solar Cells. *Nano Letters* **19**, 150–157 (2018).

50. Momma, K. & Izumi, F. *VESTA-3 for Three-Dimensional Visualization of Crystal, Volumetric and Morphology Data*. *Journal of Applied Crystallography* **44**, 1272–1276 (2011).
51. Venkatesan, N. R., Kennard, R. M., DeCrescent, R. A., Nakayama, H., Dahlman, C. J., Perry, E. E., Schuller, J. A. & Chabinye, M. L. Phase Intergrowth and Structural Defects in Organic Metal Halide Ruddlesden–Popper Thin Films. *Chemistry of Materials* **30**, 8615–8623 (2018).
52. Calabrese, J., Jones, N. L., Harlow, R. L., Herron, N., Thorn, D. L. & Wang, Y. Preparation and Characterization of Layered Lead Halide Compounds. *Journal of the American Chemical Society* **113**, 2328–2330 (1991).
53. Grancini, G., Roldán-Carmona, C., Zimmermann, I., Mosconi, E., Lee, X., Martineau, D., Nabey, S., Oswald, F., Angelis, F. D., Graetzel, M. & Nazeeruddin, M. K. One-Year Stable Perovskite Solar Cells by 2D/3D Interface Engineering. *Nature Communications* **8**, 15684 (2017).
54. Kubelka, P. & Munk, F. An Article on Optics of Paint Layers. *Z. Tech. Phys* **12** (1931).
55. Venkatesan, N. R., Labram, J. G. & Chabinye, M. L. Charge-Carrier Dynamics and Crystalline Texture of Layered Ruddlesden–Popper Hybrid Lead Iodide Perovskite Thin Films. *ACS Energy Letters* **3**, 380–386 (2018).
56. Labram, J. G., Venkatesan, N. R., Takacs, C. J., Evans, H. A., Perry, E. E., Wudl, F. & Chabinye, M. L. Charge Transport in a Two-Dimensional Hybrid Metal Halide Thiocyanate Compound. *Journal of Materials Chemistry C* **5**, 5930–5938 (2017).
57. Oga, H., Saeki, A., Ogomi, Y., Hayase, S. & Seki, S. Improved Understanding of the Electronic and Energetic Landscapes of Perovskite Solar Cells: High Local Charge Carrier Mobility, Reduced Recombination, and Extremely Shallow Traps. *Journal of the American Chemical Society* **136**, 13818–13825 (2014).
58. Savenije, T. J., Ponceca, C. S., Kunneman, L., Abdellah, M., Zheng, K., Tian, Y., Zhu, Q., Canton, S. E., Scheblykin, I. G., Pullerits, T., Yartsev, A. & Sundström, V. Thermally Activated Exciton Dissociation and Recombination Control the Carrier Dynamics in Organometal Halide Perovskite. *The Journal of Physical Chemistry Letters* **5**, 2189–2194 (2014).
59. Hutter, E. M., Gélvez-Rueda, M. C., Osherov, A., Bulović, V., Grozema, F. C., Stranks, S. D. & Savenije, T. J. Direct-Indirect Character of the Bandgap in Methylammonium Lead Iodide Perovskite. *Nature Materials* **16**, 115–120 (2017).
60. Ponceca, C. S., Savenije, T. J., Abdellah, M., Zheng, K., Yartsev, A., Pascher, T., Harlang, T., Chabera, P., Pullerits, T., Stepanov, A., Wolf, J.-P. & Sundström, V. Organometal Halide Perovskite Solar Cell Materials Rationalized: Ultrafast Charge Generation, High and Microsecond-Long Balanced Mobilities, and Slow Recombination. *Journal of the American Chemical Society* **136**, 5189–5192 (2014).

61. Brenes, R., Guo, D., Osherov, A., Noel, N. K., Eames, C., Hutter, E. M., Pathak, S. K., Niroui, F., Friend, R. H. & Islam, M. S. Metal Halide Perovskite Polycrystalline Films Exhibiting Properties of Single Crystals. *Joule* **1**, 155–167 (2017).
62. Hu, Y., Hutter, E. M., Rieder, P., Grill, I., Hanisch, J., Aygüler, M. F., Hufnagel, A. G., Handloser, M., Bein, T. & Hartschuh, A. Understanding the Role of Cesium and Rubidium Additives in Perovskite Solar Cells: Trap States, Charge Transport, and Recombination. *Advanced Energy Materials* **8**, 1703057 (2018).
63. Abdi-Jalebi, M., Andaji-Garmaroudi, Z., Cacovich, S., Stavrakas, C., Philippe, B., Richter, J. M., Alsari, M., Booker, E. P., Hutter, E. M. & Pearson, A. J. Maximizing and Stabilizing Luminescence from Halide Perovskites with Potassium Passivation. *Nature* **555**, 497 (2018).
64. Reid, O. G., Moore, D. T., Li, Z., Zhao, D., Yan, Y., Zhu, K. & Rumbles, G. Quantitative Analysis of Time-Resolved Microwave Conductivity Data. *Journal of Physics D: Applied Physics* **50**, 493002 (2017).
65. Labram, J. G. & Chabinc, M. L. Recombination at High Carrier Density in Methylammonium Lead Iodide Studied Using Time-Resolved Microwave Conductivity. *Journal of Applied Physics* **122**, 065501 (2017).
66. Stoumpos, C. C., Cao, D. H., Clark, D. J., Young, J., Rondinelli, J. M., Jang, J. I., Hupp, J. T. & Kanatzidis, M. G. Ruddlesden–Popper Hybrid Lead Iodide Perovskite 2D Homologous Semiconductors. *Chemistry of Materials* **28**, 2852–2867 (2016).
67. Silver, S., Yin, J., Li, H., Brédas, J.-L. & Kahn, A. Characterization of the Valence and Conduction Band Levels of $n = 1$ 2D Perovskites: A Combined Experimental and Theoretical Investigation. *Advanced Energy Materials* **8**, 1703468 (2018).
68. Straus, D. B. & Kagan, C. R. Electrons, Excitons, and Phonons in Two-Dimensional Hybrid Perovskites: Connecting Structural, Optical, and Electronic Properties. *The Journal of Physical Chemistry Letters* **9**, 1434–1447 (2018).
69. Reid, O. G., Yang, M., Kopidakis, N., Zhu, K. & Rumbles, G. Grain-Size-Limited Mobility in Methylammonium Lead Iodide Perovskite Thin Films. *ACS Energy Letters* **1**, 561–565 (2016).
70. Sheldrick, G. M. *SADABS* University of Göttingen. Germany, 1996.
71. Sheldrick, G. M. Crystal Structure Refinement with SHELXL. *Acta Crystallographica Section C: Structural Chemistry* **71**, 3–8 (2015).
72. Hauptman, H. Phasing Methods for Protein Crystallography. *Current Opinion in Structural Biology* **7**, 672–680 (1997).
73. Toby, B. H. & Von Dreele, R. B. GSAS-II: The Genesis of a Modern Open-Source All Purpose Crystallography Software Package. *Journal of Applied Crystallography* **46**, 544–549 (2013).

74. Dollase, W. A. Correction of Intensities for Preferred Orientation in Powder Diffraction: Application of the March Model. *Journal of Applied Crystallography* **19**, 267–272 (1986).
75. Savenije, T. J., Ferguson, A. J., Kopidakis, N. & Rumbles, G. Revealing the Dynamics of Charge Carriers in Polymer:Fullerene Blends Using Photoinduced Time-Resolved Microwave Conductivity. *The Journal of Physical Chemistry C* **117**, 24085–24103 (2013).